Generation, Recombination and Extraction of Charges in Polymer:Fullerene Bulk Heterojunction Solar Cells

Cumulative Dissertation
in partial fulfillment of the requirements of the degree of
doctor rerum naturalium (Dr. rer. nat) in Physics

Submitted to
the Faculty of Mathematics and Natural Sciences of
the University of Potsdam

by
Dipl. Phys. Steve Albrecht

Potsdam, September 2014

Published online at the
Institutional Repository of the University of Potsdam:
URL http://publishup.uni-potsdam.de/opus4-ubp/frontdoor/index/index/docId/7228/
URN urn:nbn:de:kobv:517-opus4-72285
http://nbn-resolving.de/urn:nbn:de:kobv:517-opus4-72285

Abstract

A dramatic efficiency improvement of bulk heterojunction solar cells based on electron-donating conjugated polymers in combination with soluble fullerene derivatives has been achieved over the past years. Certified and reported power conversion efficiencies now reach over 9% for single junctions and exceed the 10% benchmark for tandem solar cells. This trend brightens the vision of organic photovoltaics becoming competitive with inorganic solar cells including the realization of low-cost and large-area organic photovoltaics. For the best performing organic materials systems, the yield of charge generation can be very efficient. However, a detailed understanding of the free charge carrier generation mechanisms at the donor acceptor interface and the energy loss associated with it needs to be established. Moreover, organic solar cells are limited by the competition between charge extraction and free charge recombination, accounting for further efficiency losses. A conclusive picture and the development of precise methodologies for investigating the fundamental processes in organic solar cells are crucial for future material design, efficiency optimization, and the implementation of organic solar cells into commercial products.

In order to advance the development of organic photovoltaics, my thesis focuses on the comprehensive understanding of charge generation, recombination and extraction in organic bulk heterojunction solar cells summarized in 6 chapters on the cumulative basis of 7 individual publications.

The general motivation guiding this work was the realization of an efficient hybrid inorganic/organic tandem solar cell with sub-cells made from amorphous hydrogenated silicon and organic bulk heterojunctions. To realize this project aim, the focus was directed to the low band-gap copolymer PCPDTBT and its derivatives, resulting in the examination of the charge carrier dynamics in PCPDTBT:$PC_{70}BM$ blends in relation to by the blend morphology. The phase separation in this blend can be controlled by the processing additive diiodooctane, enhancing domain purity and size. The quantitative investigation of the free charge formation was realized by utilizing and improving the time delayed collection field technique. Interestingly, a pronounced field dependence of the free carrier generation for all blends is found, with the field dependence being stronger without the additive. Also, the bimolecular recombination coefficient for both blends is rather high and increases with decreasing internal field which we suggest to be caused by a negative field dependence of mobility. The additive speeds up charge extraction which is rationalized by the threefold increase in mobility.

By fluorine attachment within the electron deficient subunit of PCPDTBT, a new polymer F-PCPDTBT is designed. This new material is characterized by a stronger tendency to aggregate as compared to non-fluorinated PCPDTBT. Our measurements show that for F-PCPDTBT:PCBM blends the charge carrier generation becomes more efficient and the field-dependence of free charge carrier generation is weakened. The stronger tendency to aggregate induced by the fluorination also leads to increased polymer rich domains, accompanied in a threefold reduction in the non-geminate recombination

coefficient at conditions of open circuit. The size of the polymer domains is nicely correlated to the field-dependence of charge generation and the Langevin reduction factor, which highlights the importance of the domain size and domain purity for efficient charge carrier generation. In total, fluorination of PCPDTBT causes the PCE to increase from 3.6 to 6.1% due to enhanced fill factor, short circuit current and open circuit voltage. Further optimization of the blend ratio, active layer thickness, and polymer molecular weight resulted in 6.6% efficiency for F-PCPDTBT:$PC_{70}BM$ solar cells.

Interestingly, the double fluorinated version 2F-PCPDTBT exhibited poorer FF despite a further reduction of geminate and non-geminate recombination losses. To further analyze this finding, a new technique is developed that measures the effective extraction mobility under charge carrier densities and electrical fields comparable to solar cell operation conditions. This method involves the bias enhanced charge extraction technique. With the knowledge of the carrier density under different electrical field and illumination conditions, a conclusive picture of the changes in charge carrier dynamics leading to differences in the fill factor upon fluorination of PCPDTBT is attained. The more efficient charge generation and reduced recombination with fluorination is counterbalanced by a decreased extraction mobility. Thus, the highest fill factor of 60% and efficiency of 6.6% is reached for F-PCPDTBT blends, while 2F-PCPDTBT blends have only moderate fill factors of 54% caused by the lower effective extraction mobility, limiting the efficiency to 6.5%.

To understand the details of the charge generation mechanism and the related losses, we evaluated the yield and field-dependence of free charge generation using time delayed collection field in combination with sensitive measurements of the external quantum efficiency and absorption coefficients for a variety of blends. Importantly, both the yield and field-dependence of free charge generation is found to be unaffected by excitation energy, including direct charge transfer excitation below the optical band gap. To access the non-detectable absorption at energies of the relaxed charge transfer emission, the absorption was reconstructed from the CT emission, induced via the recombination of thermalized charges in electroluminescence. For a variety of blends, the quantum yield at energies of charge transfer emission was identical to excitations with energies well above the optical band-gap. Thus, the generation proceeds via the split-up of the thermalized charge transfer states in working solar cells. Further measurements were conducted on blends with fine-tuned energy levels and similar blend morphologies by using different fullerene derivatives. A direct correlation between the efficiency of free carrier generation and the energy difference of the relaxed charge transfer state relative to the energy of the charge separated state is found. These findings open up new guidelines for future material design as new high efficiency materials require a minimum energetic offset between charge transfer and the charge separated state while keeping the HOMO level (and LUMO level) difference between donor and acceptor as small as possible.

Contents

1 Introduction

1.1 Energy Turnaround for Sustainability

The 20th century was characterized by intense industrial growth fueled by the extensive use of non-renewable energy resources to meet the ever-increasing demand for energy caused by the remarkable socioeconomic prosperity. Along with that, the CO_2 pollution of the earth's atmosphere was steadily increasing by the CO_2 output especially from industrial countries like China, USA and the European Union.[1] The beginning of the 21st century marked a dramatic change in mankind's thinking about non-renewable resources for energy production. This was triggered by increased awareness of the effect of CO_2 emissions on the climate which was shown to lead to enhanced greenhouse effects, elevated temperatures and more frequent natural disasters.[2] The general public could feel that the stepwise increasing average temperature on planet earth may impact the climate conditions resulting in unusual and extreme weather conditions all over the world. The population started thinking "green" and taking care of the CO_2 footprint. One of the key events further changing the thinking about energy production was a Tsunami in 2011 in Japan that destroyed the nuclear power plant in Fukushima. After this shocking event many people, especially in Germany, wanted to avoid nuclear plants as energy production facilities. All of that triggered the request of increasing the fraction of renewable energy resources in the total energy production. This strong change in humans thinking is named the "Energy Turnaround".

In 2013 still 55.7 % of the total electrical power in Germany was produced from coal and gas.[3] Only 23.9% of the total power was generated from renewable energy sources such as windpower (8.4%), biomass (6.7%), photovoltaics (4.7%), and waterpower (3.2%).[3] The total energy consumption is projected to increase at least up to the year 2040.[4] The only way to generate more power and lower the CO_2 output at the same time is to expand energy production from renewable energy sources.

The prime renewable energy source in our solar system is the nearest star, the sun. It provides our planet earth with $174 \cdot 10^{15}$ W of radiation power.[5] Part of that power is absorbed and reflected by the atmosphere leaving $89 \cdot 10^{15}$ W to be absorbed by the land and oceans. The energy of the sunlight absorbed by the land and oceans in only 2 hours is more than the world's energy consumption in one year.[6] The energy reaching the surface of the earth in one year is twice as much as the energy available from all non-renewable energy sources on our planet.[7] That inevitably raises the question: why isn't mankind making use of the sun as central energy source?

The answer is that at the moment no photovoltaic or photothermal device for direct solar energy conversion can be fabricated, installed, and operated at a price low enough to generate the significant amount of energy needed for continuous economic growth.[8]

At the end, human's existence in several hundreds or thousands years may depend on the ability to make rational use of the energy provided by the sun to our planet every day for free.[8]

1.2 Organic Solar Cells as Cheap and Green Energy Sources

Solar cells convert energy provided by the sun directly into electrical power. The active material of photovoltaic devices can be fabricated from inorganic semiconductor crystals such as silicon and gallium arsenide with relatively high power conversion efficiencies (PCEs) of about 25.6% and 28.8% for single junctions under non-concentrated light, respectively.[9,10] However, crystalline cells suffer from the fact that production is cost intensive as the crystals need to be grown and cleaned carefully at high temperatures. Nonetheless, mono or polycrystalline silicon modules dominate the solar cell market with ca. 85% of the total cell technologies in 2012.[11]
Other so called "thin film" technologies such as copper indium gallium selenide (CIGSe), cadmium-telluride (CdTe), and micromorph silicon cells have lower efficiencies up to 21.0%, 21.0%, and 13.4%, respectively.[9] Though, thin film photovoltaic devices benefit from partially lower production costs as compared to highly crystalline cells, manufacturing of thin film photovoltaics still requires elevated temperatures or vacuum-processing impeding cheap and uncomplicated device manufacturing.

Organic solar cells made from conjugated small molecules or polymers are highly attractive. PCEs for organic solar cells have shown a tremendous increase over the past ten years and achieve up to 11.7% efficiency with the potential of further optimization.[12,13] Importantly, this technology can benefit from solution processing. That offers reduced production costs by using low temperature printing techniques together with the benefit of flexibility, light weight, less material consumption, and semitransparent devices. Also, a remarkable number of organic semiconducting molecules are available. With that, the electronic as well as the optical properties can be fine-tuned to meet special requirements. In principle organic solar devices can be of any color or degree of transparency, making them ideal for integrated facade elements in buildings.

The history of organic solar cells with efficiency enhancements from 1 to over 10% took three decades and started in 1986 when Tang published the first organic solar cell combining electron donor (D) and acceptor (A).[14] The cell was a bilayer with vacuum processed small molecules demonstrating a high fill factor (*FF*) of 65%. This showed the great potential of organic photovoltaics (OPV) when D and A are used together. Five years later, the first bulk heterojunction (BHJ) was presented that consisted of mixed D and A small molecules which have been co-evaporated to form the active layer.[15] With the concept of a BHJ the majority of the photogenerated excitations can reach the interface before recombining, thereby increasing the generated current. A further milestone in this history was the work by Sariciftci et al. in 1992, proving electron transfer from a conjugated polymer (a derivative of poly-phenylene-vinylene, PPV) to the Buckminster fullerene C_{60} in blend layers.[16] This work opened the way to the first solution processed bulk heterojunction device published in 1994 by Yu et al., making

use of the soluble PPV derivative MEH-PPV and C_{60}.[17] Only one year later the C_{60} derivate phenyl-C_{61}-butyric acid methyl ester ($PC_{60}BM$) with significantly higher solubility was synthesized by Hummelen et al.,[18] which was an improvement to C_{60} in BHJ solar cells when using the common (at that time) donor MEH-PPV.[19]

Around the year 2000, the scientific and industrial community realized the potential of this technology and with that, the intensity of research and the number of publications started to increase significantly.[20] By fine tuning of the phase separation between the soluble PPV derivative MDMO-PPV and $PC_{60}BM$ utilizing different solvents, a PCE of 2.5% could be realized in 2001.[21] One year later the donor material poly(3-hexylthiophene) (P3HT) was shown to achieve 70% external quantum efficiency (EQE) with PCBM, which was correlated with an internal quantum efficiency (IQE) close to 100%.[22] Another important development was the synthesis and implementation of $PC_{70}BM$ into organic solar cells. $PC_{70}BM$ benefits from enhanced absorptivity in the visible region as compared to $PC_{60}BM$ caused by higher dipole transition moments in the asymmetric fullerene cage of C_{70}.[23] In 2005 control over the morphological evolution of P3HT:fullerene blends was achieved via high boiling point solvents, slow growth solvent annealing in combination with thermal annealing, resulting in 4.4% efficiency.[24]

The era beyond the 5% limit started with novel donor co-polymers containing electron rich (push) and electron deficient (pulling) subunits. Early stage push-pull copolymers showed either relatively low HOMO values together with larger band-gaps like polyfluorenes (e.g. APFO-3)[25] or polycarbazoles (e.g. PCDTBT),[26] or higher HOMOs and lower band-gaps like fused thiophenes (e.g. PCPDTBT or Si-PCPDTBT).[27,28] In the former case, the open circuit voltage (V_{OC}) is high and the short circuit current (J_{SC}) is low. The latter case is characterized by higher J_{SC} but limited V_{OC}. Thus, efficiencies for PCDTBT and Si-PCPDTBT were around 6.1 and 5.5%, respectively.[29,30] The community further learned that it is essential to reduce the optical band-gap while maintaining a deep HOMO to reach high J_{SC} and high V_{OC} in parallel. A roadmap was established based on the donor HOMO and band-gap values that predicted efficiencies up to 10%.[31] Further material development was conducted inspired by this roadmap.

Another striking finding was attained by Peet and coworkers in 2007.[32] They established the use of processing additives as powerful tool to manipulate the blend morphology associated with enhanced solar cell performance. A donor material class with unexpected high performance, showing both, the combination of high V_{OC} and high J_{SC}, are polymers based on benzodithiophenes. The polymer PTB1 was one of the first polymers from this class, which showed a PCE of 5.3% in 2008.[33] Only one year later, the chemical optimization of PTB1 by the incorporation of fluorine atoms demonstrated certified efficiencies of 6.77%.[34] Further fine tuning of the side chains created the polymer PTB7, which achieved 7.4% efficiency in 2010.[35] Due to intensive interface engineering and device optimization, PTB7:$PC_{70}BM$ solar cells reached a certified PCE of 9.2% in 2012, which is among the best reported organic BHJ single junctions so far.[36]

Another strategy in the efficiency roadmap was to alter the lowest unoccupied molecular orbital (LUMO) of the fullerene to reach high V_{OC} values. The PCBM derivative indene-C_{60} bisadduct ($IC_{60}BA$)

with significantly higher LUMO values as compared to the standard acceptor PCBM was reported in 2010. P3HT:$IC_{60}BA$ showed 6.5% efficiency[37] and P3HT:$IC_{70}BA$ yields the highest efficiency for P3HT based solar cells of 7.4%,[38] however higher adduct fullerenes seem to achieve higher performance only with the homopolymer P3HT, being subject of ongoing research.[39]

In parallel to the materials development, fully solution processed organic tandem solar cells were intensively studied. The first solution processed multijunction was realized in 2007 by Gilot et al. with less than 3% efficiency.[40] Some months later, Kim and coworkers showed 6.5% efficient solution processed tandems due to the availability of materials with complementary absorption.[41] Tandem solar cell efficiencies further improved by implementing modified recombination contacts and new material combinations.[42] In 2013 Yang and coworkers achieved a certiefied PCE of 10.6% with inverted tandem cells by the development of a very promising low band-gap material[43] further improving in 2014 to 11.55% in a triple junction.[12]

1.3 Introduction into the Presented Work

As summarized in chapter 1.2, rapid success was made in the last decade regarding efficiency optimization. Despite these achievements which were mostly realized by the introduction of new polymers in a trial and error process, there is still a lack of knowledge about the fundamental working principles in organic BHJ solar cells. Therefore strong research effort is underway at the moment to improve the understanding of this fascinating type of solar cell. A deeper understanding of the fundamental working principles may lead to enhanced efficiencies. With the extended knowledge and implementation of the many advantages of organic materials into low cost production, installation, and maintenance,[44] the portion of energy produced by OPV is likely to expand in the near future, helping to fulfil a wise Energy Turnaround.

The general intention of this work is grounded in that motivation: my work should help to improve the fundamental understanding of free charge generation, recombination and extraction in organic BHJ solar cells with regard to electrical field, the energetic levels and the morphological landscape of the donor-acceptor blend. These three processes are investigated in detail in my thesis and further discussed in the next sections as well as in the summarized papers.

The scientific motivation for the cumulative publications is based on the realization of a high efficiency hybrid tandem solar cell with amorphous hydrogenated silicon (a-Si:H) and organic BHJ sub-cells. This investigation was supported by the project “Kompetenzzentrum Dünnschicht- und Nanotechnologie für Photovoltaik Berlin” (PVcomB) which comprises a sub-project focusing on the realization of a highly efficient hybrid tandem solar cell.

Compared to the variety of optical properties in organic semiconducting compounds, the absorption properties of a-Si:H are fairly fixed with decreasing absorption to longer wavelength throughout the visible range as shown in **Figure 1.1**a. Thus, to allow high efficiency in the tandem cell, complementary absorption of the organic material with regard to the a-Si:H needed to be considered. That made the

implementation of low band-gap materials necessary. When starting with the project in year 2010, the low band-gap copolymer PCPDTBT and Si-PCPDTBT were the most common materials with suitable near infrared absorption properties.

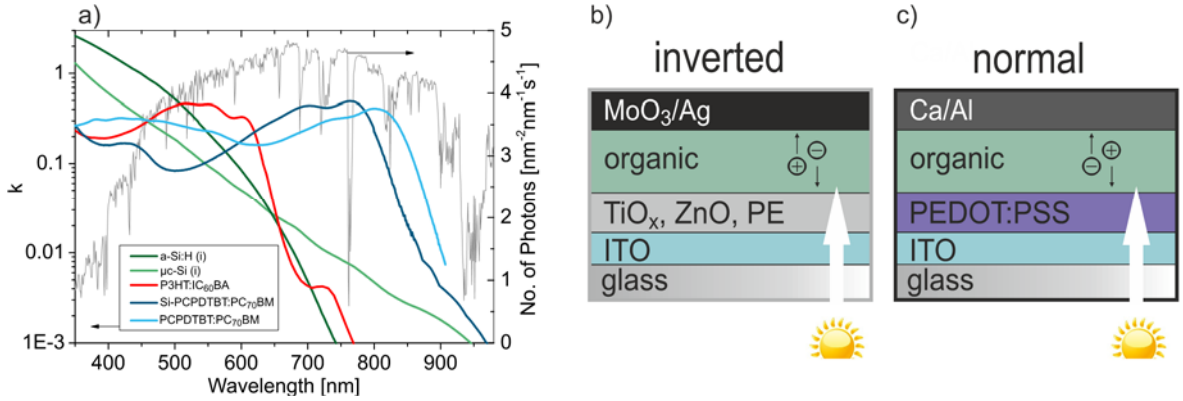

Figure 1.1 (a) The extinction coefficient k (left scale) together with the spectral photon flux density of the AM 1.5G spectrum (right scale). This comparison displays the sharp absorption onsets of the organic materials especially in the range above k=0.01. (b) Inverted device structure with the electron selective contact made from metal oxides such as TiO_x, ZnO or polyelectrolytes (PE) and the hole selective MoO_3/Ag contact as the high work-function anode. (c) Normal device structure with PEDOT:PSS covered ITO and low work-function metal cathodes.

One of the key advantages of organic materials for multijunction cells, compared to inorganic semiconductors, is the overall high absorptivity and the sharp absorption onset as can be seen in Figure 1.1a. Thus, very thin organic films of approximately 100 nm thickness can be utilized to absorb a broad range of wavelengths in single junction configuration. In the organic tandem cell configuration with only two sub-cells, the wide band-gap organic front cell thickness should be in the range of 200-300 nm for optimum light absorption.[43] Additionally it needs to have a high *FF* and V_{OC} at this optically optimized thick layer. Unfortunately, most efficient organic materials suffer from significant extraction losses if the active layer exceeds 100 nm.[45,46] This results in lower *FF*s when used as tandem front cell.[47] The inorganic (a-Si:H) has a band-gap of ca. 1.7 eV and achieves a V_{OC} of around 0.9 V together with IQEs of 100% (in the intrinsic-layer) and *FF*s above 70%, also for the thickness range of 100-250 nm. The hybrid tandem cell configuration, made from an a-Si:H front cell combined with an organic top cell, therefore, has the ability of connecting the advantages of both the inorganic a-Si:H front cell with high *FF*s over a wide thickness range and the high absorptivity organic back cell in one device.

Chapter 4 summarizes the layout and the realization of efficient hybrid tandem solar cells. One important step was the optimization of the recombination contact connecting the a-Si:H front-cell with the organic back-cell in series. After substantial device engineering, a cell with 7.5% efficiency was realized. For the organic sub-cell Si-PCPDTBT:PC_{70}BM was used which demonstrated a high reproducibility. On the bases of optical end electrical simulations, efficiency predictions as function of optical band-gap of the donor are presented together with proof-of-principle studies for increasing the J_{SC} further by light trapping with texturized front contacts.

When optimizing PCPDTBT:PCBM single junctions for the use in tandem cell configurations, we realized that so called inverted devices (see Figure 1.1b) gave higher photocurrents while also showing a better stability against cell degradation. In chapter 5 we present that the inverted structure benefits from optimized light management with 10% more absorption in the active layer at identical layer thickness. Studies on the solar cell performance as function of active layer thickness identify that the charge extraction is hampered especially in the inverted device caused by unfavorable phase segregation.

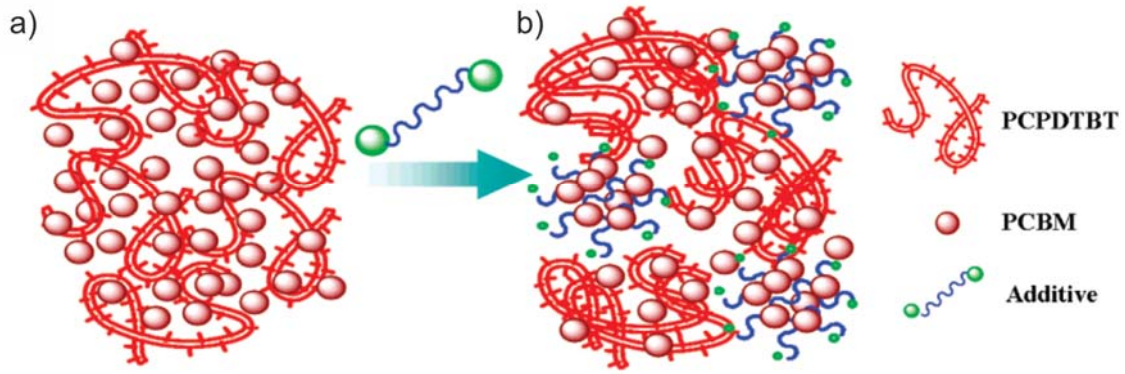

Figure 1.2 Schematic drawing of the polymer:fullerene phase separation influenced by a processing additive (e.g. diiodooctane, DIO) for PCPDTBT:PCBM blends w/o (a) or with (b) DIO. Reprinted with permission from Lee et al.[48] Copyright 2008, American Chemical Society.

A scheme showing how the additive affects the blend morphology is depicted in **Figure 1.2.** According to Lee et al.,[48] the additive should have the following two properties to effectively tune the nano-scale phase separation: First it should selectively dissolve the PCBM and second it needs to have a higher boiling point than the host solvent.[48] With that, the DIO enables the crystallization of PCPDTBT while fullerene aggregates can form slowly due to the delayed drying of PCBM as shown in Figure 1.2. The reason of the significantly improved device performance due to the altered phase separation and domain purity has been a source of controversy in the literature. When the DIO is added, both the *FF* and the J_{SC} increase dramatically. However, no clear correlation between the morphological changes and the charge generation, recombination, or extraction can be drawn from the variety of published papers considering that topic.[49-57] **Table 1.1** highlights some important findings regarding the relevant physical processes and how the mechanisms change when additives were used.

In chapter 6 we present a conclusive view of the change in charge generation, recombination, and mobility when utilizing DIO as solvent additive. We use energy filtered TEM to resolve the distinct changes in morphology e.g. domain size and purity when DIO is utilized. Discrimination between free charge generation and recombination was possible with the technique of time delayed collection field, optimized for improved time resolution. With this methodology, we experimentally showed for the first time that PCPDTBT:$PC_{70}BM$ blends processed with and without additive are limited in device performance by a pronounced field dependence of free charge generation. Together with mobility measurements from charge extraction by linearly increasing voltage, a qualitative description of the changes in carrier dynamics with DIO and the overall efficiency limitations for both samples is possible.

Table 1.1 Literature overview of findings and their explanations of charge carrier dynamics in PCPDTBT:PCBM blends with and without the use of processing additives.

1st author	method	finding / explanation
		charge generation
Lenes[49]	*JV* curve modeling	field-induced PP[a] split up
Moet[50]	*JV* curve modeling	field-induced PP split up, additive increases PP lifetime from 0.5 to 3 µs
Jarzab[51]	CT[b] emission	field-induced PP split up
Jamison[52]	TAS[c]	field independent charge generation, with DIO more free charges formed
		recombination
Agostinelli[56]	TPV[e]	BMR[d] coefficient six times higher with additive
		extraction
Cho[57]	FET[f]	four-fold increase in both hole and electron mobility
Moet[50]	*JV* curve	unaffected electron mobility with and w/o additive
Agostinelli[56]	ToF[g]	hole mobility not significantly altered by additive

[a] PP= polaron pair, [b] CT= charge transfer, [c] TAS= transient absorption spectroscopy, [d] BMR= bimolecular recombination, [e] TPV= transient photovoltage, [f] FET= field-effect transistor, [g] ToF= time of flight.

Not only processing additives, also the chemical modification of the polymer is an effective tool to tune the domain size and purity in the blend. For example, when the bridging atom in PCPDTBT is replaced from carbon to the larger bond spaced silicon, the phase separation significantly alters, alleviating the need for DIO as processing to achieve optimum performance.[30]

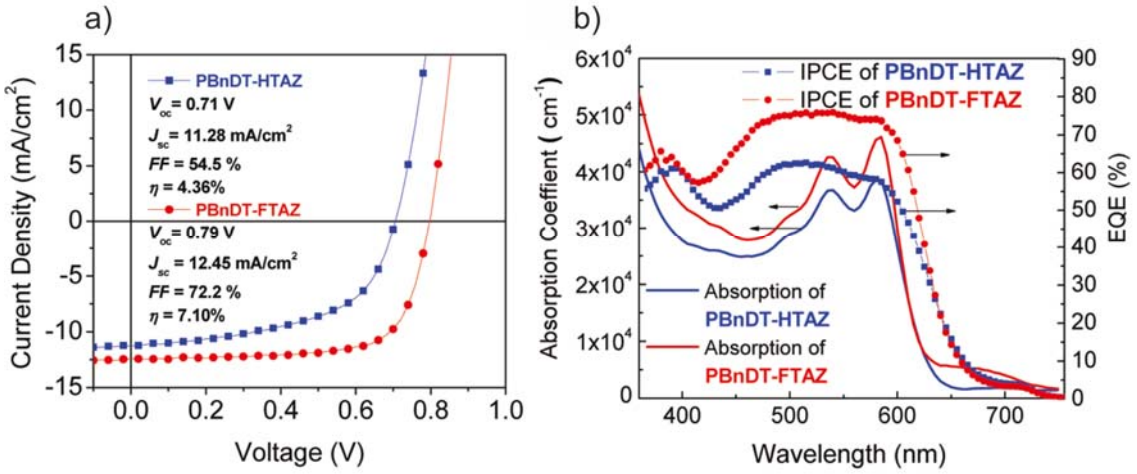

Figure 1.3 Impact of fluorination of the polymer backbone on the optical and device properties for PBnDT-xTAZ polymers blended with PCBM. Data for the non-fluorinated polymer is shown in blue and the fluorinated in red. (a) Current voltage characteristics with performance data. (b) Absorption and EQE spectra. Reprinted with permission from Price et al.[58] Copyright 2011, American Chemical Society.

Attaching fluorine atoms into the polymer backbone was shown to effectively change the solar cell device performance as well. To some extent, fluorination increases the domain purity and phase separation.[59] Comparing analog polymers with fluorinated or non-fluorinated backbones, it is generally found that the introduction of fluorine lowers the HOMO level thereby increasing the *V*oc and enhancing the *FF*, as shown in **Figure 1.3** for the polymer PBnDT-HTAZ and PBnDT-FTAZ.[58] From the general findings in literature it was not conclusively clear why the fluorine attachment enhances the *FF*, as for some polymers the hole mobility decreased with fluorination.[60] Inspired by the encouraging findings for the PBnDT-FTAZ and PTB7 polymers, and by the idea of carefully analyzing the effect of fluorination on charge carrier dynamics, we adopted this strategy to further enhance the performance of PCPDTBT blends by attaching fluorine atoms to the BT unit of PCPDTBT. Chapter 7 summarizes the findings realized with fluorinated PCPDTBT. The changes in energy levels, morphology, the enhanced

charge generation and reduced recombination resulted in improved efficiencies of 6.6%. Strong correlations between the blend morphology and the efficiency of charge generation as well as the non-geminate recombination were found.

Chapter 8 complements chapter 7 as it introduces a unique methodology for measuring the effective extraction mobility in solar cells under small fields comparable to the operational range and charge densities close to one sun illumination conditions. This new methodology makes use of the steady state charge carrier density measured with bias enhanced charge extraction as function of applied bias and illumination intensity. From that, the gradient of the quasi-Fermi level can be estimated which alternatively allows to determine the effective extraction mobility. In combination with charge generation and recombination results gained from time delayed collection field, these results explain how the enhanced generation and reduced recombination is counterbalanced by the lower mobility for mono and di-fluorinated PCPDTBT.

It is quite interesting that the efficiency of charge generation is enhanced when fluorinating PCPDTBT, although the energetic offset between the LUMO levels of the donor and PCBM, which is often considered as driving force for charge separation,[61,62] decreases with fluorination. The detailed mechanism of the charge generation pathway, including the intermediate excitations involved in charge generation is another source of controversy in the literature. Results from ultra-short pump probe experiments suggests that the charge generation is mediated by vibronically and or electronically excited “hot” charge transfer (CT) states as shown in **Figure 1.4**a.[63,64] With that, higher energy excitations should lead to more efficient charge separation as displayed by the enhanced IQE for higher excitation energies in Figure 1.4b (this reported IQE is, however, critically discussed in the literature).[65,66] As the timescale on which signals assigned to free charges appear is faster or comparable to the time of thermalization,[67] it is concluded that excitations separate before thermalizing in the CT manifold. In this context it is thought that only hot generation pathways allow IQEs close to 1, because hot CT states are highly delocalized, helping to reduce the Coulomb binding between the photogenerated hole and electron.[68]

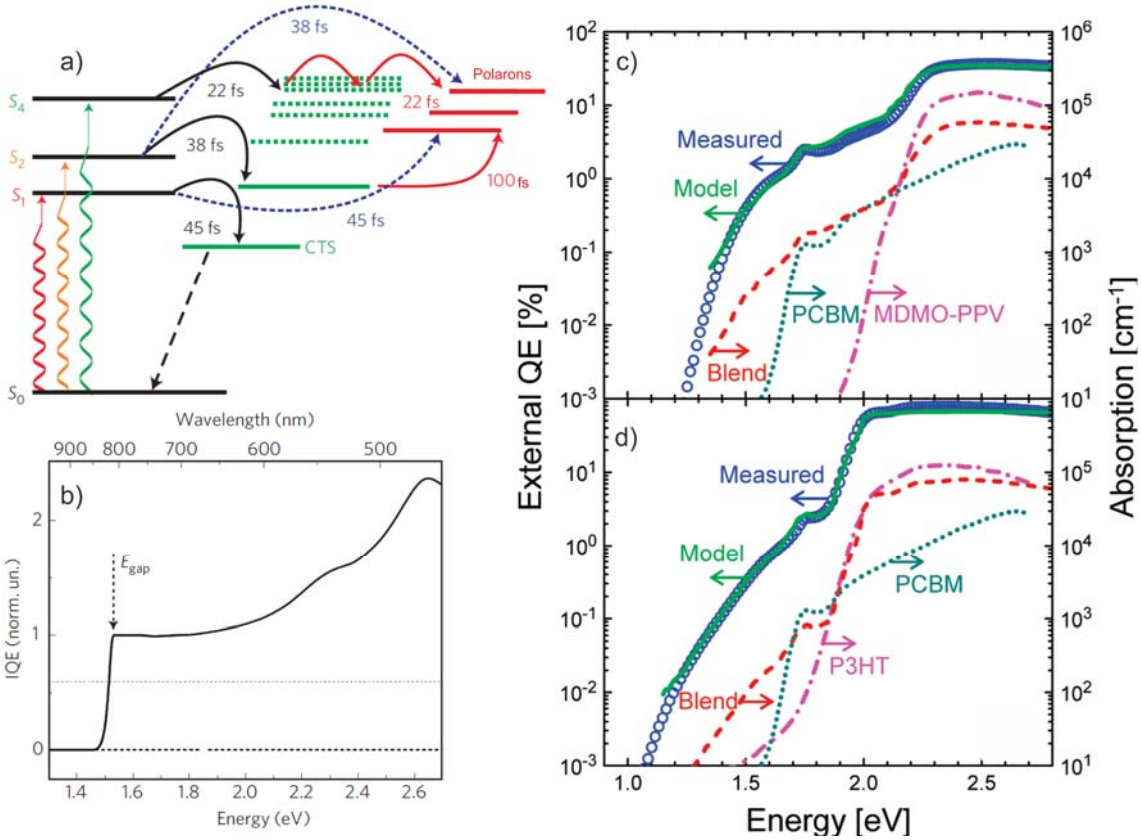

Figure 1.4 (a) Energy scheme for PCPDTBT:$PC_{70}BM$ blends describing excitations into different electronically excited singlet states S_x with timescales of charge transfer and free charge formation. (b) IQE as function of excitation energy for PCPDTBT:$PC_{70}BM$ blends. Reprinted with permission from Grancini et al.[63] Copyright 2012, Rights Managed by Nature Publishing Group. (c) and (d): absorption (right scale) and EQE (left scale) together with the modeled EQE assuming a constant IQE for (c) MDMO-PPV:PCBM and (d) P3HT:PCBM. Reprinted with permission from. Lee et al.[69] Copyright 2010, American Chemical Society.

In contrast, some groups reported the IQE to be rather independent of the excitation energy, even for photon energies below the optical band-gap of the pure donor or acceptor.[69,70] As shown in Figure 1.4c and d, the measured EQE is in perfect agreement to the EQE modeled on the basis of sensitively measured optical constants and an energy independent IQE. This result implies that excitations thermalize to the CT ground state before charges are separated. In chapter 9 we show by careful measurements of the excitation dependence of the charge generation efficiency that in a working solar cell, charge separation starts from relaxed CT ground states rather than from excited states. By the use of different fullerene derivatives with higher LUMO levels (i.e. ICBA), the energetic offset between donor and acceptor is varied. Also the excitation energy is lowered to direct CT state excitation in these blends. From the comprehensive results, detailed knowledge about the states involved in free charge formation and the energy difference dictating the efficiency of charge generation is found.

2 Fundamentals

2.1 Efficiency Limitations

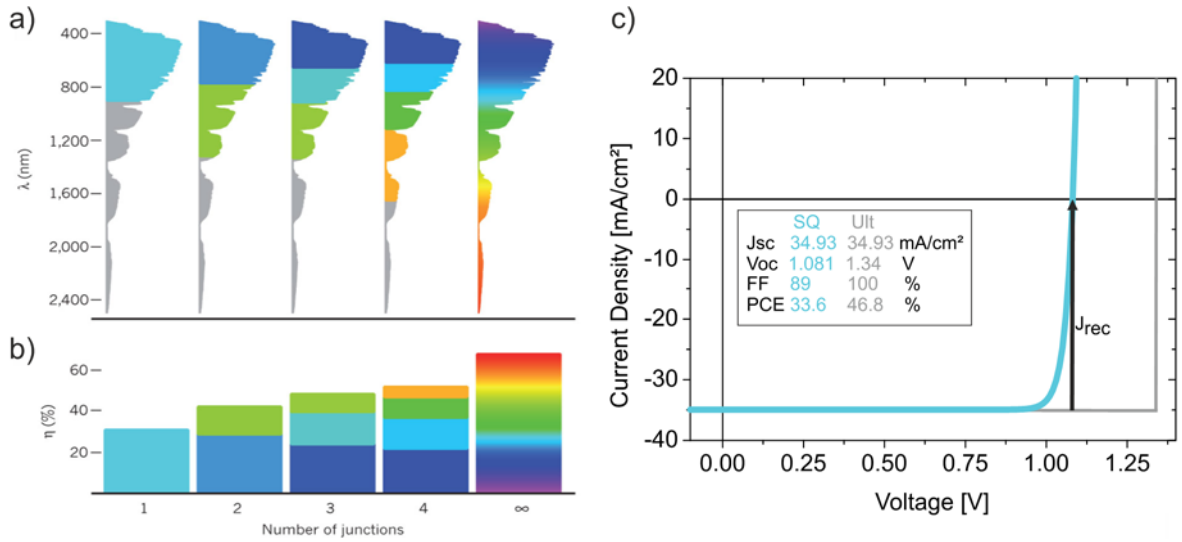

Figure 2.1 (a) AM 1.5G spectrum as a function of wavelength together with (b) the maximum attainable efficiency according to the radiative Shockley Queisser (SQ) limit as function of the number of junctions for non-concentrated sunlight. The colored areas highlight the absorption range in (a) and the efficiency (b) for each sub-cell in the multi-junction. Reprinted with permission from Greatzel et al.[71] Copyright 2012, Rights Managed by Nature Publishing Group. (c) *JV* characteristics for radiative SQ limit and the ultimate efficiency (Ult).

The maximum attainable efficiency for a single junction solar cell assuming that all photons in the incident spectra of AM1.5G illumination above the band-gap E_G are absorbed and generate collected charges is around 46.8% for E_G =1.34 eV (~925 nm), which is known as the ultimate efficiency.[72] It is striking that more than half of the energy provided by the sun is not converted to electrical power at this optimized E_G.This is due to two facts: first, photons with energy less than E_G cannot be absorbed contributing to ca. 30% loss at this band-gap. This is indicated by the resulting cover between the sun spectra and the absorbed photons contributing to this efficiency as shown in **Figure 2.1**a. Second, ca. 23% is lost in a single junction by thermalization of excitations with higher photon energies than E_G.[73] Thermalization is the thermal loss resulting from fast relaxation of charges (or excitons) down to electronically and vibronically relaxed states with energy E_G. An ideal solar cell would have a V_{OC} identical to E_G/e and a *FF* of 1, both being non-achievable under realistic conditions (see Figure 2.1b). Shockley and Queisser (SQ) developed a theory of the maximum attainable efficiency called the SQ limit.[72] They assumed the absorption to be zero below and 1 above E_G. Furthermore, detailed balance is applied which means that in thermal equilibrium (the solar cell has the same temperature as the

radiation field) the number of photons emitted due to radiative recombination equals the number of photons that are absorbed and produce charges:

$$J = 0 = J_{rec} - J_{gen} \tag{2.1}$$

Thus the generative current J_{gen} from absorption and charge creation equals the recombinative current J_{rec} from charges converted into radiative recombination. The solar cell is assumed to emit black body radiation $\Phi_{BB}(E)$ at its temperature of 300K according to Planck's law with $\Phi_{BB}(E) = 2\pi E^2/h^3c^2 \cdot (\exp(E/kT) - 1)^{-1}$. In this equation $\Phi_{BB}(E)$ is the photon flux emitted per surface unit at temperature T, h is the Planck constant and c the speed of light. Thus the recombinative current with e being the elementary charge is:

$$J_{rec} = J_0 = e\int_{E_G}^{\infty} 2\pi E^2/h^3c^2 \cdot (\mathrm{e}^{(E/kT)} - 1)^{-1}(E)dE \cong e\int_{E_G}^{\infty} 2\pi E^2/h^3c^2 \cdot \mathrm{e}^{(-E/kT)})(E)dE. \tag{2.2}$$

J_0 is known as the reverse saturation current and for $E \gg kT$ the Fermi-Dirac statistics is well described by the Boltzmann term in equation 2.2.

When applying a bias to the cell, the non-equlibrium radiation emitted by the semiconductor can be described by the generalized Planck's law introduced by Würfel using again Boltzmann approximation for $E - eV \gg kT$:

$$\Phi^*(V,E) = 2\pi E^2/h^3c^2 \cdot (\mathrm{e}^{(E-eV/kT)} - 1)^{-1} \cong 2\pi E^2/h^3c^2 \cdot \mathrm{e}^{(-E/kT)} \cdot \mathrm{e}^{(eV/kT)} \tag{2.3}$$

With that, the current due to recombination under applied bias in dark is:

$$\mathrm{J}_{rec}(V) = e\int_{E_G}^{\infty} \Phi^*(V,E)dE = \mathrm{e}^{(eV/kT)} \cdot J_0 \tag{2.4}$$

Accounting for the generative current due to absorption of black body radiation $J_{gen} = J_0$, the total extractable current in dark follows the ideal diode equation:[74]

$$J_{dark}(V) = J_{rec}(V) - J_0 = \left(e^{\frac{eV}{kT}} - 1\right)J_0, \tag{2.4}$$

Under illumination the photon flux of the sun $\Phi_{Sun}(E)$ is absorbed by the solar cell to generate an additional current:

$$J_{sun} = J_{sc} = ef\int_{E_G}^{\infty} \Phi_{Sun}(E)dE. \tag{2.5}$$

Here, f is a geometrical factor which accounts for the fraction of solar radiation reaching the surface of the earth and for $\Phi_{Sun}(E)$ either the AM 1.5G spectra or black body radiation with T~5800 K is used.[72]

Finally, the *JV* characteristic under illumination in the radiative SQ limit follows from adding the light-generated current to the dark characteristics:

$$J(V) = e\left(e^{\frac{eV}{kT}} - 1\right)\int_{E_G}^{\infty} 2\pi E^2/h^3c^2 e^{\frac{-E}{kT}}dE - ef\int_{E_G}^{\infty} \Phi_{Sun}(E)dE = \left(e^{\frac{eV}{kT}} - 1\right)\mathrm{J}_0 - \mathrm{J}_{sc} \tag{2.6}$$

From this *JV* characteristic the maximum attainable efficiency can be estimated to be 33.6% as shown in **Figure 2.1**b. Setting the current to zero in equation 2.6, the V_{OC} is the voltage at which J_{rec} equals J_{sc} (see Figure 2.1b) and can be written as:

$$V_{oc} = \frac{kT}{e} ln\left(\frac{J_{sc}}{J_0} + 1\right). \quad (2.7)$$

Thus, the V_{OC} depends on temperature and the ratio between J_0 and J_{sc}. In the radiative SQ limit at 1.34 eV band-gap, the V_{OC} is ca. 0.26 V lower as compared to E_G/e and the *FF* is ca. 89%. The maximum power point is at 0.99 V and at this point, 1% of the available power is lost by current reduction whereas 12% are lost by voltage reduction due to entropic[75] effects (see chapter 2.5).

Increasing the number of junctions in the device improves the SQ limit due to several facts: first, by extended sunlight absorption, second, by reduced thermalization losses, and finally, by reabsorption of emitted black body radiation from other sub-cells. With that, the radiative SQ limit increases to 42%, 49%, and 52% for 2,3, and 4 junction devices, respectively as shown in Figure 2.1b (assuming the sun to emit black body radiation flux at 6000K).[76] For an infinite number of junctions with a smoothly varying series of band-gaps, the efficiency increases to 68% for non-concentrated and up to 87% for the highest concentration physically possible, when the solid angle is 2π, which corresponds to 45900 times concentrated sunlight.[76]

Shockley and Queisser's original model is valid for a two band system only. When adopting this model to organic solar cells, some modifications with regard to the electronic structure of the organic BHJ are necessary.[77,78] The model needs to be extended by the CT state energy and its absorption strength relative to the band-gap absorption. Then, absorption can take place at E_{CT} and E_G while emission occurs mostly around E_{CT}. Therefore, an important parameter is the energetic difference between $E_D = E_{CT} - E_G$. With a realistic absorption ratio of 10^{-3} for CT state versus above band-gap absorption (see chapter 9), the maximum attainable efficiency is 29 and 26% for E_D= 0.3 and 0.5 eV, respectively at $E_G \sim$ 1.4 eV.[77]

Other efficiency limit estimates are more empirical, such as the model derived by Scharber et al. in 2006.[31] A constant EQE of 65% above the donor E_G and a *FF* of 65% is assumed together with the V_{OC} defined as $eV_{oc} + 0.3\,V = E_{HOMO}^{Donor} - E_{LUMO}^{Acceptor}$. Based on the measured energy levels of the PCBM acceptor which is assumed to be non-absorbing, efficiencies as function of the donor HOMO and LUMO levels (and with that of the band-gap) are predicted. The maximum attainable efficiency from this model is 11% at a band-gap of 1.3-1.4 eV and a LUMO level of 4.0eV.[31] Later, Dennler and coworkers extended this model in 2008 for tandem devices with predicted efficiencies of 15% for 1.65 and 1.3 eV band-gap of the donors in the front and rear-cell, respectively.[79] By adjusting the EQE to 80% and the *FF* of the tandem cell to 75%, which are realistic assumptions for the highest performing champion cells, the efficiency predicted by Dennler increases to 21%, as shown recently by Li et al.[80]

The champion cells presented at the moment achieve efficiencies very close to the empirical Scharber model. Further increasing the permittivity of the active materials, as proposed by a model from Koster et al.,[81] would theoretically realize efficiencies in excess of 20%. In Koster's model, the PCE is calculated

based on drift-diffusion simulations for 250 nm thick PTB7:$PC_{70}BM$ devices assuming that all photons above the band-gap are absorbed and converted to free charges with an IQE of 90%. The dielectric constant ε_r is correlated with the exciton binding energy. From this binding energy, the minimal energetic offset between the LUMOs of D and A needed for efficient charge separation is modeled. Increasing ε_r enhances the V_{OC} due to the optimized positions of the energy levels. Also, it reduces losses due to non-geminate recombination resulting in efficiencies above 20% for a three-fold increase of ε_r from 3 to 9 in this model. Some attempts have been made to correlate the permittivity to the efficiency of charge generation.[82,83] Recent results showed promising improvements of *FF* and V_{OC} in polymer/ C_{60} bilayers when the polymer side-chain was tuned to increase ε_r from 3 to 5.[84]

The assumption that all incident photons are absorbed above E_G within the active layer as assumed in the SQ limit and Kosters model is difficult to realize. Reflection, interference and parasitic absorption within the device structure cause the absorption in the thin organic active layer to vary periodically with the thickness. Efficient absorption is mostly realized in the 2nd absorption maximum, which is at an active layer thickness of 200-250 nm for many polymer:fullerene blends.[85] Unfortunately, most high efficiency BHJ cells show significant reduced *FF*s when increasing the active layer thickness due to inefficient charge-transport and collection.[46] Optimized devices, therefore, comprise thicknesses around the 1st absorption maximum, at 100 nm or even below,[30,35] though increasing the layer thicknesses to the 2nd absorption maximum would allow for a more complete absorption (see chapter 5). Therefore, alternative ways to increase the absorption at thicknesses around 100 nm are highly relevant in order to improve the PCE.

A possible way to enhance the absorption in the active layer without increasing its thickness is to adopt light trapping schemes. Light trapping due to textured front conductive oxide (TCO) surfaces[86] is widely applied to inorganic solar cells such as a-Si:H and is discussed in chapter 4. Other photon management schemes applied to organic solar cells are optical cavities,[87] antireflective coatings,[88] nanostructured back contacts,[88,89] and plasmon resonances from nanoparticles.[89] Nanostructured back contacts are usually fabricated by imprinting techniques resulting in textured active layer surfaces before deposition of the metallic back contact with significant reflection out of the normal incidence.[89] Plasmon resonances and with that absorption enhancements in the active layer at resonance wavelengths, can be realized via metallic nanoparticles in the e.g. PEDOT:PSS layer.[90] However, up to now, the highest efficiencies have been achieved with smart light management in which the device contact layers are optically optimized to achieve efficient absorption in the active layer.[91]

2.2 Low Band-Gap Donor Acceptor Copolymers

The energetic band-gap and with that the absorption onset of conjugated polymers with alternating single and double bond character is influenced by several factors as summarized in **Figure 2.2**a exemplarily for poly(3-alkylthiophene).[92] The energy of the band-gap E_G is a sum of several contributions:[93]

$$E_G = E_\Theta + E_{re} + E_{\Delta r} + E_s + E_{int} \quad (2.8)$$

Here, $E_\Theta, E_{re}, E_{\Delta r}, E_s, E_{int}$ are the contributions from backbone planarity, bond length alternation, resonance energy, different substitutions, and interchain coupling, respectively. First, the optical band-gap can be lowered with a larger conjugation length along the backbone. This can be achieved by a higher degree of backbone planarization reducing E_Θ, which can be realized by the suppression of rotational freedom or eliminated steric hindrance between repeating units. Also, forcing planarity of two adjacent units by covalent bonding or intramolecular interactions can reduce E_Θ.[93,94] Second, the resonance energy E_{re} of the system can impact the energy gap. A lower aromatic and a higher quinoid character of the mesomeric conjugated system lowers the band-gap by the loss in stabilization energy of the more instable quinoid form.[94] The transition from an aromatic to quinoid structure is correlated to the bond length alternation (described by $E_{\Delta r}$). The higher the quinoid contribution, the more double bond character is found between adjacent units, decreasing $E_{\Delta r}$.[94] In addition, the choice of different substituents (described by E_s) with electron-donating or electron withdrawing groups can alter the band-gap. For example, the alkyl side-chain in polythiophene induces a 0.2 eV reduction in band-gap.[92] Finally, the side-chains and its regioregularity also influence the aggregate formation in films and thereby the interchain coupling E_{int}. For example, regioregular P3HT exhibits a polymer backbone conformation with a reduced contribution from E_{int} due to the formation of extended aggregates in the film. Also, thermal annealing of regioregular P3HT in blends with PCBM further lowers E_{int} caused by enhanced polymer aggregation.[24] In regioirregular P3HT, the aggregation is supressed due to the steric hindrance induced by the regioirregularity.[95]

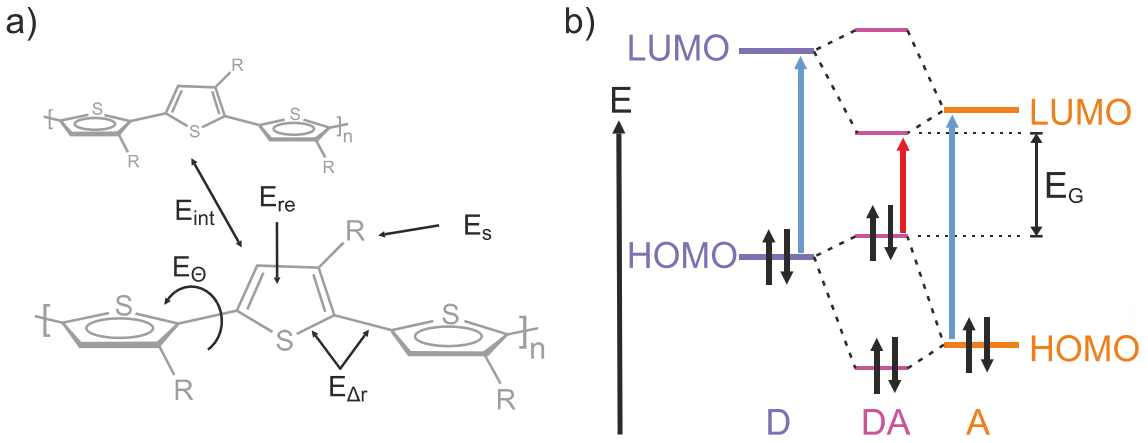

Figure 2.2 (a) Schematic representation of parameters defining the optical band-gap of poly(3-alkylthiophene). E_Θ, E_{re}, $E_{\Delta r}$, E_s, and E_{int} are the energies that contribute to the band-gap by planarity, resonance, bond length alternation, chemical substitution and interchain coupling, respectively. (b) Energy scheme displaying orbital interactions of donor (D) and acceptor (A) leading to a small band-gap E_G with low energy transitions (red arrow) resulting from strong DA interaction. Also, higher energy π–π* transitions (blue arrow) centered at either the D or the A are indicated. Figure (a) is adopted from Roncali[92] and (b) from Meijer et al.[96]

Another strategy for tailoring the band-gap is that of the donor–acceptor (DA) approach introduced in 1992 by Wynberg and co-workers to conjugated polymers.[97] Originally motivated by the idea of designing very low band-gap polymers with metallic properties,[97] this strategy has become a widely

used method for preparing conjugated polymers with narrow band-gaps.[34,98,99] The approach involves the synthesis of co-polymers comprising alternating electron-rich (donor, electron pushing) and electron-deficient (acceptor, electron pulling) repeat units. The hybridization of high-lying donor HOMO levels and low-lying acceptor LUMO levels results in an overall narrow band-gap of the copolymer as shown in Figure 2.2b.[100] Here the LUMO of the DA copolymer largely resides on the acceptor moiety and the HOMO on the donor building block.[101] The band-gap can be tuned via the electron donating and excepting strength of the D and A group, respectively. The DA polymers typically show two distinct optical absorption features leading to broad absorption characteristics.[99,102] The higher energy transition arises from π–π* transitions centered at either the donor or the acceptor unit.[103] The low energy transitions completely absent in the absorption of the D or A building blocks arise from intermolecular charge transfer (ICT) transitions.[100,104]

All the effects summarized in Figure 2.2a and b can be incorporated synergistically into the strategy of push-pull copolymers. By example, conjugated spacer units (mostly thiophene) are introduced in between the D and A to reduce steric interactions and enhance planarity to reduce E_G.[58] Also, DA copolymers with stronger quinoidal character of the subunits as for thienothiophene in PTB1 are introduced to lower the band-gap.[105] Energy-level fine-tuning by attachment of electron withdrawing fluorine atoms onto the acceptor subunit is realized for PTB7.[105] Further fine tuning of this DA copolymer was realized by side chain modification: replacing the 2-ethylhexyloxy group flanked on the BDT unit in PTB7 by 2-ethylhexyl-thienyl in the side chain creates the polymer PTB7-th with extended pi-conjugation and planarity and with that reduced optical band-gap.[106] This polymer recently achieved 9.6% in an inverted device architecture and is expected to break the 10% efficiency limit soon.[107] Further manipulation of the side chain of the BDT-unit in PTB7-th can be made by incorporation of 2-ethylhexyl-thio-thiophenyl which was shown to further decrease the optical band-gap slightly while increasing the V_{OC} in parallel, showing 8.4% PCE without the use of processing additives.[108] This material development by chemical engineering, especially the band-gap tuning, highlights the great potential for OPV against other photovoltaic systems.

2.3 From Incident Photons to Extracted Charges

The underlying mechanisms (I-IV) of charge generation, recombination and extraction are shown in **Figure 2.3**. These steps are briefly introduced with the help of the Figure, followed by a detailed discussion about the state-of-the-art knowledge of the underlying processes.

The absorption of a photon creates an excited state (exciton) in the organic material I. Due to the low permittivity, and substantial electron-electron as well as electron-vibration interactions,[109] the electron in the LUMO and the remaining hole in the HOMO are strongly bound together with binding energies of several hundred meV.[110] To overcome this binding energy the concept of an organic heterojunction was invented. By combining D and A materials with suitable energy offsets between the HOMOs and LUMOs, a charge can be transferred across the heterojunction to generate a charge transfer (CT) state after the exciton reaches the D-A interface by diffusion. The exciton diffusion is

limited to approximately 10 nm. Thus, the concept of mixing the D and A in a BHJ with phases separated on the length scale of 10-30 nm was shown to be highly efficient with IQEs approaching unity.[29] This concept makes sure that the exciton can diffuse to the interface within its lifetime followed by efficient free charge generation at the interface.

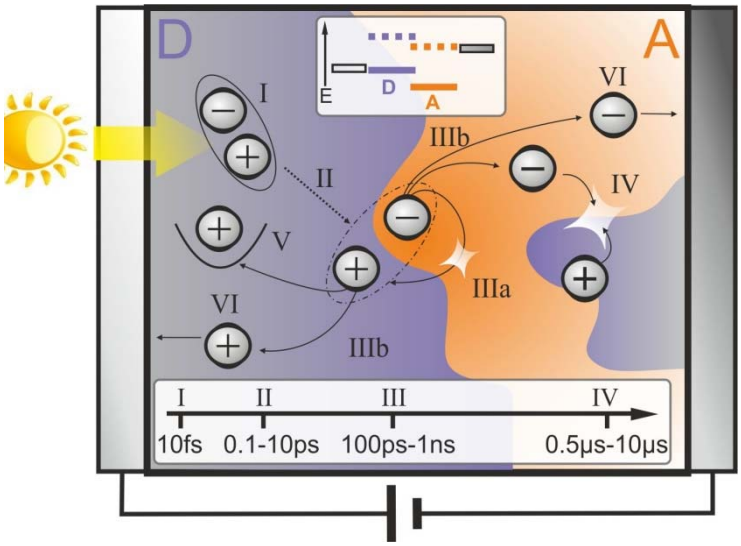

Figure 2.3 Schematic bulk heterojunction solar cell with exciton generation I, the exciton diffusion to the DA interface II with subsequent charge transfer, the geminate recombination IIIa or the separation of the initially bound polaron pair IIIb, non-geminate recombination IV, or trapping V of charges, and extraction to the electrodes VI. The timeline inset indicates the timescale of the shown events. The energy level inset indicates the energetic offset between LUMOs (dashed) and HOMOs (solid) of D and A as well as the energetic positions of suitable electrodes.

After CT state creation II from an electron transferred to the acceptor (or a hole transferred to the donor), there are two options: First, the recombination of geminate electrons and holes before they have escaped their initial Coulombic attraction. This charge loss is called geminate recombination IIIa. Second, the charges split up into free charges IIIb. Once the charges are free, they need to be extracted by the electrodes IVc to contribute to the efficiency of the cell.

Charge extraction to the electrodes is a very critical process as charge transport in the disordered organic materials with amorphous or semi-crystalline multi-phase nanostructures is governed by hopping through rather localized states. The Miller-Abraham hopping probability is a function of localization length and a Boltzmann factor for jumps upwards in energy. The Miller-Abraham approximation was used by Bässler and co-workers to arrive at the following expression for the mobility in the Gaussian disordered medium as a function of electrical field F and temperature T:[111]

$$\mu(F,T) = \mu_0 exp\left(-2/3\hat{\sigma}^2 + C[\hat{\sigma}^2 - \Sigma^2]\sqrt{F}\right). \quad (2.8)$$

Here μ_0 the zero field, zero temperature mobility, C an empirical constant, and σ and Σ are the energetic and positional disorder parameters, respectively with $\hat{\sigma} = \sigma/kT$. Thus, the mobility is temperature activated and follows the Poole-Frenkel type field-dependence $\log\mu \propto \sqrt{F}$. From equation 2.8, it follows that for high positional disorder Σ, the mobility can decrease with electrical field.[111] The overall charge carrier mobility is rather low in organic BHJ solar cells with $\mu_e, \mu_h \leq 10^{-3}$

cm²/Vs and strongly depends on the packing within the domains and the overall blend morphology (see chapter 5).

Due to the nanostructure of the BHJ, one type of charge can possibly come into contact with its non-geminate counter charge on the extraction pathway. This pair can possibly form a CT state again and recombine radiatively or non-radiatively. This carrier loss is called non-geminate recombination (NGR) IV, when the free charges have been formed via different absorption events. Due to the energetic and spatial disorder, free charges can be trapped in tail states V with low detrapping rates. A trap is defined as the Miller-Abraham hopping probability being much lower out of the trap as compared to the average hopping probability. When trapped charges recombine with a free non-geminate counter charge, the process is specified as trap-assisted recombination (further recombination specifications will follow in the next paragraph). As the overall charge carrier mobility is low in organic BHJ, the competition between charge extraction to the electrodes VI and non-geminate recombination has a significant influence on the *FF* of the solar cell.

Each process described in Figure 2.3 is determined by a specific timescale after the initial excitation. Free charge formation can be very fast on the sub-ps timescale when excitons are generated close to, or directly at the DA interface[112] and will not take longer than 1 ns with exciton diffusion to the interface.[113,114] In contrast, non-geminate recombination and extraction occurs on the 50 ns to µs timescale as shown in chapters 6 and 7.

2.4 Charge Generation

It is currently believed that charge generation occurs via the formation of CT states and its split up into free charges. The CT state is a state which is coupled to the ground state via radiative transitions. The existence of this state, only present when D and A are in close contact, is widely accepted due to the presence of new sub band-gap absorption and emission features[69] and the appearance in electron spin resonance measurements.[16]

Figure 2.4a displays the energetic states that are involved in the charge generation processes. After excitation of the donor (D*) from the ground state (GS), a charge can be transferred followed by relaxation (k_{relax}) into the relaxed CT state (CT_1). The excitation can then either separate into the charge separated (CS) state with rate k_{CS} or recombine geminately to GS with the rate k_f. As the CT state manifold is coupled to the GS via optical transitions, free charges can be generated by direct CT state excitation (G_{CT}). Also indicated is donor excitation followed by immediate free charge formation via vibronically/electronically excited “hot” states denoted with the rate k^*_{CS}.

Whether hot CT states mediate the charge generation through a more delocalized character of the involved states as discussed in the introduction has been a subject of particular interest in the literature. The more delocalized nature of hot states was shown via quantum mechanical modeling.[68,115] Hot excitations as mechanism for more efficient generation was proposed on the basis of transient absorption (TAS) and terahertz spectroscopy results,[63,64,67,68] and energy dependent EQEs.[63,68] Results from the transient measurements suggested the appearance of a free polaron signal

on very fast timescales on the order of 10-100 fs depending on the excess excitation energy.[63] This is most likely faster than a possible thermalization in the CT manifold which was found to be on the 1 ps timescale.[67] In the work by Grancini et al. a clear excitation energy dependence of optical signals assigned to polaronic states is found.[63] Bakulin et al. found that excitation of states in the CT manifold with a push laser pulse increases the efficiency of CT state split-up, with higher enhancements for low IQE systems. However this enhancement was independent of the primary excitation energy,[68] meaning that the push pulse excitation started from the same CT state. A general drawback of ultrafast pump probe experiments such as TAS is the high charge carrier density necessary for the required signal to noise ratio. Also free charge formation is most often concluded indirectly from the evolution of specific optical features in the spectrum.

In great contrast, the results of quantum efficiency measurements carefully applied to solar cells with almost direct CT_1 excitation proved that charge generation is as efficient from lower energetic CT states as for higher energy excitations.[69,70] Some BHJ system can overcome losses due to geminate recombination meaning that the IQE is nearly 1. In these systems, all CT states formed after charge transfer are split-up independent of the electrical field although free charge formation is thought to start from the thermalized CT_1 state. That is against the field enhanced charge generation model which was developed by Onsager and later refined by Braun[116] and it is counterintuitive as the Coulomb binding energy is known to be higher than the thermal energy kT in organic semiconductors. Therefore, other effects in the BHJ solar cell must account for the very efficient split-up of relaxed CT states in the absence of extra vibrational (excess) energy.

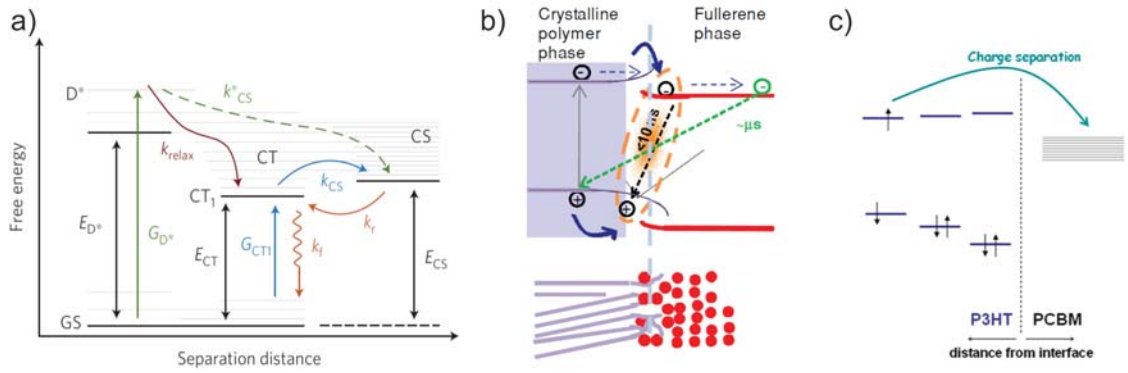

Figure 2.4 (a) Energy scheme with ground state (GS), excited donor D*, charge transfer (CT) and the charge separated states (CS). Indicated are several generation end recombination pathways and the relaxed CT state CT_1. (b) Energetics of a 3 phase morphology with crystalline polymer and aggregated fullerene phases and the intermixed phase. Reprinted with permission from Shoaee et al.[117] Copyright 2013 WILEY-VCH Verlag GmbH & Co. KGaA, Weinheim (c) Energy levels in P3HT at the PCBM interface. Reprinted with permission from McMahon et al.[118] Copyright 2011, American Chemical Society.

The blend morphology has been found to play a fundamental role in efficient charge generation. Generally the degree of polymer:fullerene intermixing, the domain size, molecular orientation as well as the domain purity play crucial roles in charge generation.[119,120] It was proposed, that a 3-phase morphology with highly intermixed phases, more crystalline and pure polymer phases, and aggregated PCBM domains, with each having a favorable domain size, is necessary to achieve high generation

yields.[117] Figure 2.4b helps to explain the efficient charge generation in organic BHJ solar cells. As proposed by Shoaee and co-workers,[117] the electron affinity (EA) of the fullerenes is higher in aggregated domains. In addition, the ionization potential (IE) of the crystalline polymer is lower as compared to the intermixed phase. That energetic landscape at the interface directs polaron pairs generated in the intermixed phase towards ordered and pure regions and helps to overcome Coulombic attractions.

With electroabsorption experiments, Gélinas et al. found that in the presence of aggregated fullerenes, the geminate pair can separate by 4nm within 40 fs.[121] At this distance, the Coulomb attraction compares to the thermal energy, so that electrons and holes separate freely without requiring excess energy for efficient charge separation. This is in agreement with results from Bernardo et al, identifying a certain fullerene crystal size under which the spatial extent of the CT state is reduced. Also from electroabsorption measurements they concluded, that the CT polarizability is correlated to the probability of CT split-up and thus is a reason for a high generation yield. The polarizability as an important parameter for charge generation was moreover postulated by Carsten et al.[122] It was shown that the difference between the ground and excited state dipole moment $\Delta\mu_{ge}$ in the polymer facilitates the formation of free charges by a larger polarizibility of the excited state with increased degree of separation between electron and hole in the exciton.[123] Burke at al. predicted that high local mobilities can enhance the geminate pair dissociation probability to unity in the 3-phase morphology.[124] Local mobilities, measured via terahertz spectroscopy, can be up to four orders of magnitude higher as compared to steady state bulk mobilities in P3HT:PCBM, thus enabling rapid escape from the geminate partner within a very short timescale.[124]

In the 3-phase morphology as described above by Shoaee and co-workers, the efficient exciton and charge transfer state split-up is solely explained for excitations within the intermixed region. In this context, excitons formed in pure regions are repelled from the intermixed region by the increased band-gap of molecules at the interface as shown in Figure 2.4c. However, according to McMahon et al.,[118] charges are also efficiently generated several Angstroms away from the interface by fast long range tunneling into partially delocalized fullerene states. In the third polymer layer away from the interface (1.14 nm distance), this process can be as fast or even faster than hopping to the interface, making it quite efficient.[118]

Even in the case without the favorable 3-phase morphology, there are two factors influencing the interfacial energy level alignment such that the CT_1 is easily separated. First, the difference of the permittivity of the D and the A can create interfacial band bending in such a way that the charges will be repelled from the interface in the higher dielectric material.[125] Second, molecular multipole moments such as dipoles orientated in a favorable direction with respect to the interface can create electrostatic fields that affect HOMO and LUMO levels to enhance free charge formation.[125]

2.5 Non-Geminate Recombination in Competition to Extraction

Non-geminate recombination occurs, when free charges meet at the DA interface and reform a CT state. This reformed CT state can recombine radiatively or non-radiatively to the GS acting as a loss channel as indicated in Figure 2.4a with the rates k_f and k_r.

To describe NGR in organic solar cells, the Langevin recombination model is often applied. According to Langevin's derivation, the limiting step for recombination is the motion of free charges towards each other via drift in the mutual Coulomb-field. The derivation considers first to have one fixed electron that creates an attractive (radial, in 3 dimensions) Coulomb field $F = e \cdot (4\pi\varepsilon_0\varepsilon_r r^2)^{-1}$ with e the elementary charge, r the electron hole distance, and ε_r and ε_0 materials and vacuum permittivity, respectively. It is assumed that holes move with the relative mobility $\mu_h + \mu_e$ being the sum of the hole mobility and the electron mobility that the electron would have when not being fixed. The recombination current density of the hole due to drift in the field of the electron is $j_{rec,h} = ep(\mu_h + \mu_e)F$ with p being the hole density. Integration of $j_{rec,h}$ entering the surface of this sphere with radius r gives the total hole recombination current per electron $I_{rec,h} = j_{rec,h} \cdot 4\pi r^2 = e^2 p(\mu_h + \mu_e)/(\varepsilon_0\varepsilon_r) = \gamma ep$. Here γ is the Langevin recombination coefficient. Now the scheme is generalized to N electrons. The recombination rate per unit volume $R = (\sum_{i=1}^{N} I_{rec,h})/eV$ is the sum of the recombination current per electron over all electrons per unit volume V. The sum can be expressed by the hole recombination current per electron $I_{rec,h}$ times N electrons in the unit volume leading to $R = Ne^2 p(\mu_h + \mu_e)/(\varepsilon_0\varepsilon_r eV) = N\gamma ep/(eV) = \gamma np$, with n being the electron density. Accounting for intrinsic holes and electrons n_i and p_i that are assumed to be constant by e.g. thermal excitation or injection, the Langevin recombination rate can finally be derived as:

$$R = \gamma(np - n_i p_i) = \frac{e(\mu_h + \mu_e)}{\varepsilon_0\varepsilon_r}(np - n_i p_i)\,. \tag{2.9}$$

In the derivation of equation 2.9, a few assumptions are made that are not fully satisfied in BHJ systems (see **Figure 2.5**a). Langevin assumes a homogeneous isotropic media. In organic BHJ, charge carriers might become trapped or are restricted to specific hopping sites. Also, a blend morphology with separate pathways for holes and electrons is not considered. Furthermore, the energetic landscape at the DA interface may act as a barrier for charge motion across this interface.

Given these assumptions, it is not surprising that the measured recombination coefficient is significantly reduced compared to the Langevin coefficient from equation 2.9 by 2-3 orders of magnitude for most DA copolymer:fullerene blends (see chapter 5 and 6) and up to 4 orders of magnitude for P3HT:PCBM.[126] This finding is rationalized by the blend morphology namely the reduced probability of free charges reaching the DA interface when traveling along the center of pure polymer filaments or fullerene aggregates.[126] In addition, when gradients in IE and EA at the interface stabilize charges away from the DA heterojunction, free charges are also hindered in reforming CT states when they are traveling in pure phases. Thus, NGR can be significantly reduced by a favorable 3-phase blend morphology with the above described interfacial energy level alignment.

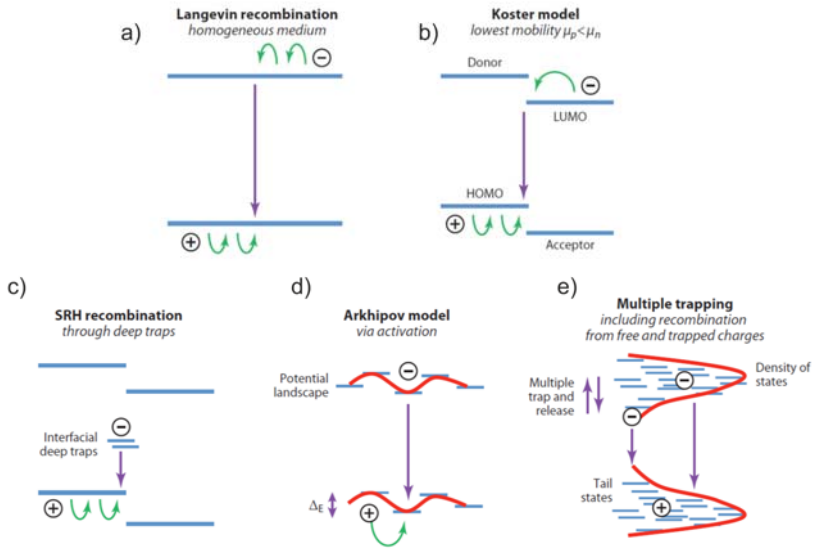

Figure 2.5: Different non-geminate recombination mechanisms. Reprinted with permission from Lakhwani et al. [127] Copyright 2014, Annual Reviews.

Further advances have been made that describe the recombination mechanism and account for the disordered morphology and trap states. As shown in Figure 2.5b, Koster pointed out that only the smaller mobility, e.g. the one for holes when $\mu_h < \mu_e$, rather than the sum of both should enter in equation 2.9. The probability of charges meeting at the DA interface is thus limited by the slower type of carrier. With the help of drift-diffusion simulations and a set of P3HT:PCBM solar cells subject to different annealing conditions to vary the electron hole mobility ratio, the model was experimentally supported.

Nelson proposed a model (Figure 2.5e) in which the recombination is limited by the detrapping of holes in presence of an exponential density of trap states.[128] Increasing the density of photogenerated charge will fill these traps and thus accelerate non-geminate recombination to $R = \gamma n p_{free}$.

The model described by Arkhipov et al. in Figure 2.5d includes disorder by random spatial fluctuations in the potential landscape ΔE of the disordered organic material.[129] In that model, the recombination rate γ depends on the Langevin recombination coefficient γ_{Lan} modified by ΔE via $\gamma \propto \Delta E \cdot \exp(-\Delta E/kT)\gamma_{Lan}$. To obtain a Langevin reduction factor of 10^{-3}, ΔE needs to be around 0.13 eV.

The prominent trap assisted recombination model (Figure 2.5c), in which recombination occurs via a density of N_t traps, was developed by Shockley, Read, and Hall (SRH) in which the recombination rate follows the expression:[130]

$$R_{SRH} = \frac{C_n C_p N_t np}{C_n(n+n_1)+C_p(p+p_1)} \text{ with } n_1 p_1 = N_{cv}\exp(-\frac{E_G}{kT}). \quad (2.10)$$

Here $C_n C_p$ are the capture cross sections for electrons and holes, respectively, and N_{cv} is the effective density of states.

In order to describe the efficiency of charge extraction, the recombination loss current can be generally expressed by:[131]

$$J_{NGR} = edR = ed\frac{n}{\tau(n)} \text{ with } \frac{1}{\tau(n)} = \gamma n^{\alpha}. \quad (2.11)$$

Here, $\tau(n)$ is the density dependent carrier lifetime and $\alpha + 1$ the recombination order which is 1 for monomolecular i.e. trap assisted SRH recombination and 2 for bimolecular recombination. The empirical reaction order $\alpha + 1$ describes how the recombination rate R scales with the charge carrier concentration. Higher recombination orders (>2) have been found experimentally in organic BHJ solar cells.[132,133] They were attributed to a recombination coefficient depending implicitly on density[132] due to a broad distribution of the density of states.[134] Additionally, the non-homogeneous distribution of carriers across the device with decreased spatial overlap between electrons and holes, especially for thin active layers, was shown to result in apparent reaction orders above two.[133]

Despite the achievements in modifying and describing several new recombination models (reduced) Langevin bimolecular recombination with a recombination order of two is mainly found to be the dominant recombination mechanism in organic BHJ solar cells.[113,135,136] Due to low charge carrier mobilities, efficient charge carrier extraction is crucial for achieving high *FF*s and high efficiencies in organic BHJ solar cells. According to equation 2.11, the recombination current depends quadratically on the charge carrier density via $J_{NGR} = ed\gamma n^2$ assuming BMR to be the dominant mechanism. At lower internal fields close to open circuit conditions, the charge extraction is slow increasing the overall amount of charges present in the device in steady state. As the recombination current depends quadratically on the density, the *FF* is sensitively linked to the lifetime $\tau(n)$. Only a scenario with high carrier lifetime characterized by a reduced BMR coefficient and rapid extraction (high mobility) can realize high *FF*s. Thus the mobility-lifetime ratio μ/τ must be maximized to achieve good performance such that the competition between recombination and extraction is won by the extraction.

2.6 The Open-Circuit Voltage

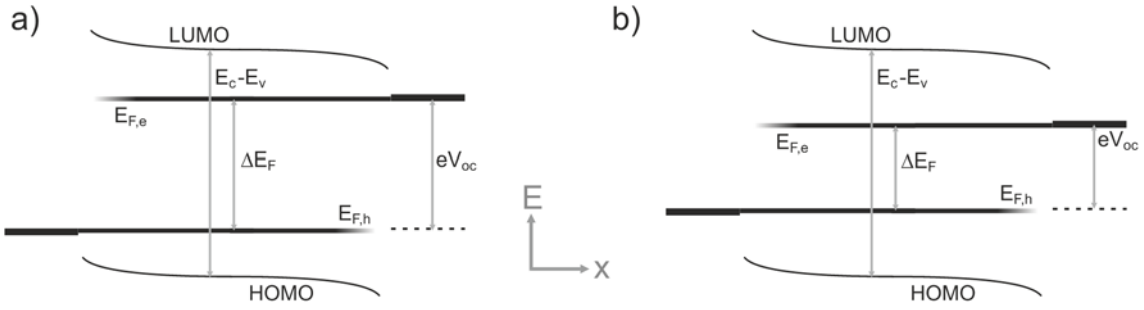

Figure 2.6: Energy level diagram with conditions at open circuit and fixed intensity, for (a) high generation, low recombination and (b) low generation, high recombination. $E_{F,e}$ and $E_{F,h}$ are the quasi-Fermi levels of electrons and holes, $E_c - E_v$ is the effective band gap.

The motion of charges in BHJ solar cells is governed by drift and diffusion. The drift and the diffusion current for e.g. electrons is:

$$J_e = J_{drift,e} + J_{diff,e} = en\mu_e E + eD_e \nabla n \quad = n\mu_e \nabla E_{F,e} \quad (2.12)$$

and the sum of the electron and the hole current is:[137]

$$J_{tot} = n\mu_e \nabla E_{F,e} + p\mu_h \nabla E_{F,h}. \quad (2.13)$$

Here, n (p) is the electron (hole) density, μ_e (μ_h) the electron (hole) mobility, $\nabla E_{F,e}$ ($\nabla E_{F,h}$) the gradient of the electron (hole) quasi-Fermi level, D_e the diffusion coefficient for electrons. At open circuit conditions, the net-current is zero and thus gradients of both quasi-Fermi levels are, in good approximation, zero and independent of position.[138] This situation is displayed in **Figure 2.6**.

To reach a high V_{OC}, electron and hole selective contacts with suitable workfunctions should be applied that form ohmic contacts in the so called pinning regime. This is mostly fulfilled when the hole selective contact is formed with a substrate workfunction being larger than the donor ionization energy and the electron selective contact should have a lower workfunction as compared to the acceptor electron affinity. With such contacts, the barrier to injection is negligible and the V_{OC} is not limited by the contacts.[134] Due to the workfunction difference, electrons (holes) are injected from the low workfunction (high workfunction) electrode into the organic semiconductor. Then, Fermi level alignment is reached by charge injection across the electrode interfaces regulating the position of LUMO (HOMO) above (below) the intrinsic contact Fermi level. The V_{OC} is then determined by the quasi-Fermi level splitting $eV_{oc} = E_{F,e} - E_{F,h}$ in the BHJ solar cell and depends on the steady state carrier density. To calculate the position of the quasi-Fermi energies, the Fermi-Dirac distribution of electrons and holes is approximated by Boltzmann statistics and a band occupation with step-function is assumed, meaning that no states can be occupied below the LUMO onset E_c for electrons and above the HOMO onset E_v for holes. Within the band, the density of state distribution is constant and with that also effective state density for holes N_h and electrons N_e is independent of energy. This leads to the following equations

$$E_{F,h} = E_v - kT \ln\left(\frac{p}{N_h}\right) \text{ and } E_{F,e} = E_c + kT\ln\left(\frac{n}{N_e}\right). \quad (2.14)$$

From equation 2.14 follows the definition of the free energy $F = U - TS$ in which U is the internal energy represented by E_v or E_c and $k\ln(p/N_h)$ or $k\ln(n/N_e)$ the entropy S. The free energy is minimized for e.g. n electrons in a sea of N_e possible states regulating the position of the quasi Fermi level. This entropic loss accounts for 12% loss of the incoming power in the AM 1.5G spectra in the radiative SQ limit as described before.

With equation 2.14, the V_{OC} can be written as:

$$eV_{oc} = E_c - E_v + kT\ln\left(\frac{pn}{N_e N_h}\right). \quad (2.15)$$

With $R = \gamma np$ and the generation rate $G = R$ at open circuit, this leads to

$$eV_{oc} = E_c - E_v + kT\ln\left(\frac{G}{\gamma N_e N_h}\right). \quad (2.16)$$

Thus, the V_{OC} mainly depends on the effective gap $E_c - E_v = E_{HOMO}^{Donor} - E_{LUMO}^{Acceptor}$ and is influenced logarithmically by the competition between generation and recombination of charges at this low internal field. According to equation 2.16, increasing the charge generation rate enhances the V_{OC}. For

some inorganic systems this is favorable as the J_{SC} can be linear in intensity with a constant *FF*, when not recombination limited, resulting in enhanced efficiency under concentrated light. However, for most organic systems, the higher V_{OC} is counterbalanced by the sublinear dependence of J_{SC} and a reduction of *FF* with higher light intensity. For typical generation rates at one sun condition in organic BHJ solar cells, $(E_c - E_v) - \Delta E_F \sim 0.5\ eV$.[134,139]

A significant enhancement of the V_{OC} can be accomplished by reducing the NGR at small internal field conditions. This was proven by Vandewal et al.[139] by reducing the amount of donor molecules dispersed in the acceptor matrix. Diluting the donor from 10 to 1% increased the V_{OC} by a reduction of the interfacial area and was accompanied by enhanced carrier lifetime and reduced NGR. On the other hand, several studies indicate that higher energetic disorder will most likely reduce the V_{OC}.[134,140] Blakesley and coworkers showed that a 100 meV disorder in a Gaussian disorder can reduce the V_{OC} by up to 0.4 V as compared to zero disorder.[134]

A very interesting finding is that the V_{OC} of ternary blends, consisting of either 2 energetically different donors and 1 A, or one D with 2 energetically different acceptors, is not necessarily limited by the smallest effective gap. In the case of 2 acceptors (A1 and A2) and 1 donor D, the V_{OC} lies between the V_{OC} of A1:D and A2:D depending on the ratio between A1:A2.[141,142] This was called the "parallel like"[142] BHJ solar cell and Street et al. attributed this discovery to the formation of delocalized CT states determined by a material-averaged electronic structure.[141] Yang and coworkers were able to use this "parallel like" concept to increase the overall efficiency of a ternary A1:A2:D blend by 30% as compared to the A1:D or A2:D blends.[142]

3 Experimental Methods

3.1 Materials and Device Preparation

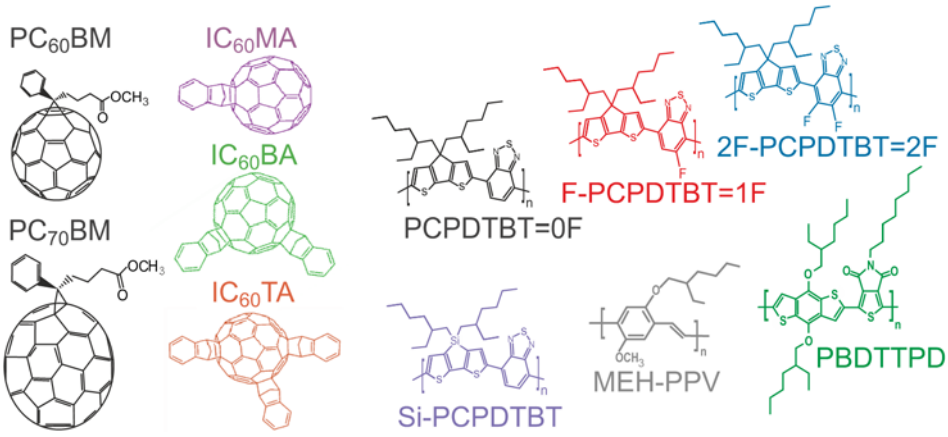

Figure 3.1 Chemical structures of the organic conjugated molecules used in this work.

The typical device structure for organic solar cells in lab research is a sandwich of the active organic layer in between two electrodes. Tin doped indium oxide (ITO) is used as the transparent conductive oxide (TCO). The metallic back electrode is made by thermally evaporated metals. If not stated otherwise, for all solar cell samples shown in this work, pre-structured ITO covered glass substrates (Optrex or Lumtec) were covered with 40-60 nm poly(3,4-ethylenedioxythiophene):poly(styrene-sulfonate) (PEDOT:PSS) (AI 4083, Clevios) which was subsequently heated at 180°C in the glove-box for about 10 min. To prepare the active layer, the donors were mixed with soluble fullerene derivatives in different weight ratios in chlorobenzene (CB) or o-dichlorobenzene (DCB) at elevated temperature, with an overall blend concentration of 15-36 mg/mL, using spin speeds around 1500 rpm for 40 sec. Appropriate amounts of diiodooctane (DIO) in between 1 and 3vol% were added to the CB when needed. The donor to fullerene weight ratio was optimized individually for each blend and was in between 1:1.5 to 1:4 by weight. All devices were finalized by thermal evaporation of 10 nm calcium (Ca) and 100 nm aluminum (Al) or silver (Ag) at a base pressure below 10^{-6} mbar. Due to the high boiling point of DIO, all DIO processed devices have been dried in UHV at room temperature for at least 3 h prior to evaporation of the back contact. The active area was defined by the overlap of ITO and metal, and was 1.0 or 1.1 mm² for transient measurements to ensure low RC-time constants. For solar cell performance comparisons 16, 6.36, or round 4.9 mm² active areas were used. All devices were encapsulated with two-component glue and a glass lid prior to air exposure.

For inverted devices a TiO_2 sol was synthesized according to Park et al.[29] under exclusion of moisture and oxygen. The final sol-gel product was diluted with methanol and spin-cast at 5000 rpm onto ITO followed by heating to 80°C for 10 min in air to form a TiO_2 layer with a thickness of 8–10 nm.

Subsequently, the samples were transferred into the nitrogen-filled glove-box and heated to 140°C for 10 min. After spin-coating of the active layer, the devices were completed by thermal evaporation of 10 nm of molybdenum-trioxide (MoO_3) and 100 nm of Ag.

Devices for hole-only current measurements were built with ITO/PEDOT:PSS bottom contacts combined with 10 nm (MoO_3) and 100nm Ag top contacts. For electron-only devices, the ITO/PEDOT:PSS bottom contact was covered with 50 nm Al and Ca/Al top contacts were used. Samples made for absorption spectroscopy have been prepared by dissolving the pure polymer or polymer fullerene blends in CB or DCB and spinning on glass substrates. The fabrication of the devices used for energy filtered TEM were made from the same solutions as used for solar cells. However, the spin speed was increased to decrease the layer thickness to about 60-70 nm. The films were then floated of in water and transferred to the TEM grid. For UPS samples, lower blend concentrations were used to reduce the film thickness to 20 nm.

Figure 3.1 displays the organic semiconductors used as active solar cell materials in this work. The acceptors $PC_{60}BM$ (>99.5% purity, Solenne), $PC_{70}BM$ (>99%, Solenne), $IC_{60}BM$ (indene C_{60} mono-adduct) (>99%, Lumtec), $IC_{60}BA$ (indene C_{60} bis-adduct) (>99%, Lumtec) or $IC_{60}TA$ (indene C_{60} tris-adduct) (>96%, Solarischem) are shown on the left. The used donors are shown on the right side. Poly[2,6-(4,4-bis(2-ethylhexyl)-4Hcyclopenta[2,1-b;3,4-b'']dithiophene)-alt-4,7-(2,1,3-benzothiadia-zole)] (PCPDTBT=0F)[27] is a low band-gap polymer which was provided by Ullrich Scherf from University of Wuppertal, with Mn between 14-19 kDa, or by Silvia Janietz from Fraunhofer Institute for Applied Polymer Research with Mn of 11 kDa. The fluorinated derivatives poly[2,6-(4,4-bis(2-ethylhexyl)-4H-cyclopenta[2,1-b;3,4-b']dithio-phene)-alt-4,7-(monofluoro-2,1,3-benzothia-diazole] (F-PCPDTBT=1F)[143,144] and poly[2,6-(4,4-bis(2-ethylhexyl)-4H-cyclopenta[2,1-b;3,4-b']dithiophene)-alt-4,7-(difluoro-2,1,3-benzothiadiazole)] (2F-PCPDTBT=2F)[43,145] were synthesized by Silvia Janietz with Mn between 11- 25 kDa and 5-10 kDa, respectively. The silicon bridged PCPDTBT derivative poly[(4,40-bis(2-ethylhexyl)dithieno[3,2-b:20,30-d]silole)-2,6-diyl-alt-(4,7-bis(2-thienyl)-2,1,3-benzo-thiadiazole)-5,50-diyl] (Si-PCPDTBT)[30] was provided by Konarka with Mn of 10 kDa. Poly(di(2-ethylhexyloxy)benzo[1,2-b:4,5-b']dithiophene-co-octyl-thieno [3,4-c]pyrrole-4,6-dione) (PBDTTPD)[146] was synthesized by Jessica Douglas at University of California Berkeley with Mn of 36 kDa. Poly[2-methoxy-5-(2-ethylhexyloxy)-1,4-phenylene-vinylene] (MEH-PPV) with Mn between 30-70 kDa was purchased from Sigma Aldrich.

3.2 Determination of the Optical Constants

The transmission of organic films (blends or single component films) on glass substrates was measured using a Varian Cary 5000 spectrophotometer in double beam mode. In this mode one beam contains the sample on a glass substrate and the other a pure glass substrate as reference sample to subtract the background absorption and reflection from the air glass interface. Absorption and reflection of the respective materials on completely covered 25x25 mm glass slides was measured with an integrating sphere. For reflection measurements of complete solar cells, thermally evaporated electrodes were

covering the complete substrate. From the reflection and transmission measurements, the optical constants of the active organic layers were deduced via simulations with a transfer matrix formalism (see paragraph 3.4) code established within the lab internship of Matthias Golke. The complete details of the simulation can be found elsewhere.[147,148] Just briefly, the complex refractive index $\tilde{n}$ of thin organic layers on thick (>1mm) glass substrates is modeled until the simulated reflection and transmission of the stack merge the measured data within a certain tolerance. To ensure a continuous function $\tilde{n}(\lambda)$ a penalty function correlating $\tilde{n}(\lambda)$ to $\tilde{n}(\lambda + 1)$ is introduced. Thicknesses necessary for the correct determination of the optical constants have been measured with surface profilometry (Dektak 3, Veeco). Optical constants of the electrode layers have been also measured via transmission and reflection or taken from literature.[149,150]

3.3 Current Voltage Characteristics

The solar cell characteristics were measured with an Oriel class ABA (A for spectral match, B for spatial uniformity, and A for temporal stability) simulator 94042A calibrated to 100 mW/cm² and a Keithley 2400 source meter. The samples were temperature controlled to 25°C during measurement. The calibration of the sun simulator was performed with a KG3 filtered silicon reference cell UPO001/055-2009 calibrated at Fraunhofer ISE. If mentioned, a mismatch correction was done according to Shrotriya et al.[151] The mismatch between the AM 1.5G spectra and the sun simulator reference cell system was below 4%, depending on the band-gap of the active material. Compared to the AM1.5G spectra, the sun simulator light output is higher in the blue to green spectral range and lower in the near infrared. The calibration was performed on an area of 4 cm² determined by the active area of the reference cell. The local intensity mismatch due the positional inhomogeneity of the intensity profile (due to the fact that the devices have much smaller active areas) was neglected. The positional error of the used sun simulator is less than 5% over the complete irradiating area of 10x 10 cm.

3.4 External and Internal Quantum Efficiency

The external quantum efficiency (EQE) was measured with monochromatic light from high-pressure tungsten or halogen lamps mechanically shopped to 90 Hz for the detection with a Princeton Applied Research lock-in amplifier (model 5302) over a 50 or 1000 Ω resistor. The intensity of the monochromatic chopped light was checked with an UV enhanced crystalline silicone solar cell (Newport 818-UV), calibrated at Newport. From integration of the EQE spectra and the spectral irradiance E_{SR} of the AM 1.5G spectra according to

$$Jsc = \frac{e}{hc} \int E_{SR} \cdot \lambda \cdot EQE(\lambda)\, d\lambda, \tag{3.1}$$

the EQE can be compared to the mismatch corrected J_{SC} measured with the sun simulator. Note that the charge carrier density in the active layer is much lower when the EQE is measured as compared to AM 1.5G illumination due to the low monochromatic light intensity. For tandem cells, continuous wave background illumination was performed with 740 nm (Roithner, H2A1-H740) or 525 nm (Alustar,

9008100) LED arrays containing three LEDs mounted on a heat sink ring. One sub-cell was optically biased with the LED array having the suitable wavelength, the other sub-cell, not absorbing the bias light strongly, was measured with the chopped monochromatic light without the application of a constant voltage offset. Applying no external voltage offset can cause some error of the measured EQE especially for low *FF* sub-cells.[152]

The internal quantum efficiency (IQE) according to

$$IQE(E) = EQE(E)/A(E), \tag{3.2}$$

was calculated by dividing the EQE by the absorption in the active layer $A(E)$. The absorption in the active layer of the solar cell device was modelled via the optical constants with a transfer matrix (TM) formalism, taking into account multi-reflections, interference in all layers (except in the thick glass substrate), and parasitic absorption of e.g. the electrodes in the solar cell stack.

The TM formalism is described in detail elsewhere.[153,154] Just briefly, the device stack with *i* layers is parameterized in *2i+1* different matrices assuming perfect flat interfaces between layers and optically isotropic as well as homogeneous layers with $\tilde{n}$ being independent of light polarization and position in the layer. One matrix (the interface matrix) is set for each interface (e.g. the *i-1,i* interface) including complex Fresnel coefficients for reflection and transmission. The layer matrix describes the light propagation with absorption through e.g. layer *i*. With the multiplication of all TMs, the total transmission through the device stacks or its total reflection can be simulated. When the optical electrical field of the layer number *n* within the device stack is desired, the multiplication of all transfer matrixes in the light propagation pathway before layer *n* relates the electrical field of light propagating in positive direction through the *n-1, n* interface to the incident plane wave. The multiplication of all matrices after layer *n* relates the light propagating in opposite direction of the incident plane wave through the *n+1, n* interface relative to the incident plane wave. The number of absorbed photons at position *x* in layer *n* is given by the modulus of the electrical field at this position as the sum of the fields propagating in both directions. Especially for thin films with reflecting back contacts, this results in absorption profiles that differ from simple Beer-Lambert light propagation.

Additionally, $A(E)$ was calculated in chapter 9 by the simplified assumption that the incoming wave passes through the active layer twice, due to reflection from the metallic cathode, according to

$$A(E) = 1 - e^{(-2d\alpha(E))} \tag{3.3}$$

with α and d being the absorption coefficient and the active layer thickness, respectively. In this simplified calculation, the IQE can be quantitatively compared to that from the TM simulation.

3.5 Charge Extraction Techniques (TDCF, BACE, Photo-CELIV)

The technique of time delayed collection field (TDCF) was first applied to a-Si:H by Mort et al.[155] in 1980 and later adopted to organic materials by Popovic[156] and coworkers in 1996 as well as Hertel et al.[157] in 2002. Some years later, Offermans and co-workers applied this technique to organic BHJ solar

cells in 2006.[158] Our group improved this method and decreased the delay between laser pulse and extraction, which was an important step to measure charge generation in several organic blends. The optical pump electrical probe methodology makes use of the different timescales for free charge formation and NGR as introduced above. By making sure that the delay time between pump and probe is well suited to ensure that free charge formation is completed and NGR is not initiated (at this charge density), charge generation as function of various parameters can be measured by the application of a high reverse bias that suppresses NGR during extraction.

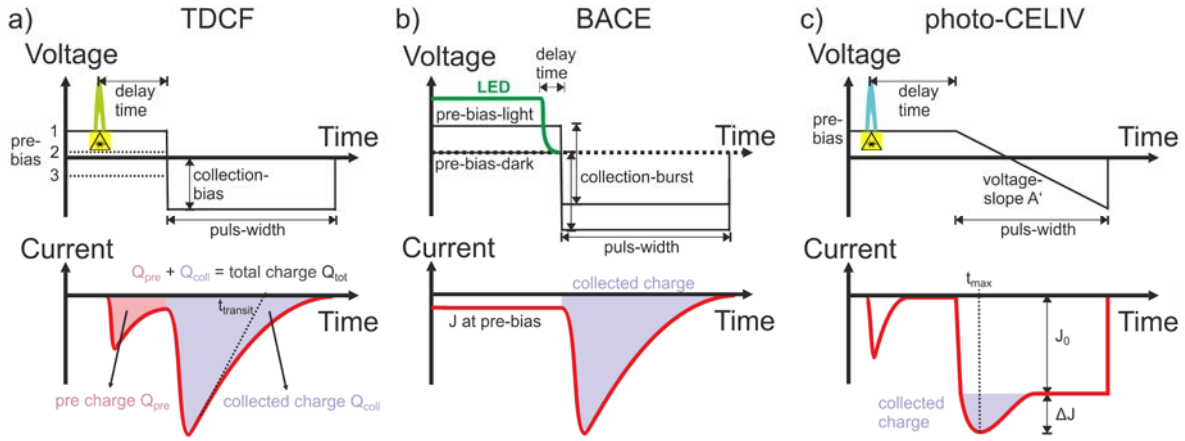

Figure 3.2 Measurement-schemes for different charge extraction techniques. The upper panel shows the applied voltage step and the illumination signal, the lower panel displays the corresponding photocurrent signal for (a) and (b) and the transient under illumination for (c). (a) Time delayed collection field (TDCF) with the characteristic photocurrent shape for ca. 150 ns delay time with two distinct current maxima (b) Bias enhanced charge extraction (BACE) (c) Photo-current extraction under linearly increasing voltages (photo-CELIV).

In our TDCF experiment, a short nanosecond laser pulse in combination with a voltage step is used to measure the generation and recombination of charges. The measurement scheme is shown in **Figure 3.2**a. The pulsed excitation (5,5 ns pulse width, 500 Hz repetition rate, 10 ns jitter) was done with a diode-pumped, Q-switched Nd:YAG laser (NT242,EKSPLA) which was frequency tripled to pump an optical parametric amplifier (OPO). The OPO output can be tuned in between 450-680 nm and 750-2000 nm by using either the signal or the idler of the OPO. In this setup, no residual parasitic wavelengths (i.e. 1064, 512, or 355 nm, or the OPO idler if signal was used) can be found when the light is tuned by the OPO. This was proven by carefully checking the beam spectra at the position of the sample with a spectrophotometer.

The possible time delay between the laser pulse and the start of the collection voltage ramp was decreased from a 150 ns setup developed by Juliane Kniepert[159] to 10-20 ns by Jona Kurpiers and is described in detail elsewhere.[160] Briefly, an Agilent 81150A pulse generator with a very fast slew rate of 2.5 ns was used to apply the pre- and collection bias to the sample. The current through the device was measured via a 50 Ω resistor in series with the sample and was recorded with a Yokogawa DL9140 oscilloscope. To reduce the effect of the laser jitter on the measurement, the pulse generator was triggered via a fast photodiode (EOT, ET-2030TTL) detecting the laser pulses at the laser output. To compensate the internal latency of the pulse generator, the laser pulses were delayed with a 85 m

long multimode fiber (LEONI) with respect to the first trigger diode. The pulses broadened to 6.4 ns after the fiber. A second fast photodiode (EOT, ET-2030) was placed after the fiber to trigger the oscilloscope. The pulse fluence was measured with a power meter (Ophir, Vega) equipped with a crystalline silicon photodiode sensor (PD300-UV) which was monitoring the pulse fluence during measurement using the reflection from a glass slide as a beam-splitter.

In the application of the measurement procedure, transients are recorded several times with the laser pulse applied to the sample and with the beam blocked by a mechanical shutter. The photocurrent signal is the difference of the averaged transient with and without the laser pulse hitting the sample. The integral over the phototransient is Q_{tot} and is a measure of the photogenerated charges. Note that the phototransient is not collecting charges that are injected at the respective pre-bias as the transients recorded in dark and with the laser pulse both measure injected charges. By calculating the difference signal, these charges are canceled out.

When applying different pre-bias conditions to the sample during the time when the laser pulse hits the sample, the field-dependence of charge generation can be measured. To make sure that non-geminate recombination or extraction losses are suppressed during the short delay between laser pulse and extraction bias, the fluence dependence needs to be checked carefully. In this way, also other effects being non-linear in charge density such as exciton-photon or exciton-exciton interactions can be ruled out. As described before, the non-geminate recombination depends quadratically (for bimolecular recombination) on free charge carrier density. Geminate recombination, however, is independent of the free charge density. Thus, the total charge should depend linearly on the laser fluence and the field-dependence of generation should be independent of fluence to make sure that these processes are not active. Then, the field-dependence of the charge generation can be directly determined from the total charge as function of pre-bias. Additionally, the collection voltage is chosen such that it is high enough to collect all charges and small enough to suppress significant injection currents when photogenerated charges are extracted.

From TDCF experiments, also, the EQE of charge generation in the absence of transport or non-geminate recombination losses can be determined as function of excitation energy and pre-bias. This is assigned here as the external generation efficiency (EGE) and can be calculated with the active area a and the laser fluence $F(E)$ via

$$EGE(E) = \frac{h \cdot c \cdot Q_{tot}(E)}{\lambda \cdot e \cdot a \cdot F(E)}. \tag{3.4}$$

The internal generation efficiency (IGE) can be calculated by dividing the EGE by the absorption $A(E)$

$$IGE(E) = EGE(E)/A(E). \tag{3.5}$$

The bimolecular recombination coefficient was iteratively calculated from the TDCF-data by tracking the evolution of the extracted charge carrier density from the device with increasing delay time. Applying the continuity equation, the following formula can be derived:

$$\frac{dQ_{coll}}{dt} = -\gamma ead(n_L p_L - n_D p_D) - \frac{dQ_{pre}}{dt}. \quad (3.6)$$

Here, $n_L p_L$ and $n_D p_D$ are the electron and hole densities under illumination and in dark, respectively. γ is the bimolecular recombination (BMR) coefficient, Q_{coll} and Q_{pre} are the integrals of the photocurrent during delay and extraction, respectively. d is the device thickness and a the active area. The term in brackets accounts for the fact that photogenerated charges recombine with both, photogenerated charges n_{ph} and injected (dark) charges n_D. The 2nd term accounts for extraction during the delay. It is assumed here that the photogeneration of charges is not affecting the electrical field distribution and the injection of charges. In the experiment, $Q_{coll} = ead(n_L - n_D)$ is not containing dark charges, because the dark transient is subtracted from the transient under illumination as described above. Assuming that $\mathrm{n} = \mathrm{p}$, $\mathrm{n_L p_L} = \mathrm{n_L^2}$ in the bracket in equation 3.6 can be written as $\left(\frac{Q_{coll}}{ead}\right)^2 + 2\frac{Q_{coll}}{ead}n_D + n_D^2 - n_D^2$ and thus

$$\frac{dQ_{coll}}{dt} = -\gamma ead\left(\left(\frac{\mathrm{Q}_{coll}}{ead}\right)^2 + 2\frac{\mathrm{Q}_{coll}}{ead}n_D\right) - \frac{dQ_{pre}}{dt}. \quad (3.7)$$

For short time intervals Δt of the delay time t_d, equation 3.7 can be rewritten as iterative formula:

$$Q_{coll}(t_d + \Delta t) - Q_{coll}(t_d) = \\ -\gamma\frac{1}{ead}[Q_{coll}^2(t_d) + 2Q_{coll}(t_d)\cdot Q_D]\Delta t - \left[Q_{pre}(t_d + \Delta t) - Q_{pre}(t_d)\right] \quad (3.8)$$

In equation 3.8, Q_D is the dark charge density which is measured with dark CELIV or dark BACE experiments for each individual pre-bias (see below).

As indicated in Figure 3.2a, the extrapolation of the initial decay towards zero photocurrent yields the transit time of charges t_{tr}. From that, the mobility $\mu(E)$ can be calculated with the extraction field E=$(V_{bi} + V_{coll})/d$. Here V_{bi} is the built in voltage that is assumed to be zero at the voltage of zero photocurrent being usually around 30 mV above the open circuit voltage:[50]

$$\mu(E) = \frac{d^2}{t_{tr}(E)\cdot(V_{bi}+V_{coll})}. \quad (3.9)$$

The transit time t_{tr} is the time photogenerated charge carriers need to travel the entire device thickness. When the initial decay of the phototransient is used, the mobility extracted is that of the faster type of carrier. When the mobilities of both types of carriers differ significantly, two regimes with different linear decays can be identified. However, the initial decay can be identified more accurately as the measured transient decay for larger timescales is typically non-linear (see Figure 6.4) due to dispersive transport or space charge effects.

The technique of bias amplified charge extraction (BACE)[161] is very useful when the number of charge carriers in the working solar cell under steady state conditions is needed. The measurement scheme and setup is comparable to TDCF as shown in Figure 3.2b. TDCF makes use of nanosecond laser pulses.

BACE instead uses a white light or monochromatic LED as illuminating source which is applied for milliseconds to get the solar cell into steady state between generation, recombination, and extraction at a certain pre-bias. This LED needs to have a fast light switch-off time to ensure that no free charges are generated at the collection field and that no NGR is active during delay. Here a high power 1W, 445 nm laser diode (insaneware) with ~ 10 ns light switch-off time mounted onto a heat sink is used. The laser diode is operated at 100 Hz repetition rate with applying the light for 9 ms to the sample to reach steady state conditions. The light is coupled into a fiber (LEONI, 60 m) for ensuring high homogeneity of the light profile. After the light is switched off, the voltage is reversed to extract all carriers without recombination losses as in TDCF. To correct for only the capacitive signal at each pre-bias condition, the following measurement procedure is applied: First the sample is held at the pre-bias V_{pre} with light and the collection is realized at the collection bias V_{coll} after the light is switched off. Second, the sample is held at zero bias in dark to avoid charge injection or photogeneration and extraction is realized at $-(V_{coll} + V_{pre})$ (see Figure 3.2b). This measurement routine ensures that the dark transient is recorded with the same bias-step as under illumination. Thus, subtraction of the charge from the two measurements accounts for the capacitive signal only and the corrected transient comprises the sum of photogenerated and injected charges at V_{bi} under illumination. The dark charge at each pre-bias was measured via BACE, but without the application of light from the laser diode. First the sample is held at V_{pre} and collection is realized at the collection bias V_{coll}. Second, the sample is held at zero bias and extraction is realized at $-\left(V_{coll} + V_{pre}\right)$. The subtraction between both transients contains the dark charge being present in the device at the respective pre-bias.

The current extraction under linearly increasing voltages (CELIV) technique was first published by Juska et al. in 2000 to determine the mobility of a-Si:H.[162] In the same year, it was applied to polymers and free charges were photogenerated by application of a laser pulse (photo-CELIV).[163] The CELIV measurements reported here used the same laser and excitation wavelength as in TDCF. The measurement scheme can be found in Figure 3.2c. The linear increasing voltage ramp was applied with an Agilent 33220A wave form generator. The resulting current transients were measured with a fast current amplifier (Femto DHPCA-100) and a digital oscilloscope (Yokogawa DL9040). To vary the field $F(t = t_{max})$ with t_{max} being the time with maximum photocurrent, the voltage slope A' was increased by varying the pulse length, keeping the peak voltage constant. The mobility was calculated according to:[164]

$$\mu = \frac{2d^2}{3A' t_{max}^2 [1+(0.18\frac{\Delta j}{j(0)})]} . \tag{3.10}$$

Dark charges were measured via CELIV without applying the laser pulse at each pre-bias. The constant capacitive current was subtracted from the CELIV transient recorded in dark to obtain the dark charge injected at the respective pre-bias.

4 Hybrid Inorganic/Organic Tandem Solar Cells with Tailored Recombination Contacts

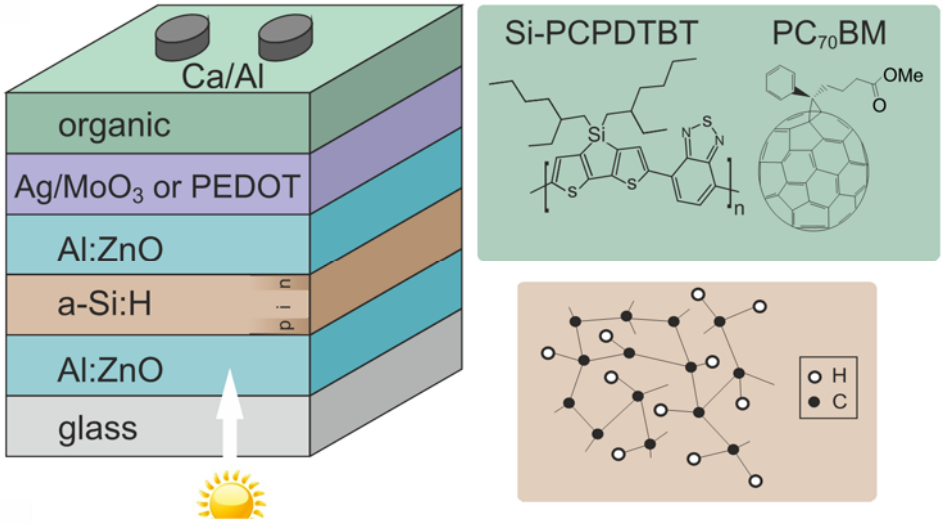

The work on hybrid tandem solar cells was the fundamental ambition to start working with the low band-gap polymer PCPDTBT and its charge carrier dynamics in blends with PCBM. Also the idea of fluorinating PCPDTBT was based on the opportunity of reaching higher open circuit voltages and higher efficiencies in the hybrid tandem solar cell. This chapter summarizes the tedious work of device engineering and finding suitable recombination contacts to realize reproducible, high efficiency tandem cells.

This chapter is based on:

S. Albrecht, B. Grootoonk, S. Neubert, S. Roland, J. Wördenweber, M. Meier, R. Schlatmann, A. Gordijn, and D. Neher, *Solar Energy Materials and Solar Cells* **2014**, 127, 157.

DOI: 10.1016/j.solmat.2014.04.020

The paper is reprinted with permission from Elsevier. Copyright, 2014 Elsevier B.V.

In this chapter, hybrid tandem cells with an a-Si:H front cell connected in series with an organic bulk heterojunction sub-cell made from a Si-PCPDTBT:$PC_{70}BM$ blend is presented. This hybrid device design is a quite new approach. In the last years, only few reports have been published using this hybrid design, with efficiencies of 1.8-3.3% [165-167] and 5.7% [168] as reported by Kim et al. and Seo et al., respectively. Kim and coworkers use a low performing organic sub-cell made of PCPDTBT:PCBM, but without using processing additives which are necessary to get good solar cell performance for this type of blend[32] as highlighted in chapter 5. The work published by Seo and coworkers makes use of the polymer PBDTTT-C having a band-gap of ~1.63 eV. To generate high currents in the organic sub-cell in combination with a-Si:H, the band-gap needs to be lowered further as discussed later in this chapter. Importantly all publications presented so far showed tandem cells with *FF*s below 50%, highlighting the challenge of using appropriate recombination contacts in this hybrid configuration. Also, both reports make use of ITO as the TCO which is typically used for organic cells but generally avoided in a-Si:H solar cells.

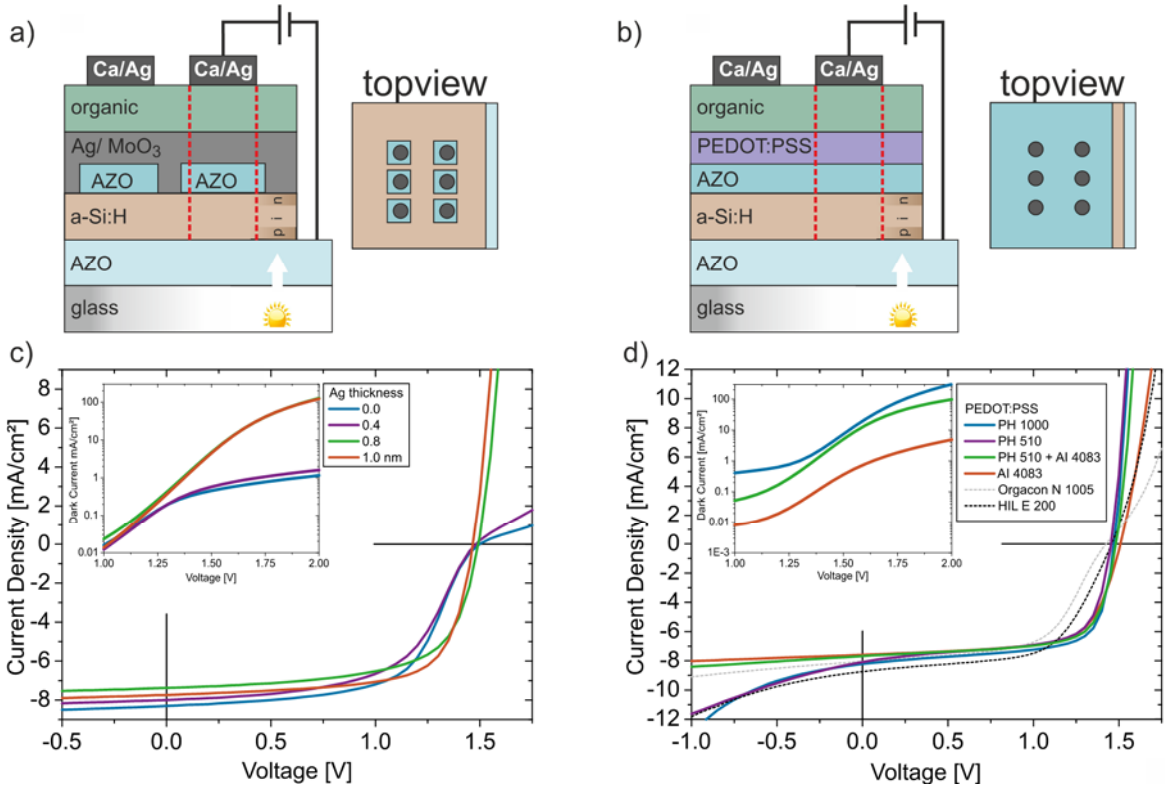

Figure 4.1 (a) Schematic device structure with a AZO/Ag/MoO_3 recombination layer, (b) device structure with a AZO/PEDOT:PSS recombination contact. In the top-view images the organic and the p-type recombination contact are neglected for simplicity. (c) *JV* characteristics of devices with the structure shown in (a). (d) *JV* characteristics of devices from (b). All *JV* characteristics shown here are measured without aperture under AM 1.5G illumination at 100 mW/cm².

One of the standard TCOs used for a-Si:H or µc-Si:H cells is aluminum doped zinc oxide (AZO).[86,169] AZO can be easily sputtered with smooth surfaces and etched with e.g. diluted HCl to texturize the front contact and generate light trapping effects.[86,170] ITO which is usually used for organic electronics suffers from the reduction by hydrogen radicals during a-Si:H or µc-Si:H layer deposition resulting in reduced transparency when applied as front contact.[171] Therefore, the hybrid layer stack presented in this

chapter is realized with AZO as the front contact and is displayed in **Figure 4.1**. The 700 nm thick front AZO is deposited via sputtering. On top of that, a layer sequence of p-type, intrinsic and n-type a-Si:H (together ~ 140 nm) is deposited via plasma enhanced chemical vapor deposition (PECVD). Finally, 70 nm back AZO is deposited via sputtering and used as the n-type layer in the recombination contact. This layer is either deposited through shadow masks or covering the complete substrate without application of a structuring mask. As the p-type layer of the recombination contact, two different approaches were investigated as shown in Figure 4.1a and b:

a) Thermally evaporated silver (≤1 nm)/ MoO_3(10 nm) on laterally structured back AZO.

b) Spin-coated pH-neutral PEDOT:PSS (60 nm) on non-structured back AZO.

The active layer of the organic sub-cell is made from a Si-PCPDTBT:$PC_{70}BM$ blend spin-coated on top of the p-type recombination layer with a thickness of 90 nm. The device is finalized by thermal evaporation of 10 nm Ca and of 600 nm Ag. The thick silver ensures that the active layer is mechanical stable against the contact finger which is directly applied at the position of the active area. When applying the direct contacting design, the active area can be defined by the metal cathode (round, ~5mm²) only. With this design, the front AZO can be fabricated without any lateral structuring. Lateral structuring of the front AZO by laser scribing caused severe problems with laser ablated particles remaining on the front AZO surface. Furthermore with this device design it is not necessary that the structured back AZO exactly overlaps with the cathode as the cathode area is smaller and can therefore be positioned with some lateral tolerance.

Figure 4.1c and d shows the *JV* characteristics of hybrid tandem solar cells made with the two different recombination contacts. The recombination contact needs to ensure ohmic recombination and should deliver a suitable work-function difference to realize that the open-circuit voltages of the individual sub-cells sum up in the tandem cell configuration. For the AZO/Ag/MoO_3 recombination contact, a significant change in the performance is measured when modifying the Ag layer thickness. If no Ag interlayer or only 0.4 nm of Ag is used, the *JV* characteristic shows a strong s-shape with reduced *FF* of about 56%. Also a low forward dark current is measured (see inset). Both findings are indicative of inefficient recombination at the recombination contact. Increasing the Ag interlayer to 0.8 nm ensures high dark current together with higher *FF*s of 65% of the tandem device. The *FF* increases further to 70% for 1 nm Ag, suggesting loss free recombination between both sub-cells. It was shown in previous reports that recombination in the tandem cell recombination contact is enhanced when ultrathin metal layers are used to form metallic recombination centers.[172]

A structured back AZO was used for these Ag/MoO_3 devices to reduce leakage from laterally collected shunt currents. In the absence of laterally structured back AZO, a higher reverse dark current and lower *FF*s were measured. When pH-neutral PEDOT:PSS (neutralized with diluted ammonia) is applied as the p-type recombination layer, structuring of the back AZO leads to losses in the V_{OC}. The structured back AZO may not be uniform in thickness due to shadow effects during deposition. Also the bare a-Si:H surface is strongly hydrophobic, reducing the wettability of the water based PEDOT:PSS suspension. Thus we used homogeneously covered back AZO for hybrid tandem cells utilizing PEDOT:PSS. The

corresponding *JV* curves are shown in Figure 4.1d. Significant differences in the performance are measured when PEDOT:PSS formulations with different conductivities are applied. Using high conductivity PEDOT:PSS results in strong dark currents at high reverse bias and reduced *FF*. With the high conductivity PEDOT:PSS layer, leakage currents from shunts in the a-Si:H layer can be collected from areas of the complete substrate. Making use of low conductivity grade formulations like AI 4083 leads to a series resistance with limits to the *FF* of 67%. The optimum between ohmic recombination in vertical direction and losses from high conductivity in lateral direction due to the collection of leakage currents is a mixture of AI 4083 and PH 510 1/1 by volume, generating *FF*s of 70% in good comparison to the Ag/MoO_3 contact.

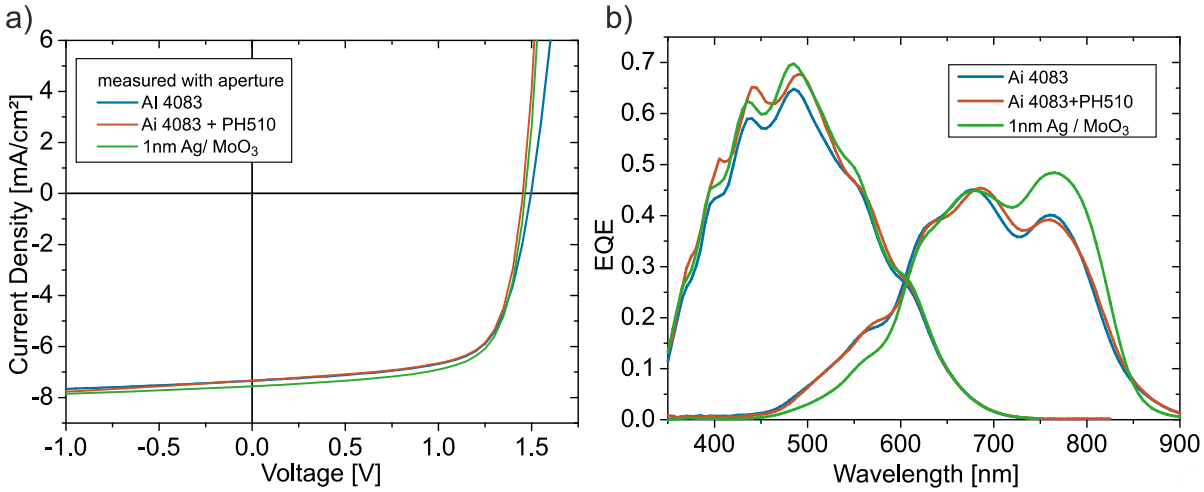

Figure 4.2 (a) *JV* characteristics measured under AM 1.5G at 100 mW/cm² with the use of an aperture. (b) Light biased EQE of the corresponding devices.

Table 4.1 Performance data of best performing hybrid tandem and single junction cells with 140 nm for a-Si:H pin and 90 nm for Si-PCPDTBT:$PC_{70}BM$ layers.

device	J_{SC} (EQE)[b] [mA/cm²]	J_{SC} [mA/cm²]	V_{OC} [mV]	*FF* [%]	PCE [%]
Tandem Cells: [c]					
Ai4083+PH510	7.48 / 7.25	7.34	1453	70.1	7.48
AI4083	7.10 / 7.22	7.42	1497	67.4	7.49
1nm Ag/ MoO3	7.52 / 7.48	7.50	1465	69.0	7.58
Single Junctions: [d]					
a-Si:H (flat AZO) [e]		9.10	942	74.5	6.38
a-Si:H (rough AZO) [e]		11.1	941	71.1	7.42
Si-PCPDTBT:$PC_{70}BM$ [f]		15.1	590	63.5	5.65

[b] from integration of the EQE of the respective sub-cell measured with background bias light, 1st value= a-Si:H, 2nd value= organic; [c] measured on round pixels with 2.5 mm diameter with an aperture of 2.4 mm diameter; [d] in configuration with reflecting metal back contacts; [e] initial efficiency measured on 1cm² active area; [f] measured on round pixels with 2.5 mm diameter without aperture.

In **Figure 4.2** the *JV* characteristics for AM 1.5G illumination through an aperture and the light-biased external quantum efficiency (EQE) spectra of best performing cells with the different recombination contacts are highlighted. When using the aperture during *JV* measurements, edge effects are reduced and the measured J_{SC} is then very comparable to the value derived from integration of the individual EQE spectra (see **Table 4.1**). The EQE spectra presented in Figure 4.2b are measured with

monochromatic continuous wave background light at 525 nm or 740 nm to address the EQEs of the individual sub-cells. The photovoltaic performance data and the J_{SC} from integration of the EQE spectra can be found in Table 4.1.

Both contact designs give high *FF*s up to 70% in the tandem configuration. Also, the fact that the V_{OC} of the tandem is close to the sum of the V_{OC} of both sub-cells in its particular single-junction configuration proves that both recombination contacts perform as a loss free series connection. At the thickness of 140 nm for the total a-Si:H sub-cell and 90 nm for the Si-PCPDTBT:$PC_{70}BM$ layer, the currents are quite balanced at 7.2 to 7.5 mA/cm². The final result is a PCE of 7.5% efficiency, which constitutes a 18 % enhancement over the flat a-Si:H single junction and a 33% enhancement over the Si-PCPDTBT:$PC_{70}BM$ cell. This result is the highest reported efficiency at the moment that utilizes hybrid inorganic/organic tandem solar cells with a-Si:H and organic sub-cells.

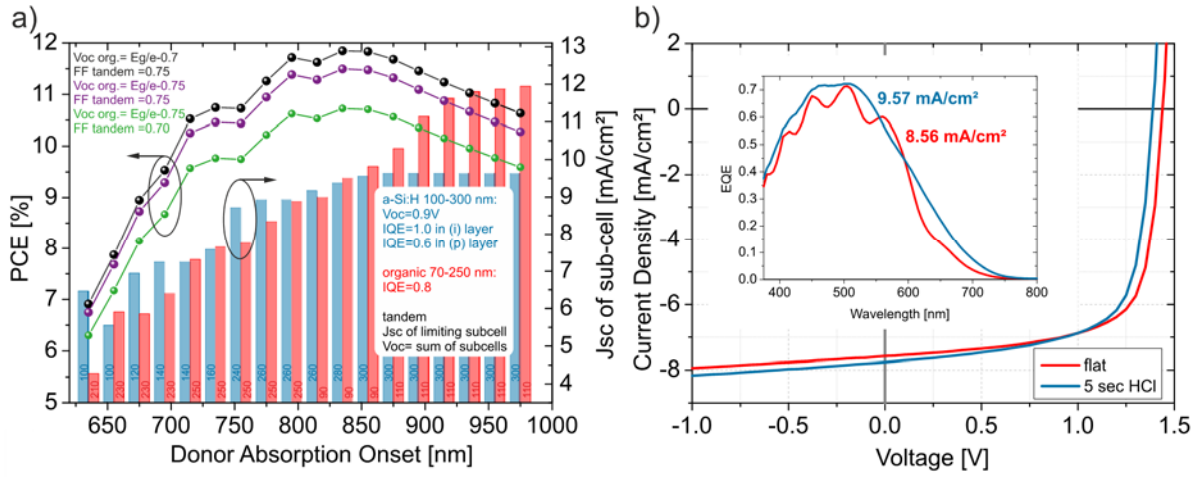

Figure 4.3 (a) Simulation of the hybrid tandem solar cell PCE (symbols) as function of donor absorption onset in the organic blend with $PC_{70}BM$. The assumptions for the PCE (left scale) can be found in the plot. The scale bars (right scale) show the current generated by the sub-cells in blue for a-Si:H and red for the organic, with the IQEs as indicated. The best performing thickness combination (in nm) is indicated vertically for each absorption onset. (b) *JV* characteristics of devices with AZO/Ag/MoO_3 as recombination layer measured under AM 1.5G at 100 mW/cm² without aperture, utilizing flat or textured front AZO (textured by etching 5 seconds in dilute HCl). The inset shows the EQE of the a-Si:H sub-cells and the J_{SC} determined from integration of the EQE spectra with the AM 1.5G spectra.

A further efficiency increase will be achievable via optimizing the donor band-gap in the blend with PCBM in the organic sub-cell. We constructed a series of optical spectra in which PCBM is blended with donors of different optical band-gaps E_G. The low energy absorption onset of the donor and with that E_G was shifted by 20 nm for each optical spectrum. The J_{SC} of both sub-cells was modeled via a transfer matrix formalism taking into account the optical parameters of the entire device stack, interference and reflection. The current generated in both sub-cells is displayed in **Figure 4.3** as bar chart as a function of donor absorption onset. For each optical band-gap, the sub-cell thicknesses were optimized to give the highest current for the sub-cell that is current limiting at this thickness combination. For the organic blend, an IQE of 0.8 was chosen. There are reports with organic bulk heterojunctions having a IQE of near unity,[29] but most of the low band-gap polymers show smaller IQE.[173,174] For the a-Si:H

sub-cell, the IQE was set to 1 in the i-layer and 0.6 in the p-layer and zero in the n-layer.[175] The simulation nicely shows that when the polymer band-gap is too large, absorption of sunlight will be mainly in a-Si:H, generating a low current in the organic sub-cell. Shifting the polymer absorption onset to energies below 1.41 eV (875 nm) increases the current generated by the organic sub-cell without further increasing the current generated in the a-Si:H sub-cell which has a maximum of ~9.6 mA/cm² without light trapping in this hybrid architecture model. The V_{OC} of the organic sub-cell is linked to the band-gap via $V_{OC}= (E_g/e) - \Delta V_{loss}$. Thus, reducing the band gap enhances J_{SC} on one side but reduces V_{OC} on the other side. Realistic values of this energetic loss offset are in between ΔV_{loss} = 0.6-0.9 V [173] and depend on the energetic position of the donor HOMO and the fullerene LUMO levels as well as on recombination losses at V_{OC}.[132] The V_{OC} of the tandem is assumed to be the sum of both sub-cells and the J_{SC} that of the limiting sub-cell. The latter one is a good approximation when both sub-cells have balanced J_{SC} and high *FF*s.[152] To calculate the tandem cell efficiency, we estimated the efficiency by the assumption of the *FF* to be 70 or 75% and ΔV_{loss} of the organic sub-cell to be 0.7 or 0.75 V. Values for the efficiency are shown on the left scale in Figure 4.3 and range from 10.5% to almost 12% with an donor absorption onset of ca. 835 nm, and layer thicknesses of 280 nm for a-Si:H and 90 nm for the organic layer. At this band-gap and thickness combination, the currents of both sub-cells are well balanced and the tradeoff between high current and high voltage is maximized. Both sub-cells have reasonable thicknesses in terms of good extraction for optimized *FF*s. This semi empiric model with realistic parameters shows the great potential of the hybrid tandem cell even in the absence of any light trapping schemes.

Light trapping in a-Si:H has been shown to greatly enhance the generated current by increasing the light absorption and reducing reflection losses. Also, light trapping has the advantage of allowing the use of thinner a-Si:H layers that significantly reduces the impact of degradation due to the Staebler-Wronski effect.[176] Usually, light trapping is achieved via texturized front TCOs like e.g. HCl etched AZO.[86,170] The etching induces a certain surface roughness with a root mean square roughness 40-100 nm and lateral features on a length scale of 400-1000 nm. In Figure 4.3b we compare hybrid solar cells similar to the design shown in Figure 4.1a but with a higher a-Si:H thickness of 180 nm and the front AZO which is flat or etched for 5 seconds in dilute (0.5%) HCl. The inset displays the EQE of the a-Si:H sub-cell. Due to the higher roughness of the etched AZO front contact, the interference fringes vanish and the overall EQE increases significantly due to light trapping. Although the organic blend layer is processed on the rough surface without the use of smoothening PEDOT:PSS, the V_{OC} and the *FF* of the tandem cell remains almost that of the flat tandem. Note that the J_{SC} of the sample on textured front AZO is not greatly increased due to the fact that the organic Si-PCPDTBT:PC_{70}BM cell is current limiting with this thicker a-Si:H. Thus enhancing the current in the a-Si:H only slightly increases the J_{SC} of the tandem with light trapping. However, this proof-of-concept shows the great potential of the hybrid tandem design in combination with light trapping schemes, with the perspective to boost the efficiency limit well above the 12% as estimated in Figure 4.3a when implementing suitable donors.

5 Light Management in PCPDTBT/$PC_{70}BM$ Solar Cells

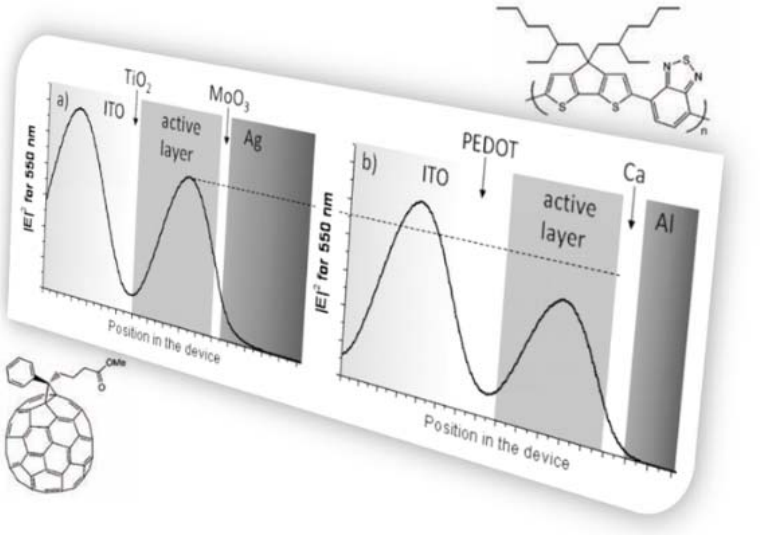

This work was motivated by the inverted device architecture showing reduced degradation and upcoming significance. Numerous publications and important efficiency records are realized with the inverted device design. By combining experiments with optical simulations, it is found that the active layer absorption can be enhanced by 10% in the inverted architecture for thin active layers. Furthermore, fundamental knowledge about light management and device physics was obtained during this work.

This chapter is based on:

S. Albrecht, S. Schäfer, I. Lange, S. Yilmaz, I. Dumsch, S. Allard, U. Scherf, A. Hertwig, D. Neher,

Organic Electronics **2012**, 13, 615.

DOI: 10.1016/j.orgel.2011.12.019

The paper is reprinted with permission from Elsevier. Copyright, 2012 Elsevier Limited.

As discussed in the introduction, organic materials benefit from high absorption coefficients. However, optical simulations for PCPDTBT:$PC_{70}BM$ (data not shown here) reveal that increasing the active layer thickness from the 1st (~100 nm) to the 2nd (~250nm) maximum of absorption would enhance the active layer absorption by more than 30%. A general drawback for most organic BHJ systems is the imbalance between extraction and non-geminate recombination. Thus, most systems are optimized to thicknesses of the first absorption maximum at 100 nm or below.[45,46]

To further increase efficiencies in organic BHJ solar cell systems, either new materials with efficient extraction and reduced non-geminate recombination or strategies to increase the active layer absorption (η_{abs}), while keeping the thickness constant need to be considered. The latter can be realized by optimizing the light management within the device stack. There is the possibility of introducing optical spacers,[29] or choosing different contact materials reducing parasitic absorptions and thereby increasing η_{abs}.[177]

The standard and inverted device architectures for organic solution processed solar cells were introduced in chapter 1.3. Inverted devices with PEDOT:PSS or MoO_3 as hole- and TiO_2, ZnO or polyelectrolytes as electron-selective contacts have gained considerable attention because of their increased air stability and higher device performance as compared to standard structures.[36,178] Thus, inverted structures are now widely used for high efficiency polymer:fullerene solar cells.[178-180]

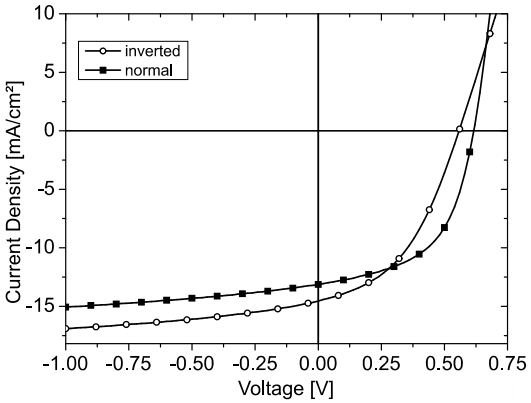

Figure 5.1 a) *JV* characteristics of 100 nm thick PCPDTBT:$PC_{70}BM$ devices (with 3vol% DIO) measured under AM 1.5G illumination at 100 mW/cm² corrected for spectral mismatch.

Figure 5.1 shows the *JV* characteristics of 100 nm thick PCPDTBT:$PC_{70}BM$ solar cells with the use of the processing additive DIO. The *FF* and the V_{OC} of the inverted device is reduced which will be discussed later. However, the J_{SC} and especially the photocurrent for reverse bias are greatly enhanced in the inverted device design although the active layer thickness is identical in both devices.

Figure 5.2a shows the measured EQE of a standard and an inverted solar cell with a PCPDTBT:$PC_{70}BM$ blend layer thickness of 100 nm. Clearly, the inverted device exhibits a higher EQE throughout the measured wavelength range from 350 to 900 nm. The fraction of absorbed light in each layer and the total reflection was modeled with a transfer matrix formalism based on the complex indices of refraction for each layer in the device stack. Comparison of the EQE and the corresponding modeled fraction of absorbed light in the active layer for the different device architectures proofs that the EQE scales well with the modeled absorption. Actually, the IQE as calculated from the EQE and the fraction

of absorbed photons is rather similar for both device structures. The deviation between measured and modeled reflection for the normal device is higher und thus the IQE is not as flat as the one presented in Figure 5.2b for the inverted device. However both IQEs have a mean value of about 71 %. This implies that the higher EQE for inverted devices originates from the higher absorption of the active layer. Figure 5.2b also displays that the variation of the IQE with wavelength is rather weak. A systematic difference in IQE for predominant polymer or the PCBM absorption as reported by Burkhard et al.[181] or a significant excitation energy dependence as published by Grancini and coworkers[63] is not found. The high quality of the modeled absorption in the device stack is proven by the very good agreement between the simulated and measured reflectivity of the full device.

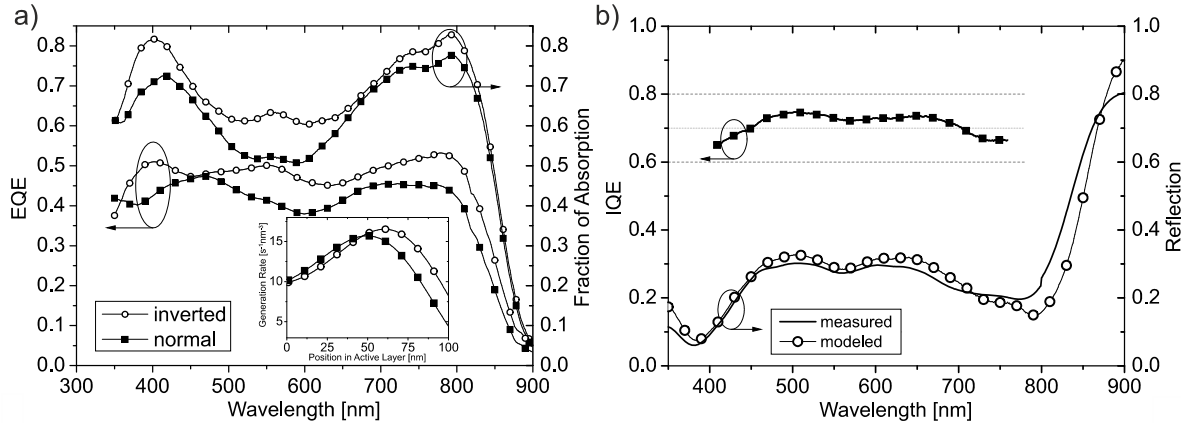

Figure 5.2 a) EQE and modeled fraction of absorbed light in standard and inverted devices with a PCPDTBT:$PC_{70}BM$ thickness of 100 nm. The inset shows the generation profile as function of position in the device b) Modeled internal quantum efficiency (IQE) together with measured and modeled reflection for a 100 nm thick inverted device.

The exciton generation rate versus position in the active layer is shown in the inset in Figure 5.2a for standard and inverted devices with a nominal active layer thickness of 100 nm. The main difference is a shift of the generation profile towards the metal electrode enhancing the rate for excited state formation near this electrode for the inverted cell geometry, partially due to the lower absorption coefficient of silver as compared to aluminum. The overall maximum is only slightly enhanced when changing to inverted devices.

It has been reported that introducing optical spacers between the active layer and the back electrode in standard devices[29] or matching the refractive index n of the front-contact to ITO[182] increases J_{SC}. Systematical optical modeling studies (data not shown) for the inverted structure of our PCPDTBT:$PC_{70}BM$ blends reveal that decreasing the MoO_3 thickness actually increases J_{SC} meaning that here, MoO_3 does primarily not function as an optical spacer, and that the inverted structure is already well optimized with a thin MoO_3 film.[183] Increasing the MoO_3 thickness moves the maximum of the generation profile even closer to the back contact, resulting in reduced total generation rate. Furthermore, decreasing the refractive index of the TiO_2 layer in the simulation caused J_{SC} to increase.

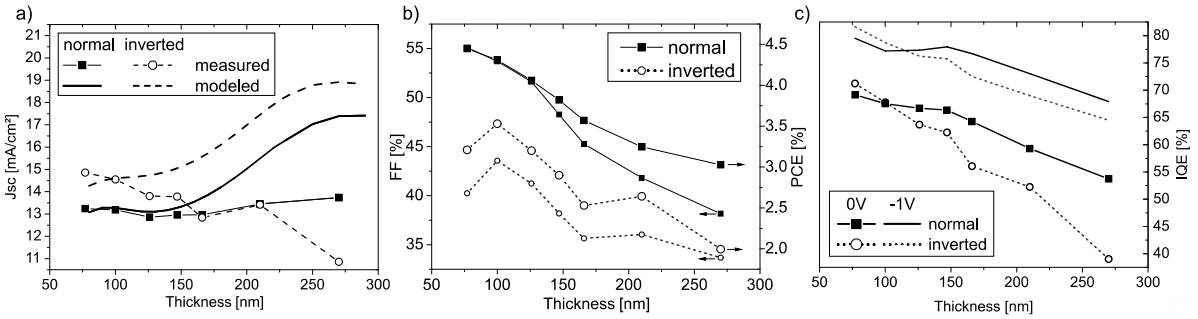

Figure 5.3 a) Measured J_{SC} from simulated AM 1.5G illumination at 100 mW/cm² corrected for spectral mismatch, plotted together with J_{SC} under the assumption of a constant IQE of 68 % as function of thickness, b) measured *FF* (left scale) and PCE (right scale), c) estimated IQE from the comparison between measured and modeled photocurrent at short circuit and -1V.

Let us now compare different active layer thicknesses for both device architectures. **Figure 5.3** shows the resulting performance parameters for inverted and standard devices with active layer thicknesses between 75 and 270 nm together with the modeled J_{SC}.

The V_{OC} is almost independent of the layer thickness for both device architectures and not shown here. However, the device performance declines with increasing thickness, and the effect is more pronounced for the inverted structure. The decrease in PCE is in part due to a continuous decrease of the *FF* with thickness as displayed by the good agreement in Figure 5.3b. The measured J_{SC} in Figure 5.2a is fairly constant at 13 mA/cm² for standard devices while it decreases from 15 to 11 mA/cm² for inverted devices. Thus, the inverted device generates more J_{SC} in the range below 150 nm only.

Interestingly, the measured J_{SC} largely deviates from the prediction (using a thickness independent IQE of 68 % in the simulation) especially for thicker layers when. The IQE used in the simulation is 3% lower than the mean average value shown in Figure 5.2b. Note that the EQE was measured at low light intensities well below the intensity of AM 1.5G illumination at 100 mW/cm². It was reported for this type of blend that the EQE is 2 % lower with one sun background illumination.[30] The simulation predicts the J_{SC} of the inverted device to be 9-15% higher than in the normal architecture for all thicknesses. In contrast, the measured current of the inverted device is lower for thicker layers. This is related to a strong continuous decrease of the IQE at short circuit conditions with increasing layer thickness, which is more pronounced for the inverted structure as shown in Figure 5.3c.

In addition, IQEs calculated from the photocurrents at -1 V, as shown in Figure 5.3c, are well comparable for both devices for a given thickness, meaning that the efficiency for converting an absorbed photon into a free carrier is almost independent of device architecture. As the IQE is very comparable at -1V and the absorption is higher for inverted devices, the photocurrent at high reverse bias is improved when using the inverted structure for all layer thicknesses. Interestingly the IQE at -1 V is ca. 10% higher as compared to short circuit conditions for the normal device which will be reconsidered in chapter 6.

Finally the poorer *FF* and J_{SC} of the inverted device should be addressed. Evidently, the lower *FF*s and thus PCEs of the inverted devices analyzed here must be related to more pronounced non-geminate

recombination losses. There are two possible explanations: First, the use of the solvent additive DIO with different solubility for PCPDTBT and $PC_{70}BM$[48] and long temporal evolution of the final blend morphology[184] may induce a polymer enriched layer on the bottom contact due to segregation. In accordance with that, Agostellini et al. reported a pronounced vertical composition profile in PCPDTBT:PCBM blends processed with the additive.[56] For the normal device the hole selective contact is at the bottom and the polymer enriched layer favors hole extraction. For the inverted device, this would result in poor electron extraction and thus enhanced recombination at this electron selective bottom contact. Also such segregation might hinder efficient collection of holes at the top contact in the inverted device structures. It is important to note that inverted devices comprising PCPDTBT:$PC_{70}BM$ layerss without using the processing additive DIO showed identical *FF*s for normal and inverted device architectures. Also, results from unipolar currents of electron only devices (as shown in **Figure 5.4**b) further strengthen this hypothesis. The current is strongly reduced when the top contact is biased positively and electrons are injected from the bottom contact with the use of the additive while extraction at the bottom contact is rather unaffected. This finding points to an electron injection barrier at the bottom contact with the use of DIO.[185]

Second, holes have been found to be the slower carriers in PCPDTBT:$PC_{70}BM$ blends.[49] As shown in Figure 5.4a, the generation profile seen from the hole-extracting contact is rather different for both types of devices. In particular, the path length for hole extraction is remarkably higher in the inverted device with a thick active layer compared the standard structure. It has been shown that these different extraction pathways can impact the *FF* of the device.[186]

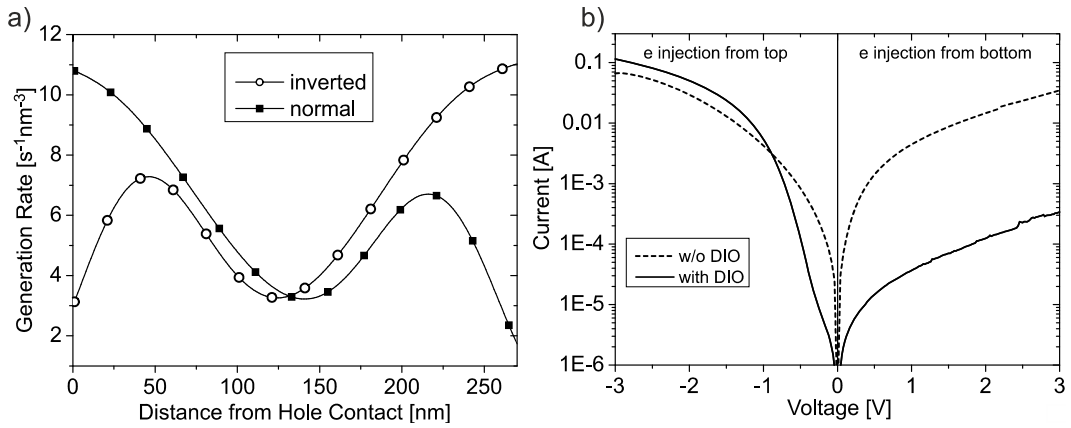

Figure 5.4 (a) Simulated exciton generation profiles versus distance from the hole selective contact for devices with an active layer thickness of 270 nm. (b) *JV* characteristic of electron only devices with ITO/PEDOT:PSS/Al bottom contacts and Ca/Al top contacts.

The presented optical simulations nicely reveal that inverted solar cells based on PCPDTBT:$PC_{70}BM$ are capable of delivering higher currents as compared to the normal devices. However, the maximum *FF*s presented here were around 55% for thin active layers and continuously decreased with thickness even for additive optimized fabrication conditions. Further work will, therefore, be devoted to the understanding of geminate and non-geminate recombination losses in these PCPDTBT:$PC_{70}BM$ blends and this issue will be resumed in the following chapters.

6 Charge Carrier Dynamics in Blends of PCPDTBT/$PC_{70}BM$: Influence of Solvent Additives

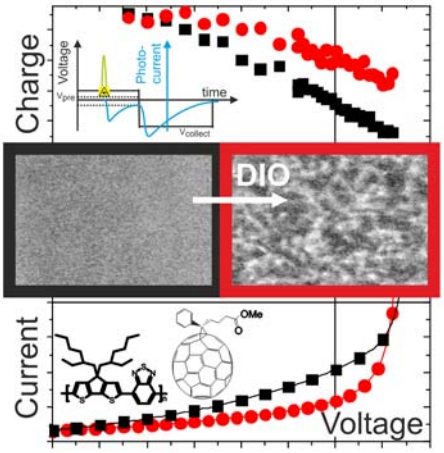

Motivated by understanding the moderate fill factor in the PCPDTBT:PCBM system, this work showed strong experimental proof for field-dependent charge generation. Additionally, the additive induced change of the morphology and the underlying differences in generation and extraction have been analyzed in detail with a TDCF setup tuned to 10 ns time resolution.

This chapter is based on:

S. Albrecht, W. Schindler, J. Kurpiers, J. Kniepert, J. C. Blakesley, I. Dumsch, S. Allard, K. Fostiropoulos, U. Scherf, D. Neher, *The Journal of Physical Chemistry Letters* **2012**, 3, 640.

DOI: 10.1021/jz3000849

The paper is reprinted with permission from American Chemical Society. Copyright, 2012 American Chemical Society.

In the previous chapter, the severe extraction losses especially for thicker active layers of additive optimized PCPDTBT:$PC_{70}BM$ blends were highlighted. Even for thin blend layers the *FF* remains below 55%. According to Table 1.1 in the introduction, no clear view on the physical processes leading to the low *FF* can be drawn from numerous publications. Furthermore, Table 1.1 highlights that there is no common agreement on the influence of the additive on the charge carrier dynamics. To study the effect of the additive DIO on the charge carrier dynamics and to quantify the processes limiting the *FF* in additive optimized PCPDTBT:$PC_{70}BM$ blends, we carefully analyzed the charge carrier dynamics of both systems in this chapter.

First, the morphological change induced by the solvent additive DIO in PCPDTBT:$PC_{70}BM$ blends was studied with energy filtered transmission electron microscopy (EFTEM)[187,188] on thin blend films representative for solar cells as displayed in **Figure 6.1**. In EFTEM, plasmon mapping is used to realize contrast between the fullerene rich and the polymer rich domains which have the maximum plasmon absorption at different energies.[187] The images in Figure 6.1 show that the morphology without use of DIO is characterized by a highly intermixed small scale phase separation. In contrast, blend layers processed with 3vol% DIO reveal a higher contrast in the plasmon maps, indicating purer polymer and fullerene phases, with an average domain size of 10-20 nm. This finding was recently described by in-situ X-ray studies revealing that the solvent additive promotes the formation of polymer crystallites during prolonged film drying.[184]

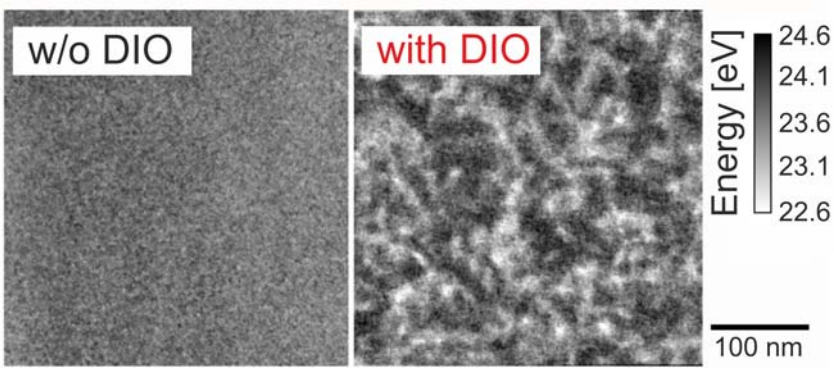

Figure 6.1 (a) Plasmon maps based on energy filtered TEM images of 70 nm thick PCPDTBT:$PC_{70}BM$ blends without and with 3vol% DIO as processing additive. The grey scale corresponds to the maximum energy loss due to plasmon absorption and dark areas refer to $PC_{70}BM$ having its maximum energy loss at higher energies as compared to the polymer.[189]

Figure 6.2a shows the solar cell characteristics measured under AM 1.5G illumination at 100 mW/cm² and the corresponding dark currents for blends processed with and w/o DIO using the normal device structure which is generally applied for studying fundamental processes in this work. For an active layer thickness of around 100 nm, the performance is greatly enhanced with the additive due to higher J_{SC} and *FF*. The solid blue line shows the difference between the *JV* characteristics under illumination for both devices. The difference has a maximum at around 0.2 V and reaches zero at approximately -3 V, meaning that the same photogenerated charge is collected at the electrodes for high internal fields.

Figure 6.2b plots on the right scale the total charge Q_{tot}, deduced from the integral over the complete phototransient measured with TDCF, as function of pre-bias for devices processed with and without DIO. These measurements were performed with an excitation wavelength of identical absorption for both blends at 500 nm using a very short time delay of 10 ns and a low pulse fluence to suppress non-geminate recombination during delay. Thus, Q_{tot} is a direct measure of free charge formation. In great contrast to recent findings by Jamieson et al.,[52] we find strong evidence for field dependent free charge formation in both PCPDTBT:$PC_{70}BM$ blends with the field-dependence being stronger without the additive. As a consequence, the efficiency for free carrier generation at short circuit conditions is substantially larger with the additive, meaning that geminate recombination is stronger suppressed in the DIO-processed blends.

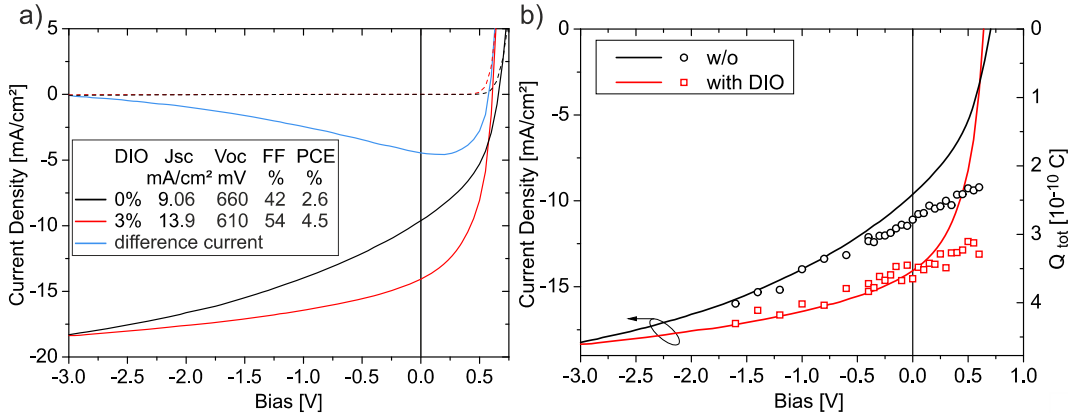

Figure 6.2 (a) *JV* characteristics of PCPDTBT:$PC_{70}BM$ blends measured under AM 1.5G illumination at 100 mW/cm² together with the corresponding dark currents and the difference in the current under illumination between the two blends. (b) Left scale: photocurrent, right scale: the total amount of generated charge Q_{tot} measured at 0.2 µJ/cm and 10 ns delay time.

Interestingly, the field-dependence of the free charge generation efficiency expressed by Q_{tot} explains well the course of the photocurrent characteristics for both blends at negative bias. At high reverse bias, the free carrier generation efficiency becomes similar for both blends, which explains why both photocurrent characteristics merge at negative voltages. Strong derivations between the generation and the steady state current are, however, measured when the bias approaches open circuit conditions, which is attributed to losses by non-geminate recombination (NGR). These derivations are more pronounced and the onset of significant NGR losses becomes obvious at a more negative bias in blends w/o DIO. Thus, NGR losses largely determine the photovoltaic properties of the blend w/o DIO at solar cell working conditions.

To address the kinetics of non-geminate recombination, experiments with increasing delay time t_d between generation and collection of charge carriers were performed. Integration of the transients during delay and during collection yielded the quantities $Q_{pre}(t_d)$ and $Q_{coll}(t_d)$, respectively with $Q_{tot}(t_d) = Q_{pre}(t_d) + Q_{coll}(t_d)$. **Figure 6.3**a exemplary shows the dependence of these quantities as a function of delay time for blends processed without and with the additive and the pre-bias set to 0.3 V. The increase of Q_{pre} with t_d is due to field-induced extraction of photogenerated carriers, leaving less charge available when the collection bias is switched on. Clearly, extraction is more rapid in blends

with DIO displayed by the faster rise of Q_{pre}, leaving fewer charge carriers in the device after a certain delay to recombine.

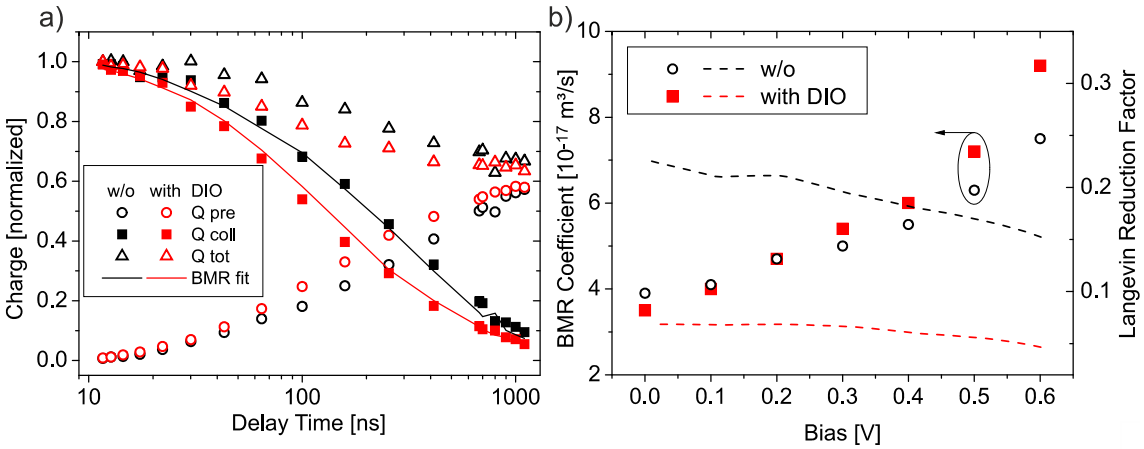

Figure 6.3 (a) Q_{pre}, Q_{coll} and Q_{tot} measured at 0.5 µJ/cm² and 0.3 V pre-bias as a function of delay time normalized to the initially generated charges. The corresponding BMR fits are shown as solid lines. (b) Left scale: bimolecular recombination (BMR) coefficient estimated from the BMR fits. Right scale: Langevin reduction factor estimated from the measured field-dependence of mobility and BMR coefficient.

For both blends, a decrease of the total extracted charge is seen already for short delay times of few tens of nanoseconds, indicating fast NGR. Also, a weak decay of Q_{tot} with delay time is observed even for V_{pre} = 0 V (data not shown), meaning that losses due to free carrier recombination cannot be neglected at short-circuit conditions. This is in accordance with the results by Li et al. providing evidence that the photocurrent is hampered by extraction.[190]

All data sets of $Q_{pre}(t_d)$ *and* $Q_{coll}(t_d)$ have been analyzed by the iterative scheme described chapter 3 to yield the kinetics of NGR. Interestingly, excellent fit to the data was possible when assuming bimolecular recombination (BMR) with a quadratic dependence of recombination rate on charge carrier density. The BMR coefficients γ_{BMR} extracted from these fits are plotted in Figure 6.3b parameterized in the pre-bias. The values for both blends are similar, rather unaffected by the pulse fluence, and more than one order of magnitude higher than BMR-coefficients measured with TDCF on annealed P3HT:PCBM,[159] meaning that NGR is very fast in the PCPDTBT:$PC_{70}BM$ blend. The overall BMR-coefficients measured with TDCF compare very well to results from TAS[113,191] and do not show the reported trend from transient photovoltage with 6 times higher BMR coefficients for blends with the additive.[56]

Notably, the BMR coefficient increases with pre-bias by a factor of three when approaching open circuit conditions. As the BMR coefficient is linearly proportional to the drift mobility of electrons and holes, we have determined its field-dependence by analyzing photo-CELIV and TDCF transients. The effective field in the photo-CELIV experiments was varied by changing the slope of the voltage ramp. Mobilities were determined by the analysis of the photo-CELIV transients according to equation 3.10.[164] For the TDCF measurements, the delay time was set to 100 ns and the collection voltage was varied from 0.5 to 1.5 V. Mobility values have been derived from the initial slopes of the photocurrent decays according to equation 3.9.

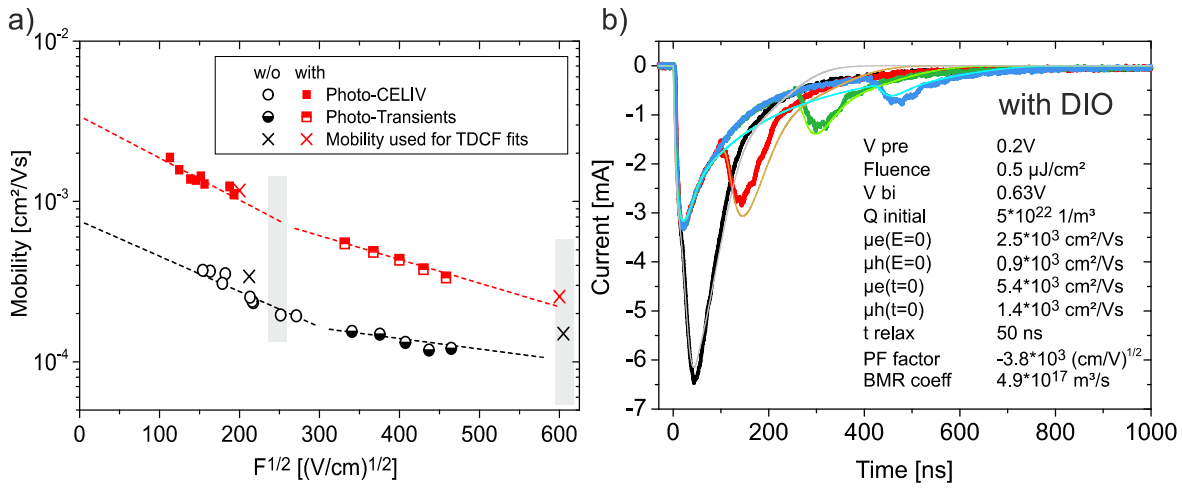

Figure 6.4 a) Field-dependent mobilities measured via photo-CELIV and TDCF. The dashed lines are guides to the eyes. The grey areas indicate the fields at J_{SC} and extraction at -3 V. b) Drift diffusion fits to TDCF Transients for 4 different delay times. The fit parameters initially, homogeneous created charges (Q initial) and BMR coefficient have been adopted from TDCF measurements. The used zero field mobilities μ(E=0) and the Poole Frenkel factor (PF factor) are indicated by the crosses in a). An exponential mobility improved the fit to the initial slope of the transients. The mobility decays from the start values $\mu_{e,h}$ (t=0) in 50 ns to the field determined mobility. The built-in field (V_{bi}) is assumed to be flat at V_0.

It was recently shown that the electron mobility in PCPDTBT:PCBM blends is higher than the hole mobility.[49] Therefore, we assume that the mobilities shown in **Figure 6.4**a correspond to electron mobilities. First, the mobility is seen to be three to four times higher with the additive pointing to the more effective charge extraction when phases become more pure. This is in great contrast to the additive-unaffected electron mobility derived from solar cell dark currents as reported by Moet et al.[50] and compares well with bipolar field-effect transistor studies showing enhanced electron mobility with additive as reported by Cho et al.[57] Second, both blends show a strong negative dependence on electric field as characteristic for materials with high spatial disorder,[111,192] and third, mobilities are not significantly altered when increasing the pulse fluence in photo-CELIV (data not shown).

Drift-diffusion simulations of entire TDCF transients were performed to verify the mobility values and the negative field-dependence as recorded in our measurements. Exemplary fits are shown in Figure 6.4b for devices with DIO and four different delay times. Values for the BMR coefficient and the electron mobility at the corresponding fields were taken from Figure 6.3b and Figure 6.4a, respectively. Best fits were obtained with hole mobilities that were 2-3 times smaller than the electron mobilities. The fit to the initial rise and decay of the TDCF transients could be significantly improved by considering a modest exponential mobility relaxation[111,193] within the first 50 ns. The agreement between the simulated and measured transients is very good, considering that the delay time was varied over a wide range from 10 ns to 400 ns.

To verify if the negative field-dependence of electron and hole mobility is the main cause for the increase in the BMR coefficient with decreasing internal field, the Langevin reduction factor $\zeta(F) = \gamma_L(F)/\gamma_{BMR}(F)$ *with* $\gamma_L = e(\mu_e(F) + \mu_h(F))/\varepsilon_o\varepsilon_r$ the Langevin-type three-dimensional recombination coefficient is calculated as function of bias. As shown in Figure 6.3b, the reduction

factor $\zeta(\mathrm{F})$ changes only gradually with bias, meaning that the field-dependence of the BMR coefficient is mainly caused by field-dependent mobilities. In the calculation, electron mobilities were taken from Figure 6.4 a and b. Also important to note is, that $\zeta(F)$ is ca. 3 times lower for devices processed with the additive, meaning that the formation of phase-separated domains of rather pure components hinders bimolecular recombination.

To conclude, a field-dependent charge carrier generation mechanism was shown for the first time in PCPDTBT:$PC_{70}BM$ blends with the field dependence being much stronger without the additive. Interestingly, the BMR coefficient is not altered by the additive but the overall recombination coefficient is rather high as compared to the P3HT:PCBM system. The additive speeds up the extraction of charge carriers, which is rationalized by the three-fold increase in mobility when using DIO. All together, the improvement in charge carrier generation and extraction is identified to cause the two-fold increase in performance when using the additive. The pronounced field dependence of charge generation and the high recombination coefficient limit the *FF* to moderate values of 55% in additive optimized blends. The next chapter highlights how fluorination of the PCPDTBT copolymer can further reduce losses from geminate and non-geminate recombination resulting in enhanced *FF*s and efficiency.

7 Fluorination of PCPDTBT: The Effect on Charge Generation and Recombination

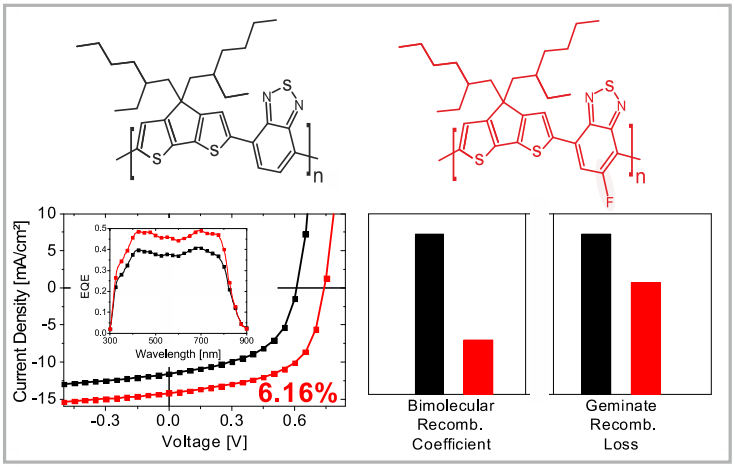

At the Polydays conference 2010 in Berlin, together with Dr. habil. Silvia Janietz, the idea of a fluorinated PCPDTBT polymer was born. At this time only few other fluorinated polymers were known that showed improved open-circuit voltage and fill factors over the non-fluorinated polymer analogues. This chapter presents a detailed study of the processes governing free charge generation and recombination in efficient devices based on the fluorinated polymer F-PCPDTBT.

This chapter is based on:

S. Albrecht, S. Janietz, W. Schindler, J. Frisch, J. Kurpiers, J. Kniepert, S. Inal, P. Pingel, K. Fostiropoulos, N. Koch, D. Neher, *Journal of the American Chemical Society* **2012**, 134, 14932.

DOI: 10.1021/ja305039j

The paper is reprinted with permission from American Chemical Society. Copyright, 2012 American Chemical Society.

Incorporation of the strong electron-withdrawing fluorine atom into the conjugated backbone of DA copolymers has become a strategy for increasing the PCE of polymer:fullerene BHJ solar cells. Often, fluorination enhanced not only the V_{OC}, but also J_{SC}, and *FF*, resulting in very efficient devices.[34,58] While the enhancement in V_{OC} is attributed to simultaneous lowering of HOMO and LUMO levels,[34] the enhancements in J_{SC} and *FF* are not conclusively described in the literature. Some fluorinated systems showed improved *FF*s although the charge carrier mobility was lowered with fluorination.[60,194]

Here, we adopt this strategy for the DA copolymer PCPDTBT and present detailed studies on how the fluorination affects the charge carrier dynamics and nano-scale morphology within the PCPDTBT:$PC_{70}BM$ system. To make a fair comparison, mono-fluorinated PCPDTBT (1F) was synthesized and compared to the non-fluorinated copolymer PCPDTBT (0F) with similar average number molecular weight of ca. 10 kDa and polydispersity of 2.1.

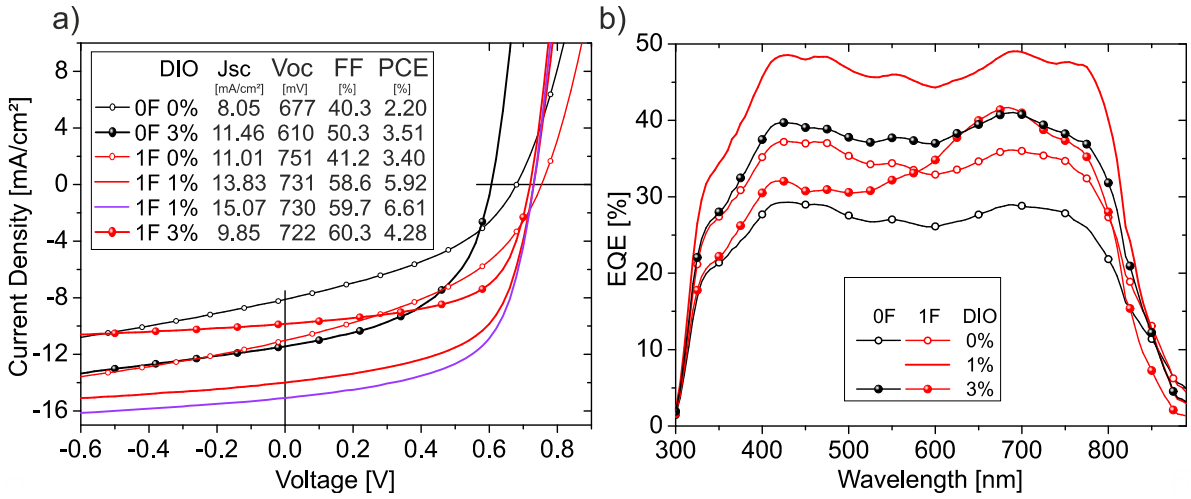

Figure 7.1 (a) *JV* characteristics measured under AM 1.5G illumination at 100 mW/cm² (corrected for spectral mismatch) for 0F and 1F blends processed with different amount of DIO. The purple line shows data for optimized 1F blends with 1:2.5 blend ratio and 90 nm active layer thickness. The inset shows the performance data as average from 6 devices except for the optimized 1F device. (b) The corresponding EQE spectra.

Figure 7.1a shows the solar cell characteristics measured under simulated AM 1.5G with 100 mW/cm² processed with different amounts of DIO and the corresponding performance data. Values for 0F based blends are lower than compared to the data presented in the previous chapter achieved with higher molecular weight 0F, but compare well to efficiencies for blends with PCPDTBT of similar molecular weight (M_w).[195] Upon fluorination V_{OC} is increased by ~130 mV which corresponds well to the increase in polymer IE measured via ultraviolet photoemission spectroscopy, in both pristine and blend layers (not shown here). Interestingly, the optimum amount of processing additive is reduced from 3 to 1% whit fluorination. Importantly, also the J_{SC} of the additive-optimized blend based on 1F is significantly higher. This higher current can be related to an enlarged EQE throughout the entire absorption range as shown in Figure 7.1b. The mean EQE of the optimized 1F blend is 10% larger compared to that of the optimized blend with 0F of almost identical M_w and still 5% larger than the mean EQE measured on blends with higher M_w.[85] In addition to a higher J_{SC} and EQE the fluorination increases the *FF* by

almost 10% in additive optimized solar cells with the same M_w. The *FFs* of the 1F based DIO processed blends actually exceed the highest value (55 %) ever reported for high M_w PCPDTBT.[32]

A further performance improvement of the 1F based blend was achieved by slightly decreasing the active layer thickness[85] and by using a 1:2.5 (instead of 1:3) blend ratio and the use of higher M_w fraction with M_n=25 kDa instead of 10 kDa. With this optimization PCEs of 6.6% are achieved highlighting that 1F outperforms high M_w PCPDTBT[32,48] and Si-PCPDTBT.[30]

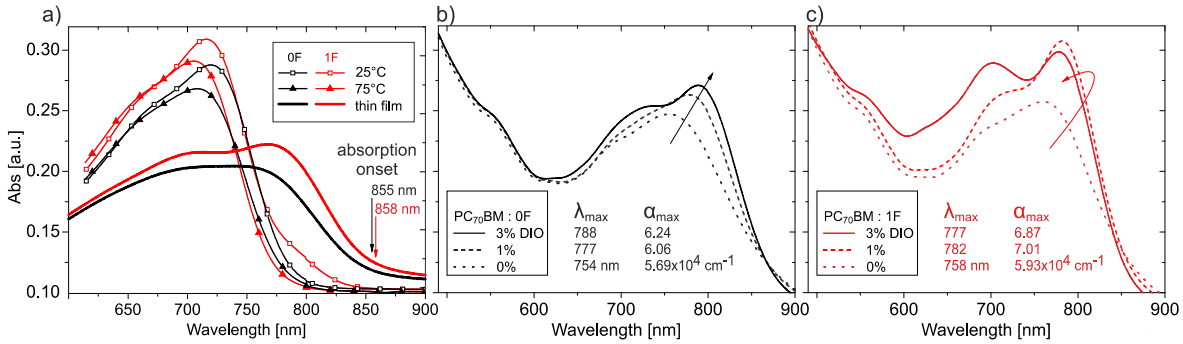

Figure 7.2 (a) Absorption spectra of pure polymer solutions at 25 and 75°C together with absorption of pure polymer films. Arrows indicate the onsets of absorption. (b) Absorption of 100 nm thick 0F based blend films (c) Absorption of 100 nm thick 1F blends.

Absorption spectra of polymer solutions, polymer films, and blend films with a thickness of 100 nm processed with different amounts of DIO are displayed in **Figure 7.2**. Comparing the pure polymer absorption in thin films and in solution in Figure 7.2a, the fluorinated polymer shows higher absorption strength as well as the higher tendency to aggregate as seen by the more pronounced shoulder at 800 nm in the room temperature spectrum. Higher absorption coefficients of fluorinated donor acceptor (DA) copolymers in solution or solid state have been shown by others.[58,196] Note that optical simulations revealed that the higher absorption coefficients of the fluorinated blends raises the fraction of photons absorbed in the active layer only slightly, meaning that fluorination must increase the IQE. Also, the optical band-gap of the solid pristine polymers (as indicated by the arrows in Figure 7.2a) is almost unchanged upon fluorination which agrees well to reports of other fluorinated copolymers.[58]

As nicely shown in Figure 7.2b, adding DIO to the 0F blend continuously increases the strength of the low energy polymer absorption centered in between 750 and 790 nm, which is explained by a higher degree of intra- and interchain ordering.[197] These effects are more pronounced for 1F based blends as seen in Figure 7.2c and indicate the high tendency of the fluorinated polymer chains to aggregate even in presence of $PC_{70}BM$ which causes the optimum amount of DIO to be reduced to 1% in solar cells.

To analyze the effect of fluorination on the morphology of blend layers with $PC_{70}BM$, plasmon maps based on EFTEM were analyzed and the resulting images are summarized in **Figure 7.3**. For both polymers, the images show that the phase separation coarsens with increasing amount of DIO, which is in agreement with results presented in the previous chapter.

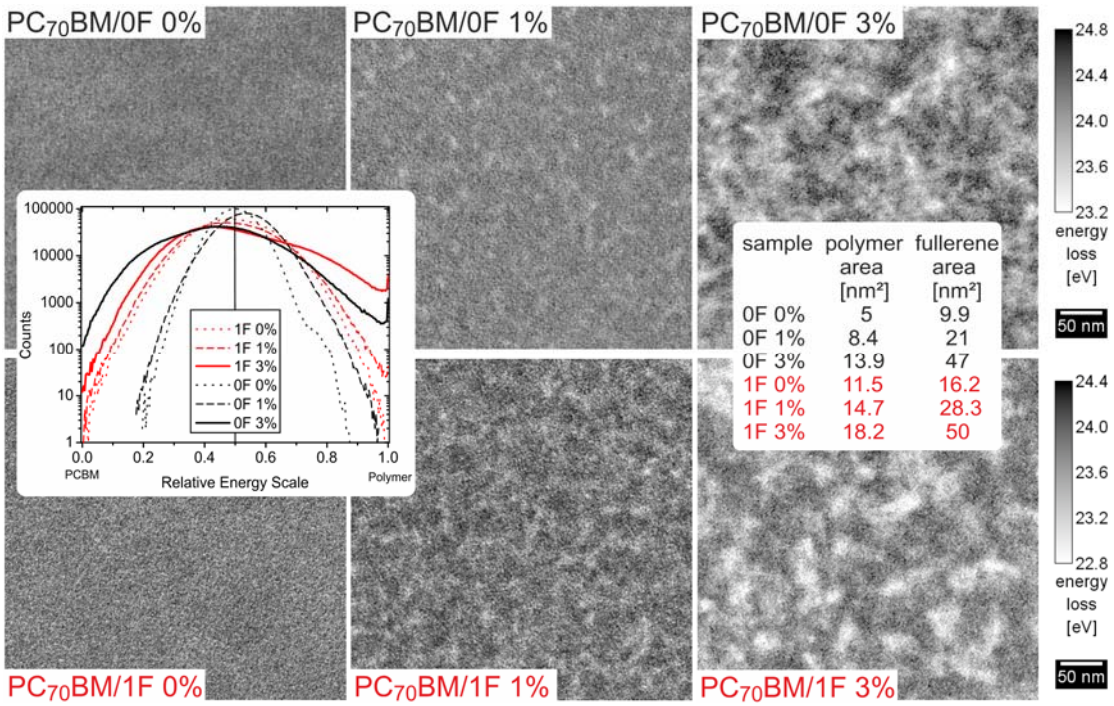

Figure 7.3 Plasmon mapping based on energy filtered TEM in films made from 0F and 1F based blends processed with different concentrations of DIO. The scale bar is the energy of maximum plasmon absorption, where dark areas refer to $PC_{70}BM$ rich phases. The insets show the histogram of the plasmon maps on a relative energy scale and the mean area of polymer and PCBM rich domains.

To quantify the structural heterogeneity of the blends, the plasmon maps have been analyzed with regard to the mean areas of domains that are rich in polymer or PCBM. The average domain size was determined by setting a threshold to the center of the energy scale shown in Figure 7.3. Then all data points with energy below (or above) this threshold were identified to be polymer (or fullerene) rich phases and then the domain size was calculated by the overall domain size divided by their number. These values are plotted in the inset in Figure 7.3. The domain areas have been deduced from TEM images which constitute 2D projections of the true 3D bulk morphology. Therefore, this analysis may underestimate the true domain area. In fact, PCPDTBT crystal sizes larger than 10 nm have been reported in DIO-processed 0F blends.[198] The histograms of the TEM images shows the pixel counts of the plasmon maps on a relative energy scale with the most left part being (almost) pure PCBM phases. The data in Figure 7.3 proof consistently that fluorination enforces the formation of more extended and more pure polymer-rich phases. Noticeably, only 1% of DIO needs to be added to the 1F-based blend to induce a polymer-rich domain area as large as that in the optimized 0F blend processed with 3% DIO. Fluorination also affects the size and purity of the fullerene-rich domains, though this effect becomes less pronounced with increasing DIO concentration. Mean areas of the polymer and fullerene-rich domains are largest for the 1F blend processed with 3 % DIO. It has been pointed out by Son et al.[199] that fluorination of the donor polymer introduces fluorophobility for PCBM, enforcing phase separation which was also reported for blends of other fluorinated DA copolymers with PCBM.[60,200]

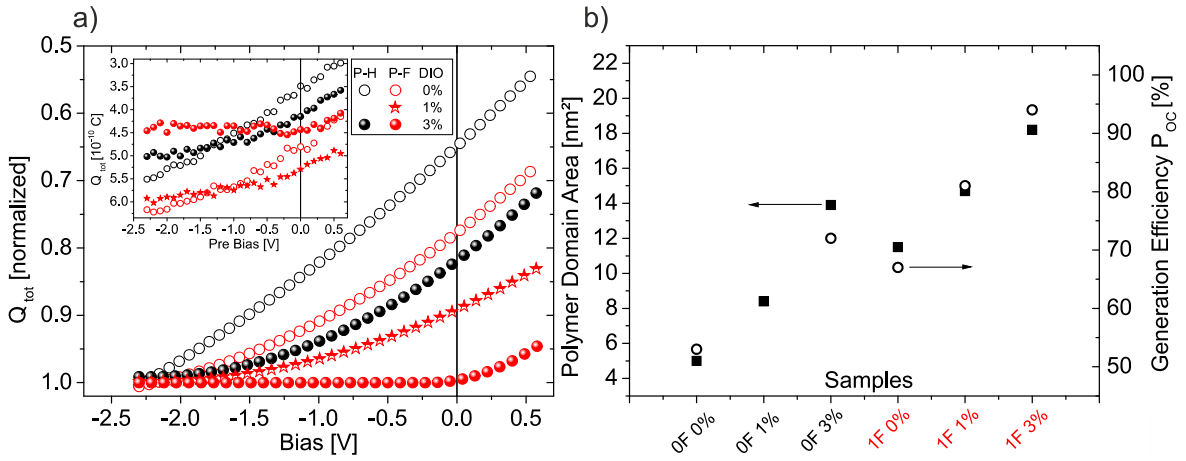

Figure 7.4 (a) Q_{tot} as function of pre-bias. Values have been smoothened and normalized to a bias of -2.3 V. The inset shows the rare, non-normalized data. (b) Comparison of the mean polymer domain size presented in Figure 7.3 (left scale) with the relative generation efficiency at open circuit conditions (right scale), being defined as the ratio of generated charges at open circuit compared to -2.3 V.

To shed some light on the fundamental processes that cause the observed increase in J_{SC} and *FF* upon fluorination, the free-carrier formation and recombination using TDCF measurements is analyzed. **Figure 7.4**a shows Q_{tot} versus pre-bias for a short delay time of 10 ns. By normalizing the generated charge to the respective value at the highest reverse bias of -2.3 V, the field-dependence of free charge carrier generation can be compared for different blends.

For 0F blends processed w/o DIO, the efficiency for free carrier generation at open circuit conditions relative to the efficiency at -2.3 V, P_{OC}, is only 53%, suggesting efficient geminate recombination. Processing the 0F based blend with 3% DIO increases P_{OC} to 72% implying a geminate loss of about 30%. These numbers compare very well to geminate losses at zero bias determined by TAS. Laquai and coworkers determined the total loss due to geminate recombination to about 50% in samples prepared without ODT and 30% in samples prepared with ODT.[113]

Importantly, the field-dependence of free charge generation becomes considerable weaker upon fluorination. Also, processing with DIO weakens the field-dependence for 1F based blends. The good correlation between P_{OC} and the mean polymer domain area in Figure 7.4b and the distinct changes of the optical absorption properties of the blends upon processing with DIO and/or fluorination suggest that a weaker field-dependence of free carrier generation is caused by the formation of larger and purer domains with better interchain order. Noticeably, 1F blends with 3% DIO characterized by rather pure polymer domains with the maximum domain size in lateral dimension show only 5% loss of the efficiency for free charge carrier formation when approaching V_{OC} compared to high reverse bias.

The inset of Figure 7.4a displays the non-normalized Q_{tot} with excitation at a wavelength of 500 nm where all studied blend layers exhibit nearly the same absorption. Apparently, fluorinated blends with DIO generate ca. 20% more free charges than their non-fluorinated counterparts, meaning that either exciton migration to the bulk heterojunction and/or free carrier formation in competition to geminate recombination must be more efficient in 1F blends. A similar enhancement is seen for the two blends

processed w/o DIO. The DA components are well intermixed in these blends, thus the fluorination most likely promotes free carrier formation via more efficient dissociation of bound polaron pairs. Although 1F based blends with 3% DIO displays the weakest field-dependence of free carrier formation, this blend shows an overall low efficiency for free carrier generation at 500 nm. This can be attributed to the presence of large and rather pure domains, implying a low probability for excitons generated on either the polymer or the $PC_{70}BM$ to reach the heterojunction.

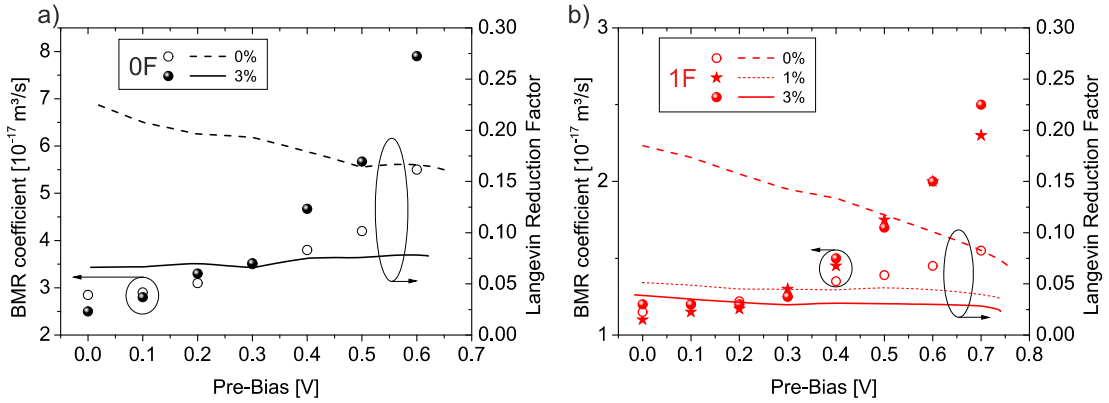

Figure 7.5 Left scale: The BMR coefficient as a function of pre-bias deduced from BMR-fits. Right scale: The Langevin reduction factor obtained from the field-dependence of mobility and the BMR coefficient.

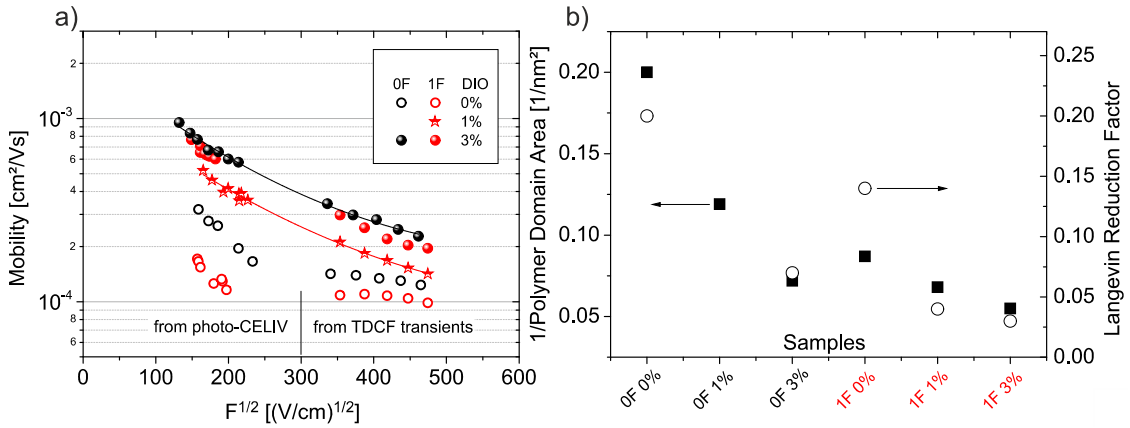

Figure 7.6 (a) Field-dependent mobilities measured with photo-CELIV and TDCF. The lines are guides to the eyes for the additive optimized blends. (b) Comparison of the inverse mean polymer domain area (left scale) deduced from plasmon maps with the Langevin reduction factor near open circuit (right scale) as shown in Figure 7.5.

To assess the kinetics of NGR, TDCF measurements with variable delay time between the laser pulse and the collection bias are performed. **Figure 7.5** shows the BMR coefficient resulting from the BMR fits for all blends and different pre-bias settings on the left scale. For all blends reasonable good fits are obtained pointing to the fact that NGR is dominated by bimolecular recombination. Noticeably, fluorination consequently reduces the BMR coefficient by a factor of 2-3 for all blends. As reported in the previous chapter, the BMR coefficient increases with decreasing internal field which we, again, relate to the negative field-dependence of the charge carrier mobility.

Figure 7.6a displays mobilities deduced from photo-CELIV and TDCF for 0F and 1F blends with different DIO concentrations. It was reported earlier that electrons are the faster charge carriers in

PCPDTBT:PCBM blends.[49] Therefore, the mobility determined by photo-CELIV and TDCF can be attributed to the electrons. The processing additive increases the electron mobility by a factor of 3-4 for 0F blends, which is in accordance with measurements in the previous chapter.

Figure 7.5 plots the Langevin reduction factor parametric in the electric field for all blends studied. In the calculation, it is again assumed that holes are 2 times slower than electrons. With that, the reduction factor is nearly independent of the internal electric field (except for the 1F blend w/o DIO), meaning that the negative field-dependence of the BMR coefficient reported above is again caused by a decrease of carrier mobility with increasing field. Additionally, a lower reduction factor is observed for fluorinated blends, and is further lowered upon processing with the additive.

Figure 7.6b plots the Langevin reduction factor near open circuit for the different blends together with the inverse of the average polymer domain area. Clearly, fluorination reduces the rate at which free carriers recombine. The apparent anti-correlation between the polymer domain size and the reduction factor suggests that this reduction is related to the presence of larger und purer domains in 1F blends. For example the reduction factor of the 1F based blend processed with 3% DIO, which has the largest mean area of the polymer-rich domains, is only 0.03, meaning that NGR in this blend is significantly suppressed compared to the Langevin limit.

This chapter highlights how fluorination of PCPDTBT improves the solar cell performance by enhancing the V_{OC}, J_{SC}, and *FF* simultaneously. With fluorination the polymer-rich phases become larger, more pure, and more crystalline. That enables significant enhancements in the efficiency of free charge formation as well as in the suppression of bimolecular recombination. However, the absolute value of the mobility is lowered with fluorination making charge extraction more inefficient. This counterbalances the reduced BMR coefficient. Thus, the *FF* of optimized 1F blends is limited to 60%. Significantly higher *FF*s can in principle be achieved when enhancing the charge extraction for fluorinated blends. The next chapter will further quantify the impact of the charge extraction efficiency on the fundamental device performance.

8 Quantifying Charge Extraction in Organic Solar Cells: The Case of Fluorinated PCPDTBT

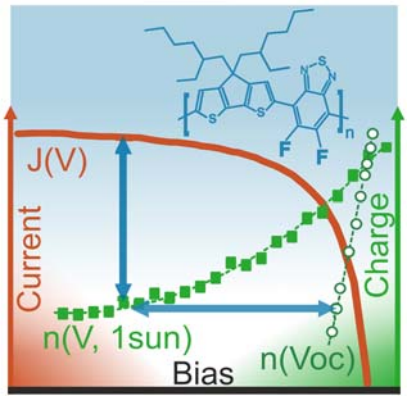

Motivated by the interest to find an explanation for the moderate change in fill factor in PCPDTBT and its mono and di-fluorinated derivatives, a novel methodology is developed that quantifies charge extraction in organic solar cells. This quantification is based on the measurement of the steady state carrier density and the determination of the gradient of the quasi-Fermi level under different illumination and bias conditions. With that methodology the effective extraction mobility for relevant solar cell working conditions can be determined.

This chapter is based on:

S. Albrecht, J.R Tumbleston, S. Janietz, I. Dumsch, S. Allard, u. Scherf, H. Ade, D. Neher, *The Journal of Physical Chemistry Letters* **2014**, 5, 1131.

DOI: 10.1021/jz500457b

The paper is reprinted with permission from American Chemical Society. Copyright, 2014 American Chemical Society.

The development of more efficient materials with reduced optical band-gaps steadily increases the J_{SC} and thus the amount of generated charges within the most efficient organic BHJ solar cells.[201] As discussed before, also thicker active layers well above 200 nm would benefit from increased short circuit currents by enhanced absorption in the active layer. Furthermore, the viable commercialization of organic BHJ solar cells profits from thicker active layers due to practical issues such as process control.[45] Therefore, charge extraction is a critical issue when more charges need to be extracted from thicker active layers in organic materials in which the mobility is a limiting factor. To further develop materials with enhanced extraction efficiency, a novel technique to determine and understand the charge carrier extraction efficiency directly applicable to solar cell working conditions is necessary.

Numerous techniques were developed that enable the determination of the mobility, each addressing free carrier motion under different method-specific conditions. Techniques such as ToF, CELIV, open circuit corrected charge carrier extraction (OTRACE),[202] and FETs have been introduced to record the motion of photogenerated charges. However, these techniques are limited by certain restrictions. ToF requires very thick active layers in the range of micrometers. CELIV, OTRACE, and also TDCF are mostly sensitive to the faster type of carrier only.[162,189] Also, as they measure mobilities under reverse bias conditions, the results might be less useful to characterize carrier motion under solar cell working conditions. FETs can selectively determine electron or hole mobilities, but charge motion is measured across the µm length scale in-plane of the device and at high charge carrier densities. Therefore FET results often differ significantly from measurements of vertical charge transport at the 100 nm length scale and at lower carrier densities.[203]

Electron and hole mobilities in the vertical direction are often determined by analyzing space charge limited currents (SCLC) in single carrier devices, but this method has several drawbacks. First, different electrodes have to be used to guarantee the selective injection of only one type of carrier. Second, the unambiguous determination of the mobilities requires measurements on different layer thicknesses.[185] Both the variation of the electrode configuration and the active layer thickness was shown to affect the blend morphology.[204,205] Also, as pointed out earlier, charge carrier densities in the SCLC regime might be larger than at one sun illumination and at a bias smaller than V_{OC}.[206]

Another strategy for determination of mobilities is the methodology of charge extraction (CE) which was introduced by Shuttle and coworkers.[207] In CE, the device is held at a certain pre-bias under constant illumination. When the light is switched off, the sample is short-circuited and the integral over the resulting current transient is equal to charge in the device. This method can quantify the mobility of charges in a solar cell under steady state illumination conditions at low internal fields via the comparison of the current density J flowing out of the device with the steady state carrier density n measured by CE. If the current density $\mathrm{J}(\mathrm{V})$ at a given bias V is caused by the drift of only one type of carrier (e.g. electrons) with a homogenous density $\mathrm{n}(\mathrm{V})$, the mobility μ can be calculated with e being the elementary charge and E the electrical field across the sample given by $\mathrm{E} = (\mathrm{V_{bi}} - \mathrm{V})/\mathrm{d}$, in which $\mathrm{V_{bi}}$ is the flat band potential and d the layer thickness:

$$\mu(\mathrm{n},\mathrm{V}) = \frac{\mathrm{J(V)}}{\mathrm{e}\cdot\mathrm{n(V)}\cdot\mathrm{E}}. \tag{8.1}$$

The reports published by Durrant and Deibel et al.[135,208] so far make use of the CE method to determine mobilities with some drawbacks: First, the charge is extracted at the low field corresponding to short circuit conditions. Kniepert et al. have previously shown that such low fields may be too small to extract all charge from the device.[209] Second, the correct determination of the internal electrical field E is not straight forward, as it requires knowledge on the flat band potential. Third, equation 8.1 does not account for charge diffusion which might be dominant close to V_{OC}.

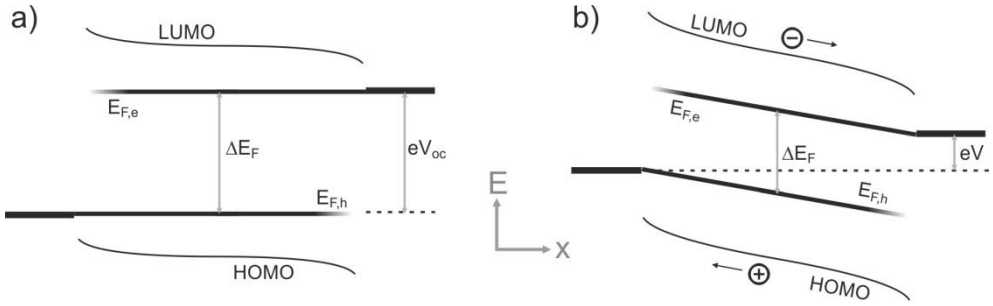

Figure 8.1: Energy level diagram with (a) conditions at open circuit, and (b) conditions at voltages smaller than open circuit, e.g. the maximum power point.

Here a novel approach is presented that determines the mobility via the precise measurement of the steady state charge carrier density with bias amplified charge extraction (BACE) and the proper estimate of the gradient of the quasi-Fermi levels driving the current. The total current J_{tot} by drift and diffusion of electrons and holes was introduced in chapter 2 being determined by $\nabla E_{F,e}$ ($\nabla E_{F,h}$), the gradient of the electron (hole) quasi-Fermi levels.[137] At open circuit conditions, the net-current is zero and thus $\nabla E_{F,e}, \nabla E_{F,h} = 0$ as is displayed in **Figure 8.1**a. As shown in chapter 2, a specific dependence of the quasi-Fermi-level splitting to the respective carrier density can be derived.[138,161]

When the external bias V is lower than V_{OC}, e.g. around the maximum power point (MPP), charges are extracted to the contacts by drift and/or diffusion, driven by a gradient of the respective quasi-Fermi level. This situation is described in Figure 8.1b. If we assume that the gradient is constant throughout the bulk of the device and identical for electrons and holes $\nabla E_{F,e} \cong \nabla E_{F,h} = \nabla E_{qF}$, as it has been shown by recent device simulations,[210,211] the following simple relation can be derived

$$\mathrm{e}V = E_{F,e} - E_{F,h} - \mathrm{d}\cdot\nabla E_{qF}. \tag{8.2}$$

Presuming that the device under steady-state illumination is at near thermal equilibrium also for non-zero currents, the carrier density in the bulk obeys the Fermi-Dirac statistics and the product of electron and hole density is again determined by the quasi-Fermi level splitting. Now, it is considered that the same carrier density n with $n_e \cong n_h$ is established in two ways: either by illumination at intensity I_1 and V_{OC} conditions, where the net-current density is zero, or by keeping the device at a lower bias than V_{OC}, but at higher illumination intensity I_2, with a measurable net-current. Because of equal carrier densities, the quasi-Fermi level splitting in the bulk is the same in both cases and equal to $\mathrm{e}\cdot V_{OC}(I_1)$ leading to:

$$\nabla E_{\mathrm{qF}}(\mathrm{n},V) = \mathrm{e}\frac{V_{oc}(n,\mathrm{I}_1)-V(n,\mathrm{I}_2)}{d}. \tag{8.3}$$

From this, the effective extraction mobility can be determined via:

$$\mu(n,V) = \frac{J(V)}{2n(V)\cdot\nabla\,\mathrm{E}_{\mathrm{qF}}(n,V)} = \frac{J(V)d}{2\mathrm{e}\cdot n(V)\cdot(V-V_{\mathrm{OC}})} \tag{8.4}$$

The factor "2" in the dominator of the equation 8.4 is needed because electrons and holes contribute both and equally to the steady state current of an illuminated solar cell. Finally, μ_{eff} is approximately related to the mobilities of electrons and holes via the following relation:

$$\mu_{eff} = \frac{2\mu_e\mu_h}{\mu_e+\mu_h} \tag{8.5}$$

Compared to earlier work, the approach presented here has several advantages. First, current and carrier densities are compared at the same internal field (bias). Second, it does not rely on any assumption about the field-dependence of charge generation. Third, precise knowledge about the flat band potential is not necessary. Also, contributions from drift and diffusion are automatically included. Most importantly, as electrons and holes contribute equally to *J* at steady state conditions, this approach measures the combined motion of both types of carriers**.** This makes it a suitable approach to quantify the extraction of photogenerated charge in competition to non-geminate recombination in solar cells under working conditions.

In the previous chapter, the enhanced generation efficiency and reduced BMR recombination was shown for 1F as compared to 0F based blends. Here the charge extraction is quantified in 0F, 1F, and 2F based blends with the introduced method to globally understand the competition between enhanced generation, reduced non-geminate recombination and lower charge carrier mobility.

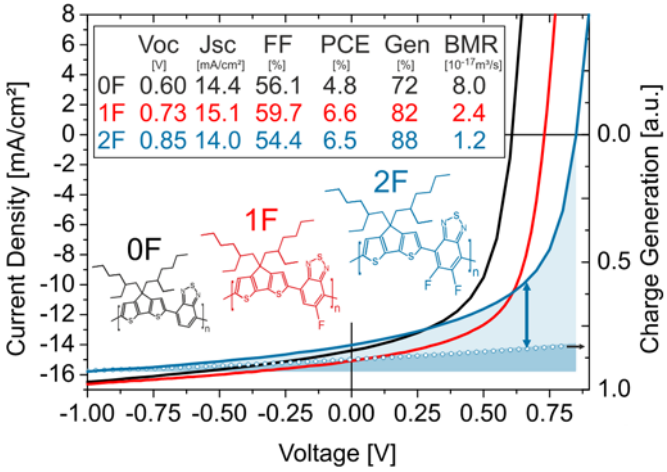

Figure 8.2: left scale: *JV* characteristics measured under AM 1.5G illumination with 100 m/cm² for additive optimized champion cells of 0F, 1F, and 2F blends. Right scale: the field-dependence of charge generation normalized to high fields for 2F blends. The dark and light colored areas highlight the loss due to the field-dependence of charge generation and NGR, respectively for 2F blends. The blue arrow indicates the current loss due to NGR at the maximum power point.

The *JV* characteristics of the additive optimized 0F, 1F, and 2F blends are displayed in **Figure 8.2**. As shown before, the mono-fluorination lowers the polymer HOMO level, resulting in an enhanced V_{OC}.

Also the field-dependence of generation described by the property Gen being the generated charges at open circuit relative to higher reverse fields and the BMR coefficient are reduced upon mono-fluorination, resulting in power conversion efficiencies above 6%.

For the 2F derivate this characteristic trend continues: 2F blends show a high V_{OC} of 850 mV, related to a further down-shift of the HOMO.[145] Importantly, 2F blends also show the weakest field-dependence of charge generation and the smallest BMR coefficient. Both effects can be explained by the morphology changes induced upon fluorination as seen in resonant X-ray scattering (R-SoXS) measurements presented in **Figure 8.3**.[212] For all polymers, the additive DIO increases the total scattering intensity, pointing to higher composition variations (i.e. purity) of the individual phases.[143] On the other hand, for a given additive concentration, fluorination leads to more pure phases, with the highest purity seen in the 2F based blend with 3 % DIO.

Interestingly, despite a significant reduction of the generation losses and of the BMR coefficient with fluorination, the *FF* of the 1F blend is only slightly larger than of the non-fluorinated system and it even decreases for 2F. This can be related to increased non-geminate recombination losses, which is 4.45mA/cm² at maximum power point (MPP) for 2F blends, as indicated by the arrow in Figure 8.2. Thus, approximately one third of the generation current is lost due to NGR at MPP for 2F blends, despite a low BMR coefficient.

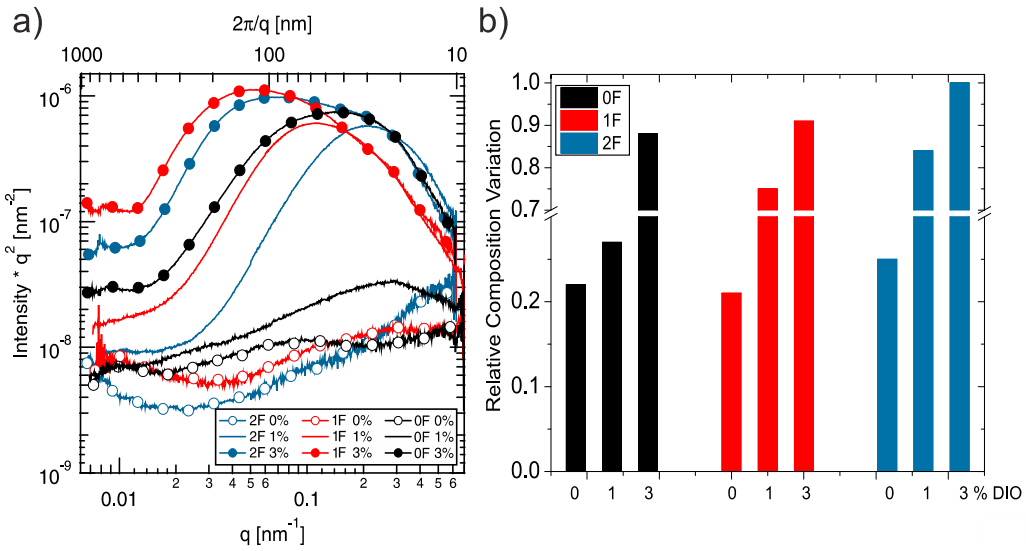

Figure 8.3: (a) Resonant soft X-ray scattering (R-SoXS) measured at 281.1 eV for 0F, 1F and 2F samples each with 0%, 1%, and 3% DIO. (b) The relative composition variations (i.e.purity) extracted from R-SoXS normalized to the most pure device which is 2F with 3% DIO.

To understand this phenomenon, the effective extraction mobility is determined with the BACE technique. **Figure 8.4** displays n(V_{OC}), the carrier density measured at V_{OC} for different illumination intensities, for the additive optimized 1F blend. As expected and shown before,[132,161] n(V_{OC}) follows an exponential dependence on V_{OC}. Also shown are carrier densities n(V) measured at a constant illumination intensity but with decreasing bias. Three intensity levels were chosen to give a J_{SC} of 7, 14, and 25 mA/cm². By definition, n(V) measured for a given illumination intensity intersects with n(V_{OC}) at the respective V_{OC}, and this point is at a higher bias for more intense illumination. The data also

show that when the bias becomes smaller than V_{OC}, the carrier density decreases continuously due to more rapid extraction. The gradient of the quasi-Fermi level driving this current for any arbitrary bias and illumination conditions is now determined by simply considering the difference $V(n)$-$V_{OC}(n)$ at the respective carrier density n, following equation 8.3. This is exemplified by the horizontal arrow in Figure 8.4. Combined with the steady state current density (vertical arrow) measured for identical illumination conditions using the same laser diode operating at the same intensity in continuous wave, the effective extraction mobility can be calculated with equation 8.4.

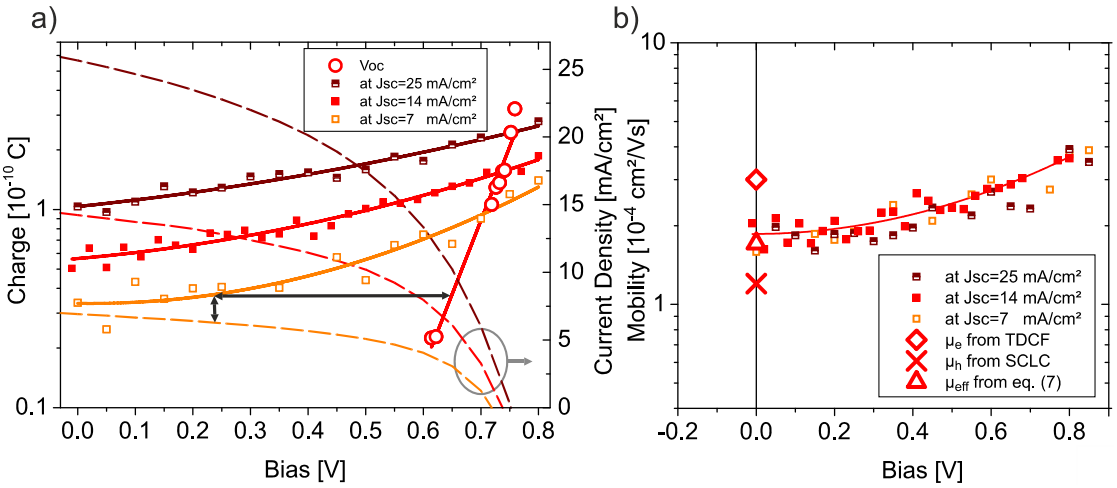

Figure 8.4: (a) Steady state charge carrier density for 1F devices measured with BACE at the respective V_{OC} for different illumination intensities and for variable bias and constant illumination conditions generating short circuit currents of 25, 14, and 7 mA/cm². The corresponding *JV* curves are plotted on the right axis. (b) Effective extraction mobility determined from the steady state densities as presented in (a), electron mobility μ_e from TDCF, hole mobility μ_h from SCLC measurements, and the effective mobility μ_{eff} according to equation 8.4 estimated from the μ_e and μ_h. Solid lines are guide to the eyes.

The results of this analysis are shown in Figure 8.4b. Near short circuit, the effective mobility is around $2 \cdot 10^{-4}$ cm²/Vs, ca. 1.5 times smaller than the mobility of the faster carriers (electrons) as reported in the previous chapter. It is also a factor ca. 1.5 higher than the hole mobility extracted from holy only devices. The effective mobility according to equation 8.5, determined from hole and electron mobility measurements, nicely fits to the effective extraction mobility estimated from BACE. We also observe a continuous increase of the effective mobility with decreasing field, confirming the previous findings of a negative field-dependence of mobility in full accordance with theoretical predictions.[192] The fact that mobilities for three different illumination intensities are comparable proofs the consistency of new approach presented here. It also shows again that the explicit dependence of mobility on carrier density is weak.

Figure 8.5a compares the carrier density $n(V_{OC})$ measured under open circuit conditions for the three different blends. Increasing the number of fluorine atoms causes a significant shift of the $n(V_{OC})$ curve to higher biases, which is mainly caused by the lowering of the polymer HOMO. Also shown are the steady state carrier densities $n(V)$, with the intensity adjusted to give a J_{SC} of 14 mA/cm² for each blend. This Figure reveals some important differences. First, though the charge extracted from 0F and 1F blends is quite comparable in the measured bias range, the $n(V)$ of the 1F blend decays more slowly

with decreasing bias. In other words a larger gradient of the quasi-Fermi level is necessary to extract the carriers in the 1F blend. This is expressed by a slightly lower mobility as shown in Figure 8.5b. More importantly, n(*V*) of the 2F-based blend is larger and it decays even more slowly with decreasing bias over the entire range. Indeed, the effective extraction mobility according to equation 8.4 is fairly low for this blend, below $2 \cdot 10^{-4}$ cm²/Vs.

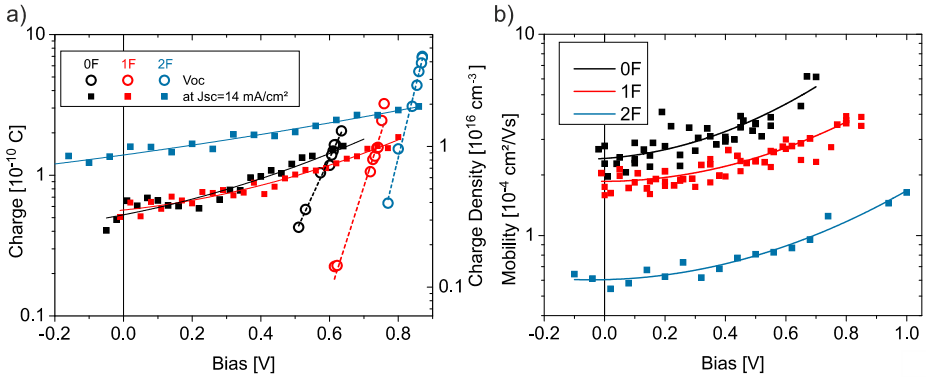

Figure 8.5: (a) Steady state charge carrier density as function of bias measured with BACE at the respective V_{OC} and illumination conditions resulting in J_{SC}=14 mA/cm². (b) Extraction mobility as function of bias estimated from BACE data as shown in (a). All lines are guide to the eyes.

With the knowledge about the effective extraction mobility, we are able to understand the trend in *FF* upon fluorination. The *FF* results from the specific interplay between field-dependence of generation, extraction and NGR. Fluorination improves charge generation, thereby reducing its field-dependence. In addition a sevenfold reduction in BMR coefficient is measured in between 0F and 2F blends. The enhanced generation and reduced NGR is counterbalanced by a significant lowering of the mobility upon fluorination. For 1F blends, this effect of reduced mobility on the *JV* characteristics is still quite weak, rendering the 1F based blend the one with the highest *FF* close to 60%. The lower extraction becomes important for 2F blends. The high carrier density remaining in the device under steady state enhances NGR losses, although this blend shows the smallest BMR coefficient. At a density n of ca. $1.5 \cdot 10^{22}$ m⁻³ and a BMR coefficient γ of $1.2 \cdot 10^{-17}$ m³·s⁻¹, the recombination current at MPP according to $J_{rec} = \gamma e d n^2$ is 4.3 mA/cm². This is in very good agreement with the current loss determined from the comparison of the current density (4.45 mA/cm²) and the field-dependent generation measured via TDCF at the MPP (as shown by the arrow in Figure 8.2).

Thus, if the effective mobility in the 2F based blend could be increased, it would achieve superior performance over the 1F and 0F polymers in blends with PCBM. Most likely, the effective mobility in 2F based blends is strongly limited by the hole mobility. We further investigated the impact of the hole mobility influencing the effective mobility and with that the *FF* on thick active layers made from polymer:PCBM blends with the presented method. By changing the amount of fluorination utilizing random copolymerization with PBnDT-HTAZ and PBnDT-FTAZ monomers, the effective mobility was continuously altered with fluorination.[213] With these results, quantification of the effective mobility with regard to high *FF*s is possible. In 2F based blends the effective mobility needs to be enhanced by a factor of 20 to increase the *FF* from 54 to over 70% at thick active layers above 300 nm when the BMR coefficient is not altered and the small field dependence neglected.

9 On the Efficiency of Charge Transfer State Splitting in Polymer Solar Cells

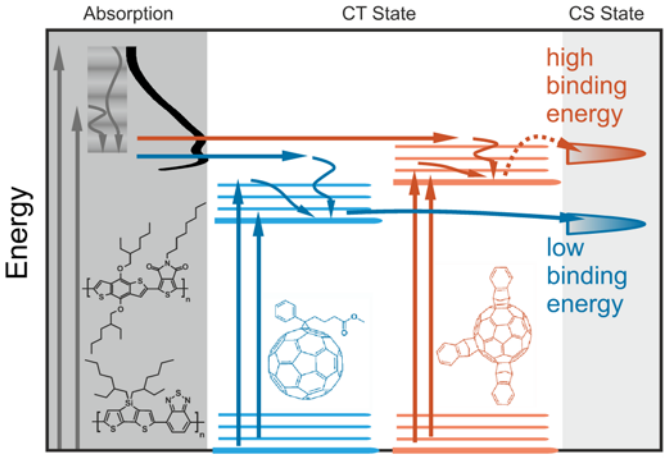

The base of this work is the fruitful collaboration with Prof. Dr. Koen Vandewal which started during the sabbatical leave of Prof. Dr. Dieter Neher to Stanford University. In a short time, a lot of interesting experiments regarding the effect of the incident photon energy on charge generation in different organic BHJ solar cell systems were performed, which provided deep and new inside into the mechanisms determining the efficiency of charge transfer state splitting.

This chapter is based on:

S. Albrecht, K. Vandewal, J. R. Tumbleston, F. S. U. Fischer, J. D. Douglas, J. M. J. Fréchet, S. Ludwigs, H. Ade, A. Salleo, D. Neher, *Advanced Materials* **2014**, 26, 2533.

DOI: 10.1002/adma.201305283

The paper is reprinted with permission from WILEY. Copyright, 2014 WILEY-VCH.

The chapter is partially based on:

K. Vandewal, S. Albrecht, E. T. Hoke, K.R. Graham, J. Widmer, J. D. Douglas, M. Schubert, W. R. Mateker, J. T. Bloking, G. F. Burkhard, A. Sellinger, J. M. J. Fréchet, A. Amassian, M. K. Riede, M. D. McGehee, D. Neher, A. Salleo *Nature Materials* **2014**, 13, 63.

DOI: 10.1038/nmat3807

The paper is reprinted with permission from Nature Publishing Group. Copyright, 2014 Nature Publishing Group.

The reasons for highly efficient charge generation despite the existence of Coulombically bound geminate pairs in organic polymer:fullerene solar cells is subject of ongoing debate. Correlations have been found between the free carrier generation yield and the energy difference $\Delta E_{CS}^{eff} = E_{S1} - E_{CS}$. Here, E_{S1} is the lowest singlet state on either the D or the A and the energy of the fully separated charge pair E_{CS} is given by the difference between the electron affinity of the A and the IE of the D. This energy difference is often referred to as driving force for charge generation and values larger than several 100 meV were proposed to be required for high performance systems.[62,110] Interestingly, this view is not applicable to the fluorinated PCPDTBT polymers discussed in the last chapters. Mono-fluorination lowered the polymer HOMO and thus increased E_{CS}, while E_{S1}remained constant. If charge carrier generation would be determined by the driving force ΔE_{CS}^{eff}, then fluorination would decrease the charge generation efficiency which is clearly not the case.

Furthermore, as introduced in chapter 2, the relevance of hot charge carrier generation in a working device is subject of controversy in the literature.[63,68] In this mechanism, the energy delivered to the system upon singlet exciton formation is partially used to form electronically and/or vibrationally excited CT states, which then possess a sufficient kinetic energy to overcome the Coulomb barrier. On the other hand, it is less clear whether charge generation in a working solar cell proceeds via such excited CT states as properly measured IQEs are independent of excitation energy on a broad energetic range.[69] Thus, pathways comprising thermalized CT states can be of equal importance.

To answer this question a comprehensive study of free carrier generation in BHJ systems with carefully tuned energetics is conducted in this chapter. First, the excitation energy dependence of the free charge formation is considered. Two different polymer:$PC_{60}BM$ model systems namely MEH-PPV:$PC_{60}BM$ and PBDTTPD:$PC_{60}BM$ are studied. MEH-PPV used as donor is characterized by a relatively inefficient and field-dependent charge carrier generation mechanism. In contrast, PBDTTPD shows efficient and field-independent charge carrier generation.

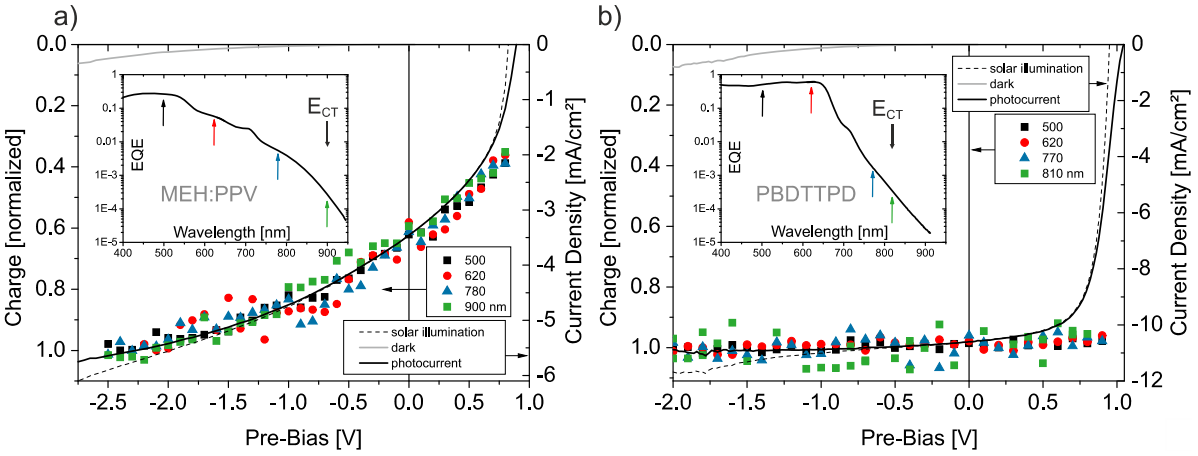

Figure 9.1 (a) *JV* characteristics under AM 1.5G illumination with 100 mW/cm² and the normalized total charge obtained from various excitation energies for MEH-PPV:PCBM blends. The inset shows the corresponding EQE (on log scale) with the wavelengths of excitation used for the measurement of the total charge and the energy of the CT state E_{CT}. (b) The similar set of data for PBDTTPD:PCBM devices.

Figure 9.1 shows *JV* curves under AM 1.5G illumination with 100 mW/cm² and the dark current of photovoltaic devices prepared with these blends. The devices have PCEs of 1.3% and 7%, for MEH-PPV and PBDTTPD donors, respectively. The field-dependence of the charge carrier generation mechanism is investigated with TDCF experiments for different excitation energies. The laser fluence is varied according to the absorption to generate comparable amounts of free charges at every photon energy. The normalized charge as function of pre-bias and excitation energy is shown on the right axes, allowing comparison with the photocurrent. For the MEH-PPV device, the dependence of the photocurrent on voltage tracks the dependence of the charge carrier generation yield, indicating that its performance is limited by its strongly field-dependent charge carrier generation mechanism, consistent with previous reports on PPV devices.[214] In contrast, for the PBDTTPD device, the yield is field independent, and reaches almost unity (see Figure 9.2b). On varying the excitation photon energy, the excitation of the D, the A, and the CT state manifold can be selectively addressed. Importantly, virtually no difference in the field-dependence of charge carrier generation is observed when exciting either the D the A or the CT state manifold. This is valid, irrespective of whether the charge generation mechanism is intrinsically field dependent as for MEH-PPV or field independent as for PBDTTPD donors. This important finding highlights that the energy gain upon singlet exciton dissociation has only a minor effect on the yield of the CT state split-up into free charge carriers.

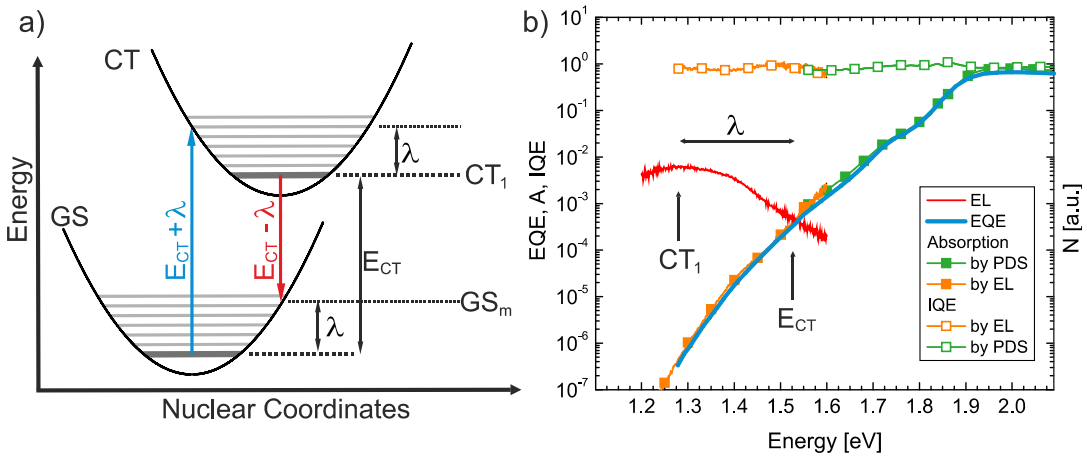

Figure 9.2 (a) Energy potential diagram of the ground state (GS) and the CT manifold with the relaxed CT state (CT_1), the reorganization energy λ and the vibronically excited ground state GS_m. (b) Measured electroluminescence (EL) and EQE spectra, with absorption measured by PDS in combination with transmission and reflection, as well as the absorption calculated from the EL emission together with the corresponding IQEs for PBDTTPD:PCBM devices.

The energy potential diagram of the electronic ground state (GS) and CT state is shown in **Figure 9.2**a. It is obvious that a direct CT_1 excitation from the GS is must be very inefficient according to the Franck-Condon principle. The excitation with energy E_{CT} will lead to a vibrationally excited state of energy $E_{CT1}+\lambda$, with λ being the reorganization energy with typical values of 0.2 eV. Direct CT_1 excitation is hampered by the low probability of thermal population of the vibronically excited ground state GS_m, which is necessary for the adiabatic optical transition to the CT_1 state. The emission, however, starts from the fully relaxed CT_1 state leading to GS_m. Thus, the maximum of the electroluminescence (EL) spectra is red-shifted as compared to the CT EQE which is displayed in Figure 9.2b. In order to detect

the quantum yield of the fully reorganized, relaxed and emissive CT_1 state, without being able to measure the absorption at energies of CT_1 emission, another approach can be followed. Under the assumption that the EL starts from the fully relaxed CT_1 state and that all involved states are in thermal equilibrium, the EL spectrum of the solar cell equals the thermal radiation described by Planck's law yielding a direct correlation between photon absorption and emission at energy E. With Boltzmann approximation for the band occupation, the absorption of photons $A(E)$ correlates to the emitted photon flux $N(E)$ according to:[137]

$$A(E) \sim (N(E)/E^2) \cdot e^{(E/kT)}. \tag{9.1}$$

Thus, the well detectable EL spectrum can be used to determine the optical absorption strength at all energies of CT emission. In combination with sensitive measurements of the EQE in the same spectral region, the IQE for direct CT_1 excitation can be determined. This analysis proved that the IQE is independent of excitation energy down to the energy of CT_1 emission. This is exemplarily shown for PBDTTPD:PCBM devices in Figure 9.2b. The very same conclusion was drawn from studies of MEH-PPV:PCBM and other BHJ systems. Thus, the general conclusion is that under working conditions, the split-up of CT states proceeds via the thermalized CT_1 state.

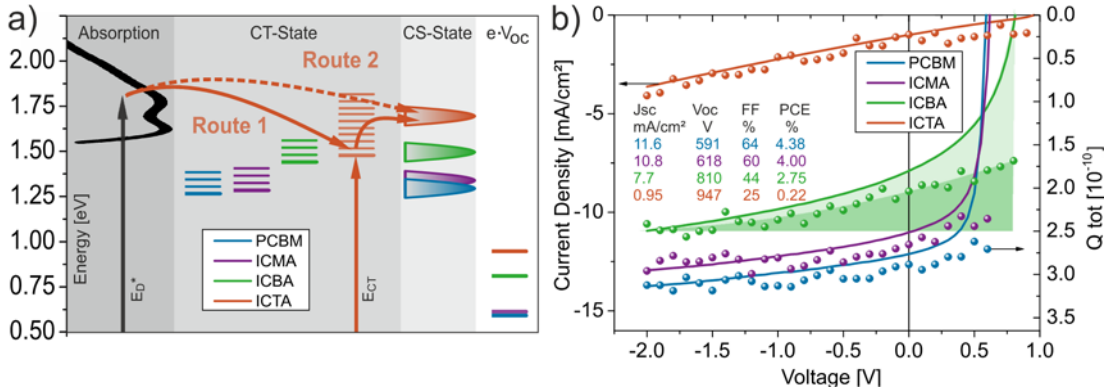

Figure 9.3 (a) Energy diagram for different Si-PCPDTBT:fullerene blends with blend main absorption, CT state manifolds, position of the charge separated (CS) states, and e·V_{OC}. Two different generation routes are indicated for the ICTA blend. Route 2: The donor excitation E_{D^*} leads to separated charges via excited CT states. Route 1: E_{D^*} excitation thermalizes in the CT manifold and then gets separated. (b) Steady state *JV* curves under AM 1.5G illumination with 100 mW/cm² (left scale) and Q_{tot} excited at 650 nm (right scale). The light and dark coloured areas show losses from NGR and field-dependent generation, respectively for Si-PCPDTBT:ICBA.

However, it was proposed that the excitation energy dependence of charge generation depends on whether the blends exhibit a small or a large driving force (in the above definition). Dimitrov and coworkers showed that for systems possessing a very small driving force, a higher photon energy of ~0.2eV above the optical band gap can effectively enhance the charge generation, correlated with a decrease in the yield of charge generation via relaxed CT state excitations.[64]

In order to further study the details of how the driving force in the above definition impacts the charge generation with respect to excitation energy, different fullerene derivatives, PCBM, ICMA, ICBA, and ICTA, having different LUMO energies are used with the silicon bridged derivative Si-PCPDTBT. This polymer is used as it can be processed without the use of an additive to give reproducible and high efficiencies. **Figure 9.3**a displays the blend film absorption spectra together with the CT state manifold,

with the position of the lowest bar indicating E_{CT}. Figure 9.2 also includes estimates for E_{CS} using values for the polymer HOMO and the fullerene LUMOs measured with CV in solution. These values are in good agreement to those given in the literature.[215,216] A continuous increase of the CT energy with increasing fullerene LUMO value is shown as expected. An exception is the case of Si-PCPDTBT blended with ICTA, where the CS state approaches the energy of the excited donor, E_{S1}, and the CT state and polymer singlet exciton state are in resonance, resulting in an E_{CT} limited by the optical band-gap of the Si-PCPDTBT.

In Figure 9.3b the corresponding *JV* curves under AM 1.5G solar illumination are presented for Si-PCPDTBT:fullerene blends. The highest performance was obtained for Si-PCPDTBT:PCBM blends (see Table 9.1). The use of ICMA, ICBA and ICTA as acceptors increased V_{OC}, but lowered *FF* and J_{SC}. To designate the main cause of the decreased *FF* and J_{SC} in multi-adduct fullerene blends as either being field-dependent free carrier generation or enhanced NGR, TDCF experiments are performed. The excitation wavelength of 650 nm has been chosen, which excites mainly the S_1 state of the Si-PCPDTBT polymer.[63] All blends exhibit almost similar absorption at this wavelength. Comparison of Q_{tot} with the *JV* curves indicates that the reduction in current and *FF* when using higher adduct fullerenes is primarily due to a reduced yield and increasing field-dependence of free charge carrier generation. Noticeably, our experiments did not reveal a pronounced increase of the BMR coefficient when replacing PCBM by higher adduct fullerenes though a slight decrease in mobility is measured (data not shown). This causes the slight increase in losses due to NGR when PCBM is replaced by ICBA as indicated by the light colored area in Figure 9.3b.

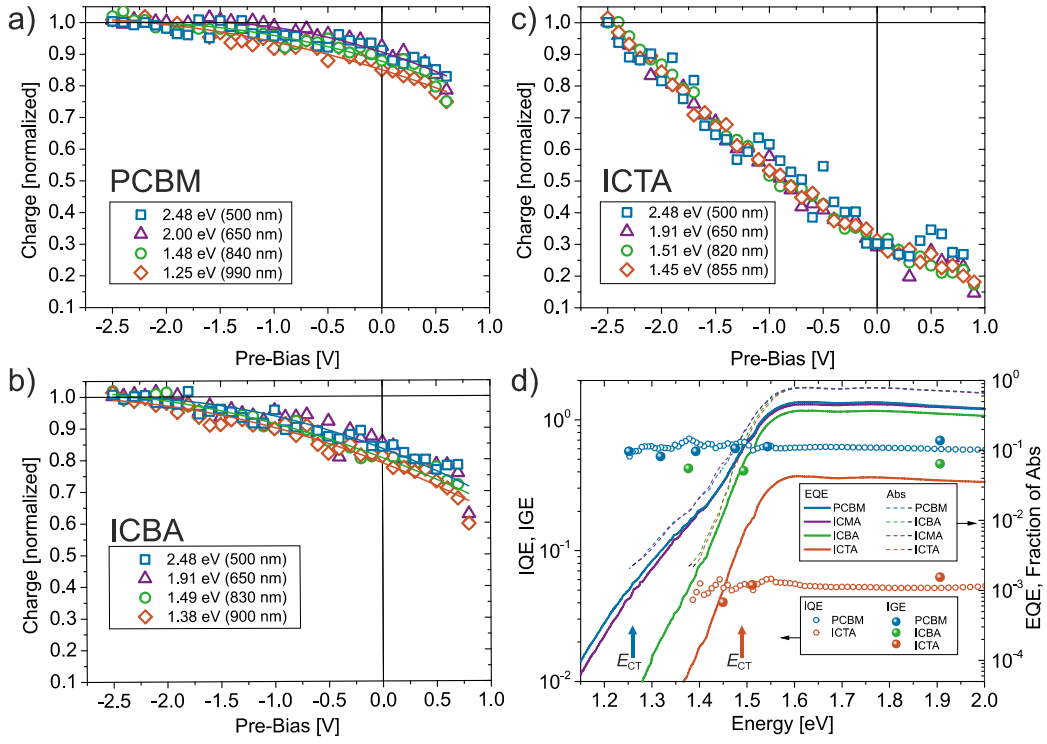

Figure 9.4 Normalized total charge versus pre-bias for different excitation wavelengths for Si-PCPDTBT blended with (a) PCBM, (b) ICBA, and (c) ICTA. (d) EQE, IQE and fraction of modeled absorption as well as the internal generation efficiency (IGE) deduced from TDCF for Si-PCPDTBT:fullerene blends.

As shown by **Figure 9.4**a-c, varying the excitation energy over a broad range has essentially no effect on the field-dependence of generation independent of which fullerene is used as donor. This result is highly remarkable as rather small changes in the fullerene energy levels, and with that of the driving force, led to considerable changes in the field-dependent charge generation. Importantly, the excitation energy independence is also seen for blends with diminishing driving force.

To substantiate this claim, IQE spectra over a wide wavelength range from the sensitive measurements of the EQE and of the absorption A(E) in conjunction with optical modelling is performed and shown in Figure 9.4d. For the Si-PCPDTBT blended with PCBM and ICTA the steady state IQE(E) and IGE(E) are independent (within the sensitivity of the used methods) of excitation energy, irrespective of whether excitation occurs in the donor, acceptor, or CT state.

These findings finally proof that the charge generation proceeds via the relaxed CT_1 state (Route 1 in Figure 9.3) irrespective of the driving force in the above definition.

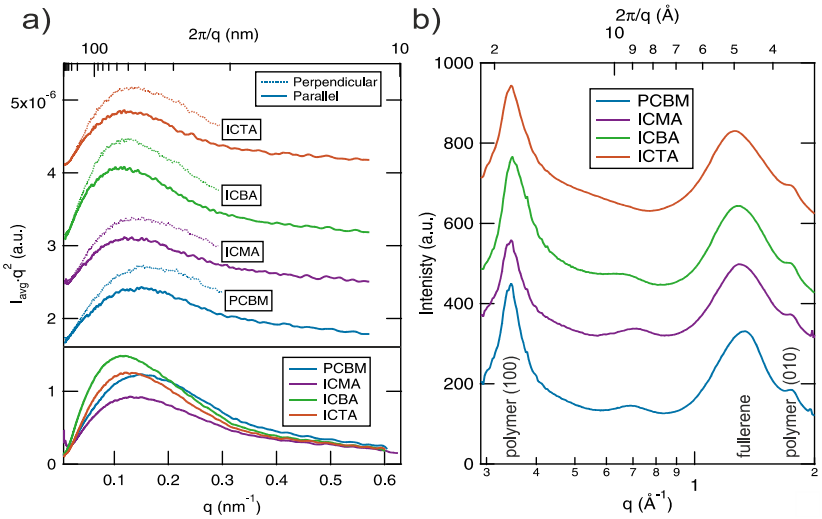

Figure 9.5 P-SoXS and GIWAXS data for Si-PCPDTBT blends with different fullerenes (a) Lorentz corrected P-SoXS sector averages for 282.5 eV photon energy. The upper traces (vertically offset for clarity) reveal anisotropic scattering with greater intensity perpendicular compared to parallel to the photon electric field polarization for all samples. The lower traces correspond to circular integration of the 2-D data. (b) Circular averages of GIWAXS 2-D scattering. GIWAXS circular averages have been shifted vertically for comparison.

A possible explanation of the decreasing charge generation efficiency in Si-PCPDTBT blends with higher adduct fullerenes can be the blend morphology. In the previous chapters, it was summarized that the morphology, i.e domain size, size distribution, and domain purity, is crucial for device performance and the underlying charge carrier dynamics. To investigate if morphology is a major factor responsible for differences in free carrier generation yield in Si-PCPDTBT:fullerene blends, polarized soft x-ray scattering (P-SoXS) is utilized. **Figure 9.5** shows results from P-SoXS together with grazing incidence wide angle x-ray scattering (GIWAXS) data when four different fullerenes are used. All blends are characterized by a similar log-normal distributions of spatial frequencies along with similar total scattering intensity, which scales with the square of the average composition variations in the samples.[212] The relative composition variations are 0.98, 0.84, 1.0, and 0.94 for Si-PCPDTBT with PCBM, ICMA, ICBA, and ICTA, respectively. Except for the somewhat lower value observed for the ICMA blend,

the relative purity of the fullerene and polymer rich domains and/or their volume fraction is thus rather constant. Also, the median characteristic length scale between domains with similar composition is very similar for all blends with 30, 30, 35, and 33 nm for Si-PCPDTBT blended with PCBM, ICMA, ICBA, and ICTA, respectively. All blends also show scattering anisotropy with greater intensity perpendicular to the photon electric field (s-scattering) compared to parallel (p-scattering). Scattering anisotropy corresponds to preferential in-plane orientation correlations of the polymer (edge-on versus face-on) relative to the fullerene domains.[119,217] It is similar in sign and magnitude for all samples and differences in molecular orientation can thus be eliminated as a contributing factor. The shape and overall intensity of the GIWAXS scattering profiles are similar for all samples, indicating that differences in polymer lamellar and π-π ordering as well as fullerene aggregation are minimal. Overall, the minor differences in active layer morphology observed cannot explain the observed differences in charge generation. The data presented so far shows that replacing PCBM with higher adduct fullerenes has a pronounced effect on the total yield and field-dependence of free charge carrier generation despite similar morphologies and the absence of hot CT state contributions.

Thus changes in charge generation efficiency must be related to interfacial energetics. To address this point, HOMO und LUMO energies of all Si-PCPDTBT:fullerene blend films were determined with in-situ spectroelectrochemistry by Florian Fischer at the University of Stuttgart. This allows the determination of energy levels more precisely than the conventional method of determining onset or half wave potentials purely from cyclic voltammograms. The energy levels of the polymer and the fullerenes in the blends were determined from the potential corresponding to the onset of changes in the characteristic absorption bands of the neutral or charged states. The HOMO and LUMO energies were calculated from the absorption onsets of the first polymer oxidation and first fullerene reduction, respectively. The resulting values are given in Table 9.1.

Table 9.1 Energy levels from CV of single component solutions and energy levels from in-situ spectroelectrochemistry data of blends together with photovoltaic properties. E_{CT} is the energy of the CT state and λ the reorganization energy, both determined from optical spectroscopy. Values in brackets are taken from Faist et al.[215] as comparison. Performance values are averages over 6 devices.

	Polymer HOMO [eV]	Fullerene LUMO [eV]	J_{SC} [mA/cm²]	V_{OC} [mV]	*FF* [%]	PCE [%]	E_{ct} [eV]	λ [eV]
Si-PCPDTBT	4.97 (5.0)							
PCBM		3.70 (3.74)						
ICMA		3.68 (3.70)						
ICBA		3.53 (3.55)						
ICTA		3.33 (3.36)						
Si-PCPDTBT:PCBM	4.86	3.88	11.6	591	64	4.38	1.26	0.27
Si-PCPDTBT:ICMA	4.86	3.81	10.8	618	60	4.00	1.28	0.27
Si-PCPDTBT:ICBA	4.86	3.60	7.7	810	44	2.75	1.45	0.22
Si-PCPDTBT:ICTA	4.86	3.40	0.95	947	25	0.22	1.49	0.22

Values of E_{CS} calculated from blend films are compared to E_{CS} determined from solution. Although the absolute values for E_{CS} in solution and in the blend are difficult to compare with regard to absolute values, due to differences in the local environment (solution versus solid state) and the technique used to determine HOMO and LUMO energies, they allow a reasonable comparison between the different fullerenes. Notably, the stabilization energy (defined as the difference between the fullerene LUMO in the solid-state blend and in solution) decreases significantly when PCBM is exchanged by ICMA, while both blends exhibit quite similar generation efficiencies. On the other hand, similar values of the stabilization energy are measured for ICBA and ICTA, despite large differences in device performance. Thus, the reduction in the stabilization energy cannot fully account for the poorer performance of the higher adduct fullerenes. Therefore, it is most likely that the efficiency of CT-split-up in the analyzed blends is intimately connected to the nature and energy of the relaxed CT state in comparison to the CS state.

Figure 9.6 relates the total photogenerated charge at short circuit to the difference between E_{CT} and E_{S1} or $E_{CS\_solution}$ for both Si-PCPDTBT and PBDTTPD as donors. The data shown in Figures 9.3 and 9.4 were also performed with PBDTTPD as donor polymer blended with PCBM, ICMA, and ICBA. These results are in full agreement to the results obtained with Si-PCPDTBT. Figure 9.6a highlights that a sharp decrease of the generation efficiency occurs only when the CT state approaches the energy of the pure excitonic states, as in Si-PCPDTBT:ICTA. At such small energy offsets the CT state and excitonic states are in resonance, mixing their wavefunctions giving the CT state a more localized and bound character, thus increasing the energetic difference between CS and CT state.[218] Related to this, significant singlet exciton recycling from the CT state has been reported for blends with higher adduct fullerenes.[215] Figure 9.6b shows the photogenerated charge to decrease continuously when the energy difference between the CS state and CT state increases, which is assigned to an increasing binding energy of the relaxed CT state.

The findings presented in this chapter lead to the remarkable conclusion that generation proceeds via the split-up of the relaxed CT_1 state irrespective of the initial excitation energy and driving force. This important conclusion opens up new guidelines for future material development that require a minimum energetic offset between CT and CS state while keeping the ΔE_{CS}^{eff} as small as possible.

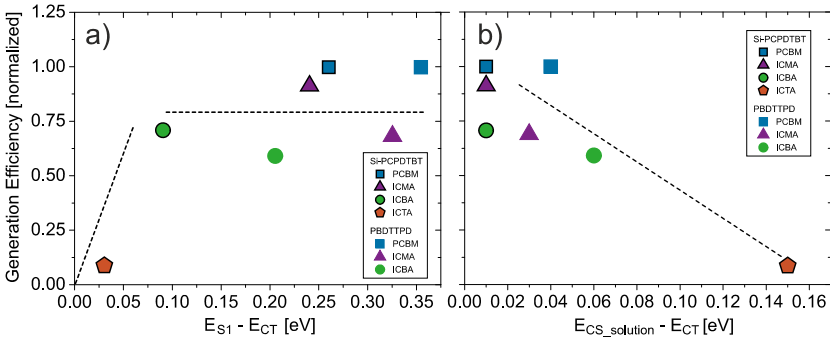

Figure 9.6 Charge generation efficiency at short circuit normalized to the PCBM blend for each donor polymer compared to the energy difference of (a) the lowest singlet state (E_{S1}) and the charge transfer state (E_{CT}) and (b) the charge separated state as measured from solution CV ($E_{CS\_solution}$) and the charge transfer state energy.

10 Conclusion

Initially motivated by the aim to develop organic solar cells with tailored properties for the realization of efficient hybrid tandem solar cells, this thesis provides a comprehensive view of the charge carrier dynamics of blends made from polymeric donors and fullerene-based acceptors. As summarized in chapter 4, with the proper choice of the organic blend, a hybrid tandem cell comprising a-Si:H and Si-PCPDTBT:$PC_{70}BM$ sub-cells connected in series via optimized recombination contacts was realized with a power conversion efficiency of 7.5%. This is by far the highest published efficiency for this hybrid tandem cell design. Optical and electrical device modelling suggests that the PCE can be increased to 12% by combining donors with suitable absorption onsets in combination with PCBM. This success initiated a more detailed understanding of the photovoltaic properties of the low band-gap polymer PCPDTBT and its derivatives, but developed further towards a comprehensive investigation of the fundamental aspects of charge generation, recombination and extraction in organic bulk heterojunction solar cells.

The most important finding of these studies was the result that the excess photon energy does not alter the efficiency and field dependence of charge carrier generation as presented in chapter 9. This scenario was independent of whether the photoactive blend had a low performance with highly field-dependent generation as for MEH-PPV:PCBM blends, or exhibited very efficient and field-independent generation like in PBDTTPD:PCBM devices. To measure the internal quantum efficiency for excitations down to energies of the electronically and vibronically relaxed CT_1 state, the inaccessible absorption at this energy was reconstructed from the CT emission, induced via the recombination of thermalized charges in electroluminescence. For a variety of blends, the internal quantum efficiency was constant throughout the entire energy range studied, which comprised the energy of the relaxed CT_1 as well as excitation energies well above the band-gap. Therefore, the generation in a working solar cell proceeds via the split-up of thermalized CT states, irrespective of the initial excitation energy. These results are in great contrast to conclusions from various fs-pump-probe experiments, which highlights the importance of applying proper illumination conditions.

With the split-up of bound polaron pairs starting from the relaxed CT_1 state, the fundamental conclusion from this part of the work is that the efficiency of charge generation is not dictated by the difference in energy between the initially excited singlet exciton, E_{S1}, and the energy of the final charge separated state, E_{CS}, which is the so-called driving force. Instead, the efficiency of charge generation will be governed by the energetic offset between the relaxed CT state and E_{CS}. Importantly, this offset is not simply determined by the HOMO and LUMO energies of the individual donor and acceptor components. Rather, the energy landscape at the donor acceptor interface and with that the

morphology at the nano- and mesoscale plays a key role. Both influences have been studied precisely in this work.

To address these issues, further studies were conducted on the low band-gap polymer Si-PCPDTBT blended with different fullerene adducts to fine-tune the driving force as presented in chapter 9. Notably, exchanging the fullerene adducts (and with that the acceptor LUMO level) had an only minor influence on the domain purity, domain size and molecular orientation. That enabled us to address solely the influence of the blend energetics on the charge carrier dynamics. In these blends, the efficiency and field dependence of free charge generation was, again, not dependent of excitation energy, independent of whether the blends exhibit a small or a large driving force. However, significant differences in the yield and field dependence of charge generation were measured when using specific fullerenes. Thereby, a direct correlation between the efficiency of free carrier generation and the energy of the relaxed CT state relative to the E_{CS} could be established.

The second set of experiments addressed the correlation between the efficiency of charge generation and the nano-scale phase separation. In a first step, the degree of phase separation in PCPDTBT:PCBM blends was tuned by the use of processing additives e.g. DIO as presented in chapter 6. Interestingly, we found that the generation of charge carriers is field dependent in this system, with enhanced and less field-dependent generation when larger and more pure polymer domains are present. In compliance with concepts currently discussed in the literature, we propose that the formation of pure donor and acceptor domains, separated by intermixed regions, stabilizes the charge separated state and supplies a sufficiently large “morphology-related” force to overcome the mutual Coulomb attraction of geminate charge pairs formed in the intermixed region. This conclusion was further confirmed in chapter 7 by extending the studies to blends with a new polymer, F-PCPDTBT, which was designed by the incorporation of a fluorinated BT unit in PCPDTBT. Fluorination is shown to further increase polymer crystallinity, domain purity, and domain size. Also, fluorination lowers the donor HOMO energy while keeping E_{S1} constant, thereby decreasing the difference between E_{S1} and E_{CS}. Despite this intentional lowering of the driving force, the efficiency of charge generation was clearly enhanced. This finding is important, as it supports the view that charge generation is largely related to morphology rather than to the energetics of the individual isolated components.

In addition, the measurements on additive-processed and fluorinated PCPDTBT-based blends conclusively highlighted that the non-geminate recombination coefficient is markedly reduced in morphologies with larger and purer domains. This is most probably due to the stabilization of free charges in more pure domains, creating a barrier to hop close to or across the donor acceptor interface. Interestingly, the suppression of non-geminate (and geminate) recombination did not always lead to improved solar cell performance, as shown in chapter 8 for the di-fluorinated PCPDTBT system. This finding pointed to the importance of charge extraction. In the past, various methods have been applied to measure the mobility of charges in donor acceptor blends, but most of these techniques are only applicable for a certain thickness range, carrier density, or device design. In chapter 8 we present a new methodology to determine the effective extraction mobility under typical solar cell operation

conditions. This method relies on the precise measurement of the steady state charge carrier densities under different electrical field and illumination conditions. These results give a conclusive picture about the processes leading to the distinct changes in the FF upon fluorination of PCPDTBT. Severe extraction problems were also identified in chapter 5, where inverted solar cells based on PCPDTBT:PCBM and especially thicker active layers yielded lower short circuit currents than regular thin cells, despite improved light absorption and charge generation. Thicker active layers well above 100 nm are highly valuable for the commercial production of organic solar cells and thus quantification of charge extraction in working solar cells becomes more and more relevant, especially with the development of higher efficiency low band-gap materials that generate more charges.

The findings presented in this work have a large implication for the future material design enabling efficient organic solar cells. As charge generation proceeds via relaxed charge transfer states, optimization of the energetic offset between CT and E_{CS} becomes highly important. Therefore, not only the energy difference between the donor HOMO level and the acceptor LUMO level need to be fine-tuned but also control must be gained over the domain purity and domain size in order to stabilize the spatially-separated charges within the individual domains, with a minimum of energetic loss associated with the charge generation process. This morphological scenario should also strongly suppress non-geminate recombination. With the efficiency of generation being optimized, the remaining issue is charge extraction. Work presented in this thesis but also ongoing work suggests the performance of blends with very efficient charge generation to be limited by a too low hole mobility. To enhance extraction, future materials require semi-crystallinity, good stacking, and fibril formation to favor transport through thicker active layers, above 300 nm thickness. All these material properties may open the way to develop organic bulk heterojunction devices that enable much higher efficiencies in the near future than the maximum attainable efficiency of 12% at the moment.

11 Bibliography

(1) http://en.wikipedia.org/wiki/List_of_countries_by_carbon_dioxide_emissions**, accessed Jan. 29. 2014**.
(2) NatCatService Munich Re, Germany 1970-2011**, version Jul. 2012**.
(3) https://www.destatis.de/DE/ZahlenFakten/Wirtschaftsbereiche/Energie/Energie.html**, accessed Apr. 22. 2014**.
(4) http://www.eia.gov/forecasts/ieo/world.cfm**, accessed Jan. 29. 2014**.
(5) http://en.wikipedia.org/wiki/Solar_energy**, accessed Jan. 15. 2014**.
(6) O. Morton *Nature* **2006**, *443*, 19.
(7) http://gcep.stanford.edu/research/exergycharts.html**, accessed Jan. 15. 2014**.
(8) E. W. McFarland *Energy & Environmental Science* **2014**, *7*, 846.
(9) http://www.nrel.gov/ncpv/images/efficiency_chart.jpg**, version 08-11-2014**.
(10) M. A. Green; K. Emery; Y. Hishikawa; W. Warta; E. D. Dunlop *Progress in Photovoltaics: Research and Applications* **2014**, *22*, 701.
(11) Fraunhofer Insitute ISE, Photovoltaics Report**, November 7, 2013**.
(12) C.-C. Chen; W.-H. Chang; K. Yoshimura; K. Ohya; J. You et al. *Advanced Materials* **2014**, DOI: 10.1002/adma.201402072.
(13) www.m-kagaku.co.jp/english/r_td/strategy/technology/topics/opv/**, accessed Jan. 29. 2014**.
(14) C. W. Tang *Applied Physics Letters* **1986**, *48*, 183.
(15) M. Hiramoto; H. Fujiwara; M. Yokoyama *Applied Physics Letters* **1991**, *58*, 1062.
(16) N. S. Sariciftci; L. Smilowitz; A. J. Heeger; F. Wudl *Science* **1992**, *258*, 1474.
(17) G. Yu; K. Pakbaz; A. J. Heeger *Applied Physics Letters* **1994**, *64*, 3422.
(18) J. C. Hummelen; B. W. Knight; F. Lepeq; F. Wudl; J. Yao et al. *Journal of Organic Chemistry* **1995**, *60*, 532.
(19) G. Yu; J. Gao; J. C. Hummelen; F. Wudl; A. J. Heeger *Science* **1995**, *270*, 1789.
(20) C. J. Brabec; S. Gowrisanker; J. J. M. Halls; D. Laird; S. Jia et al. *Advanced Materials* **2010**, *22*, 3839.
(21) S. E. Shaheen; C. J. Brabec; N. S. Sariciftci; F. Padinger; T. Fromherz et al. *Applied Physics Letters* **2001**, *78*, 841.
(22) P. Schilinsky; C. Waldauf; C. J. Brabec *Applied Physics Letters* **2002**, *81*, 3885.
(23) M. M. Wienk; J. M. Kroon; W. J. H. Verhees; J. Knol; J. C. Hummelen et al. *Angewandte Chemie International Edition* **2003**, *42*, 3371.
(24) G. Li; V. Shrotriya; J. Huang; Y. Yao; T. Moriarty et al. *Nature Materials* **2005**, *4*, 864.
(25) F. Zhang; K. G. Jespersen; C. Björström; M. Svensson; M. R. Andersson et al. *Advanced Functional Materials* **2006**, *16*, 667.
(26) N. Blouin; A. Michaud; M. Leclerc *Advanced Materials* **2007**, *19*, 2295.
(27) Z. Zhu; D. Waller; R. Gaudiana; M. Morana; D. Muhlbacher et al. *Macromolecules* **2007**, *40*, 1981.
(28) J. Hou; H.-Y. Chen; S. Zhang; G. Li; Y. Yang *Journal of the American Chemical Society* **2008**, *130*, 16144.
(29) S. H. Park; A. Roy; S. Beaupre; S. Cho; N. Coates et al. *Nature Photonics* **2009**, *3*, 297.
(30) M. C. Scharber; M. Koppe; J. Gao; F. Cordella; M. A. Loi et al. *Advanced Materials* **2010**, *22*, 367.
(31) M. C. Scharber; D. Wuhlbacher; M. Koppe; P. Denk; C. Waldauf et al. *Advanced Materials* **2006**, *18*, 789.
(32) J. Peet; J. Y. Kim; N. E. Coates; W. L. Ma; D. Moses et al. *Nature Materials* **2007**, *6*, 497.
(33) Y. Liang; Y. Wu; D. Feng; S.-T. Tsai; H.-J. Son et al. *Journal of the American Chemical Society* **2008**, *131*, 56.
(34) H.-Y. Chen; J. Hou; S. Zhang; Y. Liang; G. Yang et al. *Nature Photonics* **2009**, *3*, 649.
(35) Y. Y. Liang; Z. Xu; J. B. Xia; S. T. Tsai; Y. Wu et al. *Advanced Materials* **2010**, *22*, E135.
(36) Z. He; C. Zhong; S. Su; M. Xu; H. Wu et al. *Nature Photonics* **2012**, *6*, 591.
(37) G. Zhao; Y. He; Y. Li *Advanced Materials* **2010**, *22*, 4355.
(38) X. Guo; C. Cui; M. Zhang; L. Huo; Y. Huang et al. *Energy & Environmental Science* **2012**, *5*, 7943.
(39) M. A. Faist; S. Shoaee; S. Tuladhar; G. F. A. Dibb; S. Foster et al. *Advanced Energy Materials* **2013**, *3*, 744.
(40) J. Gilot; M. M. Wienk; R. A. J. Janssen *Applied Physics Letters* **2007**, *90*, 143512.
(41) J. Y. Kim; K. Lee; N. E. Coates; D. Moses; T. Q. Nguyen et al. *Science* **2007**, *317*, 222.
(42) J. Yang; R. Zhu; Z. Hong; Y. He; A. Kumar et al. *Advanced Materials* **2011**, *23*, 3465.
(43) J. You; L. Dou; K. Yoshimura; T. Kato; K. Ohya et al. *Nature Communications* **2013**, *4*, 1446.
(44) F. C. Krebs; N. Espinosa; M. Hösel; R. R. Søndergaard; M. Jørgensen *Advanced Materials* **2014**, *26*, 29.
(45) J. Peet; L. Wen; P. Byrne; S. Rodman; K. Forberich et al. *Applied Physics Letters* **2011**, *98*, 043301.
(46) J. A. Bartelt; Z. M. Beiley; E. T. Hoke; W. R. Mateker; J. D. Douglas et al. *Advanced Energy Materials* **2013**, *3*, 364.
(47) W. Li; A. Furlan; K. H. Hendriks; M. M. Wienk; R. A. J. Janssen *Journal of the American Chemical Society* **2013**, *135*, 5529.

(48) J. K. Lee; W. L. Ma; C. J. Brabec; J. Yuen; J. S. Moon et al. *Journal of the American Chemical Society* **2008**, *130*, 3619.
(49) M. Lenes; M. Morana; C. J. Brabec; P. W. M. Blom *Advanced Functional Materials* **2009**, *19*, 1106.
(50) D. J. D. Moet; M. Lenes; M. Morana; H. Azimi; C. J. Brabec et al. *Applied Physics Letters* **2010**, *96*.
(51) D. Jarzab; F. Cordella; J. Gao; M. Scharber; H.-J. Egelhaaf et al. *Advanced Energy Materials* **2011**, *1*, 604.
(52) F. C. Jamieson; T. Agostinelli; H. Azimi; J. Nelson; J. R. Durrant *Journal of Physical Chemistry Letters* **2010**, *1*, 3306.
(53) D. D. Nuzzo; A. Aguirre; M. Shahid; V. S. Gevaerts; S. C. J. Meskers et al. *Advanced Materials* **2010**, *22*, 4321.
(54) M. C. Scharber; C. Lungenschmied; H.-J. Egelhaaf; G. Matt; M. Bednorz et al. *Energy & Environmental Science* **2011**, *4*, 5077.
(55) D. Mühlbacher; M. Scharber; M. Morana; Z. Zhu; D. Waller et al. *Advanced Materials* **2006**, *18*, 2884.
(56) T. Agostinelli; T. A. M. Ferenczi; E. Pires; S. Foster; A. Maurano et al. *Journal of Polymer Science Part B: Polymer Physics* **2011**, *49*, 717.
(57) S. Cho; J. K. Lee; J. S. Moon; J. Yuen; K. Lee et al. *Organic Electronics* **2008**, *9*, 1107.
(58) S. C. Price; A. C. Stuart; L. Yang; H. Zhou; W. You *Journal of the American Chemical Society* **2011**, *133*, 4625.
(59) A. C. Stuart; J. R. Tumbleston; H. Zhou; W. Li; S. Liu et al. *Journal of the American Chemical Society* **2013**, *135*, 1806.
(60) B. C. Schroeder; Z. Huang; R. S. Ashraf; J. Smith; P. D'Angelo et al. *Advanced Functional Materials* **2012**, *22*, 1663.
(61) T. M. Clarke; A. M. Ballantyne; J. Nelson; D. D. C. Bradley; J. R. Durrant *Advanced Functional Materials* **2008**, *18*, 4029.
(62) H. Ohkita; S. Cook; Y. Astuti; W. Duffy; S. Tierney et al. *Journal of the American Chemical Society* **2008**, *130*, 3030.
(63) G. Grancini; M. Maiuri; D. Fazzi; A. Petrozza; H. J. Egelhaaf et al. *Nature Materials* **2013**, *12*, 29.
(64) S. D. Dimitrov; A. A. Bakulin; C. B. Nielsen; B. C. Schroeder; J. Du et al. *Journal of the American Chemical Society* **2012**, *134*, 18189.
(65) M. Scharber *Nature Materials* **2013**, *12*, 594.
(66) A. Armin; Y. Zhang; P. L. Burn; P. Meredith; A. Pivrikas *Nature Materials* **2013**, *12*, 593.
(67) A. E. Jailaubekov; A. P. Willard; J. R. Tritsch; W.-L. Chan; N. Sai et al. *Nature Materials* **2013**, *12*, 66.
(68) A. A. Bakulin; A. Rao; V. G. Pavelyev; P. H. M. van Loosdrecht; M. S. Pshenichnikov et al. *Science* **2012**, *335*, 1340.
(69) J. Lee; K. Vandewal; S. R. Yost; M. E. Bahlke; L. Goris et al. *Journal of the American Chemical Society* **2010**, *132*, 11878.
(70) T. G. J. van der Hofstad; D. Di Nuzzo; M. van den Berg; R. A. J. Janssen; S. C. J. Meskers *Advanced Energy Materials* **2012**, *2*, 1095.
(71) M. Graetzel; R. A. J. Janssen; D. B. Mitzi; E. H. Sargent *Nature* **2012**, *488*, 304.
(72) W. Shockley; H. J. Queisser *Journal of Applied Physics* **1961**, *32*, 510.
(73) M. C. Scharber; N. S. Sariciftci *Progress in Polymer Science* **2013**, *38*, 1929.
(74) U. Rau *Physical Review B* **2007**, *76*, 085303.
(75) M. D. Archer; J. R. Bolton *The Journal of Physical Chemistry* **1990**, *94*, 8028.
(76) A. D. Vos *Journal of Physics D: Applied Physics* **1980**, *13*, 839.
(77) M. Gruber; J. Wagner; K. Klein; U. Hörmann; A. Opitz et al. *Advanced Energy Materials* **2012**, *2*, 1100.
(78) T. Kirchartz; K. Taretto; U. Rau *The Journal of Physical Chemistry C* **2009**, *113*, 17958.
(79) G. Dennler; M. C. Scharber; T. Ameri; P. Denk; K. Forberich et al. *Advanced Materials* **2008**, *20*, 579.
(80) N. Li; D. Baran; G. D. Spyropoulos; H. Zhang; S. Berny et al. *Advanced Energy Materials* **2014**, DOI: 10.1002/aenm.201400084.
(81) L. J. A. Koster; S. E. Shaheen; J. C. Hummelen *Advanced Energy Materials* **2012**, *2*, 1246.
(82) M. Lenes; F. B. Kooistra; J. C. Hummelen; I. Van Severen; L. Lutsen et al. *Journal of Applied Physics* **2008**, *104*, 114517
(83) B. Bernardo; D. Cheyns; B. Verreet; R. D. Schaller; B. P. Rand et al. *Nature Communications* **2014**, *5*, 3245.
(84) N. Cho; C. W. Schlenker; K. M. Knesting; P. Koelsch; H.-L. Yip et al. *Advanced Energy Materials* **2014**, DOI:10.1002/aenm.201301857.
(85) S. Albrecht; S. Schäfer; I. Lange; S. Yilmaz; I. Dumsch et al. *Organic Electronics* **2012**, *13*, 615.
(86) J. Müller; B. Rech; J. Springer; M. Vanecek *Solar Energy* **2004**, *77*, 917.
(87) K. S. Chen; H. L. Yip; J. F. Salinas; Y. X. Xu; C. C. Chueh et al. *Advanced Materials* **2014**, *26*, 3349.
(88) J.-D. Chen; L. Zhou; Q.-D. Ou; Y.-Q. Li; S. Shen et al. *Advanced Energy Materials* **2014**, DOI: 10.1002/aenm.201301777.
(89) X. Li; W. C. H. Choy; L. Huo; F. Xie; W. E. I. Sha et al. *Advanced Materials* **2012**, *24*, 3046.
(90) K. Yao; M. Salvador; C.-C. Chueh; X.-K. Xin; Y.-X. Xu et al. *Advanced Energy Materials* **2014**, DOI: 10.1002/aenm.201400206.
(91) Z. C. He; C. M. Zhong; S. J. Su; M. Xu; H. B. Wu et al. *Nature Photonics* **2012**, *6*, 591.
(92) J. Roncali *Macromolecular Rapid Communications* **2007**, *28*, 1761.
(93) J. Roncali *Chemical Reviews* **1997**, *97*, 173.
(94) Y. J. Cheng; S. H. Yang; C. S. Hsu *Chemical Reviews* **2009**, *109*, 5868.
(95) R. Mauer; M. Kastler; F. Laquai *Advanced Functional Materials* **2010**, *20*, 2085.

(96) H. A. M. van Mullekom; J. A. J. M. Vekemans; E. E. Havinga; E. W. Meijer *Materials Science and Engineering: R: Reports* **2001**, *32*, 1.
(97) E. E. Havinga; W. Tenhoeve; H. Wynberg *Polymer Bulletin* **1992**, *29*, 119.
(98) X. Guo; N. Zhou; S. J. Lou; J. Smith; D. B. Tice et al. *Nature Photonics* **2013**, *7*, 825.
(99) L. Dou; C.-C. Chen; K. Yoshimura; K. Ohya; W.-H. Chang et al. *Macromolecules* **2013**, *46*, 3384.
(100) G. L. Gibson; T. M. McCormick; D. S. Seferos *Journal of the American Chemical Society* **2011**, *134*, 539.
(101) H. Zhou; L. Yang; S. Xiao; S. Liu; W. You *Macromolecules* **2009**, *43*, 811.
(102) N. Blouin; A. Michaud; D. Gendron; S. Wakim; E. Blair et al. *Journal of the American Chemical Society* **2008**, *130*, 732.
(103) A. P. Kulkarni; Y. Zhu; A. Babel; P.-T. Wu; S. A. Jenekhe *Chemistry of Materials* **2008**, *20*, 4212.
(104) N.-K. Persson; M. Sun; P. Kjellberg; T. Pullerits; O. Inganäs *The Journal of Chemical Physics* **2005**, *123*, 204718.
(105) T. Xu; L. Yu *Materials Today* **2014**, *17*, 11.
(106) S.-H. Liao; H.-J. Jhuo; Y.-S. Cheng; S.-A. Chen *Advanced Materials* **2013**, *25*, 4766.
(107) C.-Z. Li; C.-Y. Chang; Y. Zang; H.-X. Ju; C.-C. Chueh et al. *Advanced Materials* **2014**, DOI: 10.1002/adma.201402276.
(108) C. Cui; W.-Y. Wong; Y. Li *Energy & Environmental Science* **2014**, *7*, 2276.
(109) J.-L. Bredas *Materials Horizons* **2014**, *1*, 17.
(110) T. Clarke; A. Ballantyne; F. Jamieson; C. Brabec; J. Nelson et al. *Chemical Communications* **2009**, *0*, 89.
(111) H. Bässler *Physica Status Solidi B-Basic Research* **1993**, *175*, 15.
(112) L. G. Kaake; J. J. Jasieniak; R. C. Bakus; G. C. Welch; D. Moses et al. *Journal of the American Chemical Society* **2012**, *134*, 19828.
(113) F. Etzold; I. A. Howard; N. Forler; D. M. Cho; M. Meister et al. *Journal of the American Chemical Society* **2012**, *134*, 10569.
(114) A. A. Paraecattil; N. Banerji *Journal of the American Chemical Society* **2014**, *136*, 1472.
(115) H. Tamura; I. Burghardt *Journal of the American Chemical Society* **2013**, *135*, 16364.
(116) C. L. Braun *The Journal of Chemical Physics* **1984**, *80*, 4157.
(117) S. Shoaee; S. Subramaniyan; H. Xin; C. Keiderling; P. S. Tuladhar et al. *Advanced Functional Materials* **2013**, *23*, 3286.
(118) D. P. McMahon; D. L. Cheung; A. Troisi *The Journal of Physical Chemistry Letters* **2011**, *2*, 2737.
(119) W. Ma; J. R. Tumbleston; M. Wang; E. Gann; F. Huang et al. *Advanced Energy Materials* **2013**, *3*, 864.
(120) G. J. Hedley; A. J. Ward; A. Alekseev; C. T. Howells; E. R. Martins et al. *Nature Communications* **2013**, *4*, 2867.
(121) S. Gélinas; A. Rao; A. Kumar; S. L. Smith; A. W. Chin et al. *Science* **2014**, *343*, 512.
(122) B. Carsten; J. M. Szarko; H. J. Son; W. Wang; L. Lu et al. *Journal of the American Chemical Society* **2011**, *133*, 20468.
(123) B. Carsten; J. M. Szarko; L. Lu; H. J. Son; F. He et al. *Macromolecules* **2012**, *45*, 6390.
(124) T. M. Burke; M. D. McGehee *Advanced Materials* **2014**, *26*, 1923.
(125) S. R. Yost; T. Van Voorhis *The Journal of Physical Chemistry C* **2013**, *117*, 5617.
(126) A. Pivrikas; G. Juska; A. J. Mozer; M. Scharber; K. Arlauskas et al. *Physical Review Letters* **2005**, *94*, 176806.
(127) G. Lakhwani; A. Rao; R. H. Friend *Annual Review of Physical Chemistry* **2014**, *65*, 557.
(128) J. Nelson *Physical Review B* **2003**, *67*, 155209.
(129) G. J. Adriaenssens; V. I. Arkhipov *Solid State Communications* **1997**, *103*, 541.
(130) W. Shockley; W. T. Read *Physical Review* **1952**, *87*, 835.
(131) D. Credgington; J. R. Durrant *The Journal of Physical Chemistry Letters* **2012**, *3*, 1465.
(132) A. Maurano; R. Hamilton; C. G. Shuttle; A. M. Ballantyne; J. Nelson et al. *Advanced Materials* **2010**, *22*, 4987.
(133) T. Kirchartz; J. Nelson *Physical Review B* **2012**, *86*, 165201.
(134) J. C. Blakesley; D. Neher *Physical Review B* **2011**, *84*, 075210.
(135) D. Rauh; C. Deibel; V. Dyakonov *Advanced Functional Materials* **2012**, *22*, 3371.
(136) C. M. Proctor; M. Kuik; T.-Q. Nguyen *Progress in Polymer Science* **2013**, *38*, 1941.
(137) P. Würfel *Physics of Solar Cells: From Principles to New Concepts*, WILEY-VCH Verlag, **2008**.
(138) L. J. A. Koster; V. D. Mihailetchi; R. Ramaker; P. W. M. Blom *Applied Physics Letters* **2005**, *86*, 123509.
(139) K. Vandewal; J. Widmer; T. Heumueller; C. J. Brabec; M. D. McGehee et al. *Advanced Materials* **2014**, *26*, 3839.
(140) G. Garcia-Belmonte; J. Bisquert *Applied Physics Letters* **2010**, *96*, 113301.
(141) R. A. Street; D. Davies; P. P. Khlyabich; B. Burkhart; B. C. Thompson *Journal of the American Chemical Society* **2013**, *135*, 986.
(142) L. Yang; H. Zhou; S. C. Price; W. You *Journal of the American Chemical Society* **2012**, *134*, 5432.
(143) S. Albrecht; S. Janietz; W. Schindler; J. Frisch; J. Kurpiers et al. *Journal of the American Chemical Society* **2012**, *134*, 14932.
(144) Y. Zhang; J. Zou; C.-C. Cheuh; H.-L. Yip; A. K. Y. Jen *Macromolecules* **2012**, *45*, 5427.
(145) Y. Li; J. Zou; H.-L. Yip; C.-Z. Li; Y. Zhang et al. *Macromolecules* **2013**, *46*, 5497.
(146) C. Piliego; T. W. Holcombe; J. D. Douglas; C. H. Woo; P. M. Beaujuge et al. *Journal of the American Chemical Society* **2010**, *132*, 7595.

(147) M. Gohlke *Bestimmung optischer Konstanten dünner organischer Schichten und deren Anwendung in organischen Solarzellen*, Research Internship, University of Potsdam, **2012**.
(148) A. B. Djurišić; T. Fritz; K. Leo *Optics Communications* **1999**, *166*, 35.
(149) G. F. Burkhard; E. T. Hoke; M. D. McGehee *Advanced Materials* **2010**, *22*, 3293.
(150) C. M. Ramsdale; N. C. Greenham *Journal of Physics D-Applied Physics* **2003**, *36*, L29.
(151) V. Shrotriya; G. Li; Y. Yao; T. Moriarty; K. Emery et al. *Advanced Functional Materials* **2006**, *16*, 2016.
(152) J. Gilot; M. M. Wienk; R. A. J. Janssen *Advanced Functional Materials* **2010**, *20*, 3904.
(153) L. A. A. Pettersson; L. S. Roman; O. Inganas *Journal of Applied Physics* **1999**, *86*, 487.
(154) D. W. Sievers; V. Shrotriya; Y. Yang *Journal of Applied Physics* **2006**, *100*, 7.
(155) J. Mort; I. Chen; A. Troup; M. Morgan; J. Knights et al. *Physical Review Letters* **1980**, *45*, 1348.
(156) Z. D. Popovic *Chemical Physics Letters* **1983**, *100*, 227.
(157) D. Hertel; E. V. Soh; H. Bässler; L. J. Rothberg *Chemical Physics Letters* **2002**, *361*, 99.
(158) T. Offermans; S. C. J. Meskers; R. A. J. Janssen *Journal of Applied Physics* **2006**, *100*, 074509.
(159) J. Kniepert; M. Schubert; J. C. Blakesley; D. Neher *Journal of Physical Chemistry Letters* **2011**, *2*, 700.
(160) J. Kurpiers *Untersuchung der Ladungsträgergeneration und Rekombinationsdynamik in Polymer/Fulleren Solarzellen*, Diploma Thesis, University of Potsdam, **2013**.
(161) I. Lange; J. Kniepert; P. Pingel; I. Dumsch; S. Allard et al. *The Journal of Physical Chemistry Letters* **2013**, *4*, 3865.
(162) G. Juška; K. Arlauskas; M. Viliūnas; J. Kočka *Physical Review Letters* **2000**, *84*, 4946.
(163) G. Juška; K. Arlauskas; M. Viliūnas; K. Genevičius; R. Österbacka et al. *Physical Review B* **2000**, *62*, R16235.
(164) S. Bange; M. Schubert; D. Neher *Physical Review B* **2010**, *81*, 035209.
(165) T. Kim; J. H. Jeon; S. Han; D.-K. Lee; H. Kim et al. *Applied Physics Letters* **2011**, *98*, 183503.
(166) T. Kim; Y.-S. Kim; J. Y. Choi; J. H. Jeon; W. W. Park et al. *Synthetic Metals* **2013**, *175*, 103.
(167) T. Kim; J. Y. Choi; J. H. Jeon; Y.-S. Kim; B.-S. Kim et al. *Materials Research Bulletin* **2012**, *47*, 3040.
(168) J. H. Seo; D.-H. Kim; S.-H. Kwon; M. Song; M.-S. Choi et al. *Advanced Materials* **2012**, *24*, 4523.
(169) B. Rech; O. Kluth; T. Repmann; T. Roschek; J. Springer et al. *Solar Energy Materials and Solar Cells* **2002**, *74*, 439.
(170) B. Rech; H. Wagner *Applied Physics A* **1999**, *69*, 155.
(171) J. Wallinga; W. M. Arnoldbik; A. M. Vredenberg; R. E. I. Schropp; W. F. van der Weg *The Journal of Physical Chemistry B* **1998**, *102*, 6219.
(172) Y. Yuan; J. Huang; G. Li *Green* **2011**, *1*, 65.
(173) W. Li; W. S. Roelofs; M. M. Wienk; R. A. Janssen *Journal of the American Chemical Society* **2012**, *134*, 13787.
(174) J. You; C.-C. Chen; Z. Hong; K. Yoshimura; K. Ohya et al. *Advanced Materials* **2013**, *25*, 3973.
(175) K. Ding; T. Kirchartz; B. E. Pieters; C. Ulbrich; A. M. Ermes et al. *Solar Energy Materials and Solar Cells* **2011**, *95*, 3318.
(176) S. Schicho; D. Hrunski; R. van Aubel; A. Gordijn *Progress in Photovoltaics: Research and Applications* **2010**, *18*, 83.
(177) A. Hadipour; D. Cheyns; P. Heremans; B. P. Rand *Advanced Energy Materials* **2011**, *1*, 930.
(178) S. Woo; W. Hyun Kim; H. Kim; Y. Yi; H.-K. Lyu et al. *Advanced Energy Materials* **2014**, *4*, 1301692.
(179) A. K. K. Kyaw; D. H. Wang; V. Gupta; J. Zhang; S. Chand et al. *Advanced Materials* **2013**, *25*, 2397.
(180) H. Kang; S. Hong; J. Lee; K. Lee *Advanced Materials* **2012**, *24*, 3005.
(181) G. F. Burkhard; E. T. Hoke; S. R. Scully; M. D. McGehee *Nano Letters* **2009**, *9*, 4037.
(182) Y. Sun; C. J. Takacs; S. R. Cowan; J. H. Seo; X. Gong et al. *Advanced Materials* **2011**, *23*, 2226.
(183) T.-Y. Chu; S. Alem; P. G. Verly; S. Wakim; J. Lu et al. *Applied Physics Letters* **2009**, *95*, 063304.
(184) J. T. Rogers; K. Schmidt; M. F. Toney; G. C. Bazan; E. J. Kramer *Journal of the American Chemical Society* **2012**, *134*, 2884.
(185) R. Steyrleuthner; S. Bange; D. Neher *Journal of Applied Physics* **2009**, *105*, 064509.
(186) J. D. Kotlarski; P. W. M. Blom *Applied Physics Letters* **2012**, *100*, 013306.
(187) M. Pfannmoeller; H. Fluegge; G. Benner; I. Wacker; C. Sommer et al. *Nano Letters* **2011**, *11*, 3099.
(188) W. Schindler; M. Wollgarten; K. Fostiropoulos *Organic Electronics* **2012**, *13*, 1100.
(189) S. Albrecht; W. Schindler; J. Kurpiers; J. Kniepert; J. C. Blakesley et al. *The Journal of Physical Chemistry Letters* **2012**, *3*, 640.
(190) Z. Li; C. R. McNeill *Journal of Applied Physics* **2011**, *109*, 074513.
(191) S. Yamamoto; H. Ohkita; H. Benten; S. Ito *The Journal of Physical Chemistry C* **2012**, *116*, 14804.
(192) L. J. A. Koster *Physical Review B* **2010**, *81*, 205318.
(193) S. Chen; K. R. Choudhury; J. Subbiah; C. M. Amb; J. R. Reynolds et al. *Advanced Energy Materials* **2011**, *1*, 963.
(194) Y. Zhang; S.-C. Chien; K.-S. Chen; H.-L. Yip; Y. Sun et al. *Chemical Communications* **2011**, *47*, 11026.
(195) R. C. Coffin; J. Peet; J. Rogers; G. C. Bazan *Nature Chemistry* **2009**, *1*, 657.
(196) H. Zhou; L. Yang; A. C. Stuart; S. C. Price; S. Liu et al. *Angewandte Chemie International Edition* **2011**, *50*, 2995.
(197) J. Peet; N. S. Cho; S. K. Lee; G. C. Bazan *Macromolecules* **2008**, *41*, 8655.
(198) J. T. Rogers; K. Schmidt; M. F. Toney; E. J. Kramer; G. C. Bazan *Advanced Materials* **2011**, *23*, 2284.
(199) H. J. Son; W. Wang; T. Xu; Y. Liang; Y. Wu et al. *Journal of the American Chemical Society* **2011**, *133*, 1885.
(200) Q. Peng; X. Liu; D. Su; G. Fu; J. Xu et al. *Advanced Materials* **2011**, *23*, 4554.

(201) K. H. Hendriks; W. Li; M. M. Wienk; R. A. J. Janssen *Journal of the American Chemical Society* **2014**, *136*, 12130.
(202) A. Baumann; J. Lorrmann; D. Rauh; C. Deibel; V. Dyakonov *Advanced Materials* **2012**, *24*, 4381.
(203) C. Tanase; E. J. Meijer; P. W. Blom; D. M. De Leeuw *Physical Review Letters* **2003**, *91*, 216601.
(204) S. A. Mauger; L. Chang; S. Friedrich; C. W. Rochester; D. M. Huang et al. *Advanced Functional Materials* **2013**, *23*, 1935.
(205) S. van Bavel; E. Sourty; G. de With; K. Frolic; J. Loos *Macromolecules* **2009**, *42*, 7396.
(206) G. F. A. Dibb; T. Kirchartz; D. Credgington; J. R. Durrant; J. Nelson *Journal of Physical Chemistry Letters* **2011**, *2*, 2407.
(207) C. G. Shuttle; A. Maurano; R. Hamilton; B. O'Regan; J. C. de Mello et al. *Applied Physics Letters* **2008**, *93*, 183501.
(208) C. G. Shuttle; R. Hamilton; J. Nelson; B. C. O'Regan; J. R. Durrant *Advanced Functional Materials* **2010**, *20*, 698.
(209) J. Kniepert; I. Lange; N. J. van der Kaap; L. J. A. Koster; D. Neher *Advanced Energy Materials* **2014**, DOI: 10.1002/aenm.201301401.
(210) W. Gong; M. A. Faist; N. J. Ekins-Daukes; Z. Xu; D. D. C. Bradley et al. *Physical Review B* **2012**, *86*, 024201.
(211) W. Tress; K. Leo; M. Riede *Advanced Functional Materials* **2011**, *21*, 2140.
(212) B. A. Collins; Z. Li; J. R. Tumbleston; E. Gann; C. R. McNeill et al. *Advanced Energy Materials* **2013**, *3*, 65.
(213) W. Li; S. Albrecht; L. Yang; S. Roland; J. R. Tumbleston et al. *Journal of the American Chemical Society* **2014**, under consideration.
(214) M. Mingebach; S. Walter; V. Dyakonov; C. Deibel *Applied Physics Letters* **2012**, *100*, 193302.
(215) M. A. Faist; T. Kirchartz; W. Gong; R. S. Ashraf; I. McCulloch et al. *Journal of the American Chemical Society* **2012**, *134*, 685.
(216) Z.-L. Guan; J. B. Kim; H. Wang; C. Jaye; D. A. Fischer et al. *Organic Electronics* **2010**, *11*, 1779.
(217) B. A. Collins; J. E. Cochran; H. Yan; E. Gann; C. Hub et al. *Nature Materials* **2012**, *11*, 536.
(218) Y. S. Huang; S. Westenhoff; I. Avilov; P. Sreearunothai; J. M. Hodgkiss et al. *Nature Materials* **2008**, *7*, 483.

12 Appendix

12.1 Overview of Co-Authors Contributions to Summarized Publications

Chapter 4 is based on S. Albrecht, B. Grootoonk, S. Neubert, S. Roland, J. Wördenweber, M. Matthias, R. Schlatmann, A. Gordijn, D. Neher, *Efficient Hybrid Inorganic/Organic Tandem Solar Cells with Tailored Recombination Contacts*, Solar Energy Materials and Solar Cells 2014, 127, 157. The following contributions were made: DN and SA had the basic idea of this work. BG fabricated all inorganic layers including the a-Si:H reference measurements. SA completed the inorganic layers with the recombination contact and the organic sub-cell and conducted all tandem *JV* characteristics, the EQE measurements and the optical simulations. NS and SR helped with fruitful discussion. JW helped with the device design. DN, RS and AG supervised the project. DN, BG and SA co-edited the manuscript.

Chapter 5 is based on S. Albrecht, S. Schäfer, I. Lange, Y. Seyfullah, I. Dumsch, S. Allard, U. Scherf, A. Hertwig, and D. Neher, *Light management in PCPDTBT:PC_{70}BM solar cells: A comparison of standard and inverted device structures*, Organic Electronics 2012, 13, 615. The following contributions were made: SA and DN had the basic idea of this work. The chemists YS, ID, SAll, and US synthesized and provided the material PCPDTBT. AH performed the ellipsometry measurements. IL performed the Kelvin-probe measurement. SS helped with fruitful discussion and the determination of the optical constants of MoO_3 and PEDOT:PSS. SA fabricated all devices, including synthesis of the TiO_2 sol-gel and device optimization. SA also performed all optical and solar cell measurements together with the optical simulation. DN and SA co-edited the manuscript.

Chapter 6 is based S. Albrecht, W. Schindler, J. Kurpiers, J. Kniepert, J. C. Blakesley, I. Dumsch, S. Allard, K. Fostiropoulos, U. Scherf, and D. Neher, *On the Field Dependence of Free Charge Carrier Generation and Recombination in Blends of PCPDTBT/PC_{70}BM: Influence of Solvent Additives*, The Journal of Physical Chemistry Letters 2012, 3, 640. The following contributions were made: DN and SA had the basic idea of this work. The chemists ID, SAll, and US synthesized and provided the material PCPDTBT. JKu improved the TDCF setup to 10 ns delay time resolution. JKn wrote a code to fit the recombination coefficient. JCB helped with discussion to the field-dependence of the recombination coefficient. WS performed the TEM measurements. SA built all devices (also for TEM) and performed all TDCF, *JV*, EQE, absorption, and Photo-CELIV measurements. DN and KF supervised the project. DN and SA co-edited the manuscript.

Chapter 7 is based on S. Albrecht, S. Janietz, W. Schindler, J. Frisch, J. Kurpiers, J. Kniepert, S. Inal, P. Pingel, K. Fostiropoulos, N. Koch, and D. Neher, *Fluorinated Copolymer PCPDTBT with Enhanced Open-Circuit Voltage and Reduced Recombination for Highly Efficient Polymer Solar Cells*, Journal of the American Chemical Society 2012, 134, 14932. The following contributions were made: SJ and SA had the basic idea of this work. SJ synthesized and provided the material F-PCPDTBT. JKu improved the TDCF setup to 10 ns delay time resolution. JKn wrote a code from which the recombination coefficient can be calculated. SI helped measuring the solution absorption. PP helped measuring the FETs. WS performed the TEM measurements. JF conducted UPS measurements. SA built all devices (also for TEM and UPS) and performed all TDCF, *JV*, EQE, absorption, and Photo-CELIV measurements. DN, NK, and KF supervised the project. DN, SJ and SA co-edited the manuscript.

Chapter 8 is based on S. Albrecht, J. R. Tumbleston, S. Janietz, I. Dumsch, S. Allard, U. Scherf, H. Ade, and D. Neher, *Quantifying Charge Extraction in Organic Solar Cells: The Case of Fluorinated PCPDTBT*, The Journal of Physical Chemistry Letters 2014, 5, 1131. The following contributions were made: DN and SA had the basic idea of this work. SJ synthesized F-PCPDTBT and 2F-PCPDTBT; ID, SAll, and US synthesized PCPDTBT. JRT conducted P-SoXS and GIWAXS measurements. SA built all devices (also for R-SoXS and GIWAXS) and performed all TDCF, *JV*, and BACE measurements. DN, and HA supervised the project. DN, JRT, and SA co-edited the manuscript.

Chapter 9 is based on S. Albrecht, K. Vandewal, J.R. Tumbleston, F.S.U. Fischer, J.D. Douglas, J. M. J. Fréchet, S. Ludwigs, H. Ade, A. Salleo, and D. Neher, *On the Efficiency of Charge Transfer State Splitting in Polymer: Fullerene Solar Cells,* Advanced Materials 2014, 26, 2533. The following contributions were made: DN, KV and SA had the basic idea of this work. The chemist JDD and JMJF synthesized and provided PBDTTPD. FSUF performed the CV measurements. JRT measured P-SoXS and GIWAXS. SA built the P-SoXS, GIWAXS, reflection and transmission, and solar cell devices. SA performed TDCF, *JV*, reflection and transmission, and EQE measurements. KV performed PDS measurements and built the respective devices. DN, AS, SL, and HA supervised the project. DN, KV, JRT and SA co-edited the manuscript.

Chapter 9 also partially includes results from K. Vandewal, S. Albrecht, E.T. Hoke, K.R. Graham, J. Widmer, J.D. Douglas, M. Schubert, W.R. Mateker,J. T. Bloking, G. F. Burkhard, A. Sellinger, J.M.J. Fréchet, A. Amassian, M. K. Riede, M. D. McGehee, D. Neher, A. Salleo, *Efficient charge generation by relaxed charge-transfer states at organic interfaces*, Nature Materials 2014, 13, 63. The following contributions were made: KV, and DN designed the experiments and the theoretical background. SA prepared devices for TDCF experiments and performed TDCF. KV, WRM, ETH, KRG, JTB, MS, JW, and MKR prepared and optimized the solar cells. ETH and JTB adjusted the EQE and EL set-ups for the detection of weak signals. KV, ETH, and KRG measured the EQE and EL spectra. KV measured the PDS spectra. JDD and JMJF synthesized PBDTTPD. ASe, JMJF, AA, MKR, and MDM supervised their team members. DN and ASa supervised the overall project. KV, DN, SA, and ASa co-edited the manuscript.

12.2 List of all Publications

1. F. Kraffert, R. Steyrleuthner, S. Albrecht, D. Neher, M. C. Scharber, R. Bittl, J. Behrends*, Charge separation in PCPDTBT:PCBM from an EPR perspective,* Journal of the American Chemical Society 2014, to be published.

2. F. S. U. Fischer, D.Trefz, J. Back, N. Kayunkid, B.Tornow, S. Albrecht, D.Neher, and S. Ludwigs et al., *Solvent Vapor Annealing: Influence on Opto-Electronic Properties,* Advanced Materials 2014, under consideration.

3. W. Li, S. Albrecht, L. Yang, S. Roland, J. R. Tumbleston, T. McAfee, M. A. Kelly, L. Yan, H. Ade, D. Neher, and W. You, *Mobility-Controlled Performance of Thick Solar Cells based on Fluorinated Copolymers*, Journal of the American Chemical Society 2014, under consideration.

4. S. Albrecht, B. Grootoonk, S. Neubert, Dieter Neher et al., *Efficient Hybrid Inorganic/Organic Tandem Solar Cells with Tailored Recombination Contacts*, Solar Energy Materials and Solar Cells, 2014, 127, 157.

5. S. Albrecht, J. R. Tumbleston, S. Janietz, I. Dumsch, H. Ade, D. Neher et al., *Quantifying Charge Extraction in Organic Solar Cells: The Case of Fluorinated PCPDTBT*, The Journal of Physical Chemistry Letters 2014, 5, 1131.

6. B. Pradhan, S. Albrecht, B. Stiller, D. Neher, *Inverted organic solar cells comprising low-temperature-processed ZnO films*, Applied Physics A 2014, 115, 365.

7. S. Schaefer, S. Albrecht, D. Neher, T. F. Schulze, E. Conrad, L. Korte, B. Rech, J. Wördenweber, A. Gordijn, U. Scherf, and I. Dumsch, *Electric Field Distribution in Hybrid Solar Cells Comprising an Organic Donor Polymer and Amorphous Silicon*, Organic Photonics Photovoltaik, DOI: 10.2478/oph-2014-0004

8. C. M. Proctor, S. Albrecht, D. Neher, T. Q. Nguyen, *Overcoming geminate recombination and enhanced extraction in solution-processed small molecule solar cells*, Advanced Energy Materials 2014, DOI: 10.1002/aenm.201400230.

9. S. Albrecht, K. Vandewal, J. R. Tumbleston, F. Fischer, S. Ludwigs, H. Ade, D. Neher et al., *On the Efficiency of Charge Transfer State Splitting in Polymer: Fullerene Solar Cells*, Advanced Materials 2014, 26, 2533.

10. K. Vandewal, S. Albrecht, D. Neher, A. Salleo et al*., Efficient charge generation by relaxed charge-transfer states at organic interfaces*, Nature Materials 2014, 13, 63.

11. S. Albrecht, S. Janietz, W. Schindler, D. Neher et al., *Fluorinated Copolymer PCPDTBT with Enhanced Open-Circuit Voltage and Reduced Recombination for Highly Efficient Polymer Solar Cells*, Journal of the American Chemical Society 2012, 134, 14932.

12. S. Albrecht, W. Schindler, D. Neher et al., *On the Field Dependence of Free Charge Carrier Generation and Recombination in Blends of PCPDTBT/$PC_{70}BM$: Influence of Solvent Additives*, The Journal of Physical Chemistry Letters 2012, 3, 640.

13. S. Albrecht, S. Schäfer, I. Lange, U. Scherf, D. Neher et al., *Light management in PCPDTBT:$PC_{70}BM$ solar cells: A comparison of standard and inverted device structures*, Organic Electronics 2012, 13, 615.

14. S. Schattauer, B. Reinhold, S. Albrecht, D. Neher et al., *Influence of sintering on the structural and electronic properties of TiO_2 nanoporous layers prepared via a non-sol–gel approach*, Colloid and Polymer Science 2012, 290, 1843.

15. S. Albrecht, S. Yilmaz, I. Dumsch, S. Beaupré, D. Neher et al., *Solution Processed Organic Tandem Solar Cells*, Energy Procedia 2012, 31, 159.

12.3 Attended Conferences

1. Joint Workshop on “Energy Polymers”, 2014, Potsdam, Germany - invited talk entitled: High Performance Organic Solar Cells with Fluorinated Donor Polymers.

2. 2013 MRS Fall Meeting and Exhibit, December 1-6, 2013, Boston, USA - Poster entitled: On the Efficiency of Charge Transfer State Splitting in Polymer:Fullerene Solar Cells.

3. Next Generation Organic Photovoltaics, June 2-5, 2013, Groningen, Netherlands- talk entitled: Efficient Free Charge Carrier Generation via Low Energy Charge Transfer States in Polymer Solar Cells.

4. DPG Sringmeeting, March 10-15 2013, Regensburg, Germany - talk entitled: Efficient Free Charge Carrier Generation via Low Energy Charge Transfer States in Polymer Solar Cells.

5. 2012 MRS Fall Meeting and Exhibit, November 25-30, 2012, Boston, USA - talk entitled: Fluorinated Copolymer PCPDTBT with Enhanced Open-Circuit Voltage and Reduced Recombination.

6. DPG Sringmeeting, March 25-30, 2013, Berlin, Germany - talk entitled: Charge Carrier Dynamics in Blends of PCPDTBT/$PC_{70}BM$: The Influence of Solvent Additives.

7. E-MRS ICAM IUMRS 2011 Spring Meeting, May 10-12, 2011, Nice, France - poster entitled: Solution Processed Organic Tandem Solar Cells.

8. DPG Sringmeeting, March 13-18, 2011, Dresden, Germany - poster entitled: Solution Processed Organic Tandem Solar Cells.

12.4 Acknowledgement

First of all, I would like to thank Dieter Neher for giving me the opportunity to realize my doctoral thesis in the “physics of soft matter” group. Dieter constantly helped with plenty of fruitful discussions, wise guidelines and the confidence in my person. His encouraging, unlimited assistance enabled several important publications being the basis of this thesis.

Also, I want to thank my family especially my girlfriend Franziska Thiel who took care of our small children Elias and Alena almost every afternoon. That significantly helped me to focus on the time consuming experiments as I knew that my kids were well coached.

Furthermore I would like to thank the entire “physics of soft matter” group for continuous help with experimental and other issues. The nice conversation during daily lunchtime and the social activities such as soccer, paddling, sailing and crane inspections will remain unforgettable. Special thanks are given to Jona Kurpiers for the plenty of updates and improvements and maintenance on the TDCF and BACE setup. Also Frank Jaiser and Andreas Pucher helped with laser maintaining and hundreds of electrical engineering questions, respectively. Thanks to my former office colleges Patrick Pingel and Sahika Inal for the interesting time in our room. Furthermore thanks are given to my former project members Sebastian Schäfer and Ilja Lange, and to the current project member Steffen Roland.

Some of the results presented in this thesis are based on fruitful collaborations with other institutes and researchers. The most important was the collaboration with Koen Vandewal from University of Dresden, as very interesting results on charge generation were gained together. Special thanks are furthermore given to Silvia Janietz and Eileen Katholing from Fraunhofer Institute of Applied Polymer Research for the great collaboration with the synthesis of the fluorinated polymers. Another fruitful collaboration was established with Wolfram Schindler from Helmholtz Center Berlin regarding the transmission electron microscopy including help by Markus Wollgarten. Also, I would like to mention the collaboration with Chris Proctor and Thuc-Quyen Nguyen from University of Santa Barbara regarding the charge carrier dynamics in small molecule solar cells and the proof reading of my thesis. Furthermore, the collaboration with Sabine Ludwigs and Florian Fischer from University of Stuttgart with numerous results from spectroelectrochemistry is acknowledged. Finally, Harald Ade and John R. Tumbleston from University of North Carolina helped with very nice morphological results and Wei You from University of North Carolina is acknowledged for the collaboration with fluorinated polymers. Special thanks are given to Jan Wördenweber and Björn Grootoonk from Forschungszentrum Jülich for the constant supply of silicon solar cells. Also Bernd Rech from Helmholtz Center Berlin as well as Sebastian Neubert and Bernd Stannowski from PVcomB assisted with fruitful discussions.

The chemists Sybille Allard, Ines Dumsch, Seyfullah Ilmaz, Anke Helfer and Ullrich Scherf from University of Wuppertal helped with polymer synthesis and characterization. Last but not least, Fabian Etzold and Frédéric Laquai from Max-Planck Institute for Polymer Research helped with fruitful discussions and with GPC analysis.

12.5 Thesis Declaration

I, Steve Albrecht, hereby certify that this thesis has been written by me, that it is the record of work carried out by me, and that I did not use source material or aids other than those mentioned. The work has not been submitted to any other University.

_____ _____

Place/Date Signature

12.6 Summarized Publications

The following section contains the summarized publications ordered according to the appearance in the thesis. The papers are reprinted in original version as published in the journals. The corresponding supporting information can be found on the attached compact disc that is included at the end of the printed thesis.

Solar Energy Materials & Solar Cells 127 (2014) 157–162

Contents lists available at ScienceDirect

Solar Energy Materials & Solar Cells

journal homepage: www.elsevier.com/locate/solmat

Efficient hybrid inorganic/organic tandem solar cells with tailored recombination contacts

Steve Albrecht [a], Bjorn Grootoonk [b], Sebastian Neubert [c], Steffen Roland [a], Jan Wordenweber [b], Matthias Meier [b], Rutger Schlatmann [c], Aad Gordijn [b], Dieter Neher [a,*]

[a] Institut für Physik und Astronomie, Universität Potsdam, Karl-Liebknecht-Str. 24-25, 14476 Potsdam, Germany
[b] Forschungszentrum Jülich GmbH, Institut für Energie- und Klimaforschung (IEK-5), 52425 Jülich, Germany
[c] PVcomB/Helmholtz-Zentrum Berlin für Materialien und Energie GmbH, Schwarzschildstr. 3, 12489 Berlin, Germany

ARTICLE INFO

Article history:
Received 17 February 2014
Accepted 22 April 2014

Keywords:
Hybrid solar cells
Tandem solar cells
Organic solar cells
Bulk heterojunction
Efficiency optimization

ABSTRACT

In this work, the authors present a 7.5% efficient hybrid tandem solar cell with the bottom cell made of amorphous silicon and a Si-PCPDTBT:$PC_{70}BM$ bulk heterojunction top cell. Loss-free recombination contacts were realized by combing Al-doped ZnO with either the conducting polymer composite PEDOT:PSS or with a bilayer of ultrathin Al and MoO_3. Optimization of these contacts results in tandem cells with high fill factors of 70% and an open circuit voltage close to the sum of those of the sub-cells. This is the best efficiency reported for this type of hybrid tandem cell so far. Optical and electrical device modeling suggests that the efficiency can be increased to ~12% on combining a donor polymer with suitable absorption onset with PCBM. We also describe proof-of-principle studies employing light trapping in hybrid tandem solar cells, suggesting that this device architecture has the potential to achieve efficiencies well above 12%.

© 2014 Elsevier B.V. All rights reserved.

1. Introduction

The last decade was shaped by a tremendous increase in efficiency of organic solar cells. Both polymeric and small molecular materials processed either from solution or by vacuum deposition reached commercialization acceptable efficiencies around 10% in single junction [1,2] or tandem cell configuration [3,4]. This improvement shows the great potential of organic solar cells to be implemented into a low production and installation cost device technology [5]. One of the key advantages of organic materials is the overall high absorptivity and the sharp absorption onset. Thus, very thin organic films of approximately 100 nm thickness can be utilized to absorb almost 80% of the incident sunlight in the active organic material within a broad range of wavelengths in a device structure having the reflecting back electrode close to the active layer [6]. However, in the tandem cell configuration, the wide band-gap front cell should be in the range of 200–300 nm thickness for optimum light absorption in the case of organic front cells [3]. Additionally it needs to have a high fill factor (FF) and open circuit voltage (V_{oc}) at this optically optimized thickness. A general issue for efficient organic materials is a significant extraction loss if the active layer exceeds 100 nm [7–9]. This results in lower FFs when used as tandem front cells [10]. P3HT:ICBA is the material combination that works the best so far as front cell in organic multijunctions with appropriate thickness [3], although this blend is yet not optimized in terms of internal quantum efficiency and the optical band-gap versus open circuit voltage relation. There are other organic material combinations with comparable optical absorption onsets showing either higher V_{oc} with lacking FF at thicknesses above 200 nm [11], or a higher FF at thick layers but a smaller V_{oc} [12]. At the moment, the most promising wide band-gap organic material suitable for the front cell in a tandem configuration is the PBDTFBZS:$PC_{70}BM$ blend, reaching 7.7% efficiency in single junctions with 250 nm layer thickness [13].

Amorphous hydrogenated silicon (a-Si:H) has a band-gap of 1.7 eV and shows a V_{oc} of ~0.9 V together with internal quantum efficiencies of 100% (in the i-layer) and FFs of 70%, even for the thickness range of 100–250 nm. In optimized laboratory scale single junctions the highest reported stabilized efficiency for a-Si:H is about 10% with a ~250 nm (i) utilizing light trapping [14]. This is superior to P3HT:ICBA or other wide band-gap organic single junction cells that have been employed in tandem devices so far. a-Si:H is often used in tandem structures in combination with microcrystalline Si:H (μc-Si:H). The disadvantage of μc-Si:H is the low absorption in the red to NIR spectra as seen in Fig. 1. The hybrid tandem cell configuration, made from an a-Si:H front cell

* Corresponding author.
E-mail address: neher@uni-potsdam.de (D. Neher).

http://dx.doi.org/10.1016/j.solmat.2014.04.020
0927-0248/© 2014 Elsevier B.V. All rights reserved.

and an organic back cell therefore, combines the advantages of both the inorganic a-Si:H front cell and the organic low-band-gap back cell in one device.

Here we investigate hybrid tandem cells with a thin (~140 nm) a-Si:H front cell connected in series with an organic bulk heterojunction sub-cell made from the low band-gap donor polymer Si-PCPDTBT blended with $PC_{70}BM$. This hybrid device design is a quite new approach. In the last two years, only a few reports have been published using this hybrid design, with efficiencies of 1.8–3.3% [15–17] and 5.7% [18] as reported by Kim et al. and Seo et al., respectively. Kim and coworkers use a low performing organic sub-cell made of PCPDTBT:PCBM, but without using processing additives which are necessary to get good solar cell performance [19]. The work published by Seo and coworkers makes use of the polymer PBDTTT-C having a rather high band-gap of ~1.63 eV. To generate high currents in the organic sub-cell in combination with a-Si:H, the band-gap needs to be lowered further. Importantly, both papers show tandem cells with FFs below 50%, highlighting the importance of using appropriate recombination contacts in this hybrid configuration. Also, both reports make use of indium tin oxide (ITO) as transparent conductive oxide which is generally avoided for a-Si:H solar cells.

By using organic sub-cells with high quantum efficiencies up to 800 nm and optimized recombination contacts together with optimizing light management, we reach a power conversion efficiency (PCE) of 7.5% in a hybrid tandem cell made from a-Si:H and Si-PCPDTBT:$PC_{70}BM$ sub-cells. We present guidelines for further efficiency enhancements by tuning the polymer band-gap in the organic blend, with predicted hybrid tandem cell efficiencies close to 12%. Additionally, we show proof-of-concept studies for light trapping by textured front contacts. This strategy could further enhance the efficiency well above 12% when properly implemented in hybrid tandem solar cells.

Fig. 1 shows the absorption strength of a- and μc-Si:H together with the organic P3HT:$IC_{60}BA$ and Si-PCPDTBT:$PC_{70}BM$ blends. This comparison displays the strong absorption onsets of the organic materials compared over Si:H, especially in the range above $k=0.01$. Fig. 1 also displays the complementary absorption between a-Si:H and Si-PCPDTBT:$PC_{70}BM$, and the wide spectral range covered by these two materials.

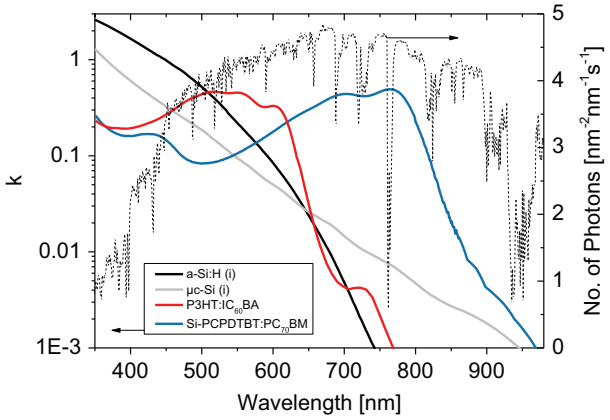

Fig. 1. (Left scale) Extinction coefficient k together with (right scale) the spectral photon flux density of AM 1.5G spectra.

2. Results

One of the standard transparent conductive oxides (TCOs) used for a-Si:H or μc-Si:H cells is aluminum doped zinc oxide (AZO) [20–22]. AZO can be easily sputtered with smooth surfaces and etched with e.g. diluted HCl to texturize the front contact and generate light trapping effects [20,23,24]. Tin doped indium oxide (ITO) which is usually used for organic electronics suffers from the reduction by hydrogen radicals during a-Si:H or μc-Si:H layer deposition resulting in reduced transparency when applied as front contact [25]. We, therefore, built our hybrid layer stack on AZO as the front contact as displayed in Fig. 2. The 700 nm thick front AZO is deposited via sputtering. On top of that, a layer sequence of p-type, intrinsic and n-type a-Si:H (together ~140 nm) is deposited via plasma enhanced chemical vapor deposition (PECVD). Finally,

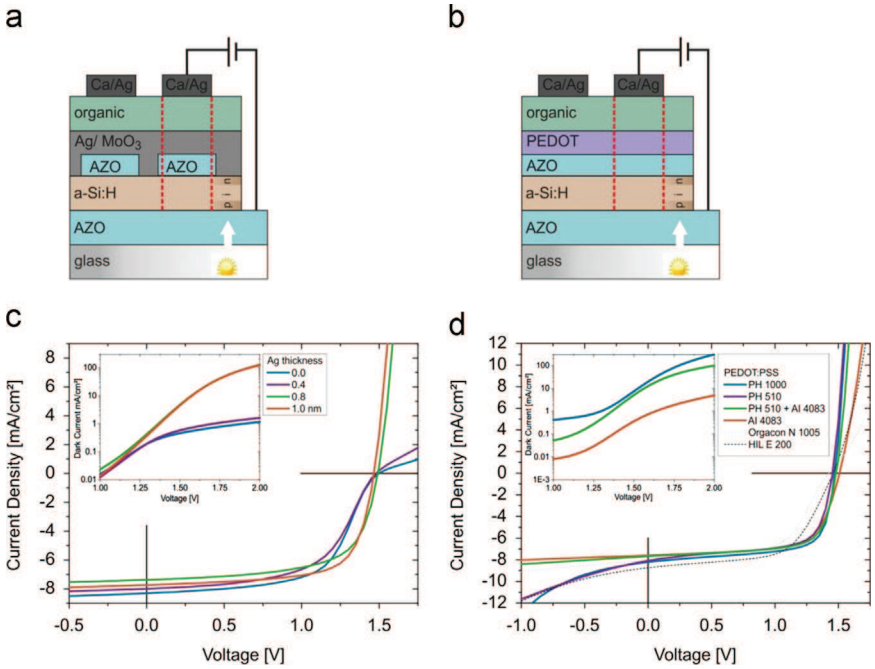

Fig. 2. (a) Schematic device structure with a Ag/MoO_3 recombination layer and (b) device structure with PEDOT:PSS as the p-type recombination contact. (c) J–V characteristics of devices with the structure shown in (a). (d) J–V characteristics of devices from (b). All J–V characteristics shown here are measured under AM 1.5G at 100 mW/cm^2 without the use of an aperture.

70 nm back AZO is deposited via sputtering and used as the n-type layer in the recombination contact. As the p-type layer of the recombination contact, either ultrathin (≤ 1 nm) silver together with 10 nm of MoO_3 thermally evaporated, or PEDOT:PSS (~ 60 nm) spin-coated from solution is used. Due to the sensitivity of AZO against acidic solutions, the PEDOT:PSS is pH-neutralized to a pH of 5. The active layer of the organic sub-cell is made from a Si-PCPDTBT:$PC_{70}BM$ blend spin-coated on top of the p-type recombination layer with a thickness of 90 nm. The device is finalized by thermal evaporation of 10 nm calcium and 600 nm of silver. The thick silver ensures that the active layer is mechanically stable against the contact finger with direct contact during *J–V* measurement. The active area is defined by the metal cathode (round, ~ 5 mm^2) only.

Fig. 2 shows the *J–V* characteristics of hybrid tandem solar cells made with two different recombination contacts. The recombination contact needs to ensure ohmic recombination and should deliver a suitable work-function difference to sum up the open-circuit voltages of the individual sub-cells. For the ultrathin Ag/MoO_3 recombination contact, a significant change in the performance is measured with changing Ag layer thickness. If no Ag interlayer or only 0.4 nm of Ag is used, the *J–V* characteristic shows a strong s-shape with reduced FF of about 56%. Also a low forward dark current is measured with 0.4 nm Ag or below (see inset). Both findings are indicative of inefficient recombination at the recombination contact. Increasing the Ag interlayer to 0.8 nm ensures high dark current together with higher FFs of 65% of the tandem device. The FF increases further to 70% for 1 nm Ag, suggesting loss free recombination between both sub-cells. A structured back AZO was used for these Ag/MoO_3 devices to reduce leakage from laterally collected shunt currents. When PEDOT:PSS is applied as the p-type recombination layer, structuring the back AZO leads to losses in the V_{oc} which are yet not understood (see Supporting information, SI). Thus we used homogeneously covered back AZO for hybrid tandem cells utilizing PEDOT:PSS. The corresponding *J–V* curves are shown in Fig. 2d. Significant differences in the performance are measured on changing the PEDOT:PSS conductivity. Using formulations with higher conductivity results in strong dark currents at high reverse bias and reduced FF. Making use of low conductivity grade formulations like AI 4083 leads to a series resistance with limits to the FF of 67%. The optimum between ohmic recombination in vertical direction and losses from high conductivity in lateral direction due to the collection of leakage currents is a mixture of AI 4083 and PH 510 1/1 by volume, generating FFs of 70% in good comparison to the Ag/MoO_3 contact.

Fig. 3 shows the *J–V* characteristics for AM 1.5G illumination through an aperture and the light-biased external quantum efficiency (EQE) spectra of best performing cells with different p-type contact layers. Note that we measure slightly higher currents without aperture, due to edge effects. With the aperture, the J_{sc} fits the current estimated from integration of the individual EQE spectra (see Table 1). The EQE spectra of the sub-cells have been measured with monochromatic cw background light at 525 nm or 740 nm to address the individual EQEs of the sub-cells. The photovoltaic performance data and the short circuit currents from integration of the EQE spectra are shown in Table 1.

Both contact designs give high FFs up to 70% in the tandem configuration. Also, the fact that the V_{oc} of the tandem is the sum of the V_{oc} of both sub-cells in its particular single-junction configuration proves that both recombination contacts perform as a loss free series connection. At the thickness of 140 nm for the total a-Si:H sub-cell and 90 nm for the Si-PCPDTBT:$PC_{70}BM$ layer the currents are quite balanced at 7.2–7.5 mA/cm^2. The final result is a PCE of 7.5% efficiency, which constitutes a 18% enhancement over the flat a-Si:H single junction and a 33% enhancement over the Si-PCPDTBT:$PC_{70}BM$ cell. This result is the highest reported efficiency for hybrid inorganic/organic tandem solar cell utilizing a-Si:H and organic sub-cells.

A further efficiency increase will be achievable via optimizing the donor band-gap in the blend with PCBM in the organic sub-cell. We constructed a series of optical spectra in which PCBM is blended with donors of different optical band-gaps E_g. The low energy absorption onset of the donor, and with that E_g, was shifted

Table 1
Performance data of best performing hybrid tandem devices with 140 nm for the complete a-Si:H cell and 90 nm Si-PCPDTBT:$PC_{70}BM$ thickness made with different recombination contacts.

Device	J_{sc}(EQE)[a] (mA/cm^2)	J_{sc} (mA/cm^2)	V_{oc} (mV)	FF (%)	PCE (%)
Tandem cells[b]					
AI 4083+PH 510	7.48 / 7.25	7.34	1453	70.1	7.48
AI 4083	7.10 / 7.22	7.42	1497	67.4	7.49
1 nm Ag/MoO_3	7.52 / 7.48	7.50	1465	69.0	7.58
Single junctions[c]					
a-Si:H (flat AZO)[d]		9.1	942	74.5	6.38
a-Si:H (rough AZO)[d]		11.1	941	71.1	7.42
Si-PCPDTBT:$PC_{70}BM$[e]		15.1	590	63.5	5.65

[a] From integration of the EQE of the respective sub-cell measured with background bias light, 1st value=a-Si:H, 2nd value=organic.
[b] Measured on round pixels with 2.5 mm diameter with an aperture of 2.4 mm diameter.
[c] In configuration with reflecting metal back contacts.
[d] Initial efficiency measured on 1 cm^2 active area.
[e] Measured on round pixels with 2.5 mm diameter without aperture.

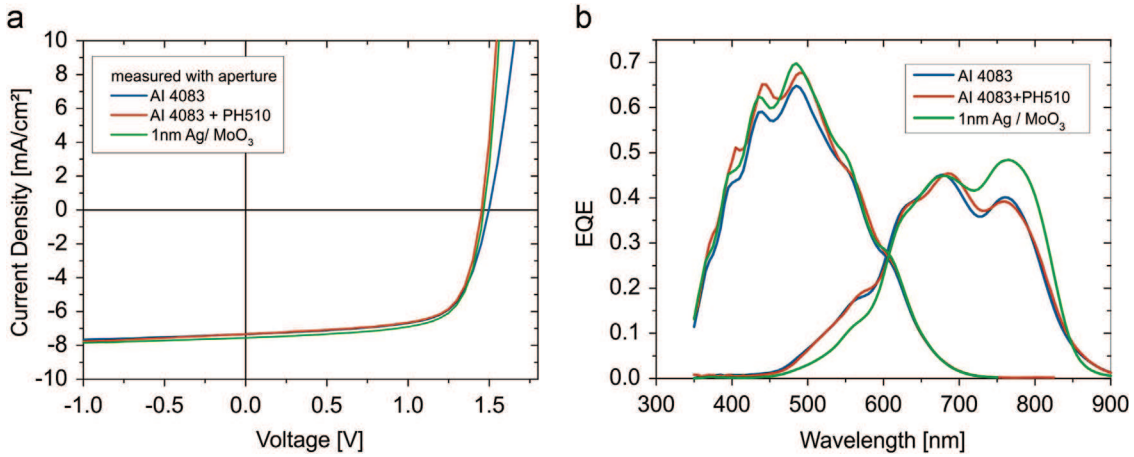

Fig. 3. (a) *J–V* characteristics measured under AM 1.5G at 100 mW/cm² with the use of an aperture and (b) light biased EQE of the corresponding devices.

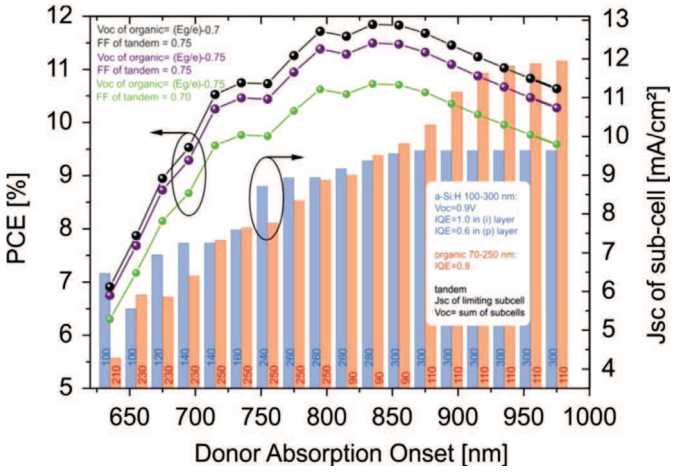

Fig. 4. Simulation of the hybrid tandem solar cell PCE (symbols) as a function of donor absorption onset in the organic blend with $PC_{70}BM$. The optical constants for the organic blend used in this simulation can be found in the SI. The assumptions for estimating the efficiency (left scale) can be found in the plot. The scale bars (right scale) show the current generated by the sub-cells in blue for a-Si:H and red for the organic, with the IQEs as indicated. The best performing thickness combination is indicated in nm vertically for each absorption onset. (For interpretation of the references to color in this figure legend, the reader is referred to the web version of this article.)

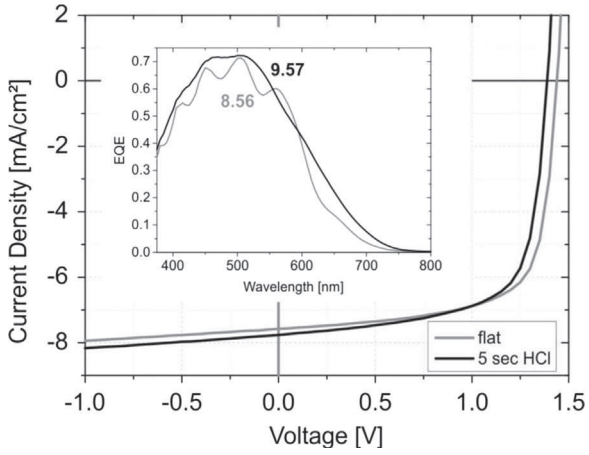

Fig. 5. *J–V* characteristics of devices with Ag/MoO_3 as recombination layer measured under AM 1.5G at 100 mW/cm² without the use of an aperture with flat or textured front AZO. The AZO is textured by etching for 5 sec in dilute HCl before a-Si:H deposition. The inset shows the EQE of the a-Si:H sub-cells and the J_{sc} determined from integration of the EQE spectra with the AM 1.5G spectra.

by 20 nm for each optical spectrum. Three optical spectra are shown exemplary in Fig. S2. The J_{sc} of both sub-cells was modeled via a transfer matrix formalism taking into account the optical parameters of the entire device stack, interference and reflection. The current generated in both sub-cells is displayed in Fig. 4 as bar chart as a function of donor absorption onset. For each optical band-gap the sub-cell thicknesses were optimized to give the highest current for the sub-cell that is current limiting at this thickness combination. For the organic blend, an IQE (the EQE divided by the fraction of absorption in the active layer) of 0.8 was chosen. There are reports with organic bulk heterojunctions having an IQE of near unity [26,27], but most of the low band-gap polymers show smaller IQE [28,29]. For the a-Si:H sub-cell, the IQE was set to 1 in the i-layer, 0.6 in the p-layer and 0 in the n-layer [30]. The simulation nicely shows that when the polymer band-gap is too large, absorption of sunlight will be mainly in a-Si:H, generating a low current in the organic sub-cell. Shifting the polymer absorption onset to energies below 1.41 eV (875 nm) increases the current generated by the organic sub-cell without further increasing the current generated in the a-Si:H sub-cell which has a maximum of ~9.6 mA/cm^2 without light trapping in this hybrid architecture model. The V_{oc} of the organic sub-cell is linked to the band-gap via $V_{oc}=(E_g/e)-\Delta V_{loss}$. Thus, reducing the band gap enhances J_{sc} on one side but reduces V_{oc} on the other side. Realistic values of this energetic loss offset are $\Delta V_{loss}=0.6$–0.9 V [28] and depend on the energy position of the donor HOMO and the fullerene LUMO levels, as well as on recombination losses at V_{oc} [31]. The V_{oc} of the tandem is assumed to be the sum of V_{oc} of both sub-cells and the J_{sc} is that of the limiting sub-cell. The latter one is a good approximation when both sub-cells have balanced J_{sc} and high FFs [32]. To calculate the tandem cell efficiency, we calculated the efficiency by the assumption of the FF to be 70% or 75% and ΔV_{loss} of the organic sub-cell to be 0.7 or 0.75 V. Values for the efficiency are shown on the left scale in Fig. 4 and range from 10.5% to almost 12% with a donor absorption onset of ~835 nm, and layer thicknesses of 280 nm for a-Si:H and 90 nm for the organic layer. At this band-gap and thickness combination, the currents of both sub-cells are well balanced and the tradeoff between high current and high voltage is maximized. Both sub-cells have reasonable thicknesses in terms of good extraction for optimized FFs. This semi-empiric model with realistic parameters shows the great potential of the hybrid tandem cell even in the absence of any light trapping schemes.

Light trapping in a-Si:H has been shown to greatly enhance the generated current due to enhancing the light absorption and reducing the reflection losses. Also, light trapping has the advantage of utilizing thinner a-Si:H layers that significantly lower the impact of degradation due to the Staebler–Wronski effect [33]. Usually, light trapping is achieved via texturized front TCOs like e.g. HCl etched AZO [20,23]. The etching induces a certain surface roughness with a root mean square roughness 40–100 nm and lateral features on a length scale of 400–1000 nm (see SI). In Fig. 5 we compare hybrid solar cells similar to the design shown in Fig. 2a but with a higher a-Si:H thickness of 180 nm and the front AZO which is flat or etched for 5 sec in diluted HCl. The inset displays the EQE of the a-Si:H sub-cell. Due to the higher roughness of the etched AZO front contact, the interference fringes vanish and the overall EQE increases significantly due to light trapping. The significant difference in surface roughness is displayed by atomic force microscopy in the SI. Although the organic blend layer is processed on the rough surface without the use of smoothening PEDOT:PSS, the V_{oc} and the FF of the tandem cell remain at almost that of the flat tandem. Note that the J_{sc} of the sample on textured front AZO is not greatly increased due to the fact that the organic Si-PCPDTBT:$PC_{70}BM$ cell is now current limiting with this thicker a-Si:H. Thus enhancing the current in the a-Si:H only slightly increases the J_{sc} of the tandem with light trapping. However, this proof-of-concept shows the great potential of the hybrid tandem design in combination with light trapping schemes, with the perspective to boost the efficiency limit well above 12% as estimated in Fig. 4 on implementing suitable donors.

3. Experimental

3.1. Optical constants

The extinction coefficient and refractive index for all inorganic layers were measured via photothermal deflection spectroscopy (PDS) [34] and ellipsometry. For the organic blends the extinction coefficient was determined by combining PDS and reflection together with transmission measurements as described in [27]. The refractive index of the organic blend was assumed to be 2 [35] in the simulation of Fig. 5.

3.2. Tandem cell fabrication

The fabrication of the inorganic sub-cell started in Jülich: 700 nm front AZO was deposited via sputtering according to [36,37] onto 1.1 mm thick Corning Eagle XG® glass substrates. After that, p-type μc-Si:H and a-SiC:H (together 25 nm), intrinsic a-Si:H (100 nm or 140 nm) and n-type a-Si:H (15 nm) layers were deposited by a radio frequency plasma enhanced chemical vapor deposition (RF PECVD) system (30×30 cm^2; 13.56 MHz), suitable for four 10×10 cm^2 substrates. The process gases used were silane (SiH_4), hydrogen (H_2), trimethylborane ($B(CH_3)_3$), monophosphane (PH_3) and methane (CH_4) applied through a showerhead electrode. The electrode gap was 12.5 mm and the deposition temperature was 220 °C resulting in substrate temperatures of ~200 °C. After deposition of the silicon layers the back AZO (70 nm) was deposited via sputtering either through shadow masks with defined areas of 4×4 mm^2 or without a mask, covering the complete substrate. Further processing was carried out in the laboratories in Potsdam: the front cell coated substrates were washed with isopropanol in an ultrasonic bath for 10 min and dried with nitrogen flow. After that the Ag/MoO_3 contact was thermally evaporated without patterning on top of the structured back AZO by thermal evaporation at base pressure below 10^{-6} mbar. The PEDOT:PSS was spin-coated from pH neutralized formulations onto the back AZO. The pH was adjusted to 5 with 10% ammonia and diluted with isopropanol (1:5) for better wetting. The PEDOT:PSS layer was dried at 140 °C for 15 min. The active layer was spin-coated in N_2 filled glove box from 1:1.5 solutions of Si-PCPDTBT:PC_{70}BM diluted in o-dichlorobenzene with 36 mg/mL overall blend concentration from 70 °C hot solutions at 1500 rpm for 40 s. Finally 10 nm of Ca and 600 nm of Ag were thermally evaporated through shadow masks defining the round active area to be 2.5 mm in diameter.

3.3. External quantum efficiency

The EQE was measured with monochromated light from tungsten lamp mechanically chopped to 140 Hz for the detection with a lock-in amplifier. The intensity of the lamp was checked with an UV enhanced crystalline silicon solar cell calibrated at Newport. The quality of the EQE setup was cross checked with a KG3 filtered crystalline silicon reference solar cell calibrated at Fraunhofer ISE. Constant background illumination was performed with 740 nm (Roithner, H2A1-H740) or 525 nm (Alustar, 9008100) LED arrays containing three LEDs mounted on a heat sink ring. One sub-cell was optically biased with the LED array having the suitable wavelength, the other sub-cell, not absorbing the bias light strongly, was measured with the chopped monochromatic light without the application of a constant voltage offset. Applying no external voltage offset can cause some error of the measured EQE especially for low FF sub-cells [32].

3.4. Solar cell characteristics

The solar cell characteristics were measured with an Oriel class ABA sun simulator calibrated to AM 1.5G and 100 mW/cm^2. The calibration of the sun simulator was done with a KG3 filtered silicon reference cell calibrated at Fraunhofer ISE. All shown data are not corrected for spectral mismatch. The mismatch factor is ca. 1.02 for a-Si:H and 0.97 for Si-PCPDTBT:PC_{70}BM.

3.5. Optical simulation

The fraction of absorption $A(E)$ in each layer of the solar cell stack and the total reflection was modeled with a transfer matrix formalism, taking into account the multi-reflections and interference of all layers assuming perfectly flat interfaces. $A(E)$ was corrected for the internal quantum efficiency and simulated for different active layer thickness combinations. The refractive index was assumed to be 2 and independent of wavelength for the constructed organic blends. For all other layers, the measured refractive index was used.

4. Conclusion

In summary, we have shown that hybrid tandem cells comprising a-Si:H and Si-PCPDTBT:PC_{70}BM sub-cells connected in series via AZO/PEDOT:PSS or AZO/Ag/MoO_3 recombination contacts generate 7.5% efficiency. By optimizing both recombination contacts, high FFs of 70% in the tandem cell are achieved. This is the best hybrid tandem cell efficiency reported for this type of device design so far. Importantly, the recombination contact and the front TCO were built with cost efficient AZO without employing ITO which is usually used in organic devices. Optical and electrical device modeling suggests that the PCE can be increased to ~12% combining a donor polymer with suitable absorption onset with PCBM. We furthermore showed proof-of-principle studies using light trapping with texturized front AZO for hybrid tandem solar cells. This device architecture has the potential to achieve efficiency well above 12%.

Acknowledgments

The authors thank Joachim Kirchhoff for the technical help with the fabrication of the inorganic layers. Bernd Rech from HZB and Bernd Stannowski from PVcomB assisted with fruitful discussions. We thank Sybille Allard and Ullrich Scherf from University of Wuppertal for giving access to Si-PCPDTBT (synthesized by Konarka) and thankfully acknowledge the help of Koen Vandewal and Joseß Klomfaß for the PDS measurements, Burkhard Stiller for AFM images, and Sebastian Schäfer for helping in the early stage of the project. The work was funded within the BMBF project PVCOMB (FKZ 03IS2151D).

Appendix A. Supporting information

Supplementary data associated with this article can be found in the online version at http://dx.doi.org/10.1016/j.solmat.2014.04.020.

References

[1] A.K.K. Kyaw, D.H. Wang, V. Gupta, J. Zhang, S. Chand, G.C. Bazan, A.J. Heeger, Adv. Mater. 25 (2013) 2397.
[2] Z. He, C. Zhong, S. Su, M. Xu, H. Wu, Y. Cao, Nat. Photonics 6 (2012) 591.
[3] J. You, et al., Nat. Commun. 4 (2013) 1446.
[4] Heliatek press release, January 16, 2013.
[5] F.C. Krebs, N. Espinosa, M. Hosel, R.R. Søndergaard, M. Jørgensen, Adv. Mater. 26 (2014) 29.
[6] S. Albrecht, S. Schäfer, I. Lange, S. Yilmaz, I. Dumsch, S. Allard, U. Scherf, A. Hertwig, D. Neher, Org. Electron. 13 (2012) 615.
[7] J Pete, et al., Appl. Phys. Lett. 98 (2011) 043301.
[8] J.A. Bartelt, et al., Adv. Energy Mater. 3 (2013) 364.
[9] Y. Sun, C.J. Takacs, S.R. Cowan, J.H. Seo, X. Gong, A. Roy, A.J. Heeger, Adv. Mater. 23 (2011) 2226.
[10] W. Li, A. Furlan, K.H. Hendriks, M.M. Wienk, R.A.J. Janssen, J. Am. Chem. Soc. 135 (2013) 5529.
[11] C. Cabanetos, A. El Labban, J.A. Bartelt, J.D. Douglas, W.R. Mateker, J.M.J. Fréchet, M.D. McGehee, P.M. Beaujuge, J. Am. Chem. Soc. 135 (2013) 4656.
[12] S.C. Price, A.C. Stuart, L. Yang, H. Zhou, W. You, J. Am. Chem. Soc. 133 (2011) 4625.
[13] K. Li, Z. Li, K. Feng, X. Xu, L. Wang, Q. Peng, J. Am. Chem. Soc. 135 (2013) 13549.
[14] S. Benagli, et al., in: Proceedings of the 24th European Photovoltaic Solar Energy Conference, Hamburg, Germany, 2009.

[15] T. Kim, J.H. Jeon, S. Han, D.-K. Lee, H. Kim, W. Lee, K. Kim, Appl. Phys. Lett. 98 (2011) 183503.
[16] T. Kim, et al., Synth. Met. 175 (2013) 103.
[17] T. Kim, J.Y. Choi, J.H. Jeon, Y.-S. Kim, B.-S. Kim, D.-K. Lee, H. Kim, S. Han, K. Kim, Mater. Res. Bull. 47 (2012) 3040.
[18] J.H. Seo, et al., Adv. Mater. 24 (2012) 4523.
[19] J. Peet, J.Y. Kim, N.E. Coates, W.L. Ma, D. Moses, A.J. Heeger, G.C. Bazan, Nat. Mater. 6 (2007) 497.
[20] J. Müller, B. Rech, J. Springer, M. Vanecek, Sol. Energy 77 (2004) 917.
[21] M. Berginski, J. Hüpkes, W. Reetz, B. Rech, M. Wuttig, Thin Solid Films 516 (2008) 5836.
[22] B. Rech, O. Kluth, T. Repmann, T. Roschek, J. Springer, J. Müller, F. Finger, H. Stiebig, H. Wagner, Sol. Energy Mater. Sol. Cells 74 (2002) 439.
[23] B. Rech, H. Wagner, Appl. Phys. A 69 (1999) 155.
[24] O. Kluth, B. Rech, L. Houben, S. Wieder, G. Schope, C. Beneking, H. Wagner, A. Loffl, H.W. Schock, Thin Solid Films 351 (1999) 247.
[25] J. Wallinga, W.M. Arnoldbik, A.M. Vredenberg, R.E.I. Schropp, W.F. van der Weg, J. Phys. Chem. B 102 (1998) 6219.
[26] S.H. Park, et al., Nat. Photonics 3 (2009) 297.
[27] K. Vandewal, et al., Nat. Mater. 13 (2014) 63.
[28] W. Li, W.S.C. Roelofs, M.M. Wienk, R.A.J. Janssen, J. Am. Chem. Soc. 134 (2012) 13787.
[29] J. You, et al., Adv. Mater. 25 (2013) 3973.
[30] K. Ding, T. Kirchartz, B.E. Pieters, C. Ulbrich, A.M. Ermes, S. Schicho, A. Lambertz, R. Carius, U. Rau, Sol. Energy Mater. Sol. Cells 95 (2011) 3318.
[31] A. Maurano, et al., Adv. Mater. 22 (2010) 4987.
[32] J. Gilot, M.M. Wienk, R.A.J. Janssen, Adv. Funct. Mater. 20 (2010) 3904.
[33] S. Schicho, D. Hrunski, R. van Aubel, A. Gordijn, Prog. Photovolt.: Res. Appl. 18 (2010) 83.
[34] W.B. Jackson, N.M. Amer, Phys. Rev. B 25 (1982) 5559.
[35] G.F. Burkhard, E.T. Hoke, M.D. McGehee, Adv. Mater. 22 (2010) 3293.
[36] M. Berginski, J. Hüpkes, M. Schulte, G. Schope, H. Stiebig, B. Rech, M. Wuttig, J. Appl. Phys. 101 (2007) 074903.
[37] J. Müller, et al., Sol. Energy Mater. Sol. Cells 66 (2001) 275.

Organic Electronics 13 (2012) 615–622

Contents lists available at SciVerse ScienceDirect

Organic Electronics

journal homepage: www.elsevier.com/locate/orgel

Light management in PCPDTBT:$PC_{70}BM$ solar cells: A comparison of standard and inverted device structures

Steve Albrecht [a], Sebastian Schäfer [a], Ilja Lange [a], Seyfullah Yilmaz [b], Ines Dumsch [b], Sybille Allard [b], Ullrich Scherf [b], Andreas Hertwig [c], Dieter Neher [a,*]

[a] Universität Potsdam, Institute of Physics and Astronomy, Soft Matter Physics, D-14476 Potsdam, Germany
[b] Bergische Universität Wuppertal, Macromolecular Chemistry and Institute for Polymer Technology, Gauss-Strasse 20, D-42097 Wuppertal, Germany
[c] Bundesanstalt für Materialwissenschaften (BAM), Unter den Eichen 44-46, D-12203 Berlin, Germany

ARTICLE INFO

Article history:
Received 25 October 2011
Received in revised form 13 December 2011
Accepted 28 December 2011
Available online 16 January 2012

Keywords:
Organic solar cells
Inverted solar cells
PCPDTBT
Low band-gap
Optical modeling

ABSTRACT

We compare standard and inverted bulk heterojunction solar cells composed of PCPDTBT:$PC_{70}BM$ blends. Inverted devices comprising 100 nm thick active layers exhibited short circuit currents of 15 mA/cm^2, 10% larger than in corresponding standard devices. Modeling of the optical field distribution in the different device stacks proved that this enhancement originates from an increased absorption of incident light in the active layer. Internal quantum efficiencies (IQEs) were obtained from the direct comparison of experimentally derived and modeled currents for different layer thicknesses, yielding IQEs of ~70% for a layer thickness of 100 nm. Simulations predict a significant increase of the light harvesting efficiency upon increasing the layer thickness to 270 nm. However, a continuous deterioration of the photovoltaic properties with layer thickness was measured for both device architectures, attributed to incomplete charge extraction. On the other hand, our optical modeling suggests that inverted devices based on PCPDTBT should be able to deliver high power conversion efficiencies (PCEs) of more than 7% provided that recombination losses can be reduced.

© 2012 Elsevier B.V. All rights reserved.

1. Introduction

The worldwide increasing demand for cheap electricity has triggered intense research on solar cells comprising organic semiconductors. Record values are currently achieved using soluble fullerene-derivatives as electron-acceptors and donor–acceptor-type co-polymers approaching and exceeding 8% efficiency [1–4]. The overall efficiency of planar solar cells is determined by several factors, one being the efficiency η_{abs} of the incident photons to be absorbed in the active layer under AM 1.5 illumination. Interference effects within the device structure cause η_{abs} to vary periodically with the thickness of the active layer. Efficient absorption is mostly realized in the 2nd absorption maximum, which is around 200–250 nm for many polymer:fullerene blends (with the optimum thickness primarily depending on the absorption properties, i.e. the long wavelength absorption onset of the active layer, see Supporting information Fig. S1).

Unfortunately, many highly efficient donor–acceptor-type co-polymers show significantly reduced fill factors (FFs) when increasing the active layer thickness. This is in contrast to the properties of the well known homopolymer poly(3-hexylthiophene) (P3HT) blended with fullerenes, where FFs exceeding 60% are measured even for blend thicknesses of up to 250 nm [5]. Optimized co-polymer devices, therefore, comprise active layers with thicknesses around the 1st absorption maximum, at 100 nm or even below [3,4,6,7], though increasing the layer thicknesses to the 2nd absorption maximum would allow a

* Corresponding author. Tel.: +49 (0) 331 977 1265; fax: +49 (0) 331 977 5615.
E-mail address: neher@uni-potsdam.de (D. Neher).

1566-1199/$ - see front matter © 2012 Elsevier B.V. All rights reserved.
doi:10.1016/j.orgel.2011.12.019

more complete absorption of the incident light. The overall reduction of device performance due to the drop in FF with increasing layer thickness has been attributed to inefficient charge-transport and collection. Therefore, alternative ways to increase the absorption while adjusting the active layer thickness to the 1st absorption maximum at around 100 nm need to be considered.

A smart strategy is to alter the optical field distribution within planar solar cell geometries [8], e.g. by the insertion of optical spacers [9,10] or by choosing different contact materials reducing parasitic absorptions and thereby increasing η_{abs} [11]. The most common device structure (here referred to as "standard") for organic solution processed solar cells is shown in Fig. 1a. The active layer is sandwiched between indium tin oxide (ITO) covered with poly(3,4ethylenedioxythiophene):poly(styrene sulfonate (PEDOT:PSS) and a low work function back electrode (Ca or Al) [4,12,13]. Inverted devices with metal-oxides like MoO_3 as hole- and TiO_2 or ZnO as electron-selective contacts have recently attracted attention because of their increased air stability compared to standard structures [14–17]. It was also shown that inverted architectures exhibits superior solar cell performance which was attributed to different absorption profiles, with reduced parasitic absorption in the PEDOT:PSS and the Ca layer [11,18]. Inverted structures are now widely used for high efficiency polymer:fullerene solar cells [15,16,19,20].

Poly[2,6-(4,4-bis(2-ethylhexyl)-4H-cyclopenta[2,1-b;3,4-b′]dithiophene)-alt-4,7-(2,1,3-benzothiadiazole)] (PCPDTBT) [21] has recently attracted considerable attention because of its low absorption band gap and high photovoltaic efficiency in blends with [6,6]-phenyl C_{71}-butyric acid methyl ester ($PC_{70}BM$). While initial studies performed on PCPDTBT:$PC_{70}BM$ processed in the standard geometry yielded a power conversion efficiency (PCE) of 3.2% [22], large improvements have been achieved by employing processing additives such as octanedithiol (ODT) and by using an inverted solar cell architecture [20,23]. However, to best of our knowledge, a comparative study of PCPDTBT:PCBM blends in standard and inverted cells has yet not been published.

Here we show that inverting the device structure of solar cells comprising a 100 nm spin-coated blend of PCPDTBT with $PC_{70}BM$ enhances the J_{sc} by 11%. Our experimental findings are rationalized by simulations of the optical field distributions within the multilayer structure with a transfer matrix formalism [8,24], which clearly illustrates an increase of the η_{abs} in the inverted device architecture. The comparison between the experimental short circuit current and the calculated η_{abs} allows the determination of the internal quantum efficiency (IQE) at simulated AM 1.5 simulation as a function of active layer thickness. We show that the IQE decreases continuously with thickness, pointing to inefficient charge carrier collection for thicker active layers.

2. Materials and methods

2.1. Solar cell fabrication

All solar cell devices were fabricated on structured ITO coated glass slides (Optrex) pre-cleaned in acetone, detergent, DI-water and isopropanol, and dried with a nitrogen gun. For standard devices, the pre-cleaned ITO substrates were plasma-cleaned and a 50–60 nm layer of PEDOT:PSS (Clevios AI 4083) was spin-cast on top. The samples were subsequently transferred into a nitrogen filled glove-box followed by annealing at 180 °C for 10 min. The active layer was spin-cast from solutions containing 1–3 blend ratios of PCPDTBT (M_w = 26,000 g/mol, PDI = 1.36, was prepared in a Stille type polycondensation following a procedure described in literature [21]) and $PC_{70}BM$ (99%, Solenne). Chlorobenzene was used as the solvent and 3 vol% diiodooctane (DIO) was added as a processing agent unless otherwise mentioned. Different layer thicknesses were attained by varying spin speed and blend concentration. Finally, 20 nm Ca and 100 nm Al were thermally evaporated with a base pressure below 10^{-6} mbar through shadow masks to define the active area to be 0.16 cm^2. For inverted devices a TiO_2 sol synthesized according to Ref. [9] was spin-cast at 5000 rpm onto ITO followed by heating to 80 °C for 10 min in air to form a TiO_2 layer with a thickness of 8–10 nm. Subsequently, the samples were transferred into the nitrogen-filled glove-box and heated to 140 °C for 10 min. After spin-coating the active layer, the devices

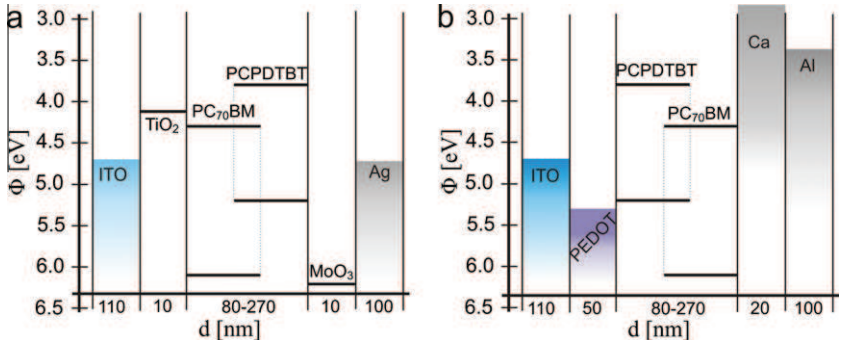

Fig. 1. Schematic device structure for (a) inverted and (b) standard device setup used in this work. The *x*-axes indicates the thickness range of each individual layer and the *y*-axes the work-functions measured with Kelvin Probe (in eV): ITO 4.7; PEDOT:PSS 5.3; Ca below 3; Al 3.3; TiO_2 4.1; MoO3 6.2 (for thicker films ~6.8); Ag 4.7. The values for HOMO and LUMO levels for the active layer were adopted from Refs. [6,35].

were completed by thermal evaporation of 10 nm of MoO_3 and 100 nm of Ag. Due to the high boiling point of DIO, all solar cells have been dried in vacuum at room-temperature for at least 5 h prior to evaporation of the back contact, since residual DIO functions as a hole trap [25].

2.2. Determination of optical constants and layer thickness

The optical constants of the metal oxides and the PEDOT:PSS were derived from transmission and reflection measurements on the respective materials on glass slides with a Varian Cary 5000 spectrophotometer equipped with an integrating sphere. Within the system air/film/substrate/air, the film thickness as well as the optical constants of the substrate and its thickness needs to be known. The optical constants of the film have been iteratively fitted point by point with the Newton–Raphson-method until the measured and theoretical reflection and transmission data converged [26]. The optical constants of the PCPDTBT:PC_{70}BM blend were deduced from spectroscopic ellipsometry of the blend layer on crystalline silicon (1 0 0) substrates by means of a M2000DI rotating compensator ellipsometer (J.A. Woollam Co.). The analysis was performed with the WVASE software (3.740). Due to the complex absorption spectrum of the blend, the generalized oscillator model employed 11 Gaussian absorption peaks between 1.5 and 6.1 eV center wavelengths. The surface roughness was implied with a 8 nm thick EMA (50% void) roughness layer. A MSE of only 3.5 shows the high accuracy of the fit. The optical constants of Ca, Al and ITO as well as Ag have been taken from literature [8,27,28]. Thicknesses have been measured with surface profilometry (Dektak 3, Veeco) for the active layer and via absorption on quartz glass substrates for the thin TiO_2 layers.

2.3. Determining the electrode work functions

The work functions have been determined via Kelvin Probe measurements as described in a recent publication [29], using highly ordered pyrolytic graphite (HOPG) as reference (work function of 4.6 eV [30]). Estimates of the work functions of all electrodes employed in our solar cells were obtained by performing measurements on the following samples: 100 nm of Ag or Al thermally evaporated on glass-slides, 10 nm of MoO_3 on Ag, 20 nm of Ca on Al, untreated ITO, 10 nm thick TiO_2 on ITO as well as 50 nm PEDOT:PSS on ITO.

2.4. External quantum efficiency (EQE)

The EQE was measured with monochromated light from tungsten lamp mechanically shopped to 140 Hz for detection with a lock-in amplifier. The intensity of the lamp was checked with an UV enhanced crystalline solar cell calibrated at Newport before each measurement. The quality of the EQE setup was cross checked with a KG3 filtered crystalline silicon reference solar cell calibrated at Fraunhofer ISE.

2.5. Solar cell characteristics

J–V characteristics were measured under illumination with an Oriel class A simulator calibrated to 100 mW/cm^2. The samples were temperature controlled to 20 °C during measurement. The calibration of the sun simulator was done with a KG3 filtered silicon reference cell calibrated at Fraunhofer ISE. All shown data (except in the Supporting information) are corrected for spectral mismatch (mismatch factor for PCPDTBT:PC_{70}BM $M = 0.95$) according to [31].

2.6. Optical modeling

The simulation of the solar cell short circuit currents have been performed by modeling the absorption of the active layer in the device stack with the transfer matrix formalism [8,24]. Comparison of the fraction of absorbed light with the measured EQE spectra at short circuit conditions yielded the internal quantum efficiency as a function of wavelength. Reflectivity spectra were measured for each cell to confirm the accuracy of the determination of the optical constants as described above.

3. Results and discussion

Fig. 1 summarizes the solar cell architectures of the studied solar cells. In the standard device configuration as shown in Fig. 1b, the active layer is sandwiched between PEDOT:PSS and Ca covered with Al. For the inverted devices the active layer is embedded between the electron selective TiO_2 and the hole selective MoO_3 contacts (Fig. 1a). Fig. 1 also shows the work functions of the different contacts as determined via Kelvin Probe measurements. The work function values are quite comparable to literature data for TiO_2 [7], MoO_3 [32] and PEDOT:PSS Clevios AI4083 [33]. We found that high FFs in the inverted geometry are only achieved with very thin TiO_2 layers (8–10 nm) while FF decreases drastically when the TiO_2 thickness of increases beyond 20 nm (see Supporting information S2). By applying 15 min UV-exposure with a Benda UV-hand-lamp to the solar cell the FF can be partially recovered even for thicker TiO_2 films, indicating that the UV-exposure promotes the trap filling thereby improving the electrical conductivity of the TiO_2 [34].

Fig. 2(a) shows the measured EQE of a standard and an inverted solar cell with a PCPDTBT:PC_{70}BM blend layer thickness of 100 nm. Clearly, the inverted device exhibits a higher EQE throughout the measured wavelength range. Accordingly, the J_{sc} of the inverted device is more than 10% higher compared to the standard structure (see Fig. 4).

Comparison of the EQE and the corresponding modeled fraction of absorbed light in the active layer for the different geometries shows that the external quantum efficiency scales well with the modeled absorption. We, actually find that the internal quantum efficiency as calculated from the EQE and the fraction of absorbed photons is rather similar for both device structures, with a mean value of about 71%. This implies that the higher EQE for inverted devices stems mainly from the higher absorption of the active layer. Also,

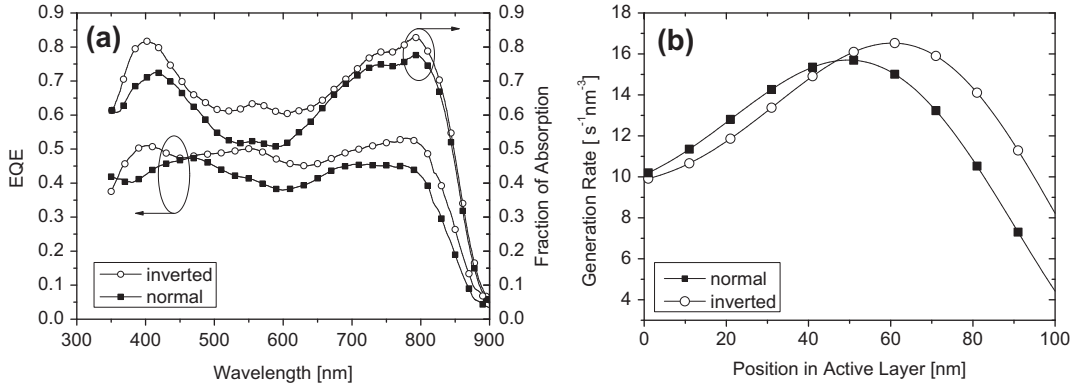

Fig. 2. (a) EQE and modeled fraction of absorbed light $A(\lambda)$ in standard and inverted devices with an active layer thickness of 100 nm. (b) Modeled exciton generation rate in the active layer as a function of position within the active layer of inverted (open circles) and standard devices (filled squares).

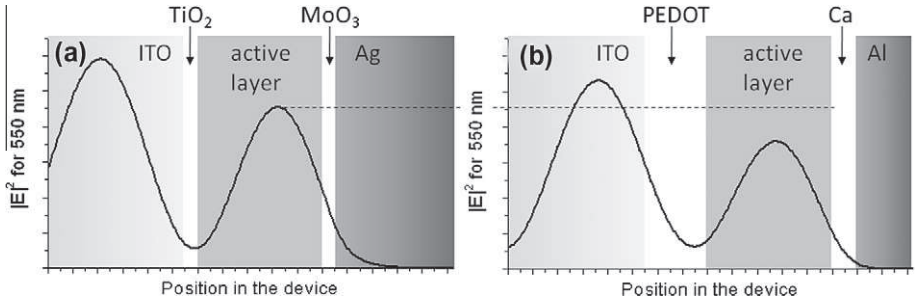

Fig. 3. Modulus squared of the optical electric field (normalized to the incoming plane wave) in the device stack for (a) inverted devices and (b) standard devices for 550 nm with the same *y*-axes scale-bar.

the variation of the IQE with wavelength is rather weak (Fig. 3) and a systematic difference in IQE for wavelength-ranges where the polymer or the PCBM absorption is dominant as reported by Burkhard et al. [36] has not been found. The high quality of the modeled absorption in the device stack is shown by the very good agreement between the modeled and measured reflectivity of the full device (Fig. S5).

According to Petersson et al. [24], the energy dissipation Q_{act} in the active layer at position x is given by

$$Q_{act}(x,\lambda) = \frac{1}{2} c\varepsilon_0 \alpha n |E(x,\lambda)|^2 \quad (1)$$

Evidently, Q_{act} is proportional to the refractive index n and the absorption coefficient α of the active layer as well as the modulus squared of the optical electric field $|E(x,\lambda)|^2$ normalized to the incoming field. Knowing the power of the incoming AM 1.5 spectrum, the exciton generate rate $g(x)$ can be calculated by dividing $Q_{act}(x,\lambda)$ by the energy of a single photon at wavelength λ and integrating over the wavelength range determined by the transmission through the ITO (λ_{begin}) and absorption onset of the active layer (λ_{end}) [8,37].

$$g(x) = \int_{\lambda_{begin}}^{\lambda_{end}} \frac{\lambda}{hc} Q_{act}(x,\lambda) d\lambda \quad (2)$$

In Eq. (2) the photon to exciton conversion efficiency is assumed to be one meaning that every single photon absorbed in the active layer initially creates an exciton. The exciton generation rate versus position in the active layer is shown in Fig. 2(b) for standard and inverted devices with a nominal active layer thickness of 100 nm. The main difference is a shift of the generation profile towards the back-electrode. Interestingly, the rate for excited state formation near the back electrode is considerably larger for the inverted cell geometry, which accounts in part for the higher J_{sc} of this device.

The normalized modulus of the optical electric field is shown in Fig. 3 for inverted (a) and standard devices (b) with an active layer thickness of 100 nm for a wavelength of 550 nm. This wavelength has been chosen as the difference in EQE and absorption between the two device stacks is most prominent at 550 nm. Inversion of the layer structure causes a slight shift of the maximum of the electric field towards the back electrode but mainly increases the overall modulus throughout the whole active layer.

It has been reported that introducing optical spacers between the active layer and the back electrode in standard devices [9] or matching the refractive index of the front-contact to ITO [7] increases J_{sc}. Systematical optical modeling studies (data not shown) for the inverted structure of our PCPDTBT:$PC_{70}BM$ blends showed that decreasing the MoO_3 thickness actually increases J_{sc} meaning that the MoO_3 layer inserted between the active material and the metallic Ag contact does primarily not function as an optical spacer, and that the inverted structure is already well

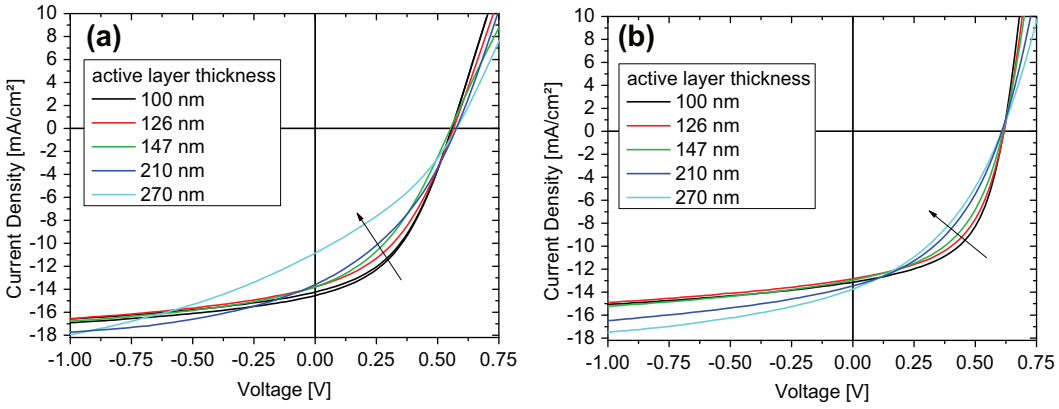

Fig. 4. *J–V* characteristics of devices with different active layer thickness in (a) inverted and (b) standard device structure. All characteristics were measured under simulated AM 1.5G illumination calibrated to 100 mW/cm^2 and corrected for spectral mismatch.

optimized with a thin MoO_3 film [38]. Increasing the MoO_3 thickness moves the maximum of the modulus squared of the optical electric field closer to the back contact, resulting in a reduced exciton generation rate. Also, decreasing the refractive index of the TiO_2 in the simulation caused J_{sc} to increase. According to our simulations, further improvement of light absorption in the active region for a blend thickness of 100 nm can only be achieved when applying light trapping mechanisms, which is beyond the scope of this paper.

In the next step, a systematic variation of the active layer thickness was performed. Fig. 4 shows the resulting *J–V* characteristics under simulated AM 1.5G spectra at 100 mW/cm^2 for inverted (a) and standard (b) devices, with active layer thicknesses between 100 and 270 nm. The photovoltaic parameters derived from these curves are summarized in Fig. 5.

For both device architectures, the device performance declines with layer thickness, but the effect is more pronounced for the inverted structure. This decrease is in part due to a continuous decrease of the FF with thickness. Also, the measured short-circuit currents derivate largely from the prediction by optical modeling (using a constant internal quantum efficiency of 68%) at high layer thickness. In particular, we find that J_{sc} is higher for the inverted structure for a layer thickness smaller than ca. 170 nm, while it drops considerably below the value for the standard device architecture for high thicknesses. This is in contrast to optical modeling which predict J_{sc} of the inverted device to be 9–15% higher for all thicknesses, with a maximum difference at around 175 nm. Poor fill factors and low short circuit currents have been attributed to either a field-dependent efficiency of free carrier generation or to recombination losses. In the former case, the photocurrent will scale with the internal electric field, which is not the case in our devices (see Fig. S3). Also, regular and inverted devices exhibit different fill factors for the same layer thickness (having almost the same open circuit voltage), ruling out field-dependent generation as the main process governing the photocurrent characteristics. This is in accordance with recent findings by Jamieson et al. [39]. Alternatively, low fill factor of PCPDTBT:fullerene solar cells have been explained by significant, possible trap-assisted, recombination [22,40,41]. Recently, Bailey et al. presented a detailed study on the interrelation between blend morphology, carrier transport and photovoltaic properties of a blend of a related polymer, poly[N-9″-hepta-decanyl-2,7-carbazole-*alt*-5,5-(4′,7′-di-2-thienyl-2′,1′,3′-benzothiadiazole)] (PCDTBT), with $PC_{70}BM$ [42]. These authors concluded that the decrease in device performance with layer thickness is due to trap-assisted recombination in presence of a broad distribution of holes traps, and that deep traps are caused by the rather low structural order in these blends. It was also suggested that recombination losses decrease with increasing inverse bias.

Therefore, to evidently show that inverting the device structure improves light absorption for all layer thicknesses, we have compared the light-generated current at the most negative bias of −1 V to the absorption efficiency $\eta_{abs}^{blend}d$ which is the fraction of incident photons absorbed in the active layer, accounting for the spectral irradiance $I(\lambda)$ of the AM 1.5G illumination integrated over the wavelength-range of the blend absorption.

$$\eta_{abs}^{blend}(d) = \frac{\int_{350\ nm}^{900\ nm} \lambda \cdot A(\lambda, d) \cdot I(\lambda) d\lambda}{\int_{350\ nm}^{900\ nm} \lambda \cdot I(\lambda) d\lambda} \quad (3)$$

In Eq. (3), $A(\lambda, d)$ is the fraction of light absorbed in the active layer at a given wavelength λ and thickness d. The comparison is shown in Fig. 6(a). In accordance with the prediction by optical modeling, the photocurrent of the inverted device at −1 V exceeds the current of the corresponding regular structure for all layer thicknesses. Also, the reverse-bias currents are largest at a layer thickness of 270 nm, which complies with the predicted behavior. Finally, IQEs calculated from the photocurrents at −1 V are well comparable for both devices for a given thickness (Fig. 6(b)), meaning that the efficiency for converting an absorbed photon into a free carrier is independent of device architecture.

We finally, like to address the poorer fill factor and short circuit current in the inverted device. Following the arguments outlined above, the balance between extraction and recombination of free charge carriers must be more

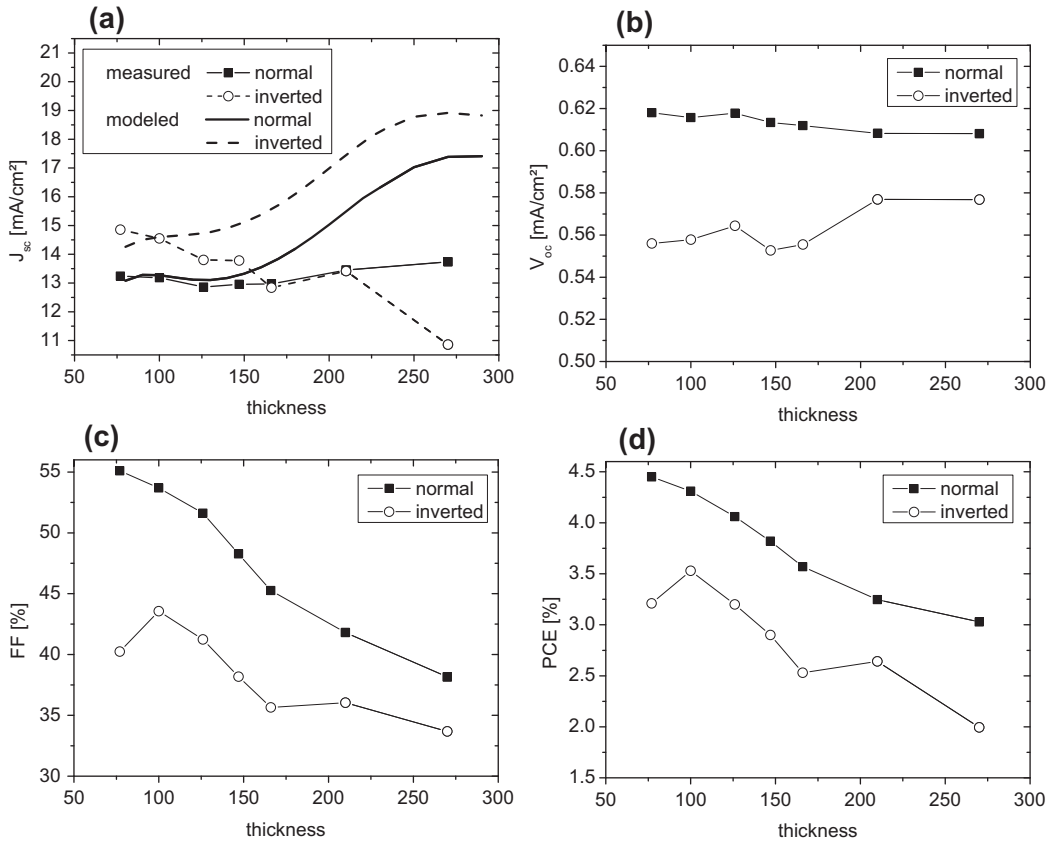

Fig. 5. (a) Measured J_{sc} from simulated AM 1.5G at 100 mW/cm^2 corrected for spectral mismatch for inverted (dashed line + open circles) and standard cells (solid line + filled squares), plotted together with modeled short circuit current under the assumption of a constant IQE of 68% for inverted (dashed black line) and standard cells (solid black line), (b) measured open circuit voltages, (c) measured fill factors, (d) measured power conversion efficiency.

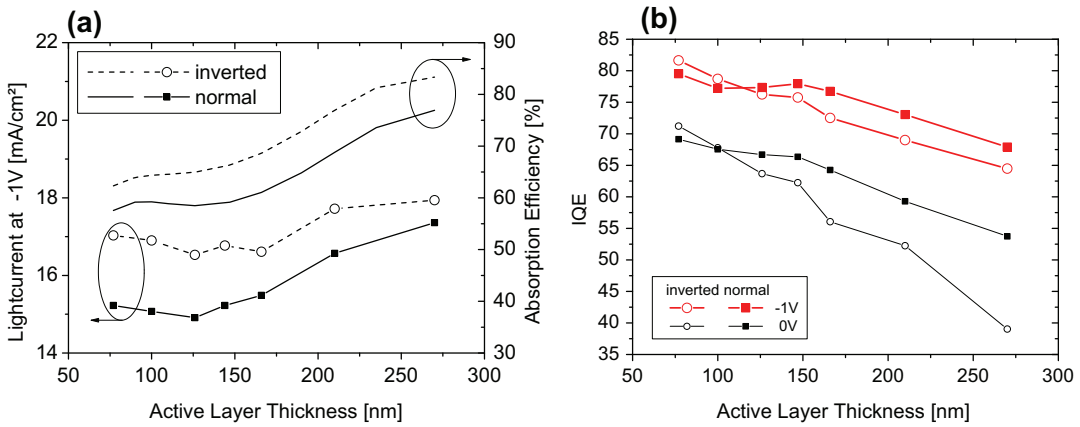

Fig. 6. (a) Comparison of the current under illumination of AM 1.5G irradiance with 100 mW/cm^2 at −1 V and the absorption efficiency of the blends in the wavelength range between 350 and 900 nm, (b) internal quantum efficiency for different layer thicknesses, calculated from measured (under AM 1.5G with 100 mW/cm^2) currents at 0 V (black) and −1 V (red) and the modeled fraction of absorption in the active layer for inverted (open circles) and standard devices (filled squares). (For interpretation of the references to colour in this figure legend, the reader is referred to the web version of this article.)

unfavorable in the inverted device. Holes have been found to be the slower carriers in PCPDTBT:$PC_{70}BM$ blends [43]. As shown in Fig. 7, the generation profile seen from the hole-extracting contact is rather different for both types of devices. In particular, the path length for hole extraction is remarkably higher in the inverted device with a thick active layer compared the standard structure. This in turn might increase the amount of holes occupying traps and concurrently enforce trap-assisted recombination. In addition, the PCPDTBT phase was shown to undergo slow

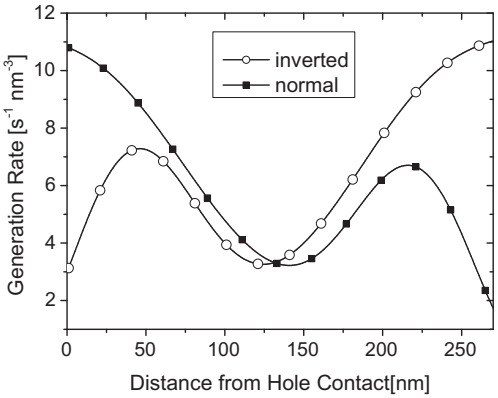

Fig. 7. Simulated exciton generation profile versus distance from the hole selective contact for normal (filled squares) and inverted (open circles) devices with an active layer thickness of 270 nm.

drying in presence of the additive, which can promote segregation of the hole-transporting PCPDTBT towards the bottom contact. Agostellini et al. reported a pronounced vertical composition profile in PCPDTBT:PCBM blends processed with the additive [41]. Such segregation might aggravate the collection of holes at the top contact in the inverted device structures. Note that weak segregation will have an only minor affect on the optical field profile. In fact, we find very good agreement between the modeled and measured reflectance on ITO/TiO_2-substrates when assuming that the optical constants are homogeneous throughout the entire layer. Evidently, the lower fill factors and power conversion efficiencies of our inverted devices must be related to more pronounced recombination losses, caused either by vertical phase segregation or different path length of hole extraction in the two types of devices. Here it is important to note that inverted devices comprising a 140 nm thick annealed P3HT:PCBM blend layer exhibited very high FFs and a Voc equal to the standard structure (see Supporting information S2), even in absence of UV exposure. Annealed P3HT:PCBM layers were shown to have reduced coefficients for bimolecular recombination, which is probably related to the high structural and electronic order in this particular blend system [44–46].

4. Conclusion

In summary, we have shown that inverted device stacks comprising a 100 nm thick bulk heterojunction composed of PCPDTBT and $PC_{70}BM$ show 11% larger short circuit currents compared to the standard device structure. Optical modeling of the optical field distribution in the different device stacks proves that this enhancement originates from an increased absorption of incident light in the active layer. The internal quantum efficiency for both architectures was found to be ~70% for a layer thickness of 100 nm, but it decreased continuously with layer thickness. The simultaneous deterioration of the FF for increasing thickness indicates that charge collection becomes increasingly inefficient for thicker blend layers, probably caused by strong mono- or bimolecular recombination. On the other hand, our optical simulations show that inverted solar cells based on PCPDTBT:$PC_{70}BM$ are capable of delivering high efficiencies at larger active layer thicknesses, provided that recombination losses can be suppressed. Noticeably, a J_{sc} of 19.0 mA/cm^2 is predicted for a moderate internal quantum efficiency of 70% and a layer thicknesses around 270 nm. Assuming a V_{oc} of 0. 61 V and a FF of 62%, a PCE of more than 7% should be achievable for the inverted device structure. Further work will, therefore, be devoted to the understanding and reduction of extraction losses in these blends.

Acknowledgements

S.A. acknowledges Dr. Basudev Pradhan and Ulrike Schreiber for the help with the TiO_2 synthesis and Dr. James Blakesley for the modification of the optical modeling software. This work was funded by the Bundesministerium für Bildung und Forschung (BMBF) within the PVcomB project (FKZ 03IS2151D).

Appendix A. Supplementary data

Supplementary data associated with this article can be found, in the online version, at doi:10.1016/j.orgel.2011.12.019.

References

[1] Konarka Press Release, 2010.
[2] Solarmer Press Release, 2010.
[3] T.-Y. Chu, J. Lu, S. Beaupré, et al., J. Am. Chem. Soc. 133 (2011) 4250.
[4] Y.Y. Liang, Z. Xu, J.B. Xia, et al., Adv. Mater. 22 (2010) E135.
[5] C.J. Brabec, S. Gowrisanker, J.J.M. Halls, et al., Adv. Mater. 22 (2010) 3839.
[6] M.C. Scharber, M. Koppe, J. Gao, et al., Adv. Mater. 22 (2010) 367.
[7] Y. Sun, C.J. Takacs, S.R. Cowan, et al., Adv. Mater. 23 (2011) 2226.
[8] G.F. Burkhard, E.T. Hoke, M.D. McGehee, Adv. Mater. 22 (2010) 3293.
[9] S.H. Park, A. Roy, S. Beaupre, et al., Nat. Photonics 3 (2009) 297.
[10] R. Schueppel, R. Timmreck, N. Allinger, et al., J. Appl. Phys. 107 (2010) 6.
[11] A. Hadipour, D. Cheyns, P. Heremans, et al., Adv. Energy Mater. 1 (2011) 930.
[12] R.C. Coffin, J. Peet, J. Rogers, et al., Nat. Chem. 1 (2009) 657.
[13] C. Piliego, T.W. Holcombe, J.D. Douglas, et al., J. Am. Chem. Soc. 132 (2010) 7595.
[14] C. Waldauf, M. Morana, P. Denk, et al., Appl. Phys. Lett. 89 (2006) 3.
[15] Y.-J. Cheng, C.-H. Hsieh, Y. He, et al., J. Am. Chem. Soc. 132 (2010) 17381.
[16] Y.M. Sun, J.H. Seo, C.J. Takacs, et al., Adv. Mater. 23 (2011) 1679.
[17] C.-Y. Li, T.-C. Wen, T.-H. Lee, et al., J. Mater. Chem. 19 (2009) 1643.
[18] T. Ameri, G. Dennler, C. Waldauf, et al., J. Appl. Phys. 103 (2008) 6.
[19] C.M. Amb, S. Chen, K.R. Graham, et al., J. Am. Chem. Soc. 133 (2011) 10062.
[20] M. Morana, H. Azimi, G. Dennler, et al., Adv. Funct. Mater. 20 (2010) 1180.
[21] Z. Zhu, D. Waller, R. Gaudiana, et al., Macromolecules 40 (2007) 1981.
[22] D. Mühlbacher, M. Scharber, M. Morana, et al., Adv. Mater. 18 (2006) 2884.
[23] J. Peet, J.Y. Kim, N.E. Coates, et al., Nat. Mater. 6 (2007) 497.
[24] L.A.A. Pettersson, L.S. Roman, O. Inganas, J. Appl. Phys. 86 (1999) 487.
[25] S. Cho, J.K. Lee, J.S. Moon, et al., Org. Electron. 9 (2008) 1107.
[26] K. Peter, Diploma Thesis, University of Konstanz, 1993.
[27] C.M. Ramsdale, N.C. Greenham, J. Phys. D: Appl. Phys. 36 (2003) L29.
[28] E. Palik, Handbook of Optical Constants of Solids, vol. 1, Academic Press Limited, 1995.
[29] I. Lange, J.C. Blakesley, J. Frisch, et al., Phys. Rev. Lett. 106 (2011) 216402.

[30] M.M. Beerbom, B. Lägel, A.J. Cascio, et al., J. Electron Spectrosc. 152 (2006) 12.
[31] V. Shrotriya, G. Li, Y. Yao, et al., Adv. Funct. Mater. 16 (2006) 2016.
[32] M. Kroger, S. Hamwi, J. Meyer, et al., Appl. Phys. Lett. 95 (2009) 3.
[33] S. Kirchmeyer, A. Elschner, K. Reuter, Pedot: Principles and Applications of an Intrinsically Conductive Polymer, Taylor and Francis Group, 2011.
[34] S. Sista, M.H. Park, Z.R. Hong, et al., Adv. Mater. 22 (2010) 380.
[35] H.-Y. Chen, J. Hou, S. Zhang, et al., Nat. Photon 3 (2009) 649.
[36] G.F. Burkhard, E.T. Hoke, S.R. Scully, et al., Nano Lett. 9 (2009) 4037.
[37] D.W. Sievers, V. Shrotriya, Y. Yang, J. Appl. Phys. 100 (2006) 7.
[38] T.-Y. Chu, S. Alem, P.G. Verly, et al., Appl. Phys. Lett. 95 (2009) 063304.
[39] F.C. Jamieson, T. Agostinelli, H. Azimi, et al., J. Phys. Chem. Lett. 1 (2010) 3306.
[40] M. Morana, M. Wegscheider, A. Bonanni, et al., Adv. Funct. Mater. 18 (2008) 1757.
[41] T. Agostinelli, T.A.M. Ferenczi, E. Pires, et al., J. Polym. Sci. Part B: Polym. Phys. 49 (2011) 717.
[42] Z.M. Beiley, E.T. Hoke, R. Noriega, et al., Adv. Energy Mater. 1 (2011) 954.
[43] M. Lenes, M. Morana, C.J. Brabec, et al., Adv. Funct. Mater. 19 (2009) 1106.
[44] A. Pivrikas, G. Juska, A.J. Mozer, et al., Phys. Rev. Lett. 94 (2005).
[45] I.A. Howard, R. Mauer, M. Meister, et al., J. Am. Chem. Soc. 132 (2010) 14866.
[46] J. Kniepert, M. Schubert, J.C. Blakesley, et al., J. Phys. Chem. Lett. 2 (2011) 700.

THE JOURNAL OF PHYSICAL CHEMISTRY Letters

Letter

pubs.acs.org/JPCL

On the Field Dependence of Free Charge Carrier Generation and Recombination in Blends of PCPDTBT/$PC_{70}BM$: Influence of Solvent Additives

Steve Albrecht,[†] Wolfram Schindler,[‡] Jona Kurpiers,[†] Juliane Kniepert,[†] James C. Blakesley,[†] Ines Dumsch,[§] Sybille Allard,[§] Konstantinos Fostiropoulos,[‡] Ullrich Scherf,[§] and Dieter Neher*,[†]

[†]Institute of Physics and Astronomy, Soft Matter Physics, Universität Potsdam, D-14476 Potsdam, Germany

[‡]Helmholtz-Zentrum Berlin für Materialien und Energie, Hahn-Meitner-Platz 1, D-14109 Berlin, Germany

[§]Macromolecular Chemistry and Institute for Polymer Technology, Bergische Universität Wuppertal, Gauss-Strasse 20, D-42097 Wuppertal, Germany

Supporting Information

ABSTRACT: We have applied time-delayed collection field (TDCF) and charge extraction by linearly increasing voltage (CELIV) to investigate the photogeneration, transport, and recombination of charge carriers in blends composed of PCPDTBT/$PC_{70}BM$ processed with and without the solvent additive diiodooctane. The results suggest that the solvent additive has severe impacts on the elementary processes involved in the photon to collected electron conversion in these blends. First, a pronounced field dependence of the free carrier generation is found for both blends, where the field dependence is stronger without the additive. Second, the fate of charge carriers in both blends can be described with a rather high bimolecular recombination coefficients, which increase with decreasing internal field. Third, the mobility is three to four times higher with the additive. Both blends show a negative field dependence of mobility, which we suggest to cause bias-dependent recombination coefficients.

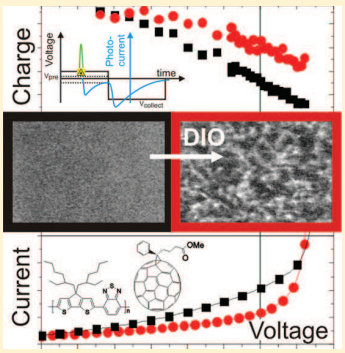

SECTION: Macromolecules, Soft Matter

The outlook brightens for organic photovoltaics because a dramatic efficiency improvement has been reported over the last 3 years with the introduction of new copolymers as donors in combination with the electron acceptor PCBM.[1] A smart strategy toward higher power conversion efficiencies (PCEs) is to reduce the band gap of the donating polymer by combining electron-rich and electron-deficient units within the conjugated main chain.[2,3] For some of these polymers, the photovoltaic performance of the resulting bulk heterojunction (BHJ) can be controlled with the help of solvent additives.[4−7] One of these polymers is poly[2,6-(4,4-bis(2-ethylhexyl)-4*H*-cyclopenta[2,1-b;3,4-b″]dithiophene)-alt-4,7-(2,1,3-benzothiadiazole)] (PCPDTBT), introduced in 2006 by Konarka Technology Inc.[3] For BHJ solar cells composed of PCPDTBT/$PC_{70}BM$, addition of the processing additive diiodooctane (DIO) was shown to increase the performance by a factor of 2 up to 5.5%.[6,8] Unfortunately, PCPDTBT/PCBM devices exhibit low fill factors (FFs), implying a strong dependence of the photogenerated current upon internal bias. Though the FF improves considerably upon processing with DIO, it still remains well below the values reported for other high-performance copolymer/fullerene blends.[2,5,9] Therefore, the main cause of the low FF in PCPDTBT/PCBM blends and the impact of the solvent additive on the elementary processes involved in the generation and recombination of charges in these blends is the subject of numerous recent publications.[10−19]

Lenes et al. successfully modeled the current−voltage characteristics of PCPDTBT/PCBM blends (processed without DIO) by considering free carrier generation via field-induced separation of coulombically bound polaron pairs (PPs).[20] It was proposed that the low FF in this blend is caused by geminate recombination with a rather short lifetime of the bound pair. It was further proposed that addition of DIO increases this lifetime, from ∼500 ns to 3 μs.[17] Field-dependent dissociation of PPs in blends processed without additives was also concluded on the basis of the field-suppressed emission from charge-transfer excitons by Jarzab et al.[15] On the other hand, recent studies with transient absorption spectroscopy (TAS) showed the efficiency for free carrier formation to be independent of the applied bias in PCPDTBT/$PC_{70}BM$ blend devices. The higher short-circuit current in DIO-processed devices was attributed to a higher yield of PP dissociation in conjunction with reduced geminate recombination.[14] An overall more efficient generation of free charges with additive was also revealed by studies of the photoinduced absorption[18] and the

Received: January 20, 2012
Accepted: February 9, 2012
Published: February 9, 2012

ACS Publications © 2012 American Chemical Society

emission of CT states.[19] These observations are in accordance with earlier conclusions by the Konarka group that low FFs in PCPDTBT/$PC_{70}BM$ blends are caused by non-geminate recombination of free carriers rather than by field-dependent split up of bound PPs in competition to geminate recombination.[3] Surprisingly, Agostinelli et al. found the bimolecular recombination (BMR) coefficient at identical charge densities to be 6 times higher for blends with the additive, despite the larger FF of these devices.[10] Regarding charge-transport properties, a 4-fold increase of the BIFET mobility of electrons and holes in PCPDTBT/$PC_{70}BM$ processed with DIO was reported.[11] On the other hand, dark currents in PCPDTBT/PCBM devices were shown to be unaffected by the additive, implying a very weak impact of the processing conditions on vertical charge transport.[17] In agreement to this, the hole mobility in time-of-flight (TOF) measurements was not significantly altered by the additive.[10]

Here, we present studies of the charge carrier dynamics with time-delayed collection field (TDCF)[21,22] and photo-CELIV measurements in blends of PCPDTBT/$PC_{70}BM$, processed without and with DIO. In TDCF, carriers are photogenerated with a nanosecond laser pulse at a certain prebias typical for solar cell operation and subsequently extracted with a constant, high reverse bias which is applied after a defined delay time. We optimized our TDCF setup to decrease the minimum delay time to only 10 ns; see the Supporting Information (SI). This allowed us to obtain detailed information on the field dependence of charge carrier generation and recombination with exceptional high temporal resolution. The pulse fluence was chosen to vary between 0.2 and 0.5 $\mu J/cm^2$, which yielded a strictly linear dependence of the photogenerated charge carrier density on light intensity (see Figure S2 in SI). The initial photogenerated carrier densities were comparable to steady-state densities under AM 1.5G illumination at 1 sun conditions.[23] Field-dependent mobilities were measured via photo-CELIV[24] or deduced from the linear extrapolation of the initial photocurrent decay in the TDCF extraction transients.[21,25]

Solar cell samples were prepared on structured ITO (Optrex) coated with 60 nm PEDOT/PSS (Clevios AI 4083). The blend solution (1/3 by weight) of PCPDTBT (M_w = 22300 g/mol, PDI = 1.31) and $PC_{70}BM$ (Solenne) in chlorobenzene was spincoated with or without 3 vol % DIO, yielding an active layer thickness of 100 nm. The samples were finalized by thermal evaporation of Ca (20 nm) and Al (100 nm) with an active area of 1.1 mm^2. All samples were encapsulated with epoxy resin and a glass lid prior to air exposure (see SI for details on sample preparation and measurement techniques).

The morphological change induced by the solvent additive DIO was studied with plasmon mapping based on energy-filtered transmission electron microscopy (EFTEM)[26] on thin films representative of solar cells (Figure 1). The corresponding energy loss spectra for PCPDTBT, $PC_{70}BM$, and the blend films (Figure S1 in SI) show that areas with the loss peak at ~25 eV (black areas in Figure 1) are rich in $PC_{70}BM$.[26] The morphology without use of DIO is characterized by a highly intermixed small-scale phase separation. Blend layers processed with 3 vol % DIO reveal a higher contrast in the plasmon maps, indicating purer polymer and fullerene phases, with an average domain size of 10−20 nm.

The significant coarsening of the blend morphology with the use of DIO is accompanied by the appearance of a distinct shoulder at 800 nm in the optical absorption spectrum (see Figure S1b, SI). This indicates stronger polymer aggregation

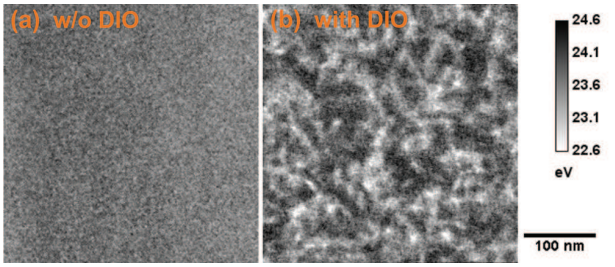

Figure 1. Plasmon maps based on EFTEM images of thin films made of 1/3 blends of PCPDTBT/$PC_{70}BM$ (a) without additive and (b) with 3 vol % DIO. The dark areas refer to $PC_{70}BM$ (see SI).

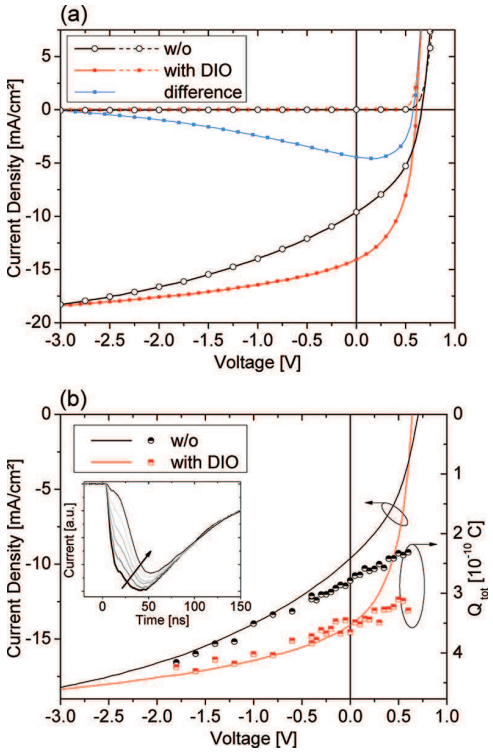

Figure 2. (a) $J-V$ characteristics measured under AM 1.5G at 100 mW/cm^2 from blends of PCPDTBT/$PC_{70}BM$ processed with (red) and without DIO (black). Also shown are the corresponding dark currents (dashed lines + symbols) and the difference in the current under illumination (blue line) between the two blends. (b) Left scale: photocurrent for blends with (red) and without (black) DIO. Right scale: total amount of extracted charge for blends with (red) and without (black) DIO as a function prebias during excitation. Transients were recorded with a delay time of 10 ns and a pulse fluence of 0.2 $\mu J/cm^2$. The inset shows the corresponding TDCF transients for blends with additive and V_{pre} ranging from −0.4 to 0.6 V.

and higher intrachain and interchain order within the polymer aggregates.[6] Note that a higher crystallinity in the PCPDTBT phase of PCPDTBT/$PC_{70}BM$ blend layers processed with DIO has been shown by X-ray diffraction experiments.[10,27]

Figure 2a shows the solar cell characteristics measured under AM 1.5G at 100 mW/cm^2 and the corresponding dark currents for blends processed without and with DIO. For an active layer thickness of around 100 nm, the performance data without (with) the additive are J_{sc} = 9.6 (13.9) mA/cm^2, V_{oc}= 0.66 (0.61) V,

dx.doi.org/10.1021/jz3000849 | J. Phys. Chem. Lett. 2012, 3, 640−645

FF = 42 (54)%, and PCE = 2.6 (4.5)%. Thus, the main increase in performance stems from the higher J_{sc} and FF. The solid blue line shows the difference between the $J-V$ characteristics under illumination for devices processed with and without the additive. The difference has a maximum at around 0.2 V and vanishes at approximately −3 V, meaning that approximately the same photogenerated charge is collected at the electrodes at high negative bias under AM1.5 illumination.[17]

To address a possible field dependence of free carrier formation, we performed TDCF experiments with variable prebias (between −2 and 0.6 V) and a very short delay of 10 ns before application of the collection bias (V_{coll} = −3 V). The short delay time was chosen to prevent any losses due to non-geminate recombination prior to the rapid extraction of carriers under the strong collection field. M. A. Loi and co-workers recently studied the steady-state and transient fluorescence properties of PCPDTBT/$PC_{70}BM$ blends processed without the additive. These measurements revealed a bias-independent CT exciton lifetime of 480 ps.[15] Their study also suggested that the formation of such emissive CT excitons proceeds via a weakly bound PP precursor state, which sets the upper limit for the PP lifetime to below 1 ns. This finding was confirmed by recent transient absorption measurements by F. Laquai and co-workers on blends processed with or without additive (unpublished results). These experiments showed a fast subnanosecond decay of strongly bound CT states with lifetimes similar to those reported by M. A. Loi. In addition, blends prepared without the additive displayed a decay component on the time scale of several nanoseconds, which was attributed to the recombination of loosely bound (or spatially trapped) PPs. Therefore, if field-assisted split up of bound PPs is involved in free carrier formation, this process shall be essentially completed before application of the collection bias 10 ns after photoexcitation. In other words, the amount of charge extracted by the electrodes at short t_d and different prebias settings is a direct measure of the field dependence of free carrier formation.

Figure 2b plots the total amount of collected charge Q_{tot} (defined as the integral over the entire current transient) for different values of V_{pre} for devices processed with and without DIO. These measurements were performed with a wavelength of identical absorption for both blends (see Figure S1b, SI). Note that Q_{tot} is the total photogenerated charge that survives geminate and non-geminate recombination and is extracted by the electrodes in the course of the experiment at the specific settings of t_d and V_{pre}.[21] Two particularities can be attained from these experiments. First, the total extracted charge increases with increasing internal field for both blends, indicative of a field-assisted formation of free charges via bound PPs. This finding is in agreement with results presented by Jarzab et al. showing reduced geminate recombination in PCPDTBT/PCBM blends as the field is increased.[15] Second, the field dependence of generation is stronger for blends without the additive. As a consequence, the efficiency for free carrier generation at short-circuit conditions is substantially larger with the additive, meaning that geminate recombination is suppressed more strongly in the DIO-processed blends. Our finding of a field-dependent efficiency for free carrier formation is at variance with the results from TAS experiments performed in the Durrant group described above. These TAS experiments were performed at a much higher fluence of 8 $\mu J/cm^2$, and the probe pulse was delayed by, at minimum, 50 ns. According to our measurements, such high excitation densities lead to severe non-geminate recombination losses even for very short delay (see, e.g., Figures S2 and S4, SI).

Interestingly, the field dependence of the free charge generation efficiency expressed by Q_{tot} agrees well with the course of the photocurrent characteristics for both blends at negative bias and explains the overall higher steady-state photocurrents of the DIO-processed device (see Figures 2b and S3, SI). At high reverse bias, the free carrier generation efficiency becomes identical for both blends, which is the reason why both photocurrent characteristics merge at negative voltages. Strong derivations are, however, measured when the bias approaches open-circuit conditions, which we attribute to losses by non-geminate recombination. These derivations are more pronounced, and they become obvious at a more negative bias for devices processed without DIO, meaning that non-geminate recombination losses largely determine the photovoltaic properties of these blends at solar cell working conditions.

To address the kinetics of non-geminate recombination, we performed experiments with increasing time delay t_d (in steps of Δt) between the generation and collection of charge carriers. Integration of the transients during delay and during collection yielded the quantities $Q_{pre}(t_d)$ and $Q_{coll}(t_d)$, respectively, with $Q_{tot}(t_d) = Q_{pre}(t_d) + Q_{coll}(t_d)$. Figure 3 shows the

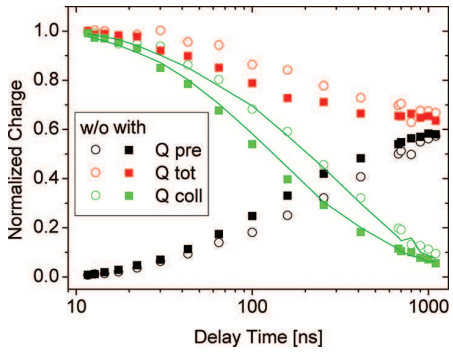

Figure 3. Values for $Q_{pre}(t_d)$, $Q_{coll}(t_d)$, and $Q_{tot}(t_d)$ as determined from TDCF transients recorded for a prebias of 0.3 V as a function of delay time for blends with (filled symbols) and without (open symbols) DIO and corresponding BMR fits (solid lines) according to eq S1 in the SI. The values are normalized to the initially generated charge.

dependence of these quantities as a function of delay time for blends processed without and with the additive for V_{pre} set to 0.3 V. The increase of Q_{pre} with t_d is due to field-induced extraction of photogenerated carriers at pre-bias conditions, leaving less charge available when the collection bias is switched on. Clearly, extraction is more rapid in blends with DIO, leaving fewer charge carriers in the device after a certain delay to recombine. This confirms that the morphology of the blend processed with the additive enables faster extraction of photogenerated charge carriers.

For both blends, a decrease of the total extracted charge is seen already for short delay times of a few tens of nanoseconds, indicating efficient non-geminate recombination. As shown in Figure S4 (SI), a weak decay of Q_{tot} with delay time is observed even for V_{pre} = 0 V, meaning that losses due to free carrier recombination cannot be neglected at short-circuit conditions. This is in accordance with the results by Li et al., providing evidence that the photocurrent is hampered by extraction.[16]

All data sets of $Q_{pre}(t_d)$ and $Q_{coll}(t_d)$ have been analyzed by an iterative scheme described in the SI to yield the kinetics

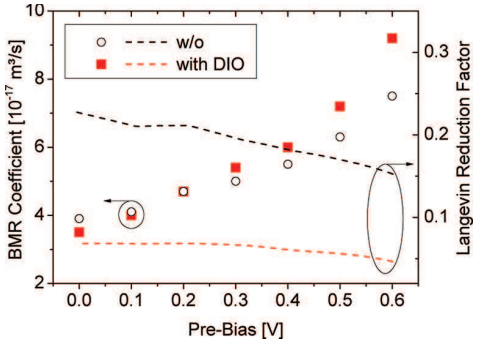

Figure 4. Left scale: BMR coefficient γ_{BMR} for blends with (red filled squares) and without (black open circles) additive, estimated from the fits of TDCF transients with variable delay times between the laser pulse and collection bias to eq S1 (SI) for different prebias. The excitation fluence was 0.5 μJ/cm^2. The corresponding fits can be found in Figure S4 (SI). Right scale: Langevin reduction factor $\zeta(F)$ for blends with (red dashed line) and without (black dashed line) DIO, estimated from the measured field dependence of mobility.

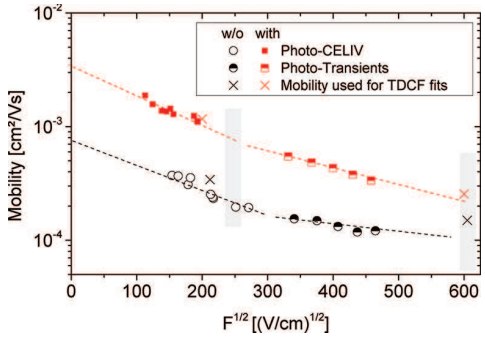

Figure 5. Field-dependent mobilities determined from photo-CELIV (full or open symbols) and TDCF (half-filled symbols) measurements covering a wide range of electrical field on blends processed with (red) or without the additive (black). The dashed lines are guides to the eyes. The gray areas indicate the fields at J_{sc} and extraction at −3 V. The crosses show relaxed electron mobilities at the corresponding fields of 0.2 and −3 V, which gave the best fit to complete TDCF transients with a drift diffusion model in Figure S5 (SI).

of non-geminate recombination (see Figure S4 (SI) for further data and fits). Interestingly, excellent fit to the data was possible when assuming BMR. The BMR coefficients γ_{BMR} extracted from these fits are plotted in Figure 4 parameterized in V_{pre}. The values for both blends are rather high, ranging from 3.5 to 9.2×10^{-17} m^3/s at short and open circuit, respectively. This is more than 1 order of magnitude higher than BMR coefficients measured with TDCF on the annealed P3HT/PCBM system,[21] meaning that non-geminate recombination is very fast in the PCPDTBT/PC$_{70}$BM blend. Interestingly, the absolute value of the coefficient is not altered by the additive. The overall BMR coefficients reported here are higher than those determined by quasi-steady-state TPV measurements when the charge carrier density is set to 5×10^{16} cm^{-3} for both blends.[10] We assume that initially created "hot" charge carriers have a slightly higher mobility and, therefore, a higher recombination rate compared to that of energetically relaxed charge carriers as measured by TPV.

Notably, the BMR coefficient increases with prebias by a factor of 3 when approaching V_{oc}. As the BMR coefficient is linearly proportional to the drift mobility of electrons and holes, we have determined its field dependence by analyzing photo-CELIV and TDCF transients. The effective field in the photo-CELIV experiments was varied by changing the slope of the voltage ramp, which started 2 μs after the laser pulse. Mobilities were determined by the analysis of the photo-CELIV transients according to Bange et al.[24] No change in the mobility values was seen when varying the delay time between the laser pulse and voltage ramping between 0.1 and 2 μs, ruling out a pronounced mobility relaxation at times larger than 100 ns after photoexcitation. For the TDCF measurements, the delay time was set to 100 ns, and the collection voltage was varied from 0.5 to 1.5 V. A lower collection bias caused strong non-geminate recombination during collection, while photocurrent decays at higher biases were limited by the RC time of the setup. Mobility values have been derived from the initial slopes of the photocurrent decays. Flat band was assumed to be at the bias V_0 of zero photocurrent, which is 20−30 mV higher than V_{oc}.[17] The so-obtained mobilities are plotted in Figure 5. It was recently shown that the electron mobility in PCPDTBT/PCBM blends is higher than the hole mobility.[20] Therefore, we assume that the mobilities shown in Figure 5 correspond to electron mobilities. First, the mobility is seen to be three to four times higher with the additive. Second, both blends show a strong negative dependence on electric field, as is characteristic for materials with high spatial disorder.[28] Mobilities with a negative field dependence have occasionally been observed in TOF or CELIV experiments on high mobility materials.[29,30] Note that space charge limited current (SCLC) measurements on PCPDTBT/PCBM blends processed without the additive were modeled with a mobility that increased with bias (and carrier density).[20] These unipolar current measurements analyze the flow of charges injected via ohmic contacts at forward bias in the dark. It has been shown recently that the density of injected carriers at bias voltages larger than V_{oc} might well exceed the photogenerated charge carrier density created under solar cell illumination conditions.[31] Therefore, mobilities extracted from SCLC measurements should be used with care when interpreting the field dependence of extraction and recombination of photogenerated carriers at voltages below flat band conditions. Drift−diffusion simulations of entire TDCF transients were performed to verify the mobility values and the negative field dependence recorded in our measurements. Exemplary fits are shown in Figure S5 (SI) for a prebias of 0.2 V, a collection bias of −3 V, and four different delay times. Values for the BMR coefficient at the corresponding fields were taken from Figure 5. Best fits were obtained with electron mobilities comparable or slightly higher than the ones plotted in Figure 5 and using hole mobilities that were 2−3 times smaller than the electron mobilities. The fit to the initial rise and decay of the TDCF transients could be considerably improved by considering a modest mobility relaxation[28,32] within the first 50 ns. The agreement between the simulated and measured transients is excellent, considering that the delay time was varied over a wide range from 10 to 400 ns.

We propose that the negative field dependence of electron and hole mobility is the main cause for the increase in the BMR coefficient with decreasing internal field (increasing device bias). This is demonstrated by the field dependence of the measured Langevin reduction factor $\zeta(F) = \gamma_{BMR}(F)/\gamma_L(F)$, with $\gamma_L = e(\mu_e(F) + \mu_h(F))/\varepsilon_o\varepsilon_r$ the Langevin-type three-dimensional recombination coefficient. As shown in Figure 4, $\zeta(F)$ changes only gradually with bias, meaning that the field

dx.doi.org/10.1021/jz3000849 | J. Phys. Chem. Lett. 2012, 3, 640−645

dependence of the BMR coefficient is mainly caused by field-dependent mobilities. In the calculation, electron mobilities were taken from Figure 5, and hole mobilities were derived from the TDCF transient fits, with an identical field dependence as that for electrons. Note that $\zeta(F)$ is ~3 times lower for devices processed with the additive, meaning that the formation of phase-separated domains of rather pure components slows down BMR.

It was pointed out that a pronounced dependence of the mobility on charge carrier density might cause an increase of the BMR coefficient when approximating open-circuit conditions.[23] With decreasing internal field, the overall carrier density becomes higher due to slower extraction of the photogenerated charge. However, charge-density-dependent mobility measurements with photo-CELIV and cw backlight illumination (data not shown) did not show a significant increase in mobility up to 1 sun illumination conditions in our blends. We also performed TDCF experiments with the pulsed excitation density ranging from 0.2 to 0.5 $\mu J/cm^2$. In this range, the BMR coefficient was not significantly altered by the pulsed intensity. We, therefore, conclude that carrier mobilities and, with that, non-geminate recombination coefficients in our PCPDTBT/PCBM blends exhibit an only modest dependence on carrier concentration at solar cell working conditions.

In summary, we have performed measurements of the charge carrier dynamics in solar cells composed of 1:3 blends of PCPDTBT/$PC_{70}BM$ processed with and without the additive DIO utilizing the techniques of TDCF and photo-CELIV. In contrast to the well-known P3HT/PCBM system, we found that the generation of charge carriers is field-dependent in PCPDTBT/$PC_{70}BM$ blends, with the dependence being stronger without the additive. The BMR coefficient increases from 3 to 9×10^{-17} m^3/s when the internal field decreases from short- to open-circuit conditions. The coefficient by itself is not altered by the additive when compared at the same bias. Compared to P3HT/PCBM, the BMR coefficient and also the Langevin reduction factor is 1 order of magnitude higher in PCPDTBT/$PC_{70}BM$ blends. The additive speeds up the extraction of charge carriers, which is rationalized by the three-fold increase in mobility in the blends with DIO. Blends processed with and without DIO exhibit a strong negative field dependence of mobility, which is proposed to cause the observed increase in the BMR coefficient when approaching open-circuit conditions. All together, the improvement in charge carrier generation and extraction is identified to cause the two-fold increase in performance when using the additive. The overall moderate performance of the PCPDTBT blends, even when processed with DIO, is proposed to arise from the field-dependent generation of free carriers and the rather high recombination coefficients, which even increase at low internal fields.

■ ASSOCIATED CONTENT

Supporting Information

Details on sample fabrication and measurement techniques, electron energy loss spectra, and thin film absorption, Q_{tot} and EQEs from TDCF measurements with different pulse fluences, comparison of ratios (steady-state current versus total extracted charge) between the two blends, Q_{tot}, Q_{pre}, and Q_{coll} for different delay times at 0.0, 0.3, and 0.6 V prebias together with the corresponding BMR fits, and drift diffusion fits to TDCF transients for different delay times. This material is available free of charge via the Internet at http://pubs.acs.org.

■ AUTHOR INFORMATION

Corresponding Author

*E-mail: neher@uni-potsdam.de.

Notes

The authors declare no competing financial interest.

■ ACKNOWLEDGMENTS

S.A. acknowledges Marcel Schubert and Sebastian Bange for fruitful discussions. W.S. acknowledges Markus Wollgarten for the cowork with the TEM data. This work was funded by the Bundesministerium für Bildung und Forschung (BMBF) within the PVcomB (FKZ 03IS2151D) and the SOHyb (FKZ 03X3525A) Project.

■ REFERENCES

(1) Service, R. F. Outlook Brightens for Plastic Solar Cells. *Science* **2011**, *332*, 293−293.

(2) Chu, T.-Y.; Lu, J.; Beaupré, S.; Zhang, Y.; Pouliot, J.-R. m.; Wakim, S.; Zhou, J.; Leclerc, M.; Li, Z.; Ding, J.; et al. Bulk Heterojunction Solar Cells Using Thieno[3,4-*c*]pyrrole-4,6-dione and Dithieno[3,2-*b*:2′,3′-*d*]silole Copolymer with a Power Conversion Efficiency of 7.3%. *J. Am. Chem. Soc.* **2011**, *133*, 4250−4253.

(3) Mühlbacher, D.; Scharber, M.; Morana, M.; Zhu, Z.; Waller, D.; Gaudiana, R.; Brabec, C. High Photovoltaic Performance of a Low-Bandgap Polymer. *Adv. Mater.* **2006**, *18*, 2884−2889.

(4) Amb, C. M.; Chen, S.; Graham, K. R.; Subbiah, J.; Small, C. E.; So, F.; Reynolds, J. R. Dithienogermole As a Fused Electron Donor in Bulk Heterojunction Solar Cells. *J. Am. Chem. Soc.* **2011**, *133*, 10062−10065.

(5) Liang, Y. Y.; Xu, Z.; Xia, J. B.; Tsai, S. T.; Wu, Y.; Li, G.; Ray, C.; Yu, L. P. For the Bright Future-Bulk Heterojunction Polymer Solar Cells with Power Conversion Efficiency of 7.4%. *Adv. Mater.* **2010**, *22*, E135−E138.

(6) Peet, J.; Kim, J. Y.; Coates, N. E.; Ma, W. L.; Moses, D.; Heeger, A. J.; Bazan, G. C. Efficiency Enhancement in Low-Bandgap Polymer Solar Cells by Processing with Alkane Dithiols. *Nat. Mater.* **2007**, *6*, 497−500.

(7) Price, S. C.; Stuart, A. C.; Yang, L.; Zhou, H.; You, W. Fluorine Substituted Conjugated Polymer of Medium Band Gap Yields 7% Efficiency in Polymer−Fullerene Solar Cells. *J. Am. Chem. Soc.* **2011**, *133*, 4625−4631.

(8) Lee, J. K.; Ma, W. L.; Brabec, C. J.; Yuen, J.; Moon, J. S.; Kim, J. Y.; Lee, K.; Bazan, G. C.; Heeger, A. J. Processing Additives for Improved Efficiency from Bulk Heterojunction Solar Cells. *J. Am. Chem. Soc.* **2008**, *130*, 3619−3623.

(9) Sun, Y.; Takacs, C. J.; Cowan, S. R.; Seo, J. H.; Gong, X.; Roy, A.; Heeger, A. J. Efficient, Air-Stable Bulk Heterojunction Polymer Solar Cells Using MoOx as the Anode Interfacial Layer. *Adv. Mater.* **2011**, *23*, 2226−2230.

(10) Agostinelli, T.; Ferenczi, T. A. M.; Pires, E.; Foster, S.; Maurano, A.; Müller, C.; Ballantyne, A.; Hampton, M.; Lilliu, S.; Campoy-Quiles, M.; et al. The Role of Alkane Dithiols in Controlling Polymer Crystallization in Small Band Gap Polymer:Fullerene Solar Cells. *J. Polym. Sci., Part B: Polym. Phys.* **2011**, *49*, 717−724.

(11) Cho, S.; Lee, J. K.; Moon, J. S.; Yuen, J.; Lee, K.; Heeger, A. J. Bulk Heterojunction Bipolar Field-Effect Transistors Processed with Alkane Dithiol. *Org. Electron.* **2008**, *9*, 1107−1111.

(12) Clarke, T.; Ballantyne, A.; Jamieson, F.; Brabec, C.; Nelson, J.; Durrant, J. Transient Absorption Spectroscopy of Charge Photogeneration Yields and Lifetimes in a Low Bandgap Polymer/Fullerene Film. *Chem. Commun.* **2009**, 89−91.

(13) Hwang, I. W.; Cho, S.; Kim, J. Y.; Lee, K.; Coates, N. E.; Moses, D.; Heeger, A. J. Carrier Generation and Transport in Bulk Heterojunction Films Processed with 1,8-Octanedithiol As a Processing Additive. *J. Appl. Phys.* **2008**, *104*, 9.

(14) Jamieson, F. C.; Agostinelli, T.; Azimi, H.; Nelson, J.; Durrant, J. R. Field-Independent Charge Photogeneration in PCPDTBT/PC(70)BM Solar Cells. *J. Phys. Chem. Lett.* **2010**, *1*, 3306−3310.
(15) Jarzab, D.; Cordella, F.; Gao, J.; Scharber, M.; Egelhaaf, H.-J.; Loi, M. A. Low-Temperature Behaviour of Charge Transfer Excitons in Narrow-Bandgap Polymer-Based Bulk Heterojunctions. *Adv. Energy Mater.* **2011**, *1*, 604−609.
(16) Li, Z.; McNeill, C. R. Transient Photocurrent Measurements of PCDTBT:PC(70)BM and PCPDTBT:PC(70)BM Solar Cells: Evidence for Charge Trapping in Efficient Polymer/Fullerene Blends. *J. Appl. Phys.* **2011**, *109*.
(17) Moet, D. J. D.; Lenes, M.; Morana, M.; Azimi, H.; Brabec, C. J.; Blom, P. W. M. Enhanced Dissociation of Charge-Transfer States in Narrow Band Gap Polymer:Fullerene Solar Cells Processed with 1,8-Octanedithiol. *Appl. Phys. Lett.* **2010**, *96*, 213506.
(18) Nuzzo, D. D.; Aguirre, A.; Shahid, M.; Gevaerts, V. S.; Meskers, S. C. J.; Janssen, R. A. J. Improved Film Morphology Reduces Charge Carrier Recombination into the Triplet Excited State in a Small Bandgap Polymer-Fullerene Photovoltaic Cell. *Adv. Mater.* **2010**, *22*, 4321−4.
(19) Scharber, M. C.; Lungenschmied, C.; Egelhaaf, H.-J.; Matt, G.; Bednorz, M.; Fromherz, T.; Gao, J.; Jarzab, D.; Loi, M. A. Charge Transfer Excitons in Low Band Gap Polymer Based Solar Cells and the Role of Processing Additives. *Energy Environ. Sci.* **2011**, *4*, 5077−5083.
(20) Lenes, M.; Morana, M.; Brabec, C. J.; Blom, P. W. M. Recombination-Limited Photocurrents in Low Bandgap Polymer/Fullerene Solar Cells. *Adv. Funct. Mater.* **2009**, *19*, 1106−1111.
(21) Kniepert, J.; Schubert, M.; Blakesley, J. C.; Neher, D. Photogeneration and Recombination in P3HT/PCBM Solar Cells Probed by Time-Delayed Collection Field Experiments. *J. Phys. Chem. Lett.* **2011**, *2*, 700−705.
(22) Popovic, Z. D. A Study of Carrier Generation Mechanism in X-Metal-Free Phthalocyanine. *J. Chem. Phys.* **1983**, *78*, 1552−1558.
(23) Maurano, A.; Hamilton, R.; Shuttle, C. G.; Ballantyne, A. M.; Nelson, J.; O'Regan, B.; Zhang, W.; McCulloch, I.; Azimi, H.; Morana, M.; et al. Recombination Dynamics as a Key Determinant of Open Circuit Voltage in Organic Bulk Heterojunction Solar Cells: A Comparison of Four Different Donor Polymers. *Adv. Mater.* **2010**, *22*, 4987−4992.
(24) Bange, S.; Schubert, M.; Neher, D. Charge Mobility Determination by Current Extraction under Linear Increasing Voltages: Case of Nonequilibrium Charges and Field-Dependent Mobilities. *Phys. Rev. B* **2010**, *81*, 035209.
(25) Cowan, S. R.; Street, R. A.; Cho, S. N.; Heeger, A. J. Transient Photoconductivity in Polymer Bulk Heterojunction Solar Cells: Competition between Sweep-out and Recombination. *Phys. Rev. B* **2011**, *83*, 8.
(26) Pfannmoeller, M.; Fluegge, H.; Benner, G.; Wacker, I.; Sommer, C.; Hanselmann, M.; Schmale, S.; Schmidt, H.; Hamprecht, F. A.; Rabe, T.; et al. Visualizing a Homogeneous Blend in Bulk Heterojunction Polymer Solar Cells by Analytical Electron Microscopy. *Nano Lett.* **2011**, *11*, 3099−3107.
(27) Rogers, J. T.; Schmidt, K.; Toney, M. F.; Kramer, E. J.; Bazan, G. C. Structural Order in Bulk Heterojunction Films Prepared with Solvent Additives. *Adv. Mater.* **2011**, *23*, 2284−2288.
(28) Bässler, H. Charge Transport in Disordered Organic Photoconductors — A Monte-Carlo Simulation Study. *Phys. Status Solidi B* **1993**, *175*, 15−56.
(29) Bange, S.; Kuksov, A.; Neher, D.; Vollmer, A.; Koch, N.; Ludemann, A.; Heun, S. the Role of Poly(3,4-Ethylenedioxythiophene):Poly(Styrenesulphonate) As a Hole Injection Layer in a Blue-Emitting Polymer Light-Emitting Diode. *J. Appl. Phys.* **2008**, *104*, 104506.
(30) Mozer, A. J.; Sariciftci, N. S.; Pivrikas, A.; Osterbacka, R.; Juska, G.; Brassat, L.; Bassler, H. Charge Carrier Mobility in Regioregular Poly(3-hexylthiophene) Probed by Transient Conductivity Techniques: A Comparative Study. *Phys. Rev. B* **2005**, *71*, 035214.
(31) Dibb, G. F. A.; Kirchartz, T.; Credgington, D.; Durrant, J. R.; Nelson, J. Analysis of the Relationship between Linearity of Corrected Photocurrent and the Order of Recombination in Organic Solar Cells. *J. Phys. Chem. Lett.* **2011**, *2*, 2407−2411.
(32) Chen, S.; Choudhury, K. R.; Subbiah, J.; Amb, C. M.; Reynolds, J. R.; So, F. Photo-Carrier Recombination in Polymer Solar Cells Based on P3HT and Silole-Based Copolymer. *Adv. Energy Mater.* **2011**, *1*, 963−969.

JACS
JOURNAL OF THE AMERICAN CHEMICAL SOCIETY

Article

pubs.acs.org/JACS

Fluorinated Copolymer PCPDTBT with Enhanced Open-Circuit Voltage and Reduced Recombination for Highly Efficient Polymer Solar Cells

Steve Albrecht,[†] Silvia Janietz,[‡] Wolfram Schindler,[§] Johannes Frisch,[⊥] Jona Kurpiers,[†] Juliane Kniepert,[†] Sahika Inal,[†] Patrick Pingel,[†] Konstantinos Fostiropoulos,[§] Norbert Koch,[§,⊥] and Dieter Neher*[,†]

[†]Institut für Physik und Astronomie, Universität Potsdam, Karl-Liebknecht-Strasse 24-25, 14476 Potsdam, Germany

[‡]Fraunhofer Institut für Angewandte Polymerforschung, Geiselbergstrasse 69, 14476 Potsdam, Germany

[§]Helmholtz-Zentrum Berlin für Materialien und Energie GmbH, Hahn-Meitner-Platz 1, 14109 Berlin, Germany

[⊥]Institut für Physik, Humboldt-Universität zu Berlin, Brook-Taylor-Strasse 6, 12489 Berlin, Germany

Supporting Information

ABSTRACT: A novel fluorinated copolymer (F-PCPDTBT) is introduced and shown to exhibit significantly higher power conversion efficiency in bulk heterojunction solar cells with $PC_{70}BM$ compared to the well-known low-band-gap polymer PCPDTBT. Fluorination lowers the polymer HOMO level, resulting in high open-circuit voltages well exceeding 0.7 V. Optical spectroscopy and morphological studies with energy-resolved transmission electron microscopy reveal that the fluorinated polymer aggregates more strongly in pristine and blended layers, with a smaller amount of additives needed to achieve optimum device performance. Time-delayed collection field and charge extraction by linearly increasing voltage are used to gain insight into the effect of fluorination on the field dependence of free charge-carrier generation and recombination. F-PCPDTBT is shown to exhibit a significantly weaker field dependence of free charge-carrier generation combined with an overall larger amount of free charges, meaning that geminate recombination is greatly reduced. Additionally, a 3-fold reduction in non-geminate recombination is measured compared to optimized PCPDTBT blends. As a consequence of reduced non-geminate recombination, the performance of optimized blends of fluorinated PCPDTBT with $PC_{70}BM$ is largely determined by the field dependence of free-carrier generation, and this field dependence is considerably weaker compared to that of blends comprising the non-fluorinated polymer. For these optimized blends, a short-circuit current of 14 mA/cm^2, an open-circuit voltage of 0.74 V, and a fill factor of 58% are achieved, giving a highest energy conversion efficiency of 6.16%. The superior device performance and the low band-gap render this new polymer highly promising for the construction of efficient polymer-based tandem solar cells.

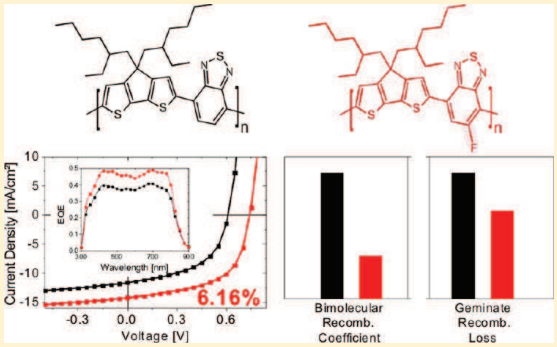

INTRODUCTION

A dramatic improvement in the efficiency of bulk heterojunction (BHJ) solar cells based on electron-donating conjugated polymers in combination with soluble fullerene derivatives has been achieved over the past 3 years. Certified power conversion efficiencies (PCEs) now reach 9% for single junctions and exceed the 10% benchmark for tandem solar cells.[1−3] This trend brightens the vision of organic photovoltaics becoming competitive with inorganic solar cells. Most such high-performance cells comprise donor−acceptor (DA) copolymers following the concept introduced by Wynberg and co-workers.[4] The introduction of adequate donor and acceptor units led to lower polymer highest molecular orbital (HOMO) energies for enhanced open-circuit voltage (V_{oc}) in blends with [6,6]-phenyl C_{70}-butyric acid methyl ester ($PC_{70}BM$).[5−8] In parallel, the copolymer band-gap was continuously reduced to improve matching of the polymer absorption with the sun spectrum, resulting in higher short-circuit currents (J_{sc}).[6,9,10] Control over the blend morphology has been achieved with the help of solvent additives.[6,10−13]

One of these copolymers is poly[2,6-(4,4-bis(2-ethylhexyl)-4*H*-cyclopenta[2,1-b;3,4-b′]dithiophene)-*alt*-4,7-(2,1,3-benzothiadiazole)] (PCPDTBT),[14] and its silicon- and germanium-bridged derivatives, PSBTBT[15,16] and PGe1-EH,[17] respectively. These polymers have low band-gaps of around 1.45 eV. Blends with $PC_{70}BM$ exhibit high external quantum efficiencies throughout the entire visible spectrum extending up to 800 nm, resulting in one of the highest J_{sc} values yet reported for BHJ single-junction cells[9,18] and PCEs of 4.5−5.5% for

Received: May 24, 2012
Published: August 6, 2012

ACS Publications © 2012 American Chemical Society

PCPDTBT.[11,12] PCPDTBT and PSBTBT have also been used to form the red- to near-infrared-absorbing subcell in state-of-the-art polymer tandem solar cells.[19,20] A major drawback of PCPDTBT in blends with $PC_{70}BM$ is the moderate fill factor (FF), caused by strong non-geminate recombination and a significantly field-dependent generation of free charge-carriers.[21−23] Also, the V_{oc} is only moderate due to the high-lying HOMO level of PCPDTBT. Thus, further improvement of the PCE requires that both the V_{oc} and the FF can be enlarged without deteriorating the favorable optical properties and high internal quantum efficiencies of these polymer blends.

Recently, the V_{oc} of blend devices comprising PCPDTBT or PSBTBT was increased by altering the chemical nature of the electron deficient unit of these DA copolymers. These alterations were motivated by the work of Blouin et al., who showed that replacing the 2,1,3-benzothiadiazole (BT) unit by 2,1,3-benzoxadiazole (BO) simultaneously lowers the HOMO and LUMO energy.[24] Hoven et al. designed a PSBTBO polymer with slightly larger V_{oc} compared to PSBTBT.[25] The overall performance, however, was limited to below 5% due to a lower FF and J_{sc}, and no overall improvement was achieved by replacing the BT with the BO unit. Also Bijleveld et al. synthesized a variety of PCPDT-X polymers.[26] They found a superior performance of PCPDTBO against PCPDTBT due to a higher open V_{oc} and higher FF, resulting in a PCE of 2.5% vs 1.9%, respectively. Again, the J_{sc} and the EQE in the near-IR were lower with BO, and no attempt was made to optimize the blend morphology with solvent additives.

An alternative strategy to improve the V_{oc} is to attach fluorine atoms to the electron-deficient subunits of low-band-gap DA copolymers.[5,27,28] It was shown that this approach simultaneously lowers the HOMO and LUMO level energies, while having no or only minor effect on the optical band-gap.[5,7,29,30] Accordingly, BHJ solar cells comprising these fluorinated copolymers in combination with electron-accepting soluble fullerenes exhibited higher V_{oc} than blends with the corresponding non-fluorinated derivatives.[5,7,27,30−32] Surprisingly, fluorination also improved the J_{sc} values[5,7,30,31,33] and the FFs.[5,7,30−34] These improvements have been explained by high hole mobilities and/or a specific phase-separated morphology of such blends.

In this work, we describe the synthesis and characterization of a novel polymer, poly[2,6-(4,4-bis(2-ethylhexyl)-4*H*-cyclopenta[2,1-b;3,4-b′]dithiophene)-*alt*-4,7-(5-fluoro-2,1,3-benzothiadiazole)] (F-PCPDTBT), formed by the attachment of fluorine to the BT unit of PCPDTBT. Fluorinated benzothiadiazole was first introduced by Li et al. as a new electron-deficient unit in DA copolymers.[33] Due to the strong impact of molecular weight (MW) on solar cell performance,[9,11,12] the polymers PCPDTBT and F-PCPDTBT were synthesized with equivalent MW and compared in blends with $PC_{70}BM$ with regard to solar cell performance and charge-carrier dynamics. Using the techniques of time-delayed collection field (TDCF) and photocharge extraction by linearly increasing voltage (photo-CELIV), conclusive information on the field dependence of charge-carrier generation and non-geminate recombination as well as on transport properties was derived. Plasmon mapping based on energy-filtered transmission electron microscopy (TEM) and ultraviolet photoelectron spectroscopy (UPS) was applied to study the impact of fluorination on the morphology and electronic structure of the blend.

The new polymer F-PCPDTBT shows a lower-lying HOMO level, resulting in a major increase of the V_{oc} to 0.74 V in additive-optimized blends compared to 0.61 V for PCPDTBT. More importantly, the FF and J_{sc} increase from 50% to 59% and from 11.5 to 13.8 mA/cm^2, respectively, which is explained by reduced geminate and non-geminate recombination. In total, fluorination improves the PCE from 3.6% to 6.0% for equivalent MW and preparation conditions. Further optimization of the blend ratio and active layer thickness lead to a PCE of 6.16% for F-PCPDTBT:$PC_{70}BM$ blends. We note that this is below the efficiencies of state-of-the-art single-junction solar cells reported for other polymer:fullerene blends.[6−8,10,35] However, the large V_{oc} in combination with a high quantum efficiency in the near-IR makes F-PCPDTBT extremely attractive for application in polymer tandem solar cells. Published record values for such devices are currently around 8.6%, using the polymer PBDTT-DPP. The extended absorption range and the superior EQE of F-PCPDTBT-based blends compared to the currently best-performing PBDTT-DPP polymer may allow considerable improvement of the overall tandem device performance.[3]

SYNTHESIS

The alternating copolymers poly[2,6-(4,4-bis(2-ethylhexyl)-4*H*-cyclopenta[2,1-b;3,4-b′]dithiophene)-*alt*-4,7-(2,1,3-benzothiadiazole)] (**PCPDTBT**), here referred to as **P−H**) and poly[2,6-(4,4-bis(2-ethylhexyl)-4*H*-cyclopenta[2,1-b;3,4-b′]dithiophene)-*alt*-4,7-(5-fluoro-2,1,3-benzothiadiazole] (**F-PCPDTBT**, here referred to as **P−F**) were synthesized by microwave-assisted Stille cross-coupling polymerization[9] as outlined in Scheme 1. The preparations of the bis-

Scheme 1. Synthesis of PCPDTBT (P−H) from Monomers 1 and 2 and F-PCPDTBT (P−F) from Monomers 1 and 3

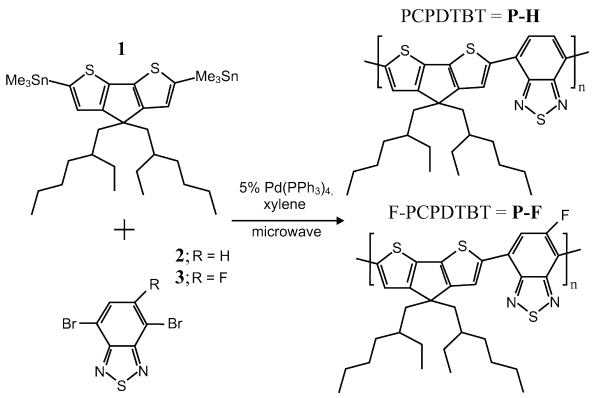

stannylated cyclopentadithiophene[14,36] (**1**) and the 4,7-dibromo-2,1,3-benzothiadiazole[36,37] (**2**) were adapted from literature procedures. The 4,7-dibromo-5-fluoro-2,1,3-benzothiadiazole (**3**) was synthesized starting from 4-fluoro-1,2-phenylenediamine. The ring-closure reaction was done with thionyl chloride, following a bromination with HBr and bromine which is described in the Supporting Information (SI). A stoichiometric ratio of 1:1.15 was applied for the microwave polymerization reaction. The number-average molecular weight (M_n) is around 10 kg/mol with a polydispersity of 2 for both polymers (**P−H** and **P−F**) as determined by high-temperature gel permeation chromatography (GPC) at 135 °C in trichlorobenzene (see Table 1). The attachment of fluorine to the BT unit leads to a more rigid polymer backbone, which reduces its solubility in organic solvents. Differential scanning calorimetry (DSC) measurements did not show any transition peaks for both polymers in temperature range between 0

Table 1. Characterization of the Polymers P−H and P−F Together with Optical, Transport, and Electronic Properties

	yield [%]	M_n[a] [g/mol]	PDI[b]	λ_{max}[c] [nm]	α_{max}[d] [cm^{-1}]	λ_{onset}[e] [nm]	Eg_{opt}[e] [eV]	IE[f] [eV]	$\mu_{h\ FET}$[g] [$cm^2/(V{\cdot}s)$]	$\mu_{h\ SCLC}$[h] [$cm^2/(V{\cdot}s)$]
P−H	51	10 950	2.09	742	1.67×10^5	855	1.451	5.25	1.4×10^{-3}	1.0×10^{-4}
P−F	67	10 128	2.13	767	1.96×10^5	858	1.446	5.35	1.0×10^{-3}	0.6×10^{-4}

[a]Number-average molecular weight. [b]Polydispersity index. [c]Wavelength of maximum absorption in thin films (see SI). [d]Absorption coefficient deduced from thin-film absorption. [e]Determined by the onset of thin-film absorption, indicated by the arrows in Figure S5. [f]Data obtained from UPS measurements of pure polymer films on PEDOT:PSS substrates. [g]In-plane hole mobility measured with field effect transistors (see SI). [h]Vertical hole mobility deduced from space-charge-limited currents (see SI).

and 270 °C. Thermogravimetric analysis demonstrated high thermal stability of **P−F**, with only 1 wt % loss at 400 °C as shown in the SI.

ELECTRONIC PROPERTIES OF THE POLYMERS IN THE PRISTINE AND BLEND LAYERS

As reported for other DA copolymers, fluorination lowers the polymer ionization energy (IE) in both pristine and blend layers. Figure 1a,b shows the secondary electron cutoff and the

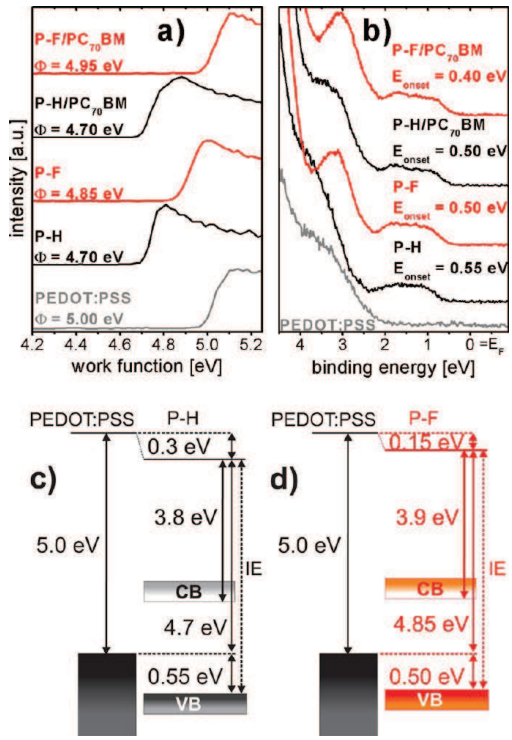

Figure 1. (a,b) Ultraviolet photoelectron spectra of ITO/PEDOT:PSS substrates covered with **P−H** (black) and **P−F** (red) and in additive optimized blends of **P−H**/$PC_{70}BM$ (black) and **P−F**/$PC_{70}BM$ (red): (a) the secondary electron cutoff and (b) the valence band region. Also shown is the energy level alignment diagram (with the IE shown as the dashed line) for ITO/PEDOT:PSS substrates covered with pristine (c) **P−H** and (d) **P−F**.

valence band (VB) region of pristine **P−H** and **P−F** films on PEDOT:PSS and of polymer/$PC_{70}BM$ blends processed with 3% diiodooctane (DIO) for **P−H** and 1% DIO for **P−F** (these concentrations were found to give optimum solar cell performance as outlined in detail below). The work function (Φ) of the PEDOT:PSS layer was 5.0 eV. Compared to the PEDOT:PSS covered substrate, Φ for the polymer-coated samples is smaller by 0.30 (**P−H**) and 0.15 eV (**P−F**). From the pristine polymer spectra the VB onset was found at 0.55 and 0.50 eV below the substrate Fermi energy (E_F) for **P−H** and **P−F**, respectively. Combining these data results in an IE of 5.25 eV for **P−H** and 5.35 eV for **P−F**, meaning that the position of the VB onset is 0.1 eV deeper with fluorination (see Figure 1c,d for the respective energy schemes). The position of the conduction band (CB) onset is estimated by setting the energetic difference between the CB and the VB onsets to the optical band-gab Eg_{opt} (see Table 1). Similar values for the IE compared to the pristine polymer films are obtained for polymer/$PC_{70}BM$ blend films ($IE_{P-H(blend)}$ = 5.20 eV and $IE_{P-F(blend)}$ = 5.35 eV). Assuming that there is no surface dipole layer formation between the polymer and the fullerene-rich domains, **P−F** has a 0.1 eV larger energetic offset between the VB onset of the polymer and the LUMO of $PC_{70}BM$ compared to **P−H**. Note that the UPS spectra of the blend films in the low binding energy region are dominated by features from the polymer, and no features attributed to the molecular levels of $PC_{70}BM$ are observed. We conclude that the topmost layer of the blend films consists only of the pristine polymers.

OPTICAL PROPERTIES OF PRISTINE POLYMER AND BLEND LAYERS

Non-normalized absorption spectra of **P−H**/$PC_{70}BM$ and **P−F**/$PC_{70}BM$ blend films with a thickness of 100 nm processed with different amounts of DIO are displayed in Figure 2. As has

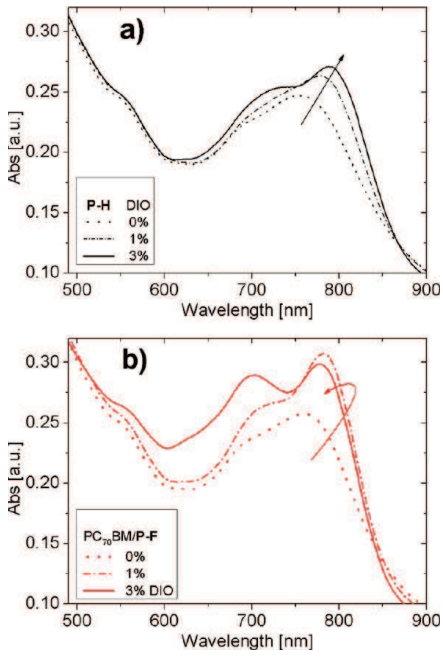

Figure 2. Absorption spectra (not normalized) from 100 nm thick films of polymers **P−H** (a) and **P−F** (b) blended with $PC_{70}BM$ in a 1:3 weight ratio processed without DIO (dots), with 1% DIO (dashed lines), and with 3% DIO (solid lines).

dx.doi.org/10.1021/ja305039j | J. Am. Chem. Soc. 2012, 134, 14932−14944

been reported before, adding DIO to **P−H**/$PC_{70}BM$ continuously increases the strength of the low-energy polymer absorption centered around 800 nm, which is explained by a higher degree of intra- and interchain ordering.[38] Recent in situ X-ray studies revealed that the solvent additive promotes the formation of polymer crystallites during prolonged film drying.[39] These effects are more pronounced for the **P−F**-based blends, with the long-wavelength peak dominating the spectra already at a DIO concentration of 1%, indicating a high tendency of the **P−F** chains to aggregate even in presence of $PC_{70}BM$. A higher tendency for chain aggregation is indicated in absorption spectra taken on the pristine polymers in solution and solid states, as shown in Figure S5 in the SI. Son et al. reported improved intermolecular order in pristine layers of fluorinated polythienothiophene-*co*-benzodithiophenes (PTBs).[32] It was proposed that the fluorinated polymers exhibit a more planar backbone conformation, allowing for a more regular packing in the solid state. The authors further suggested that intermolecular interaction might be enhanced upon F-attachment via the interaction of fluorinated electron-deficient units and electron-rich aromatic rings. Strong intermolecular interaction was proposed by Li et al. to cause a reduced stacking distance in pristine layers of fluorinated BDT:BT copolymers.[33] We also note the overall higher absorbance of blends with **P−F** for comparable thickness and processing conditions, which is particularly evident in the wavelength range dominated by the polymer. As this effect is seen also in the solution- and solid-state spectra of the pristine layers, we explain this feature on the basis of the higher absorption cross section of the fluorinated chains. Higher absorption coefficients of fluorinated DA copolymers in solution or solid state have been shown by others,[7,31] but a conclusive explanation for this enhancement is still missing. Peak positions and absorption coefficients for the pristine and the blend layers are summarized in Tables 1 and 2. As a combined effect of a higher absorption cross section and improved aggregation, blends comprising F-PCPDTBT exhibit higher solid-state absorption coefficients, especially in the red part of the spectrum. Note that the optical band-gap of the solid pristine polymers (determined by extrapolation of the linear decay of absorption around 810 nm to zero absorbance as indicated by the arrows in Figure S5) is almost unchanged upon fluorination, despite a 0.1 eV increase of the IE upon fluorination. This is in accordance with previous reports on other fluorinated DA copolymers.[5,7,33]

Table 2. Optical Characterization of Polymers P−H and P−F Blended with $PC_{70}BM$, Processed with Different Amounts of Additive

	DIO [%]	$\lambda_{max,1}$ [nm]	$\alpha_{max,1}$ [10^4 cm^{-1}]	$\lambda_{max,2}$[a] [nm]	$\alpha_{max,2}$[a] [10^4 cm^{-1}]
P−H	0	754	5.69	692	5.14
P−H	1	777	6.06	696	5.41
P−H	3	788	6.24	730	5.84
P−F	0	758	5.93	692	5.38
P−F	1	782	7.01	709	6.04
P−F	3	777	6.87	702	6.66

[a]This spectral feature appears as a shoulder in the spectra of the layers processed without DIO.

MORPHOLOGICAL PROPERTIES OF THE BLEND LAYERS

To analyze the effect of fluorination on the morphology of blends layers with $PC_{70}BM$, we performed plasmon mapping based on energy-filtered TEM.[40,41] For blends of materials with low degree of crystallinity, conventional TEM relies mainly on the mass density contrast. In contrast, the method employed here makes use of the different characteristic plasmon energies of the two active blend components to identify polymer- and fullerene-rich domains with high spatial resolution. Figure 3 shows the corresponding plasmon maps for both PCPDTBT and F-PCPDTBT-based blends processed with different amounts of DIO. These figures plot the energy of the maximum plasmon absorption for each lateral coordinate. Reference measurements on pristine layers showed that the energy of maximum plasmon absorption is 25.1 eV for pure $PC_{70}BM$, 22.4 eV for the pure **P−H**,[22] and 22.2 eV for **P−F**. Thus, the black areas in Figure 3 refer to $PC_{70}BM$-rich domains. For both **P−H** and **P−F**, the images show that the phase separation coarsens with increasing amount of the additive, which is in agreement with earlier studies on **P−H**-based blends using conventional TEM under defocusing conditions.[12,18]

To quantify the structural heterogeneity of the blends, the plasmon maps have been analyzed with regard to the mean areas of domains that are polymer- and PCBM-rich (with respect to the composition of a homogeneous 1:3 mixture of both components). These values are plotted in Table 3. Details of the analysis and histograms showing the number of pixels with a certain plasmon energy can be found in the SI. These data prove consistently that fluorination enforces the formation of more extended and purer polymer-rich phases. We attribute this to the stronger tendency of the F-PCPDTBT to aggregate, as outlined above. Noticeably, only 1% of DIO needs to be added to the **P−F**-based blend to induce a polymer-rich domain area as large as that in the optimized **P−H** blend processed with 3% DIO. Fluorination also affects the size and purity of the fullerene-rich domains, though this effect becomes less pronounced with increasing DIO concentration. Mean areas of the polymer and fullerene-rich domains are largest for the **P−F** blend processed with 3% DIO. It has been pointed out by Son et al. that fluorination of the donor polymer introduces fluorophobility for PCBM, enforcing phase separation between the donor and acceptor components in the blend layer.[32] Improved phase separation into purer and larger domains was also reported for blends of other fluorinated DA copolymers with PCBM.[30,33,34] Note that the domain areas listed in Table 3 have been deduced from TEM images which constitute 2D projections of the true 3D bulk morphology. Therefore, the analysis of such pictures underestimates the true domain area. In fact, PCPDTBT crystal sizes larger than 10 nm have been reported in DIO-processed **P−H** blends.[42,43]

BHJ SOLAR CELL CHARACTERISTICS

Figure 4a shows the steady-state solar cell characteristics measured under simulated AM 1.5G with 100 mW/cm^2 for the two polymers blended with $PC_{70}BM$ and processed with different amounts of DIO. The corresponding performance data are listed in Table 4. Values for **P−H**-based blends are lower than state-of-the-art reports with high-molecular-weight polymers[11,12,18] but compare well to efficiencies for blends with PCPDTBT of similar MW.[9] Upon fluorination V_{oc} is increased

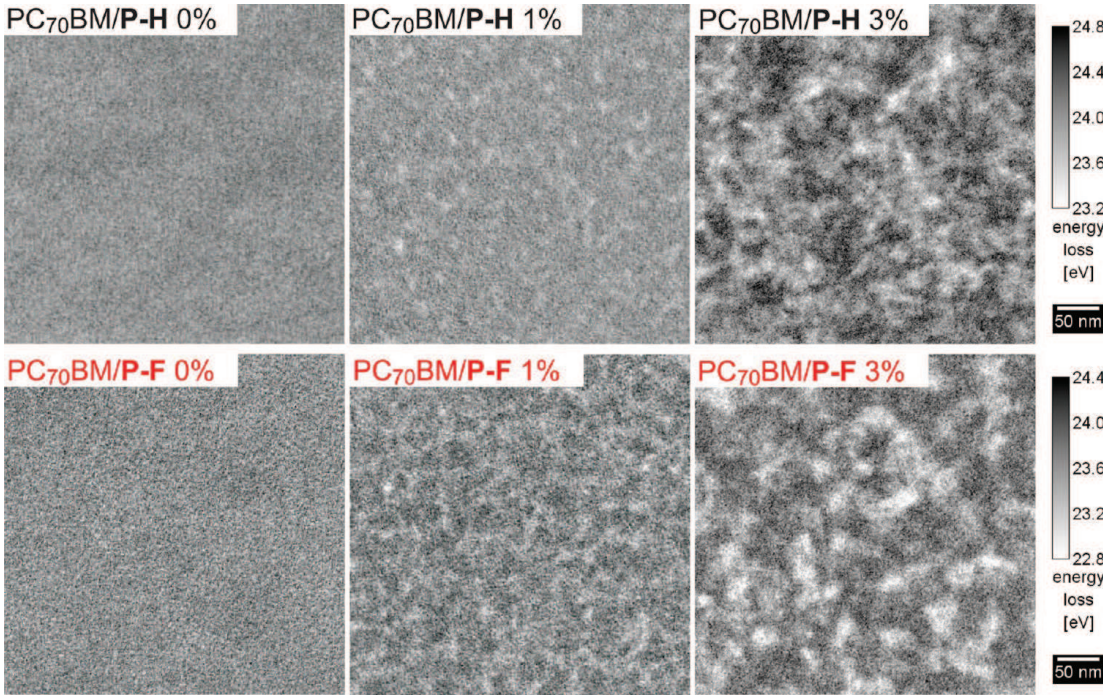

Figure 3. Plasmon mapping based on energy-filtered TEM of films made from blends of **P−H** (upper panel) and **P−F** (lower panel) with $PC_{70}BM$ at a 1:3 weight ratio and processed with different concentrations of DIO. The amount of DIO was 0, 1, and 3% for the images displayed in the left, middle, and right columns, respectively. The scale bar is the energy of maximum plasmon absorption (energy loss), where dark areas refer to $PC_{70}BM$-rich phases (see text and SI).

Table 3. Mean Area of the Domains Assigned to the Polymer- or PCBM-Rich Phase for P−H and P−F Blended with $PC_{70}BM$, Processed with Different Amounts of Additive

		domain area[a] [nm^2]	
	DIO [%]	polymer	$PC_{70}BM$
P−H	0	5[b]	9.9
P−H	1	8.4	21
P−H	3	13.9	47
P−F	0	11.5	16.2
P−F	1	14.7	28.3
P−F	3	18.2	50

[a]See SI for the details on the calculation of the domain area. [b]A domain area of 5 nm^2 is close to the size of one pixel (2 nm^2) in the plamon maps, meaning that within the resolution of the experiment the **P−H**:$PC_{70}BM$ blend processed without DIO is a homogeneous mixture of the two components.

by ~130 mV. Within the accuracy of the UPS measurement, the increase in V_{oc} corresponds well to the increase in polymer IE upon fluorine attachment, which is 100 meV for the pristine layer and 150 meV for the blend.

In accordance with the absorption and TEM data, the optimum amount of processing additive is reduced from 3% to 1% due to the stronger tendency of **P−F** to aggregate. Importantly, also the J_{sc} of the additive-optimized blend with **P−F** is significantly higher (13.8 mA/cm^2 for **P−F** with 1% DIO compared to 11.46 mA/cm^2 for **P−H** with 3% DIO). This higher current can be related to an enlarged EQE throughout the entire absorption range as shown in Figure 4b, approaching values of 50% between 400−500 and 700−800 nm. Note that the mean EQE of our optimized **P−F** blend is 10% larger compared to that of the optimized blend with **P−H** of almost

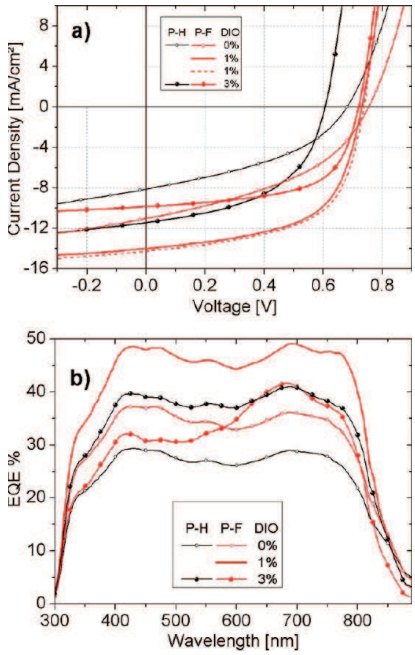

Figure 4. (a) Solar cell characteristics measured under simulated AM 1.5G irradiation with 100 mW/cm^2 (corrected for spectral mismatch) for 100 nm thick blends of **P−H** (black) and **P−F** (red) with $PC_{70}BM$ (1:3 ratio), processed without DIO (lines + open circles), with 1% DIO (solid lines), and with 3% DIO (lines + filled circles). The dashed line shows data for a **P−F**:$PC_{70}BM$ blend with an optimized blend ratio of 1:2.5, a DIO concentration of 1%, and a ca. 90 nm active layer thickness. (b) Corresponding external quantum efficiency spectra.

dx.doi.org/10.1021/ja305039j | J. Am. Chem. Soc. 2012, 134, 14932−14944

Table 4. Photovoltaic Properties and Characteristic Parameters Describing the Generation, Transport, and Recombination of the Polymers P−H and P−F in 1:3 Blends with $PC_{70}BM$

	DIO [%]	J_{sc}[a] [mA/cm^2]	V_{oc}[a] [mV]	FF[a] [%]	PCE[a] [%]
P−H	0	8.05	677	40.3	2.20
P−H	1	10.39	640	46.5	3.09
P−H	3	11.46	610	50.3	3.51 (3.59)
P−F	0	11.01	751	41.2	3.40
P−F	1	13.83	731	58.6 (59.6)	5.92 (5.98)
P−F[b]	1	14.08	740	58.0	6.04 (6.16)
P−F	3	9.85	722	60.3	4.28

[a]Data have been averaged over 6 devices; the performance of the best device is given in parentheses. Standard deviation of PCE was less than 0.06. [b]Optimized device with a blend ratio of 1:2.5 and an active layer thickness of ∼90 nm.

identical MW and still 5% larger than the mean EQE measured on blends with higher-MW **P−H**.[44] Optical simulations with a transfer matrix formalism (not shown here) revealed that the higher absorption coefficients of the fluorinated blends raise the fraction of photons absorbed in the active layer only slightly, meaning that fluorination must also increase the efficiency of converting an absorbed photon into an extracted carrier. As outlined in the Introduction, higher J_{sc} values and EQEs have occasionally been reported for blends of other fluorinated DA copolymers with PCBM.[5,7,30,31,33]

In addition to a higher J_{sc} and EQE, the fluorination increases the FF by almost 10% in additive optimized solar cells with the same MW. The FFs of all our **P−F**-based DIO processed blends actually exceed the highest value (55%) ever reported for high-MW PCPDTBT.[11]

A further improvement of the **P−F**:$PC_{70}BM$ blend performance was achieved by slightly decreasing the active layer thickness[44] and by using a 1:2.5 (instead of 1:3) blend ratio, allowing the blend to absorb more strongly in the red to infrared part of the spectrum. We note that FF is not significantly altered when the blend ratio is varied between 1:3 and 1:2.5. Thus, we presume that the charge-carrier dynamics is only weakly affected by the small change in blend ratio. These optimized blends exhibited PCEs of up to 6.16% (6.04% on average), meaning that **P−F** outperforms high-molecular-weight PCPDTBT[11,12] and PSBTBT.[16,45]

CHARGE-CARRIER GENERATION AND RECOMBINATION

To shed some light on the fundamental processes causing the observed increase in J_{sc} and FF upon fluorination, we studied the efficiency for free-carrier formation and recombination using TDCF measurements.[46] The measurement scheme is outlined in the SI. With TDCF, charges are generated with a nanosecond laser pulse at voltages (pre-bias, V_{pre}) typical for solar cell operation. After a defined delay time a high constant reverse bias (collection bias, V_{coll}) is applied to extract all laser-generated charges which did not undergo recombination or which had not been extracted during the delay. Performing experiments with different pre-bias and delay time allows us to assess both the efficiency of free-carrier formation and non-geminate recombination as functions of bias.[22,46]

Field Dependence of Free-Carrier Generation. To address the effect of electric field on the generation of free carriers from the splitting of bound polaron pairs (PPs), TDCF experiments must be conducted under conditions where significant non-geminate recombination losses during delay and extraction are absent. It was shown before that free-carrier generation from either hot excitons or bound PPs in PCPDTBT is fully completed within a few nanoseconds after pulsed illumination.[47−50] Our previous TDCF studies on high-molecular-weight PCPDTBT showed that non-geminate recombination is insignificant within the first few tens of nanoseconds after excitation at moderate pulse fluences.[22] This was also proven by the linear dependence of the extracted charge on pulse fluence when setting the delay to 10 ns.[22] In this linear range the pulse fluence can be adjusted to create charge-carrier densities being comparable to 1 sun steady-state conditions.[51] Performing TDCF measurements in this range with different pre-bias and a short delay time between laser pulse and extraction, therefore, allows us to directly address the field dependence of free charge-carrier generation.

Figure 5a shows the total extracted charge Q_{tot} (being the integral over the whole current transient) versus applied bias during generation for a delay time of 10 ns. As non-geminate recombination is insignificant under these conditions, Q_{tot} is a direct measure of the free charge generated by the laser pulse at a given bias in competition with geminate recombination. By normalizing the generated charge to the respective value at the

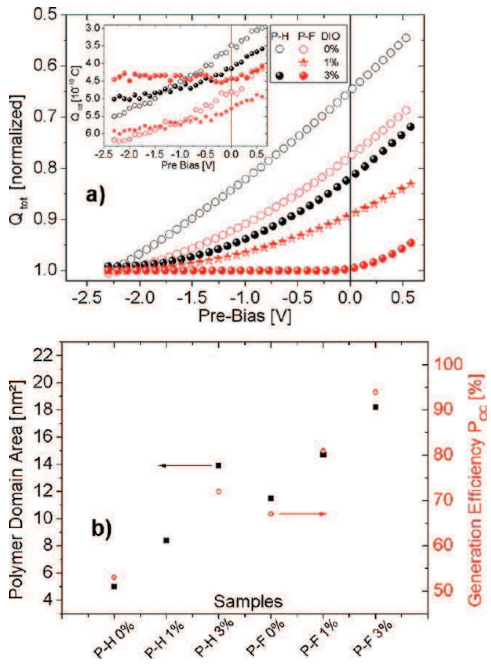

Figure 5. (a) Total extracted charge Q_{tot} deduced from TDCF measurements with 10 ns delay and 0.25 μJ/cm^2 pulse fluence as a function of pre-bias. Blends with **P−H** (black) and with **P−F** (red) are plotted for different amounts of additive: without DIO (open circles), with 1% DIO (stars), and with 3% DIO (filled circles). Values have been smoothed and normalized to the generated charge at the highest accessible bias of −2.3 V. The *y*-axis is scaled downward for better comparison with the negative photocurrent. The inset shows the raw, non-normalized data. (b) Comparison of the mean polymer domain size deduced from the plasmon maps in Figure 3 (left scale, black) with the relative generation efficiency P_{oc} at open-circuit conditions (right scale, red), being defined as the ratio of generated charges at open circuit compared to −2.3 V (see Table 5).

Table 5. Characteristic Parameters Describing the Generation, Transport, and Recombination of the Polymers P−H and P−F in 1:3 Blends with $PC_{70}BM$

	DIO [%]	P_{oc}[a] [%]	γ_{sc}[b] [10^{-17} m^3/s]	γ_{oc}[b] [10^{-17} m^3/s]	μ_e[c] [10^{-4} $cm^2/(V{\cdot}s)$]	ζ[d]
P−H	0	53	2.9	6.5	2.3	0.2
P−H	3	72	2.5	8.0	6.0	0.07
P−F	0	67	1.2	1.7	1.2	0.14
P−F	1	81	1.1	2.4	4.2	0.04
P−F	3	94	1.2	2.6	5.7	0.03

[a]The relative dissociation probability, P_{oc}, is the amount of generated charges close to V_{oc} relative to the charge generated at −2.3 V. [b]Bimolecular recombination coefficients γ_{SC} and γ_{oc} at short and open circuit, respectively. [c]Mobility deduced from photo-CELIV at a field strength of 200 $V^{1/2}{\cdot}cm^{-1/2}$. [d]Langevin reduction factor ζ estimated from the measured mobility at a field strength of 175 $V^{1/2}{\cdot}cm^{-1/2}$;

highest reverse bias of −2.3 V, the field dependence of free charge-carrier generation, i.e., the variation of Q_{tot} with pre-bias, can be compared for different blends. In great contrast to the well-known P3HT:PCBM system showing no field dependence of free charge generation,[46] the performances of all blends studied here are strongly limited by the field-dependent splitting of bound PPs.

For blends of **P−H** with $PC_{70}BM$ processed without DIO, we find that the efficiency for free-carrier generation at open-circuit conditions relative to the efficiency at −2.3 V, P_{oc}, to be only 53% (Table 5), suggesting efficient geminate recombination. Processing with 3% DIO increases P_{oc} to ca. 72%, implying a geminate loss of about 30%. These numbers compare very well to geminate losses at zero field determined by TAS. For example, Laquai and co-workers determined the total loss due to geminate recombination to about 50% in samples prepared without ODT and 30% in samples prepared with ODT.[49] More recently, Yamamoto and co-workers estimated the geminate loss in blends of PCPDTBT and $PC_{70}BM$ processed with 2% DIO to be 30%.[50]

Importantly, the field dependence of free charge generation becomes considerably weaker upon fluorination, which is clearly evident when comparing blends with **P−H** and **P−F** processed with the same amount of DIO. Also, processing with DIO weakens this field dependence, as shown earlier for non-fluorinated PCPDTBT.[22] The good correlation between P_{oc} and the mean polymer domain area in Figure 5b, and the distinct changes of the optical absorption properties of the blends upon processing with DIO and/or fluorination, suggest that a weaker field dependence of free-carrier generation is caused by the formation of larger (and probably purer) domains with better interchain order. Noticeably, blends with **P−F** processed with 3% DIO, whose morphology is characterized by rather pure polymer domains with the maximum domain size in lateral dimension, show only a 5% loss of efficiency for free charge-carrier formation when approaching V_{oc}.

The inset of Figure 5a shows the non-normalized raw data for the extracted free charge as a function of pre-bias. Note that the excitation was at a wavelength of 500 nm, where all studied blend layers exhibit nearly the same absorption (see Figure 2). Apparently, additive-optimized blends with **P−F** generate ~20% more free charges than their **P−H** counterparts over the entire bias range studied here for a comparable number of absorbed photons, meaning that exciton migration to the bulk heterojunction and/or free-carrier formation in competition with geminate recombination must be more efficient when using fluorinated donor polymers. As a similar enhancement is seen for the two blends processed without DIO where the donor and acceptor components are well intermixed, we presume that the fluorination promotes free-carrier formation via more efficient dissociation of bound PPs. Recently, a correlation has been established between the efficiency for free-carrier formation and the charge-transfer characteristics of DA polymers.[52] It was shown that fluorination increases the difference between the ground- and excited-state dipole moment $\Delta\mu_{ge}$ for PTB polymers, indicating enhanced charge transfer during excitation, which in turn shall facilitate the formation of free charges.[52] We propose that a similar mechanism causes the efficient formation of free charges in the fluorinated PCPDTBT as measured with TDCF.

Although blends with **P−F** processed with 3% DIO display the weakest field dependence of free-carrier formation, this blend shows an overall low efficiency for free-carrier generation at 500 nm. We attribute this to the presence of large and rather pure domains, implying a low probability for excitons generated on either the polymer or the $PC_{70}BM$ to reach the heterojunction. Note that the EQE in these blends is reduced mainly in the wavelength range where the $PC_{70}BM$ absorption is dominant, consistent with the appearance of large fullerene clusters in the plasmon maps in Figure 3, as discussed above.

Non-geminate Recombination. It was recently shown that the performance of blends of PCPDTBT with $PC_{70}BM$ is severely limited by efficient non-geminate recombination within the solar cell working regime, even in additive-optimized blends.[21,22] To assess the efficiency and kinetics of non-geminate recombination, we performed TDCF measurements with variable delay time between the laser pulse and the collection voltage. Figure 6 shows the results for **P−H**- and **P−F**-based additive optimized blends with a pre-bias setting close to the respective V_{oc}. Here, Q_{pre} is the charge extracted during delay. At conditions close to V_{oc} the drift of the photogenerated

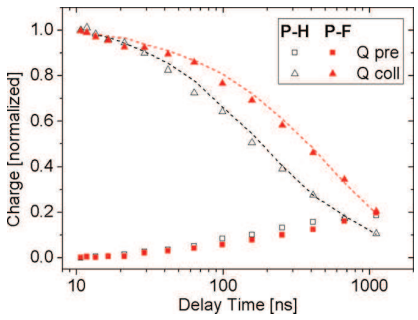

Figure 6. Precharge Q_{pre} and collected charge Q_{coll} derived from TDCF transients with different delay times and pre-bias setting close to V_{oc} (V_{pre} = 0.6 V for **P−H** and 0.7 V for **P−F**). The dashed lines are the corresponding BMR fits. Data are normalized to the initially photogenerated charge for better comparison.

dx.doi.org/10.1021/ja305039j | J. Am. Chem. Soc. 2012, 134, 14932−14944

charge-carriers is very slow, and Q_{pre} increases only gradually with time. Q_{coll} is the charge collected after a defined delay time by application of the collection bias, i.e., the charge which has not been extracted and which did not undergo non-geminate recombination during delay.[46] With increased delay time, more and more charges recombine non-geminately, leaving less charge available for extraction. Obviously, more charge can be collected for blends with **P−F** at a specific delay time, meaning that non-geminate recombination of charges must be reduced.

Fits to the experimental data with an iterative routine according to eq S1 (see SI) are represented by the dashed lines in Figure 6. The decay of Q_{coll} with delay time can be well described by second-order bimolecular recombination (BMR) with γ_{BMR} being the bimolecular recombination coefficient. The agreement between the experimental data and the fit is very good, considering that γ_{BMR} is the only adjustable parameter. Values for γ_{BMR} at different pre-bias are plotted in Figure 7. The

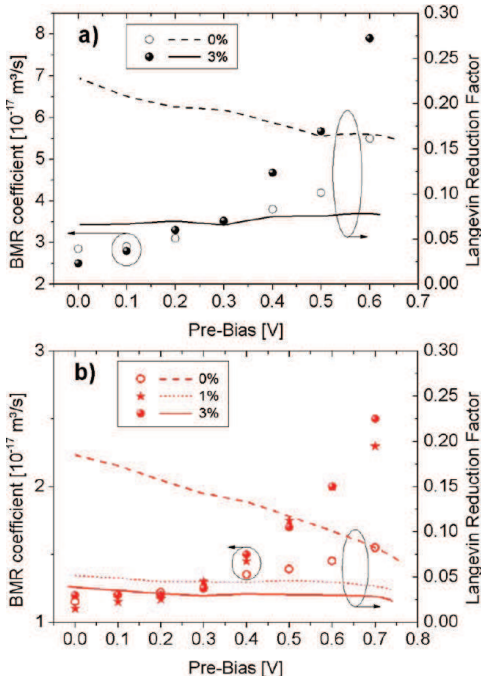

Figure 7. Left scale: Bimolecular recombination coefficient γ_{BMR} as a function of pre-bias deduced from fits (using eq S1) to the decay of the collected charge as shown in Figure S8. (a) Blends containing **P−H** (black) without additive (open circles) and with 3% DIO (filled circles). (b) Blends containing **P−F** (red) without additive (open circles), with 1% DIO (stars), and with 3% DIO (circles) Right scale: Langevin reduction factor obtained from the measured mobility and its field dependence for (a) **P−H**-based blends (black) processed without DIO (dashed line) or with 3% DIO (solid line) and (b) **P−F**-based blends (red) processed without DIO (red dashed line), with 1% DIO (red dotted line), and with 3% DIO (red solid line).

BMR coefficients of all blends are rather high, ranging between 1×10^{-17} and 8×10^{-17} m^3/s. These values are considerably larger than those reported for annealed blends of P3HT and PCBM, which are typically of the order of 10^{-18} m^3/s, meaning that non-geminated recombination is efficient in all of our blends. Our values for **P−H** blends at V_{oc} agree very well with zero-field BMR coefficients (measured with TAS at moderate carrier densities) in PCPDTBT:$PC_{61}BM$ blends processed without (3.2×10^{-17} m^3/s) or with (6.3×10^{-17} m^3/s) ODT as determined by Etzold et al.,[49] and they show reasonable agreement with $\gamma_{BMR} = 10 \times 10^{-17}$ m^3/s measured for a PCPDTBT:$PC_{70}BM$ blend processed with DIO by Yamamoto et al.[50] Noticeably, fluorination consistently reduces γ_{BMR} by a factor of 2−3 for blends processed either with or without DIO (see also Table 2). As outlined below, this reduction is a consequence of a smaller mobility in combination with a lowering of the Langevin reduction factor.

Figure 7 also shows that γ_{BMR} increases with increasing bias (decreasing internal electric field) for all measured blends, meaning that the coefficient is largest near open-circuit conditions. A proncouned increase of γ_{BMR} with decreasing field has recently been reported for higher-molecular-weight PCPDTBT.[22] This behavior was attributed to a pronounced negative field dependence of the charge-carrier mobility in the blend layers. Koster pointed out that a negative field dependence of mobility is generally expected for phase-separated blends of materials with distinctly different HOMO and LUMO energies.[53] In such blends, charges moving, e.g., in the donor phase occasionally need to perform jumps against the electric field direction to circumvent domains formed by the acceptor. Increasing the electric field reduces the rate for these back-jumps, decreasing the overall mobility of charge-carriers.

Figure 8 shows mobilities deduced from photo-CELIV measurements with variable voltage slopes in the low-field regime (below 300 $V^{1/2}$ $cm^{-1/2}$) following the analysis proposed by Bange et al.,[54] and mobilities at higher electric fields derived from TDCF measurements by extrapolating the initial photocurrent slope to zero[46] as outlined in the SI. In the

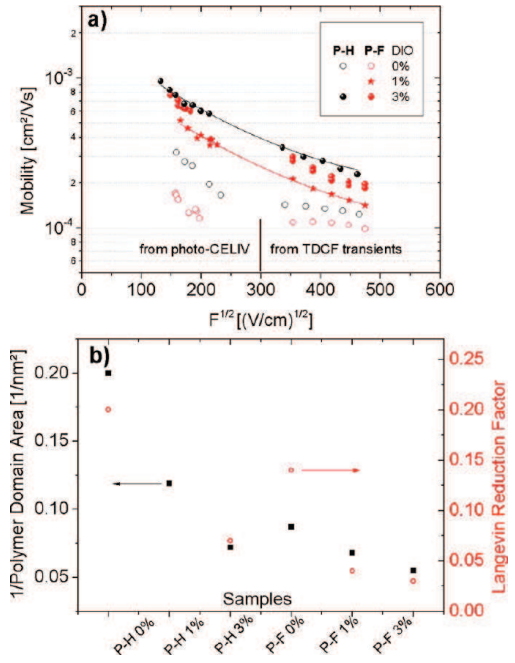

Figure 8. (a) Field-dependent mobilities measured with photo-CELIV (values in the field range below 300 $V^{1/2}$ $cm^{-1/2}$) and TDCF (values in the field range above 300 $V^{1/2}$ $cm^{-1/2}$) for blends with **P−H** (black) and **P−F** (red), without additive (open circles), with 1% DIO (stars), and with 3% DIO (circles). The lines are guides to the eyes for the additive optimized blends. (b) Comparison of the inverse mean polymer domain area (left scale, black) deduced from plasmon maps with the Langevin reduction factor (right scale, red) as shown in Table 5.

dx.doi.org/10.1021/ja305039j | J. Am. Chem. Soc. 2012, 134, 14932−14944

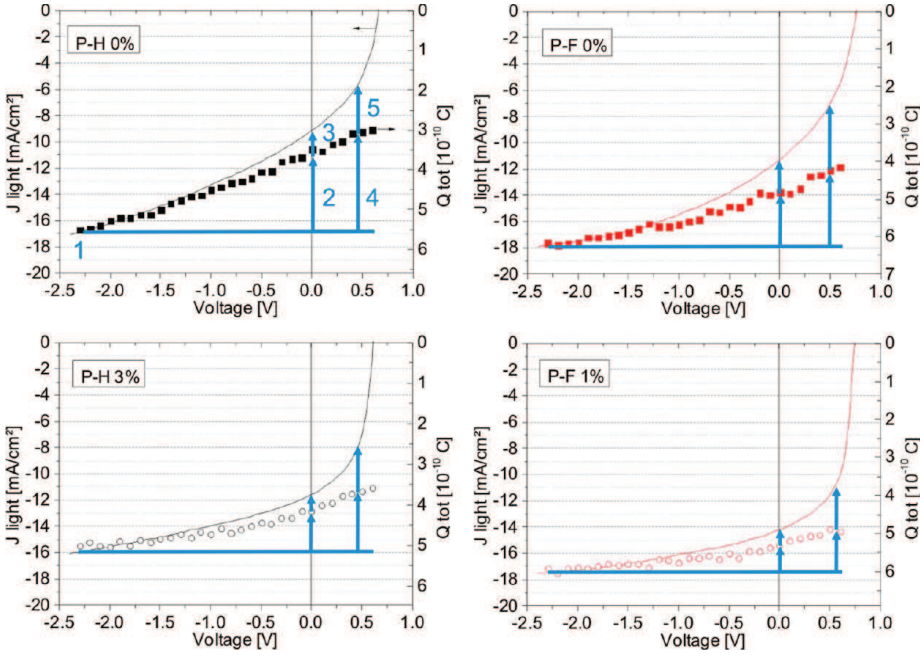

Figure 9. Measured $J-V$ characteristics under simulated AM 1.5G illumination, J_{light} (left scale) compared to the total charge Q_{tot} measured by TDCF at different pre-bias (right scale), for blends containing **P−H** (left) or **P−F** (right). Devices were processed either without (upper row) or with the optimum concentration of the solvent additive DIO (lower row). Q_{tot} is scaled to match the current under illumination at a bias of −2.3 V. Arrows show geminate and non-geminate losses at short circuit and the maximum power point (see Table 6 for the assignment of the arrows and the corresponding loss currents).

latter case, the extraction bias was varied between 0.5 and 1.5 V to ensure that the decay is not determined by recombination (as for lower fields) and not limited by the RC time (as for higher fields). It was reported earlier that electrons are the faster charge-carriers in PCPDTBT:PCBM blends.[23] Therefore, we attribute the mobility determined by photo-CELIV and TDCF to the electrons. We find that the processing additive increases the electron mobility by a factor of 3−4 for blends with either **P−H** or **P−F**, which is in accordance with earlier measurements on PCPDTBT.[22,55]

Interestingly, we measured lower mobilities for blends of the fluorinated donor polymer processed without DIO. Presuming that we record electron mobilities in all cases, this observation is rather surprising at first glance. However, attachment of the electron-withdrawing fluorine might lead to higher local dipole moments along conjugated polymer segments, resulting in a broadening of the density of states in both the electron- and the hole-transporting phases for highly intermixed blends.[56] In accordance with this interpretation, we find that fluorination reduces both the lateral and vertical hole mobility in pristine PCPDTBT layers, despite better chain packing (see SI). Also, increasing the domain size upon processing with DIO caused the mobility of the **P−F**-based blend to approach the value measured on the non-fluorinated system (see also the 3% DIO data in Table 2). In these blends with well-separated domains, electrons will move a greater distance to the donor-phase, which will diminish the possible distortion of electron transport by molecular dipoles located in the polymer phase.

Knowing the field dependence of γ_{BMR} and the carrier mobility in the same layer allows us to compare the BMR coefficient in the different blends with the Langevin recombination coefficient for three-dimensional recombination in an homogeneous medium, $\gamma_L(F) = e[\mu_e(F) + \mu_h(F)]/\varepsilon_o\varepsilon_r$. Here μ_e and μ_h are the mobility of electrons and holes, respectively, e the elementary charge, and F the internal electric field.[22] Blends of conjugated polymers and fullerene often reveal a reduced BMR recombination, as expressed by a Langevin reduction factor $\zeta(F) = \gamma_{BMR}(F)/\gamma_L(F)$ smaller than 1.[57,58] Experimental and theoretical work suggested that phase separation of the donor and acceptor components in pure domains suppresses recombination.[22,59−64] Figure 7 plots $\zeta(F)$ for all blends studied. In calculating $\gamma_L(F)$, we assumed that μ_h is 2 times smaller than μ_e over the entire field range, as shown earlier for high-molecular-weight PCPDTBT.[22] We find that $\zeta(F)$ is nearly independent of the internal electric field F (except for the F-PCPDTBT blend processed without DIO), meaning that the negative field dependence of γ_{BMR} reported above is mainly caused by a decrease of carrier mobility with increasing field. Second and more important, we consistently observe lower values of $\zeta(F)$ for blends containing **P−F**, and $\zeta(F)$ is further lowered upon processing with the additive.

Figure 8b plots the Langevin reduction factor near V_{oc} for the different blends together with the inverse of the average polymer domain area. Clearly, fluorination reduces the rate at which free carriers recombine. The apparent anti-correlation between the polymer domain size and ζ suggests that this reduction is related to the presence of larger and purer domains in blends with **P−F**. For example, ζ of the **P−F**-containing blend processed with 3% DIO, which has the largest mean area of the polymer-rich domains, is only 0.03, meaning that non-geminate recombination in this blend is significantly suppressed compared to the Langevin limit.

Table 6. Geminate (GEM) and Non-geminate (NG) Loss Currents in 1:3 Blends of P−H or P−F with $PC_{70}BM$, Processed with Different Amounts of DIO

	DIO [%]	1 $J_{gen}(-2.3\ V)$ [mA/cm^2]	2[a] $J_{GEM}(SC)$ [mA/cm^2]	3[a] $J_{NG}(SC)$ [mA/cm^2]	4[a] $J_{GEM}(MPP)$ [mA/cm^2]	5[a] J_{NG} (MPP) [mA/cm^2]	MPP [V]
P−H	0	16.74	5.74	1.88	7.39	3.62	0.45
P−H	3	15.93	3.19	1.14	4.48	3.27	0.46
P−F	0	17.81	4.13	2.45	5.70	4.97	0.50
P−F	1	17.48	2.22	1.08	3.16	3.49	0.56

[a]Loss currents 2−5 are described in text and shown by the arrows in Figure 9.

DISCUSSION

The knowledge of the field dependence of free-carrier generation allows us to assess the geminate and non-geminate losses that limit the device performance of our blends.

For this, we express the current flowing through the device under illumination $J_{light}(V)$ in terms of current densities describing the generation and non-geminate loss of free charge carriers in the active layer per unit area:

$$J_{light}(V) = J_{gen}(V) - J_{NG}(V) \quad (1)$$

Here, J_{gen} is the generation current density (the generated free charge per unit area and time) and J_{NG} the loss current density including non-geminate recombination and diffusion to the wrong contact. Figure 9 plots the bias-dependent light current $J_{light}(V)$ together with $Q_{tot}(V)$, the latter being a direct measure for the efficiency of free-carrier generation at the given voltage.

For all blends, the course of the current−voltage characteristics $J_{light}(V)$ at sufficiently negative reverse bias follows $Q_{tot}(V)$, meaning that non-geminate recombination losses are negligible at these conditions and that the field-dependent free-carrier generation rate determines J_{light} under simulated AM 1.5G illumination. Therefore, $Q_{tot}(V)$ can be translated into $J_{gen}(V)$ via

$$J_{gen}(V) = J_{gen}(-2.3\ V)\frac{Q_{tot}(V)}{Q_{tot}(-2.3\ V)} \quad (2)$$

Clearly, $J_{gen}(V)$ is smaller than $J_{gen}(-2.3\,V)$ under solar cell working conditions, meaning that geminate recombination of bound polaron pairs competes with their dissociation into free charges in the corresponding voltage regime. This loss can be approximated by $J_{GEM}(V) = J_{gen}(-2.3\ V) - J_{gen}(V)$. As most J−V characteristics do not saturate at reverse bias, we presume that geminate recombination is still active at −2.3 V, meaning that the given $J_{GEM}(V)$ are minimum values for the total geminate loss.

Table 6 summarizes J_{GEM} and J_{NG} at short-circuit conditions (SC) and at the maximum power point (MPP), respectively. These losses are also indicated by arrows in Figure 9. For the **P−H** blend processed without DIO, geminate recombination losses are severe. Geminate recombination reduces the photoinduced current density by at least 34% at SC, and this loss increases further to 44% at the MPP. The progressive increase in J_{GEM} with increased bias is a major cause for the low FF of this device. Geminate recombination losses are reduced by processing with DIO and fluorination of the donor polymer. For the optimized **P−F** blend, geminate recombination losses are only 13% at SC, increasing slightly to 18% when going to the MPP. These numbers are significantly smaller than the corresponding values (20% and 28%) for the optimized **P−H** blend.

Regarding non-geminate losses in devices processed without DIO, $J_{NG}(SC)$ and $J_{NG}(MPP)$ are smaller than the corresponding geminate losses, meaning that these devices are mainly limited by field-dependent generation. Interestingly, the non-geminate losses are larger for the **P−F** blend, despite the lower coefficient for non-geminate recombination. These larger losses can be rationalized by the rather small charge mobility in this blend, which slows down carrier extraction and makes the photogenerated charge vulnerable to free-carrier recombination. For devices processed with DIO, non-geminate losses are rather insignificant at SC (ca. 10% with regard to J_{gen} at short circuit) but they become relevant at the MPP. Noticeably, the slightly lower mobility of the optimized **P−F** blend is counterbalanced by its lower γ_{BMR}, and non-geminate loss currents are similar in the optimized devices (ca. 24−29% at MPP with respect to $J_{gen}(MPP)$. Therefore, the increase in FF of the DIO-processed blends upon fluorination is mainly caused by a weaker field dependence of the free-carrier generation current and a larger V_{oc}.

Recently, a morphological model was proposed to explain the efficient (and field-independent) free-carrier formation in P3HT:PCBM blends.[65] This model relies on a particular nanomorphology with a less ordered arrangement of the polymer chains at the heterojunction compared to the interior of the P3HT nanocrystallites. By this, polymer chains adjacent to PCBM domains exhibit a lower HOMO and a higher LUMO, forming an energetic barrier for photogenerated holes approaching the fullerene phase and thus slowing down geminate recombination. As shown above by absorption spectroscopy and plasmon mapping, chain aggregation and ordering is clearly improved upon fluorination. Possibly, those domains might possess different degrees of order at the interface and in the interior, causing photogenerated holes to be energetically stabilized away from the heterojunction, preventing rapid geminate recombination. Similar to this, these energetic barriers will also inhibit the intimate contact between free holes and electrons, rendering non-geminate recombination less effective than in a homogeneous 3D donor−acceptor mixture. This is exactly what is seen here, where **P−F** blends with a higher degree of chain aggregation exhibit a smaller Langevin reduction factor.

Though fluorination reduces losses due to geminate and non-geminate recombination, the average IPCE of the optimized **P−F** blend is only 50%, meaning that half of the incident photons are not converted to collected electrons at J_{sc}. A fundamental limit to the IPCE of these devices is that the optimum layer thickness is below 100 nm. Increasing the active layer thickness beyond 100 nm continuously decreased FF, J_{sc}, and PCE, due to inefficient carrier extraction.[16,44] Optical modeling with a transfer matrix formalism revealed that only ∼70% of the incident light is absorbed in an active layer with

optimum thickness.[44] Also, IPCE spectra are measured at short-circuit conditions. As pointed out above, geminate recombination reduces J_{light} at SC by at least 13%, even for the optimized **P−F** blend. In total, inefficient light absorption and geminate recombination limits the IPCE of this blend to ca. 60%. The IPCE might be further reduced by charge-carrier diffusion to the wrong contact[66] or by extraction of bound PPs at the electrodes.[67] Clearly, further improvement of the IPCE not only requires the application of light trapping schemes or optical spacers[68,69] but also asks for strategies to further reduce geminate and non-geminate losses.

Here, we point out that our study uses polymers of moderate MW ($M_n \approx 10$ kg/mol). It has been shown for other polymer:PCBM blends[9,70−72] that increasing the polymer's MW substantially improves the photovoltaic performance. This phenomena has been related to a concomitant increase of charge-carrier mobility, which promotes charge extraction in competition with non-geminate recombination. In fact, devices made with **P−H** of higher MW ($M_n \approx 17\,000$ g/mol) in our laboratory had EQEs of 2.6 (4.5) when processed without (with) 3% DIO.[44] Very recently (after submission of this manuscript), Jen and co-workers compared the properties of fluorinated PCPDTBT with $M_n = 23\,400$ g/mol with those of regular PCPDTBT of comparable M_n.[73] In a device geometry similar to the one employed by us, their PCPDTBT-based blends processed without an additive gave a PCE of 2.75%, and the efficiency was considerably improved to 5.51% upon fluorination. Although these authors noted that addition of processing additives did not improve PCE further, the combined optimization of the polymer MW, polymer:fullerene blend ratio, and additive concentration might further improve device performance beyond the record efficiency of 6.16% reported here.

Finally, we emphasise that significant improvements of J_{sc} and FF upon fluorine attachment have similarly been reported for other fluorine-substituted copolymers (see Introduction). We therefore propose that the main conclusion of this work—that fluorination improves the solar cell performance not only by increasing the V_{oc} but also by a reduced field dependence of carrier generation and a reduced efficiency for non-geminate recombination—is applicable to most other blend systems comprising F-substituted DA copolymers.

CONCLUSION

In summary, the synthesis and the photovoltaic properties of a new polymer, F-PCPDTBT, designed by fluorination of the BT unit in PCPDTBT, are described. The new polymer gives superior solar cell performance in blends with $PC_{70}BM$. Our measurements show that this enhancement can be mainly attributed to two fundamental effects caused by the fluorination. First, the IE of F-PCPDTBT is 0.1−0.15 eV larger than that of PCPDTBT. This results in a larger energetic difference between the HOMO of the polymer and the LUMO of $PC_{70}BM$, increasing the V_{oc} from 0.61 to 0.74 V. Second, charge-carrier generation becomes more efficient even under reverse bias conditions, and the field dependence of free charge-carrier generation is weakened, meaning that the geminate recombination is strongly reduced. Also, fluorination causes a 3-fold reduction in the non-geminate recombination coefficient at conditions of V_{oc} counterbalancing the reduction in charge-carrier mobility upon fluorine attachment. As a consequence, the FF is increased by 8% and the J_{sc} rises from 11.5 to 14 mA/cm^2 upon fluorine substitution.

We find that the fluorinated polymer has a stronger tendency to aggregate, reducing the optimum amount of processing additive from 3% to 1%. Following arguments put forward to explain the negligible effect of electric field on free charge generation in P3HT:PCBM blends,[65] we assign the superior performance of the optimized F-PCPDTBT:$PC_{70}BM$ blend to the formation of well-ordered polymer aggregates, which stabilizes holes within the hole-transporting polymer phase.

In total, fluorination of PCPDTBT causes the PCE to increase from 3.6% to 6.0% for identical device processing and comparable (medium) molecular weight. Further optimization of the blend ratio and active layer thickness resulted in 6.16% efficiency for F-PCPDTBT:$PC_{70}BM$ solar cells. Our optimized F-PCPDTBT:$PC_{70}BM$ blends clearly outperform the most efficient PCPDTBT:fullerene devices reported so far. As these blends exhibit a high external quantum efficiency of 50% over a broad spectral range, extending from 400 to 800 nm, they are well suited for building the red- to infrared-absorbing subcell of highly efficient polymer tandem solar cells.

ASSOCIATED CONTENT

Supporting Information

Details on the synthesis of the monomers and polymers, sample fabrication and testing, pristine polymer absorption spectra, current voltage characteristics of unipolar devices and OFETs, histograms of the plasmon maps, as well as Q_{tot}, Q_{pre}, and Q_{coll} for different delay times and pre-bias together with the corresponding BMR fits. This material is available free of charge via the Internet at http://pubs.acs.org.

AUTHOR INFORMATION

Corresponding Author

neher@uni-potsdam.de

Notes

The authors declare no competing financial interest.

ACKNOWLEDGMENTS

The authors acknowledge Sybille Allard and Anke Helfer from University of Wuppertal for the high-temperature GPC and Monika Ehlert from University of Potsdam for the TGA measurement. S.J. acknowledges Eileen Katholing for help with the synthesis. W.S. acknowledges Markus Wollgarten for co-work with the TEM data. The work was funded within the BMBF project PVCOMB (FKZ 03IS2151D) and SOHyb (FKZ 03X3525).

REFERENCES

(1) Konarka press release, Feb 28, 2012.
(2) Polyera press release, Feb 1, 2012.
(3) Dou, L.; You, J.; Yang, J.; Chen, C.-C.; He, Y.; Murase, S.; Moriarty, T.; Emery, K.; Li, G.; Yang, Y. *Nat. Photon.* **2012**, *6*, 180−185.
(4) Havinga, E. E.; Tenhoeve, W.; Wynberg, H. *Polym. Bull.* **1992**, *29*, 119−126.
(5) Chen, H.-Y.; Hou, J.; Zhang, S.; Liang, Y.; Yang, G.; Yang, Y.; Yu, L.; Wu, Y.; Li, G. *Nat. Photon.* **2009**, *3*, 649−653.
(6) Chu, T.-Y.; Lu, J.; Beaupré, S.; Zhang, Y.; Pouliot, J.-R. M.; Wakim, S.; Zhou, J.; Leclerc, M.; Li, Z.; Ding, J.; Tao, Y. *J. Am. Chem. Soc.* **2011**, *133*, 4250−4253.
(7) Price, S. C.; Stuart, A. C.; Yang, L.; Zhou, H.; You, W. *J. Am. Chem. Soc.* **2011**, *133*, 4625−4631.
(8) Amb, C. M.; Chen, S.; Graham, K. R.; Subbiah, J.; Small, C. E.; So, F.; Reynolds, J. R. *J. Am. Chem. Soc.* **2011**, *133*, 10062−10065.

(9) Coffin, R. C.; Peet, J.; Rogers, J.; Bazan, G. C. *Nature Chem.* **2009**, *1*, 657−661.
(10) Liang, Y. Y.; Xu, Z.; Xia, J. B.; Tsai, S. T.; Wu, Y.; Li, G.; Ray, C.; Yu, L. P. *Adv. Mater.* **2010**, *22*, E135−E138.
(11) Peet, J.; Kim, J. Y.; Coates, N. E.; Ma, W. L.; Moses, D.; Heeger, A. J.; Bazan, G. C. *Nat. Mater.* **2007**, *6*, 497−500.
(12) Lee, J. K.; Ma, W. L.; Brabec, C. J.; Yuen, J.; Moon, J. S.; Kim, J. Y.; Lee, K.; Bazan, G. C.; Heeger, A. J. *J. Am. Chem. Soc.* **2008**, *130*, 3619−3623.
(13) Chu, T. Y.; Alem, S.; Tsang, S. W.; Tse, S. C.; Wakim, S.; Lu, J. P.; Dennler, G.; Waller, D.; Gaudiana, R.; Tao, Y. *Appl. Phys. Lett.* **2011**, *98*, 3.
(14) Zhu, Z.; Waller, D.; Gaudiana, R.; Morana, M.; Muhlbacher, D.; Scharber, M.; Brabec, C. *Macromolecules* **2007**, *40*, 1981−1986.
(15) Hou, J.; Chen, H.-Y.; Zhang, S.; Li, G.; Yang, Y. *J. Am. Chem. Soc.* **2008**, *130*, 16144−16145.
(16) Scharber, M. C.; Koppe, M.; Gao, J.; Cordella, F.; Loi, M. A.; Denk, P.; Morana, M.; Egelhaaf, H. J.; Forberich, K.; Dennler, G.; Gaudiana, R.; Waller, D.; Zhu, Z. G.; Shi, X. B.; Brabec, C. J. *Adv. Mater.* **2010**, *22*, 367−370.
(17) Gendron, D.; Morin, P. O.; Berrouard, P.; Allard, N.; Aich, B. R.; Garon, C. N.; Tao, Y.; Leclerc, M. *Macromolecules* **2011**, *44*, 7188−7193.
(18) Morana, M.; Azimi, H.; Dennler, G.; Egelhaaf, H.-J.; Scharber, M.; Forberich, K.; Hauch, J.; Gaudiana, R.; Waller, D.; Zhu, Z.; Hingerl, K.; van Bavel, S. S.; Loos, J.; Brabec, C. J. *Adv. Funct. Mater.* **2010**, *20*, 1180−1188.
(19) Kim, J. Y.; Lee, K.; Coates, N. E.; Moses, D.; Nguyen, T. Q.; Dante, M.; Heeger, A. J. *Science* **2007**, *317*, 222−225.
(20) Yang, J.; Zhu, R.; Hong, Z.; He, Y.; Kumar, A.; Li, Y.; Yang, Y. *Adv. Mater.* **2011**, *23*, 3465−3470.
(21) Agostinelli, T.; Ferenczi, T. A. M.; Pires, E.; Foster, S.; Maurano, A.; Müller, C.; Ballantyne, A.; Hampton, M.; Lilliu, S.; Campoy-Quiles, M.; Azimi, H.; Morana, M.; Bradley, D. D. C.; Durrant, J.; Macdonald, J. E.; Stingelin, N.; Nelson, J. *J. Polym. Sci. Part B: Polym. Phys.* **2011**, *49*, 717−724.
(22) Albrecht, S.; Schindler, W.; Kurpiers, J.; Kniepert, J.; Blakesley, J. C.; Dumsch, I.; Allard, S.; Fostiropoulos, K.; Scherf, U.; Neher, D. *J. Phys. Chem. Lett.* **2012**, 640−645.
(23) Lenes, M.; Morana, M.; Brabec, C. J.; Blom, P. W. M. *Adv. Funct. Mater.* **2009**, *19*, 1106−1111.
(24) Blouin, N.; Michaud, A.; Gendron, D.; Wakim, S.; Blair, E.; Neagu-Plesu, R.; Belletete, M.; Durocher, G.; Tao, Y.; Leclerc, M. *J. Am. Chem. Soc.* **2008**, *130*, 732−742.
(25) Hoven, C. V.; Dang, X.-D.; Coffin, R. C.; Peet, J.; Nguyen, T.-Q.; Bazan, G. C. *Adv. Mater.* **2010**, *22*, E63−E66.
(26) Bijleveld, J. C.; Shahid, M.; Gilot, J.; Wienk, M. M.; Janssen, R. A. J. *Adv. Funct. Mater.* **2009**, *19*, 3262−3270.
(27) Liang, Y.; Feng, D.; Wu, Y.; Tsai, S.-T.; Li, G.; Ray, C.; Yu, L. *J. Am. Chem. Soc.* **2009**, *131*, 7792−7799.
(28) Zhang, Y.; Chien, S.-C.; Chen, K.-S.; Yip, H.-L.; Sun, Y.; Davies, J. A.; Chen, F.-C.; Jen, A. K. Y. *Chem. Commun.* **2011**, *47*, 11026−11028.
(29) Babudri, F.; Farinola, G. M.; Naso, F.; Ragni, R. *Chem. Commun.* **2007**, 1003−1022.
(30) Peng, Q.; Liu, X.; Su, D.; Fu, G.; Xu, J.; Dai, L. *Adv. Mater.* **2011**, *23*, 4554−4558.
(31) Zhou, H.; Yang, L.; Stuart, A. C.; Price, S. C.; Liu, S.; You, W. *Angew. Chem., Int. Ed.* **2011**, *50*, 2995−2998.
(32) Son, H. J.; Wang, W.; Xu, T.; Liang, Y.; Wu, Y.; Li, G.; Yu, L. *J. Am. Chem. Soc.* **2011**, *133*, 1885−1894.
(33) Li, Z.; Lu, J.; Tse, S.-C.; Zhou, J.; Du, X.; Tao, Y.; Ding, J. *J. Mater. Chem.* **2011**, *21*, 3226−3233.
(34) Schroeder, B. C.; Huang, Z.; Ashraf, R. S.; Smith, J.; D'Angelo, P.; Watkins, S. E.; Anthopoulos, T. D.; Durrant, J. R.; McCulloch, I. *Adv. Funct. Mater.* **2012**, *22*, 1663−1670.
(35) He, Z.; Zhong, C.; Huang, X.; Wong, W.-Y.; Wu, H.; Chen, L.; Su, S.; Cao, Y. *Adv. Mater.* **2011**, *23*, 4636−4643.
(36) Lange, A.; Krueger, H.; Ecker, B.; Tunc, A. V.; von Hauff, E.; Morana, M. *J. Polym. Sci. Part A: Polym. Chem.* **2012**, *50*, 1622−1635.
(37) Pilgram, K.; Zupan, M.; Skiles, R. *J. Heterocycl. Chem.* **1970**, *7*, 629−633.
(38) Peet, J.; Cho, N. S.; Lee, S. K.; Bazan, G. C. *Macromolecules* **2008**, *41*, 8655−8659.
(39) Rogers, J. T.; Schmidt, K.; Toney, M. F.; Bazan, G. C.; Kramer, E. J. *J. Am. Chem. Soc.* **2012**, *134*, 2884−2887.
(40) Herzing, A. A.; Richter, L. J.; Anderson, I. M. *J. Phys. Chem. C* **2010**, *114*, 17501−17508.
(41) Schindler, W.; Wollgarten, M.; Fostiropoulos, K. *Org. Electron.* **2012**, *13*, 1100−1104.
(42) Rogers, J. T.; Schmidt, K.; Toney, M. F.; Kramer, E. J.; Bazan, G. C. *Adv. Mater.* **2011**, *23*, 2284−2288.
(43) Gu, Y.; Wang, C.; Russell, T. P. *Adv. Energy Mater.* **2012**, *2*, 683−690.
(44) Albrecht, S.; Schäfer, S.; Lange, I.; Yilmaz, S.; Dumsch, I.; Allard, S.; Scherf, U.; Hertwig, A.; Neher, D. *Org. Electron.* **2012**, *13*, 615−622.
(45) Chen, H.-Y.; Hou, J.; Hayden, A. E.; Yang, H.; Houk, K. N.; Yang, Y. *Adv. Mater.* **2010**, *22*, 371−375.
(46) Kniepert, J.; Schubert, M.; Blakesley, J. C.; Neher, D. *J. Phys. Chem. Lett.* **2011**, *2*, 700−705.
(47) Hwang, I. W.; Soci, C.; Moses, D.; Zhu, Z.; Waller, D.; Gaudiana, R.; Brabec, C. J.; Heeger, A. J. *Adv. Mater.* **2007**, *19*, 2307−2312.
(48) Jarzab, D.; Cordella, F.; Gao, J.; Scharber, M.; Egelhaaf, H.-J.; Loi, M. A. *Adv. Energy Mater.* **2011**, *1*, 604−609.
(49) Etzold, F.; Howard, I. A.; Forler, N.; Cho, D. M.; Meister, M.; Mangold, H.; Shu, J.; Hansen, M. R.; Mullen, K.; Laquai, F. *J. Am. Chem. Soc.* **2012**, *134*, 10569−10583.
(50) Yamamoto, S.; Ohkita, H.; Benten, H.; Ito, S. *J. Phys. Chem. C* **2012**, *116*, 14804−14810.
(51) Maurano, A.; Hamilton, R.; Shuttle, C. G.; Ballantyne, A. M.; Nelson, J.; O'Regan, B.; Zhang, W.; McCulloch, I.; Azimi, H.; Morana, M.; Brabec, C. J.; Durrant, J. R. *Adv. Mater.* **2010**, *22*, 4987−4992.
(52) Carsten, B.; Szarko, J. M.; Son, H. J.; Wang, W.; Lu, L.; He, F.; Rolczynski, B. S.; Lou, S. J.; Chen, L. X.; Yu, L. *J. Am. Chem. Soc.* **2011**, *133*, 20468−20475.
(53) Koster, L. J. A. *Phys. Rev. B* **2010**, *81*, 205318.
(54) Bange, S.; Schubert, M.; Neher, D. *Phys. Rev. B* **2010**, *81*, 035209.
(55) Cho, S.; Lee, J. K.; Moon, J. S.; Yuen, J.; Lee, K.; Heeger, A. J. *Org. Electron.* **2008**, *9*, 1107−1111.
(56) Dieckmann, A.; Bassler, H.; Borsenberger, P. M. *J. Chem. Phys.* **1993**, *99*, 8136−8141.
(57) Pivrikas, A.; Juska, G.; Mozer, A. J.; Scharber, M.; Arlauskas, K.; Sariciftci, N. S.; Stubb, H.; Osterbacka, R. *Phys. Rev. Lett.* **2005**, 94.
(58) Deibel, C.; Wagenpfahl, A.; Dyakonov, V. *Phys. Rev. B* **2009**, *80*, 075203.
(59) Groves, C.; Greenham, N. C. *Phys. Rev. B* **2008**, *78*, 155205.
(60) Deibel, C.; Baumann, A.; Dyakonov, V. *Appl. Phys. Lett.* **2008**, 93.
(61) Hamilton, R.; Shuttle, C. G.; Oâ€Regan, B.; Hammant, T. C.; Nelson, J.; Durrant, J. R. *J. Phys. Chem. Lett.* **2010**, *1*, 1432−1436.
(62) Mauer, R.; Howard, I. A.; Laquai, F. d. r. *J. Phys. Chem. Lett.* **2010**, *1*, 3500−3505.
(63) Howard, I. A.; Mauer, R.; Meister, M.; Laquai, F. *J. Am. Chem. Soc.* **2010**, *132*, 14866−14876.
(64) Guo, J. M.; Ohkita, H.; Benten, H.; Ito, S. *J. Am. Chem. Soc.* **2010**, *132*, 6154−6164.
(65) McMahon, D. P.; Cheung, D. L.; Troisi, A. *J. Phys. Chem. Lett.* **2011**, *2*, 2737−2741.
(66) Sokel, R.; Hughes, R. C. *J. Appl. Phys.* **1982**, *53*, 7414−7424.
(67) Strobel, T.; Deibel, C.; Dyakonov, V. *Phys. Rev. Lett.* **2010**, 105.
(68) You, J.; Li, X.; Xie, F.-x.; Sha, W. E. I.; Kwong, J. H. W.; Li, G.; Choy, W. C. H.; Yang, Y. *Adv. Energy Mater.* **2012**, DOI: 10.1002/aenm.201200108.

(69) Wang, D. H.; Park, K. H.; Seo, J. H.; Seifter, J.; Jeon, J. H.; Kim, J. K.; Park, J. H.; Park, O. O.; Heeger, A. J. *Adv. Energy Mater.* **2011**, *1*, 766−770.
(70) Tong, M.; Cho, S.; Rogers, J. T.; Schmidt, K.; Hsu, B. B. Y.; Moses, D.; Coffin, R. C.; Kramer, E. J.; Bazan, G. C.; Heeger, A. J. *Adv. Funct. Mater.* **2010**, *20*, 3959−3965.
(71) Schilinsky, P.; Asawapirom, U.; Scherf, U.; Biele, M.; Brabec, C. J. *Chem. Mater.* **2005**, *17*, 2175−2180.
(72) Ma, W.; Kim, J. Y.; Lee, K.; Heeger, A. J. *Macromol. Rapid Commun.* **2007**, *28*, 1776−1780.
(73) Zhang, Y.; Zou, J.; Cheuh, C.-C.; Yip, H.-L.; Jen, A. K. Y. *Macromolecules* **2012**, *45*, 5427−5435.

THE JOURNAL OF PHYSICAL CHEMISTRY Letters

Letter

pubs.acs.org/JPCL

Quantifying Charge Extraction in Organic Solar Cells: The Case of Fluorinated PCPDTBT

Steve Albrecht,[†] John R. Tumbleston,[‡] Silvia Janietz,[§] Ines Dumsch,[∥] Sybille Allard,[∥] Ullrich Scherf,[∥] Harald Ade,[‡] and Dieter Neher*[,†]

[†]Institut für Physik und Astronomie, Universität Potsdam, Karl-Liebknecht-Str. 24-25, 14476 Potsdam, Germany

[‡]Department of Physics, North Carolina State University, 421 Riddick Hall, Raleigh, North Carolina 27695-8202, United States

[§]Fraunhofer Institut für Angewandte Polymerforschung, Geiselbergstr. 69, 14476 Potsdam, Germany

[∥]Bergische Universität Wuppertal, Institut für Polymertechnologie, Gauss-Str. 20, 42097 Wuppertal, Germany

Supporting Information

ABSTRACT: We introduce a new and simple method to quantify the effective extraction mobility in organic solar cells at low electric fields and charge carrier densities comparable to operation conditions under one sun illumination. By comparing steady-state carrier densities at constant illumination intensity and under open-circuit conditions, the gradient of the quasi-Fermi potential driving the current is estimated as a function of external bias and charge density. These properties are then related to the respective steady-state current to determine the effective extraction mobility. The new technique is applied to different derivatives of the well-known low-band-gap polymer PCPDTBT blended with $PC_{70}BM$. We show that the slower average extraction due to lower mobility accounts for the moderate fill factor when solar cells are fabricated with mono- or difluorinated PCPDTBT. This lower extraction competes with improved generation and reduced nongeminate recombination, rendering the monofluorinated derivative the most efficient donor polymer.

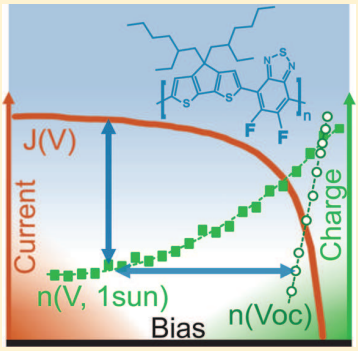

SECTION: Energy Conversion and Storage; Energy and Charge Transport

Bulk heterojunction solar cells made from polymeric or small donor molecules blended with the fullerene PCBM gained intense attraction due to their diverse advantages over other photovoltaic technologies such as low weight, flexibility, semi-transparency, and the opportunity for fast roll-to-roll processing.[1] A significant number of papers were published in the last several years in this fast growing field. Most of these publications demonstrate routes for device optimization,[2,3] new materials,[4,5] and understanding the underlying mechanism of charge generation,[6−8] recombination,[9,10] and extraction.[11,12]

Some of these systems show highly efficient charge generation, with internal quantum efficiencies near unity irrespective of the internal field,[13] resulting in power conversion efficiencies (PCEs) of 8.5%.[4] However, most of these high-efficiency devices have very thin active layers, below 100 nm only.[14] Increasing the thickness would benefit from higher light absorption and is desired in terms of ease of fabrication.[15] However, when the active layer thickness is increased, the fill factor and, with that, the overall PCE are reduced significantly for the majority of polymer/fullerene combinations.[14,15] Low fill factors (FF) are caused by photocurrent losses that depend on the internal electric field. There are two major causes: a field-dependent free charge generation competing with geminate recombination and inefficient free charge extraction in competition with nongeminate recombination. Field-dependent generation has been identified as a major loss channel in several organic photovoltaic systems, in particular, for those with highly intermixed donor−acceptor blends.[13,16,17] Geminate recombination was successfully suppressed when the nanoscale morphology revealed aggregated polymer chains and pure fullerene clusters.[18−20] Various reports showed that nongeminate recombination in organic solar cells is dominated by bimolecular recombination,[9,21−24] which is a nonlinear process with a quadratic dependence of the loss current on carrier density. Therefore, nongeminate losses will become dominant for slow extraction, as it causes a large steady-state carrier density in the bulk of the active medium. This makes the correct determination of the bimolecular recombination coefficient and of charge carrier mobilities, both determining the efficiency of extraction under solar cell working conditions, fundamental for a conclusive understanding of the device performance and for further efficiency enhancements.

Transient techniques such as transient absorption spectroscopy,[24] transient photovoltage,[10] or time-delayed collection field (TDCF)[16] are commonly applied to quantify nongeminate recombination losses. With regard to mobilities, a wide variety of techniques has been developed, each addressing free carrier motion under a different method-specific condition. Transient

Received: March 4, 2014
Accepted: March 13, 2014
Published: March 13, 2014

 © 2014 American Chemical Society

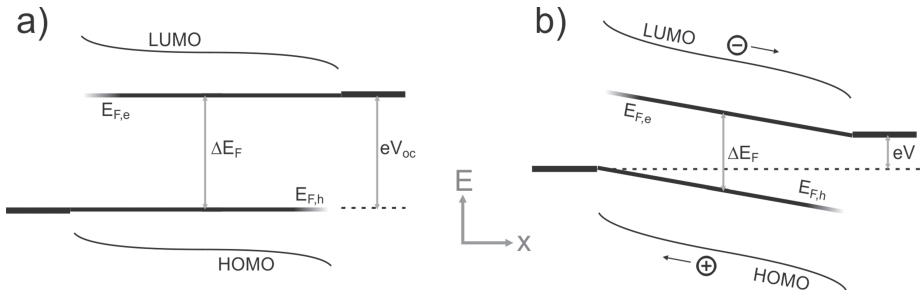

Figure 1. Energy level diagram with (a) conditions at open circuit and (b) conditions at voltages smaller than open circuit, for example, the maximum power point.

photoconductivity techniques such as time-of-flight (ToF), charge extraction by linearly increasing voltage (CELIV),[25] open-circuit corrected charge carrier extraction (OTRACE),[26] or TDCF[16] have been introduced to record the motion of photogenerated charge. ToF requires very thick active layers in the range of micrometers. CELIV, OTRACE, and TDCF are mostly sensitive to the faster type of carrier only.[16,25] Also, because they measure mobilities under reverse bias conditions, they might be less useful to characterize carrier motion under solar cell working conditions. Field effect transistors (FETs) can selectively determine electron or hole mobilities, but charge motion is measured across the micrometer length scale in-plane of the device and at high charge-carrier densities. Therefore, FET results often differ significantly from measurements of vertical charge transport on the 100 nm length scale and at lower carrier densities.[27]

Steady state electron and hole mobilities in the vertical direction are often determined by analyzing space-charge-limited currents (SCLCs) in single carrier devices, but this method has several drawbacks. First, different electrodes have to be used to guarantee the selective injection of only one type of carrier. Second, the unambiguous determination of the mobilities requires measurements on different layer thicknesses.[28] Both the variation of the electrode configuration and the active layer thickness were shown to affect the blend morphology.[29,30] Also, charge-carrier densities in the SCLC regime might be larger than at one sun illumination and at a bias smaller than V_{oc}.[31] Finally, the technique measures the motion of injected charges, while the majority of carriers in a working solar cell are photogenerated.

More recently, Durrant and coworkers introduced a method to quantify the mobility of charges in a solar cell under steady-state illumination conditions at low internal fields.[32] This technique relies on the comparison of the current density J flowing out of the device with the steady-state carrier density n measured by charge extraction (CE). If the current density $J(V)$ at a given bias V is caused by the drift of only one type of carrier with a homogeneous density $n(V)$, the mobility μ can be calculated from

$$\mu(n, V) = \frac{J(V)}{e \cdot n(V) \cdot E} \tag{1}$$

Here e is the elementary charge and E is the electrical field across the sample given by $E = (V_{fb} - V)/d$, where V_{fb} is the flat band potential and d is the layer thickness. In conventional CE, the device is held at a certain prebias under constant illumination. When the light is switched off, the sample is short-circuited and the integral over the resulting current transient is taken as a measure for the charge in the device. In the original work by Durrant and coworkers, the short-circuit current density J_{sc} was compared with the charge density also under short-circuit conditions.[32] Later, Deibel et al. related the short current density J_{sc} to n at open-circuit conditions, thereby making use of the field-independent generation efficiency in the studied system.[23] In both publications, the charge was extracted with an internal field corresponding to short-circuit conditions, typically on the order of (2 to 5) $\times$ 10^6 V/m. We have previously shown that such low fields may be too small to extract all charge from the device.[33] Also, the correct determination of the internal electrical field E is not straightforward, as it requires knowledge of the flat band potential. Finally, eq 1 does not account for charge diffusion, which might be dominant close to V_{oc}.

Here we propose a novel approach to determine the charge mobility via the precise measurement of the steady-state charge-carrier density with bias-amplified charge extraction (BACE),[33,34] and the proper estimate of the gradient of the quasi-Fermi levels being the driving force for the current. This approach makes use of a more general equation describing the motion of charges by drift and diffusion in a semiconductor, accounting for both drift and the diffusion currents for, for example, electrons

$$J_e = J_{drift,e} + J_{diff,e} = en_e\mu_e E + eD_e\nabla n_e = n_e\mu_e\nabla E_{F,e} \tag{2a}$$

and thus

$$J_{tot} = n_e\mu_e\nabla E_{F,e} + n_h\mu_h\nabla E_{F,h} \tag{2b}$$

Here n_e (n_h) is the electron (hole) density, μ_e (μ_h) is the electron (hole) mobility, $\nabla E_{F,e}$ ($\nabla E_{F,h}$) is the gradient of the electron (hole) quasi-Fermi level, and J_{tot} is the sum of both the electron and the hole current.[35] Under open-circuit conditions, both quasi-Fermi levels are constant throughout the device and the net-current is zero.[36] This situation is displayed in Figure 1a. If selective ohmic contacts are applied (one for electron, the other for holes), the open-circuit voltage is equal to the quasi-Fermi level splitting in the bulk

$$eV_{oc} = E_{F,e} - E_{F,h} \tag{3}$$

Importantly, for every semiconductor there is a specific dependence of the quasi-Fermi-level energy and the respective carrier density.[34,36,37] In most cases, a relation with the general form of $E_{F,e} - E_{F,h} = a + b\cdot\ln(n_e n_h/c)$ can be derived, with a, b, and c being parameters related to the specific energetics of the semiconductor and temperature.[34,38] Under open-circuit conditions, this leads to a material-specific dependence of carrier density.[34,39]

When the external bias V is lower than V_{oc}, for example, around the maximum power point (MPP), electrons and holes

are extracted to the contacts by drift or diffusion, driven by a gradient of the respective quasi-Fermi level. This situation is described in Figure 1b. If we assume that the gradient is constant throughout the bulk of the device and identical for electrons and holes $\nabla E_{F,e} \cong \nabla E_{F,h} = \nabla E_{qF}$, as it has been shown by recent device simulations,[40,41] the following simple relation can be derived

$$eV = E_{F,e} - E_{F,h} - d\cdot\nabla E_{qF} \quad (4)$$

The assumption of constant quasi-Fermi-level gradients throughout the bulk of the device might become invalid when the photocurrent becomes limited by space-charge effects in the case of highly imbalanced mobilites. In this situation, the electrical field in the device is partially screened by the accumulation of the slower carrier, leading to a pronounced inhomogeneity of the electric field and carrier density throughout the layer thickness. Space-charge formation is indicated by a typical square-root dependence of photocurrent with bias[42,43] that is not seen here. Further work will be conducted in follow-up publications to validate the assumption of the constant gradient of the quasi-Fermi-level with simulations for different conditions.

Presuming that the device under steady-state illumination is at near thermal equilibrium also for nonzero currents, the carrier density in the bulk obeys the Fermi−Dirac statistics and the product of electron and hole density is again determined by the quasi-Fermi level splitting. We now consider the case that the same carrier density $n = (n_e \cong n_h)$ is established in two ways: either by illumination under intensity I_1 and V_{oc} conditions, where the net-current density is zero, or by keeping the device at a lower bias than V_{oc} but at higher illumination intensity I_2, with a measurable net current. Because of equal carrier densities, the quasi-Fermi level splitting in the bulk is the same in both cases and equal to $e\cdot V_{oc}(I_1)$ leading to

$$\nabla E_{qF}(n, V) = e\frac{V_{oc}(n, I_1) - V(n, I_2)}{d} \quad (5)$$

From this, the effective extraction mobility can be determined via

$$\mu_{eff}(n, V) = \frac{J(V)}{2n(V)\cdot\nabla E_{qF}(n, V)} = \frac{J(V)d}{2e\cdot n(V)\cdot(V - V_{oc})} \quad (6)$$

Note that the factor "2" in the dominator of the eq 6 is due to the fact that electrons and holes both contribute equally to the steady-state current of an illuminated solar cell. Finally, μ_{eff} is related to the mobilities of electrons and holes via the following simple relation (see Supporting Information, SI)

$$\mu_{eff} = \frac{2\mu_e\mu_h}{\mu_e + \mu_h} \quad (7)$$

Compared with previous work, our approach has several advantages. First, current and carrier densities are compared at the same internal field (bias). Second, it does not rely on any assumption about the field-dependence of charge generation nor does it require knowledge about the flat band potential. Also, contributions from drift and diffusion are automatically included. Most importantly, because electrons and holes contribute equally to J under steady-state conditions, this approach measures the combined motion of both types of carriers. This makes it a suitable approach to quantify the extraction of photogenerated charge in competition with nongeminate recombination.

We now apply this method to blends of PCBM with the well-known polymer PCPDTBT (0F) and its fluorinated derivatives 1F-PCPDTBT (1F) and 2F-PCPDTBT (2F). The chemical structures and JV characteristics of the additive optimized blends are displayed in Figure 2a. As shown before, the

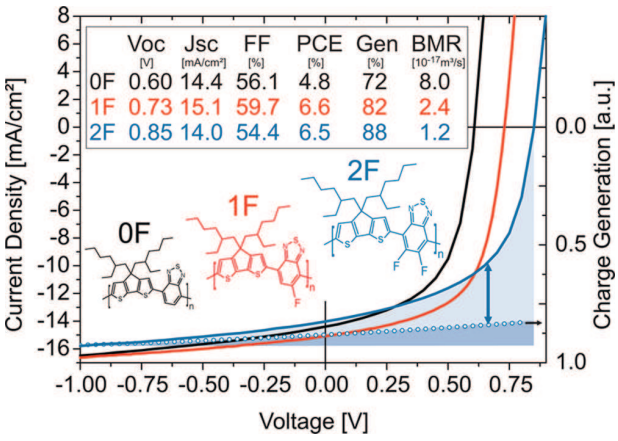

Figure 2. (a) Left scale: JV characteristics measured under simulated AM 1.5G spectra for additive optimized champion cells of blends made from $PC_{70}BM$ with PCPDTBT = 0F (black), F-PCPDTBT = 1F (red), and 2F-PCPDTBT = 2F (blue). Right scale: the field dependence of charge generation normalized to high fields for 2F blends (blue open circles). The dark and light colored areas highlight the loss due to the field dependence of charge generation and nongeminate recombination (NGR), respectively, for the 2F blend. The blue arrow indicates the current loss due to NGR at the maximum power point.

monofluorination lowers the polymer HOMO level, resulting in an enhanced V_{oc}. Also, the field dependence of generation (expressed by the parameter Gen) and the bimolecular recombination (BMR) coefficient are reduced upon monofluorination, resulting in PCEs above 6%.[19,44] For the difluorinated derivate, this characteristic trend continues: 2F blends show a high V_{oc} of 850 mV, related to a further downshift of the HOMO.[45] Importantly, 2F blends also show the weakest field dependence of charge generation and the smallest BMR coefficient. (See Figure S1 in the SI.) Both effects can be explained by the morphology changes induced upon fluorination, as seen in resonant X-ray scattering (R-SoXS) measurements (Figure 3).[46] For all polymers, the additive DIO increases the total scattering intensity, pointing to higher composition variations (i.e., purity) of the individual phases.[19] For a given additive concentration, fluorination leads to more pure phases, with the highest purity seen in the 2F-based blend with 3% DIO.

Interestingly, despite a significant reduction of the generation losses and of the BMR coefficient with fluorination, the FF of the 1F blend is only slightly larger than that of the nonfluorinated system, and it even decreases for 2F. This can be related to increased nongeminate recombination loss, which is 4.45 mA/cm^2 at MPP for 2F blends, as indicated by the arrow in Figure 2. Thus, approximately one-third of the generation current is lost due to nongeminate recombination at MPP for 2F blends despite a low BMR coefficient.

dx.doi.org/10.1021/jz500457b | J. Phys. Chem. Lett. 2014, 5, 1131−1138

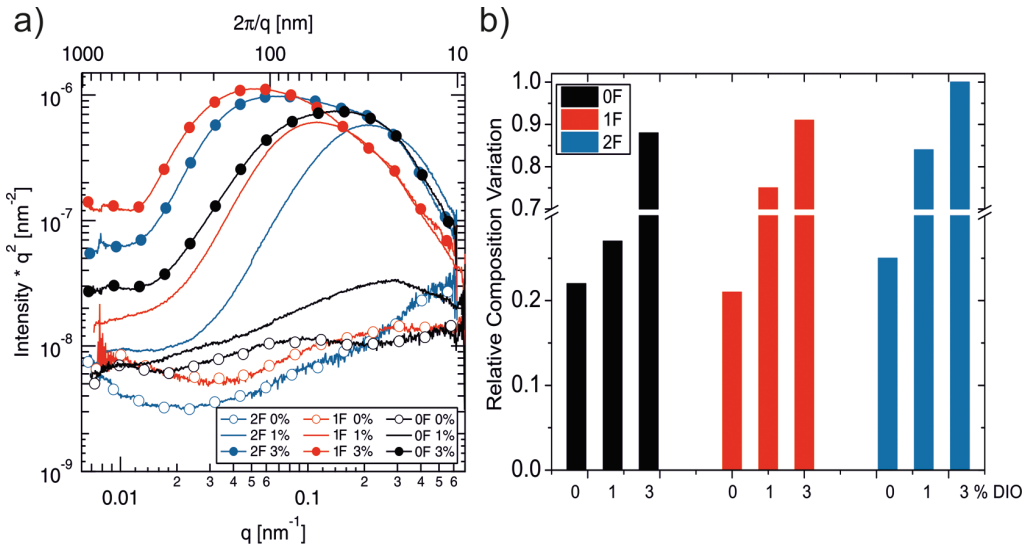

Figure 3. (a) Resonant soft X-ray scattering (R-SoXS) at 284.1 eV for 0F, 1F, and 2F samples each with 0, 1, and 3% DIO. (b) Relative composition variations (i.e., purity) extracted from R-SoXS for all blends normalized to the most pure device, which is 2F with 3% DIO.

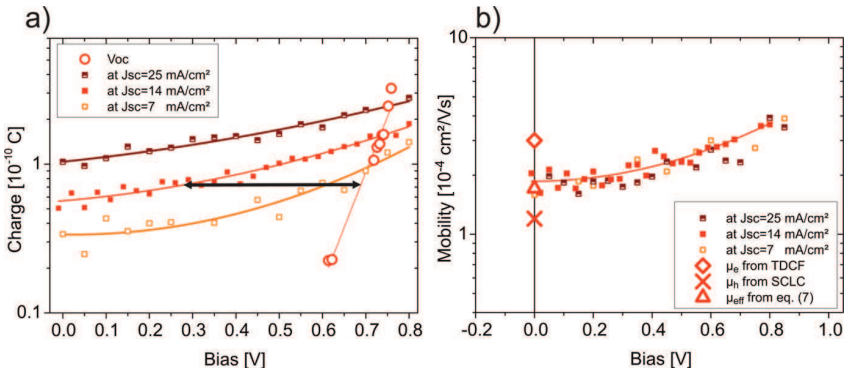

Figure 4. (a) Steady-state charge-carrier density for 1F devices measured with BACE at the respective V_{oc} for different illumination intensities (circles) and for variable bias and constant illumination conditions, which generates a short-circuit current J_{sc} = 25.5, 14, and 7 mA/cm^2 (squares). (b) Mobility determined from the steady-state densities as presented in panel a (squares), electron mobility μ_e from TDCF[19] (diamond), hole mobility μ_h from SCLC measurements as shown in the SI (cross), and the effective mobility μ_{eff} according to eq 7 (triangle). Solid lines are guide to the eyes.

The effective extraction mobility was determined with the BACE technique as introduced recently by our group to understand this phenomenon.[33,34] To avoid errors due to nongeminate recombination losses during extraction, we applied a high reverse bias to extract all carriers within the BACE technique. Here the sample is illuminated at an applied prebias (V_{pre}) with a high-power 445 nm laser diode. Applying the light for several milliseconds ensures that steady state between generation, recombination, and extraction is reached. Then, the light is switched off within ca. 10 ns and the external bias is rapidly changed from prebias to a high reverse bias within ~15 ns, which extracts all charge from the device. The short delay time ensures sufficient suppression of nongeminate recombination between steady-state and extraction conditions.[16] Figure 4 shows $n(V_{oc})$, the carrier density measured at open circuit for different illumination intensities, for the additive optimized 1F blend. As expected and shown before,[10,34] $n(V_{oc})$ follows an exponential dependence on V_{oc}. Also shown are carrier densities $n(V)$ measured at a constant illumination intensity but with decreasing bias. Three intensity levels were chosen to give a J_{sc} of 7, 14, and 25.5 mA/cm^2. By definition, $n(V)$ measured for a given illumination intensity intersects with $n(V_{oc})$ at the respective V_{oc}, and this point is at a higher bias for more intense illumination. The data also show that when the bias becomes smaller than V_{oc} the carrier densities decrease continuously due to more rapid extraction of the carriers. Following the arguments previously outlined, it is now possible to determine the gradient of the quasi-Fermi level position driving this current for any arbitrary bias and illumination conditions by simply considering the difference $V(n)-V_{oc}(n)$ at the respective carrier density n, following eq 5. This is exemplified by the horizontal arrow in Figure 4. Combined with the extracted current density known from the steady-state JV characteristics for identical illumination conditions (using the same laser diode operating under continuous wave conditions), the effective extraction mobility can be calculated with eq 6.

The results of this analysis are shown in Figure 4b. Near short circuit, the average extraction mobility is around 2 × 10^{-4} cm^2/(V s), ca. 1.5 times smaller than the mobility of the faster

dx.doi.org/10.1021/jz500457b | J. Phys. Chem. Lett. 2014, 5, 1131−1138

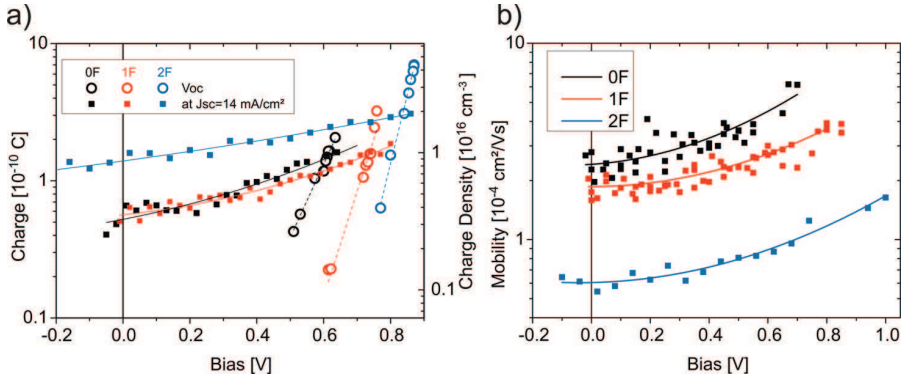

Figure 5. Steady-state charge-carrier density for (a) 0F (black), 1F (red), and 2F devices (blue) measured with BACE at the respective V_{oc} for different illumination intensities (circles) and under illumination conditions resulting in J_{sc} = 14 mA/cm^2 with varying bias (squares). (b) Extraction mobility values estimated from the steady-state carrier density as shown in panel a. All lines are guide to the eyes.

carrier (electrons) as reported previously[16] and a factor ca. 1.5 higher than the hole mobility extracted from hole-only devices. (See Figure S2 in the SI.) The effective mobility according to eq 7, determined from hole and electron mobility measurements, nicely fits to the effective extraction mobility estimated from steady-state carrier densities. We also observe a continuous increase in the average extraction mobility with increasing bias (decreasing field), confirming our previous findings[16] and in full accordance with theoretical predictions.[47] The fact that mobilities extracted from the data for three different illumination intensities are comparable proves the consistency of our approach. It also shows that the explicit dependence of mobility on carrier density is weak.

In the previous analysis, a homogeneous distribution of electrons and holes within the layer has been assumed. In this case, the total extracted charge is $Q_{extr} = (dA/2)(n_e + n_h)$.The factor "2" in the dominator takes into account the fact that electrons and holes travel, on average, through half of the layer upon extraction. If, however, the charge-density profile under steady state conditions is inhomogeneous,[37,48] the extracted charge is not an exact measure of the total charge in the active layer. This will induce a certain error in the determined value of μ_{eff}, particularly when performing measurements at very different bias or for different film thickness. Because all of our measurements are on devices with similar thickness and at comparable current densities, the relative error made when comparing extraction mobilities for our three blends will be quite small.

Figure 5a compares the carrier density $n(V_{oc})$ measured under open-circuit conditions for the three different blends. Increasing the number of fluorine atoms causes a significant shift of the $n(V_{oc})$ curve to higher biases, which is mainly caused by the lowering of the polymer HOMO. Also shown are the steady-state carrier densities $n(V)$, with the intensity adjusted to give a J_{sc} of 14 mA/cm^2 for each blend. This Figure reveals some important differences. First, although the charge extracted from 0F and 1F blends is quite comparable in the measured bias range, the $n(V)$ of the 1F blend decays more slowly with decreasing bias. In other words, a larger gradient of the quasi-Fermi level is necessary to extract the carriers in the 1F blend. This is expressed by a slightly lower mobility, as shown in Figure 5b. More importantly, $n(V)$ of the 2F-based blend is larger, and it decays even more slowly with decreasing bias over the entire range. Indeed, the effective extraction mobility according to eq 6 is fairly low for this blend, below 2 × 10^{-4} cm^2/(V s).

To illustrate the different extraction properties of the three polymers, we have plotted in Figure S3 in the SI the gradient of the quasi-Fermi potential (as expressed by $V_{oc}-V$) and the bulk quasi-Fermi level splitting as a function of the current. A significantly larger gradient is needed for 2F compared with 1F and especially to 0F to drive the same current density. More importantly, the bulk quasi-Fermi level splitting in the 2F-based blend decreases very moderately with increasing current. As a matter of fact, $E_{F,e}-E_{F,h}$ at a current density of 14 mA/cm^2 is only 0.043 eV lower than that under open-circuit conditions, implying a high carrier density and efficient nongeminate recombination.

With this knowledge about the effective extraction mobility, we are able to understand the trend in FF upon fluorination. As previously mentioned, the shape of the *JV* curve and, with that, the value of FF result from the specific field dependence of generation, extraction, and nongeminate recombination. Fluorination improves charge generation, thereby reducing the field dependence of charge generation. In addition, we see a seven-fold reduction in BMR coefficient in between the 0F and the 2F blend. The enhanced generation and reduced nongeminate recombination is counterbalanced by a significant lowering of the mobility upon fluorination. For 1F blends, this effect of reduced mobility on the *JV* characteristics is still quite weak, rendering the 1F-based blend the one with the highest FF. The lower extraction becomes important for 2F blends; the high carrier density remaining in the device under steady-state enhances nongeminate recombination losses, although this blend shows the smallest BMR coefficient. At a density n of ca. 1.5 × 10^{22} m^{-3} and a BMR coefficient γ of 1.2 × 10^{-17} m^3·s^{-1}, the recombination current at MPP according to $J_{rec} = \gamma e d n^2$ is 4.3 mA/cm^2. This is in very good agreement with the current loss determined from the comparison of the current density and the field-dependent generation measured via TDCF at the MPP (as shown by the arrow in Figure 2).

In summary, we introduce a new and simple technique to estimate the effective extraction mobility for charge-carrier densities close to one sun illumination condition and in the small field regime typical for solar cell operation. This method takes into account drift and diffusion and is applicable to a wide range of illumination conditions, feasible to determine the field and charge density dependence of the mobility independently. With this average extraction mobility being accurately

dx.doi.org/10.1021/jz500457b | J. Phys. Chem. Lett. 2014, 5, 1131−1138

determined, a conclusive picture of the processes leading to distinct changes in the FF upon fluorination of the low-band-gap donor polymer PCPDTBT is gained. With the more efficient generation and reduced recombination counter-balanced by a decreased extraction mobility, the highest FF (close to 60%) and PCE (6.6%) are reached with the monofluorinated F-PCPDTBT, while the blend with 2F-PCPDTBT blends has an only moderate FF of 54%, which limits the PCE to 6.5%. If the negative impact on mobility could be avoided, the 2F material would achieve superior performance. Our results provide important insight into the fact that simple molecular modifications can affect multiple device parameters, and improved understanding is required before a rational design paradigm for synthesis can be established.

EXPERIMENTAL SECTION

Materials. PCPDTBT with M_n = 18.5 kDa and M_w = 25 kDa was synthesized following a procedure described in literature.[49] F-PCPDTBT was synthesized with M_n= 21.5 and M_w = 51 kDa, as previously described.[19] Poly[2,6-(4,4-bis(2-ethylhexyl)-4*H*-cyclopenta[2,1-*b*;3,4-*b*′]dithiophene)-*alt*-4,7-(5,6-difluoro-2,1,3-benzothiadiazole] (2F-PCPDTBT) was synthesized as follows: 4,7-Dibromo-5,6-difluoro-2,1,3-benzothiadiazole 223 mg (0.71 mol), 4,4-bis(2-ethylhexyl)-2,6-bis-(trimethylstannyl)-4*H*-cyclopenta[2,1-*b*:3,4-benzothiadiazole] 600 mg (0.8238 mmol), and 5 mL of *p*-xylene containing $Pd(PPH)_3)_4$ 20 mg (5 mol % relative to Br) were charged in a microwave tube in the glovebox. The tube was sealed and removed from the glovebox into to the microwave reactor for polymerization. The following reaction conditions were used: 120 °C for 5 min, 140 °C for 5 min, and 170°c for 40 min. The originated polymer solution was cooled to ∼60 °C and precipitated into 300 mL of methanol. The polymer was dissolved in $CHCl_3$ (200 mL) and mixed with a solution of sodium diethyldithiocarbamate trihydrate (10 g) in distilled water (200 mL). The mixture was strongly stirred at 80 °C overnight under nitrogen. The organic phase was separated and washed three times with water, dried over $MgSO_4$, filtrated, and concentrated. The concentrated solution was precipitated in CH_3OH again. After drying, the polymer was extracted with methanol (12 h), hexan (6 h), aceton (6 h), and chloroform (6 h) and finally precipitated in methanol. The molecular weight was M_n = 5 kDa and M_w = 9.05 kDa, and the yield = 30%. ^{1}H NMR (500 MHz, $CDCl_3$) results are as follows: δ 8.20−8.40 (br, 2H); 2.0−2.2 (br, m, 4H);1.4−0.4 (br, m, 30H). Note that a higher molecular weight of 2F-PCPDTBT was obtained from synthesis. However, because of its low solubility,[45] this fraction was not processable at room temperature in CB. Thus the higher M_n fraction yielded lower performance due to the need for changing the solvent and increasing the solution temperature during spin coating. All molecular weights were determined via gel permeation chromatography at elevated temperatures (135 °C) in high-boiling-point solvent trichlorobenzene to reduce aggregation effects.

Devices. Solar cell devices were fabricated on prestructured indium tin oxide (ITO)-coated glass slides (Lumtec) cleaned in acetone, detergent, DI water, and isopropanol and dried with a nitrogen gun. After that, the ITO was plasma-cleaned and subsequently a 40 nm layer of PEDOT (Clevios AI 4083) was spin-cast on ITO. Annealing of the PEDOT:PSS was performed in a nitrogen-filled glovebox at 180 °C for 10 min. For transient devices, the active layer was spin-cast from solutions containing 1/3 (by weight) blend of donors and $PC_{70}BM$ (99%, Solenne). Only champion solar cell devices made with 1F had a 1/2.5 blend ratio. Chlorobenzene with different amounts of diiodooctane (DIO) was used as the processing solvent. The total blend concentration was 36 mg/mL, and spin coating was performed at 1500−2000 rpm for 40 s to give active layer thicknesses between 90 and 100 nm. To complete the solar cell devices, 10 nm Ca and 100 nm Al were thermally evaporated with a base pressure below 10^{-6} mbar through shadow masks to define the active area to be 6.0 mm^2 for solar cell characteristics and 1.1 mm^2 for TDCF.

Measurements. TDCF and BACE are described in detail elsewhere.[16,33,34] Here a 445 nm 1 W laser diode (Insaneware) with ∼10 ns light switch-off time mounted onto a heat sink was used for BACE measurements. The light was coupled to a fiber (LEONI, multimode, 60 m long) to ensure high homogeneity of the light profile. Resonant soft X-ray scattering (R-SoXS) was performed at Beamline 11.0.1.2 of the Advanced Light Source (ALS)[50] by floating films onto SiN windows. Composition variations were determined from scattering at 282.5 and 284.1 eV, where optical contrast between polymer and fullerene was high but absorption was low, thus minimizing fluorescence background and beam damage. Optical contrast was determined by measuring the optical constants of neat materials with scanning transmission X-ray microscopy (STXM) at beamline 5.3.2.2 of the ALS,[51] followed by Kramers−Kronig transformation.[52] Optical contrast differences between blends based on 0F, 1F, and 2F were minimal. The 1-D R-SoXS scattering averaged intensity was multiplied by q^2 (i.e., Lorentz correction), which corresponds to an azimuthal integration of the 2-D data.

ASSOCIATED CONTENT

Supporting Information

Field dependence of charge generation and bimolecular recombination fits for all blends. Mobility determined with hole-only devices measured in the SCLC regime for 1F-based blends. Derivation of eq 7 and the quasi-Fermi-level gradient and quasi-Fermi-level splitting as a function of current density. This material is available free of charge via the Internet at http://pubs.acs.org.

AUTHOR INFORMATION

Corresponding Author

*E-mail: neher@uni-potsdam.de.

Notes

The authors declare no competing financial interest.

ACKNOWLEDGMENTS

We acknowledge Eileen Katholing from Fraunhofer Institute for the help with the synthesis of 1F and 2F. Steve Albrecht thanks Jona Kurpiers and Ilja Lange from University of Potsdam for assistance with the BACE setup. The work was funded within the BMBF project PVCOMB (FKZ 03IS2151D). X-ray characterization and analysis by J.R.T. and H.A. were supported by DOE, OS, BES, MSE (DE-FG02-98ER45737). X-ray data were acquired at Beamlines 5.3.2.2 and 11.0.1.2 of the ALS, which is supported by DOE (DE-AC02-05CH1123). Thanks are given to David Kilcoyne at beamline 5.3.2.2 and Cheng Wang and Anthony Young at beamline 11.0.1.2 for assistance with data acquisition.

REFERENCES

(1) Krebs, F. C.; Espinosa, N.; Hösel, M.; Søndergaard, R. R.; Jørgensen, M. 25th Anniversary Article: Rise to Power − OPV-Based Solar Parks. *Adv. Mater.* **2014**, *26*, 29−39.

(2) He, Z.; Zhong, C.; Su, S.; Xu, M.; Wu, H.; Cao, Y. Enhanced Power-Conversion Efficiency in Polymer Solar Cells Using an Inverted Device Structure. *Nat. Photon.* **2012**, *6*, 591−595.

(3) Ye, L.; Zhang, S.; Ma, W.; Fan, B.; Guo, X.; Huang, Y.; Ade, H.; Hou, J. From Binary to Ternary Solvent: Morphology Fine-Tuning of D/A Blends in PDPP3T-Based Polymer Solar Cells. *Adv. Mater.* **2012**, *24*, 6335−6341.

(4) Cabanetos, C.; El Labban, A.; Bartelt, J. A.; Douglas, J. D.; Mateker, W. R.; Fréchet, J. M. J.; McGehee, M. D.; Beaujuge, P. M. Linear Side Chains in Benzo[1,2-b:4,5-b′]dithiophene−Thieno[3,4-c]pyrrole-4,6-dione Polymers Direct Self-Assembly and Solar Cell Performance. *J. Am. Chem. Soc.* **2013**, *135*, 4656−4659.

(5) Zhang, M.; Guo, X.; Zhang, S.; Hou, J. Synergistic Effect of Fluorination on Molecular Energy Level Modulation in Highly Efficient Photovoltaic Polymers. *Adv. Mater.* **2014**, *26*, 1118−1123.

(6) Gélinas, S.; Rao, A.; Kumar, A.; Smith, S. L.; Chin, A. W.; Clark, J.; van der Poll, T. S.; Bazan, G. C.; Friend, R. H. Ultrafast Long-Range Charge Separation in Organic Semiconductor Photovoltaic Diodes. *Science* **2014**, *343*, 512−516.

(7) Paraecattil, A. A.; Banerji, N. Charge Separation Pathways in a Highly Efficient Polymer: Fullerene Solar Cell Material. *J. Am. Chem. Soc.* **2014**, *136*, 1472−1482.

(8) Kaake, L. G.; Jasieniak, J. J.; Bakus, R. C.; Welch, G. C.; Moses, D.; Bazan, G. C.; Heeger, A. J. Photoinduced Charge Generation in a Molecular Bulk Heterojunction Material. *J. Am. Chem. Soc.* **2012**, *134*, 19828−19838.

(9) Wetzelaer, G.-J. A. H.; Van der Kaap, N. J.; Koster, L. J. A.; Blom, P. W. M. Quantifying Bimolecular Recombination in Organic Solar Cells in Steady State. *Adv. Energy Mater.* **2013**, *3*, 1130−1134.

(10) Maurano, A.; Hamilton, R.; Shuttle, C. G.; Ballantyne, A. M.; Nelson, J.; O'Regan, B.; Zhang, W.; McCulloch, I.; Azimi, H.; Morana, M.; et al. Recombination Dynamics as a Key Determinant of Open Circuit Voltage in Organic Bulk Heterojunction Solar Cells: A Comparison of Four Different Donor Polymers. *Adv. Mater.* **2010**, *22*, 4987−4992.

(11) Tress, W.; Corvers, S.; Leo, K.; Riede, M. Investigation of Driving Forces for Charge Extraction in Organic Solar Cells: Transient Photocurrent Measurements on Solar Cells Showing S-Shaped Current−Voltage Characteristics. *Adv. Energy Mater.* **2013**, *3*, 873−880.

(12) Dibb, G. F. A.; Muth, M. A.; Kirchartz, T.; Engmann, S.; Hoppe, H.; Gobsch, G.; Thelakkat, M.; Blouin, N.; Tierney, S.; Carrasco-Orozco, M. Influence of doping on charge carrier collection in normal and inverted geometry polymer: fullerene solar cells. *Sci. Rep.* **2013**, *3*, 3335.

(13) Vandewal, K.; Albrecht, S.; Hoke, E. T.; Graham, K. R.; Widmer, J.; Douglas, J. D.; Schubert, M.; Mateker, W. R.; Bloking, J. T.; Burkhard, G. F.; et al. Efficient Charge Generation by Relaxed Charge-Transfer States at Organic Interfaces. *Nat. Mater.* **2014**, *13*, 63−68.

(14) Bartelt, J. A.; Beiley, Z. M.; Hoke, E. T.; Mateker, W. R.; Douglas, J. D.; Collins, B. A.; Tumbleston, J. R.; Graham, K. R.; Amassian, A.; Ade, H.; et al. The Importance of Fullerene Percolation in the Mixed Regions of Polymer−Fullerene Bulk Heterojunction Solar Cells. *Adv. Energy Mater.* **2013**, *3*, 364−374.

(15) Peet, J.; Wen, L.; Byrne, P.; Rodman, S.; Forberich, K.; Shao, Y.; Drolet, N.; Gaudiana, R.; Dennler, G.; Waller, D. Bulk Heterojunction Solar Cells with Thick Active Layers and High Fill Factors Enabled by a Bithiophene-co-thiazolothiazole Push-Pull Copolymer. *Appl. Phys. Lett.* **2011**, *98*, 043301.

(16) Albrecht, S.; Schindler, W.; Kurpiers, J.; Kniepert, J.; Blakesley, J. C.; Dumsch, I.; Allard, S.; Fostiropoulos, K.; Scherf, U.; Neher, D. On the Field Dependence of Free Charge Carrier Generation and Recombination in Blends of PCPDTBT/PC70BM: Influence of Solvent Additives. *J. Phys. Chem. Lett.* **2012**, 640−645.

(17) Mingebach, M.; Walter, S.; Dyakonov, V.; Deibel, C. Direct and Charge Transfer State Mediated Photogeneration in Polymer-Fullerene Bulk Heterojunction Solar Cells. *Appl. Phys. Lett.* **2012**, *100*, 193302.

(18) Kniepert, J.; Schubert, M.; Blakesley, J. C.; Neher, D. Photogeneration and Recombination in P3HT/PCBM Solar Cells Probed by Time-Delayed Collection Field Experiments. *J. Phys. Chem. Lett.* **2011**, *2*, 700−705.

(19) Albrecht, S.; Janietz, S.; Schindler, W.; Frisch, J.; Kurpiers, J.; Kniepert, J.; Inal, S.; Pingel, P.; Fostiropoulos, K.; Koch, N.; et al. Fluorinated Copolymer PCPDTBT with Enhanced Open-Circuit Voltage and Reduced Recombination for Highly Efficient Polymer Solar Cells. *J. Am. Chem. Soc.* **2012**, *134*, 14932−14944.

(20) Proctor, C. M.; Albrecht, S.; Neher, D.; Nguyen, T. Q. Overcoming geminate recombination and enhancing extraction in solution-processed small molecule solar cells. *Adv. Energy Mater.* **2014**, DOI: 10.1002/aenm.201400230.

(21) Guo, J. M.; Ohkita, H.; Benten, H.; Ito, S. Charge Generation and Recombination Dynamics in Poly(3-hexylthiophene)/Fullerene Blend Films with Different Regioregularities and Morphologies. *J. Am. Chem. Soc.* **2010**, *132*, 6154−6164.

(22) Proctor, C. M.; Kuik, M.; Nguyen, T.-Q. Charge carrier recombination in organic solar cells. *Prog. Polym. Sci.* **2013**, *38*, 1941−1960.

(23) Rauh, D.; Deibel, C.; Dyakonov, V. Charge Density Dependent Nongeminate Recombination in Organic Bulk Heterojunction Solar Cells. *Adv. Funct. Mater.* **2012**, *22*, 3371−3377.

(24) Etzold, F.; Howard, I. A.; Forler, N.; Cho, D. M.; Meister, M.; Mangold, H.; Shu, J.; Hansen, M. R.; Mullen, K.; Laquai, F. The effect of solvent additives on morphology and excited-state dynamics in PCPDTBT:PCBM photovoltaic blends. *J. Am. Chem. Soc.* **2012**, *134*, 10569−10583.

(25) Juška, G.; Arlauskas, K.; Viliūnas, M.; Kočka, J. Extraction Current Transients: New Method of Study of Charge Transport in Microcrystalline Silicon. *Phys. Rev. Lett.* **2000**, *84*, 4946−4949.

(26) Baumann, A.; Lorrmann, J.; Rauh, D.; Deibel, C.; Dyakonov, V. A New Approach for Probing the Mobility and Lifetime of Photogenerated Charge Carriers in Organic Solar Cells Under Real Operating Conditions. *Adv. Mater.* **2012**, *24*, 4381−4386.

(27) Tanase, C.; Meijer, E. J.; Blom, P. W.; De Leeuw, D. M. Unification of the Hole Transport in Polymeric Field-Effect Transistors and Light-Emitting Diodes. *Phys. Rev. Lett.* **2003**, *91*, 216601.

(28) Steyrleuthner, R.; Bange, S.; Neher, D. Reliable Electron-Only Devices and Electron Transport in N-Type Polymers. *J. Appl. Phys.* **2009**, *105*, 064509.

(29) Mauger, S. A.; Chang, L.; Friedrich, S.; Rochester, C. W.; Huang, D. M.; Wang, P.; Moulé, A. J. Self-Assembly of Selective Interfaces in Organic Photovoltaics. *Adv. Funct. Mater.* **2013**, *23*, 1935−1946.

(30) van Bavel, S.; Sourty, E.; de With, G.; Frolic, K.; Loos, J. Relation between Photoactive Layer Thickness, 3D Morphology, and Device Performance in P3HT/PCBM Bulk-Heterojunction Solar Cells. *Macromolecules* **2009**, *42*, 7396−7403.

(31) Dibb, G. F. A.; Kirchartz, T.; Credgington, D.; Durrant, J. R.; Nelson, J. Analysis of the Relationship between Linearity of Corrected Photocurrent and the Order of Recombination in Organic Solar Cells. *J. Phys. Chem. Lett.* **2011**, *2*, 2407−2411.

(32) Shuttle, C. G.; Hamilton, R.; Nelson, J.; O'Regan, B. C.; Durrant, J. R. Measurement of Charge-Density Dependence of Carrier Mobility in an Organic Semiconductor Blend. *Adv. Funct. Mater.* **2010**, *20*, 698−702.

(33) Kniepert, J.; Lange, I.; van der Kaap, N. J.; Koster, L. J. A.; Neher, D. A Conclusive View on Charge Generation, Recombination, and Extraction in As-Prepared and Annealed P3HT:PCBM Blends: Combined Experimental and Simulation Work. *Adv. Energy Mater.* **2014**, DOI: 10.1002/aenm.201301401.

(34) Lange, I.; Kniepert, J.; Pingel, P.; Dumsch, I.; Allard, S.; Janietz, S.; Scherf, U.; Neher, D. Correlation between the Open Circuit

Voltage and the Energetics of Organic Bulk Heterojunction Solar Cells. *J. Phys. Chem. Lett.* **2013**, *4*, 3865−3871.
(35) Würfel, P. *Physics of Solar Cells: From Principles to New Concepts*; Wiley-VCH: Weinheim, Germany, 2005.
(36) Koster, L. J. A.; Mihailetchi, V. D.; Ramaker, R.; Blom, P. W. M. Light Intensity Dependence of Open-Circuit Voltage of Polymer: Fullerene Solar Cells. *Appl. Phys. Lett.* **2005**, *86*, 123509.
(37) Kirchartz, T.; Nelson, J. Meaning of Reaction Orders in Polymer:Fullerene Solar Cells. *Phys. Rev. B* **2012**, *86*, 165201.
(38) Blakesley, J. C.; Neher, D. Relationship between Energetic Disorder and Open-Circuit Voltage in Bulk Heterojunction Organic Solar Cells. *Phys. Rev. B* **2011**, *84*, 075210.
(39) Credgington, D.; Durrant, J. R. Insights from Transient Optoelectronic Analyses on the Open-Circuit Voltage of Organic Solar Cells. *J. Phys. Chem. Lett.* **2012**, *3*, 1465−1478.
(40) Gong, W.; Faist, M. A.; Ekins-Daukes, N. J.; Xu, Z.; Bradley, D. D. C.; Nelson, J.; Kirchartz, T. Influence of Energetic Disorder on Electroluminescence Emission in Polymer:Fullerene Solar Cells. *Phys. Rev. B* **2012**, *86*, 024201.
(41) Tress, W.; Leo, K.; Riede, M. Influence of Hole-Transport Layers and Donor Materials on Open-Circuit Voltage and Shape of I−V Curves of Organic Solar Cells. *Adv. Funct. Mater.* **2011**, *21*, 2140−2149.
(42) Mihailetchi, V. D.; Wildeman, J.; Blom, P. W. M. Space-Charge Limited Photocurrent. *Phys. Rev. Lett.* **2005**, *94*, 126602.
(43) Zhu, Y. B.; Ang, L. K. Analytical Re-Derivation of Space Charge Limited Current in Solids Using Capacitor Model. *J. Appl. Phys.* **2011**, *110*, 094514.
(44) Zhang, Y.; Zou, J.; Cheuh, C.-C.; Yip, H.-L.; Jen, A. K. Y. Significant Improved Performance of Photovoltaic Cells Made from a Partially Fluorinated Cyclopentadithiophene/Benzothiadiazole Conjugated Polymer. *Macromolecules* **2012**, *45*, 5427−5435.
(45) Li, Y.; Zou, J.; Yip, H.-L.; Li, C.-Z.; Zhang, Y.; Chueh, C.-C.; Intemann, J.; Xu, Y.; Liang, P.-W.; Chen, Y.; et al. Side-Chain Effect on Cyclopentadithiophene/Fluorobenzothiadiazole-Based Low Band Gap Polymers and Their Applications for Polymer Solar Cells. *Macromolecules* **2013**, *46*, 5497−5503.
(46) Collins, B. A.; Li, Z.; Tumbleston, J. R.; Gann, E.; McNeill, C. R.; Ade, H. Absolute Measurement of Domain Composition and Nanoscale Size Distribution Explains Performance in PTB7:PC71BM Solar Cells. *Adv. Energy Mater.* **2013**, *3*, 65−74.
(47) Koster, L. J. A. Charge Carrier Mobility in Disordered Organic Blends for Photovoltaics. *Phys. Rev. B* **2010**, *81*, 205318.
(48) Deibel, C.; Wagenpfahl, A.; Dyakonov, V. Origin of Reduced Polaron Recombination in Organic Semiconductor Devices. *Phys. Rev. B* **2009**, *80*, 075203.
(49) Zhu, Z.; Waller, D.; Gaudiana, R.; Morana, M.; Muhlbacher, D.; Scharber, M.; Brabec, C. Panchromatic Conjugated Polymers Containing Alternating Donor/Acceptor Units for Photovoltaic Applications. *Macromolecules* **2007**, *40*, 1981−1986.
(50) Gann, E.; Young, A. T.; Collins, B. A.; Yan, H.; Nasiatka, J.; Padmore, H. A.; Ade, H.; Hexemer, A.; Wang, C. Soft X-ray Scattering Facility at the Advanced Light Source with Real-Time Data Processing and Analysis. *Rev. Sci. Instrum.* **2012**, *83*, 045110.
(51) Kilcoyne, A. L. D.; Tyliszczak, T.; Steele, W. F.; Fakra, S.; Hitchcock, P.; Franck, K.; Anderson, E.; Harteneck, B.; Rightor, E. G.; Mitchell, G. E.; et al. Interferometer-Controlled Scanning Transmission X-Ray Microscopes at the Advanced Light Source. *J. Synchrot. Radiat.* **2003**, *10*, 125−136.
(52) Yan, H.; Wang, C.; McCarn, A. R.; Ade, H. Accurate and Facile Determination of the Index of Refraction of Organic Thin Films Near the Carbon Absorption Edge. *Phys. Rev. Lett.* **2013**, *110*, 177401.

nature materials

ARTICLES

PUBLISHED ONLINE: 17 NOVEMBER 2013 | DOI: 10.1038/NMAT3807

Efficient charge generation by relaxed charge-transfer states at organic interfaces

Koen Vandewal[1]*, Steve Albrecht[2], Eric T. Hoke[1], Kenneth R. Graham[1,3], Johannes Widmer[4], Jessica D. Douglas[5], Marcel Schubert[2], William R. Mateker[1], Jason T. Bloking[1], George F. Burkhard[1], Alan Sellinger[1†], Jean M. J. Fréchet[3,5], Aram Amassian[3], Moritz K. Riede[4†], Michael D. McGehee[1], Dieter Neher[2]* and Alberto Salleo[1]*

Interfaces between organic electron-donating (D) and electron-accepting (A) materials have the ability to generate charge carriers on illumination. Efficient organic solar cells require a high yield for this process, combined with a minimum of energy losses. Here, we investigate the role of the lowest energy emissive interfacial charge-transfer state (CT_1) in the charge generation process. We measure the quantum yield and the electric field dependence of charge generation on excitation of the charge-transfer (CT) state manifold via weakly allowed, low-energy optical transitions. For a wide range of photovoltaic devices based on polymer:fullerene, small-molecule:C_{60} and polymer:polymer blends, our study reveals that the internal quantum efficiency (IQE) is essentially independent of whether or not D, A or CT states with an energy higher than that of CT_1 are excited. The best materials systems show an IQE higher than 90% without the need for excess electronic or vibrational energy.

The mechanism of free charge carrier generation in synthetic organic semiconductors has generated substantial interest recently, as these materials show great promise for low-cost and large-area photovoltaics. In these materials, the lowest energy excited states are strongly bound excitons, which decay before dissociating into free charge carriers with appreciable yield. This fundamental hurdle has been overcome with the introduction of electron-donor/electron-acceptor (D/A) interfaces[1–3]. As opposed to devices consisting of neat organic semiconductors[4,5], free carriers are generated at such interfaces with a yield quasi-independent of photon energy within the spectral range of strong active layer absorption[6–11]. For the best performing materials systems, IQEs approaching and even exceeding 90% (refs 7–11) have been reached. However, free charge carrier generation at organic interfaces is typically associated with an energy loss, which ultimately reduces the power conversion efficiency of the system. Hence, a detailed understanding of the free charge carrier generation mechanisms at organic/organic interfaces, and the origin of the associated energy losses is of crucial importance for future rational design of D and A materials and interfaces.

Figure 1a shows schematically the possible pathways for the generation of free charge carriers on photoexcitation of the donor semiconductor into its excited manifold (D*; ref. 12). At the D/A interface, electron transfer from D* to A results in the formation of a CT state. This CT state can decay to the ground state (GS) or produce the desired charge-separated state (CS), which, unlike the CT state, is not coupled to the GS. In the CS state, the charge carriers have overcome the Coulomb binding energy and can freely migrate in the active layer. Optical transitions between the GS and CT state manifold are however possible and both CT absorption and CT emission at energies below the optical gap of D and A have been detected, albeit with low oscillator strength[13–15].

It has been proposed[16–18] that excess photon energy assists in the generation of free charge carriers. Delocalized, higher energy CT states, dissociating with a rate constant k_{CS}^{*}, are postulated in this case to be the main precursors of free charge carriers. According to this scenario the relaxed emissive CT state (CT_1) will act as a trap and the quantum yield for free carrier generation of this state is expected to be very low and strongly field dependent. If, however, relaxation within the CT state manifold to CT_1 is much faster than charge separation via these higher energy states ($k_{relax} \gg k_{CS}^{*}$), the free carrier yield will be exclusively determined by the competition between dissociation (rate constant k_{CS}) and recombination (rate constant k_f) of the thermally relaxed CT manifold. If free carrier generation follows this mechanism, its quantum yield and field dependence will not depend on photon energy, even for direct excitation into the CT state manifold. Rather, free charge carrier generation will be determined by the interfacial energy landscape, which connects the relaxed CT to the CS states.

By using femtosecond laser spectroscopy it was recently shown that photoexcitation dynamics depend on photon energy. Furthermore, transient absorption signals have been detected on timescales faster than relaxation within the CT manifold[17,18]. These measurements are suggestive of ultrafast CT splitting processes and invoke the role of 'hot' states, where excess energy provided by the energy level offsets between the neat materials is used to overcome the binding energy of interfacial CT states. However, the question

[1]Department of Materials Science and Engineering, Stanford University, 476 Lomita Mall, Stanford, California 94305, USA, [2]Institute of Physics and Astronomy, University of Potsdam, Karl-Liebknecht-Straße 24-25, 14476 Potsdam, Germany, [3]King Abdullah University of Science and Technology (KAUST), Thuwal 23955-6900, Saudi Arabia, [4]Institut für Angewandte Photophysik TU Dresden, George-Bähr-Strasse 1, 01062, Dresden, Germany, [5]Department of Chemistry, University of California, 727 Latimer Hall, Berkeley, California 94720, USA. †Present addresses: Department of Chemistry and Geochemistry, Colorado School of Mines, Golden, Colorado 80401, USA (A.S.); Department of Physics, University of Oxford, Clarendon Laboratory, Parks Road, Oxford OX1 3PU, UK (M.K.R.). *e-mail: vandewal@stanford.edu; neher@uni-potsdam.de; asalleo@stanford.edu

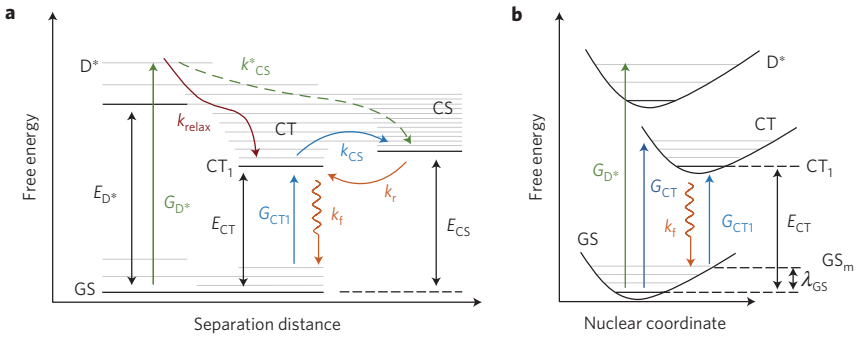

Figure 1 | Energetics of the relevant states at a D/A interface. a, State diagram. Absorption of a photon with energy higher than E_{D*} generates the donor excited state D* at a rate G_{D*}. There are several possible pathways for the generation of a CS state. Pathways with rate constants k^*_{CS} bypass the vibrationally relaxed and lowest energy CT state (CT_1) and compete with thermal relaxation (k_{relax}). CT_1 can decay radiatively (k_f) to the GS or dissociate (k_{CS}), forming CS. The inverse of the latter process, population of CT_1 from CS, occurs at a rate k_r. **b**, Potential energy surfaces of GS, and low-energy CT and D* states. Higher energy electronic CT and D* states are omitted for clarity. Optical excitation into CT_1 (G_{CT1}) occurs on excitation with a photon energy $E_{CT} - \lambda_{GS}$, from the vibrationally excited ground state GS_m. Such transitions from higher energy ground states are the inverse of CT emission, which peaks at photon energy $E_{CT} - \lambda_{GS}$.

remains as to the extent by which these 'hot' effects influence the actual photovoltaic device performance. Further, it is unclear whether CT_1 is always necessarily strongly bound ($E_{CS} - E_{CT} \gg kT$, where k is the Boltzmann constant and T the temperature) or whether there exists the possibility in some D/A systems that CT_1 is sufficiently delocalized to ensure efficient dissociation of this state.

This work aims at determining whether charge separation at D/A heterojunctions illuminated by sunlight is mainly preceded by the formation of a thermally relaxed CT state (CT_1) or whether it predominantly occurs via higher energy, more delocalized CT states, bypassing CT_1. To elucidate to what extent the 'hot' CT states play a role in the charge carrier generation mechanism, a determination of the quantum yield and field dependence of charge generation as a function of excitation energy, down to selective excitation of CT_1, is necessary.

Here, we present measurements of the field dependence of charge carrier generation on direct excitation of the CT state manifold. The presence of such field dependence is taken as a hallmark of the need for a driving force to dissociate CT states into free charge carriers. To investigate whether photon energy in excess of the CT_1 energy can provide this driving force, we perform a detailed analysis of electroluminescence emission spectra and external quantum efficiency (EQE) spectra. Sensitive techniques allow us to determine the quantum yield of carrier generation by CT_1 and compare it with the carrier generation yield for higher energy D, A and CT excitations. We study a number of D/A combinations including polymer:fullerene, small-molecule:C_{60} and polymer:polymer blends with varying photovoltaic performance and, surprisingly, find that the field dependence and absolute value of the quantum yield for free carrier generation for all studied D/A interfaces has little dependence on whether or not the initially generated excited state has energy in excess of the energy of CT_1. Importantly, we demonstrate that a high and field-independent IQE does not necessarily require that free carrier formation proceeds primarily via higher energy 'hot' states. In fact, present state-of-the-art bulk heterojunction layers produce a high yield of free charge carriers (>90%) because of very efficient dissociation of CT_1 into free charge carriers.

First we compare two polymer:$PC_{61}BM$ model systems, which, on excitation of the donor polymer, have respectively a relatively inefficient and field-dependent charge carrier generation mechanism (MEH-PPV:$PC_{61}BM$), and an efficient and field-independent charge carrier generation mechanism (PBDTTPD:$PC_{61}BM$). Figure 2a,b shows current density–voltage (J–V) curves under solar illumination and in the dark of photovoltaic devices prepared with these blends as active layers. The devices have a power conversion efficiency of ~1.3% (MEH-PPV:$PC_{61}BM$) and ~7% (PBDTTPD:$PC_{61}BM$). Device preparation details can be found in the Supplementary Information. The field dependence of the charge carrier generation mechanism on photoexcitation of the D*, A* and CT manifold is investigated by time-delayed collection field (TDCF) experiments. The total extracted charge carrier density using this technique is a direct measure of the free carrier generation yield at a certain bias voltage[19,20]. The relative yield, as a function of bias voltage and excitation energy, is shown on the right axes in Fig. 2a,b, allowing comparison with the photocurrent, that is, the difference between the J–V curves taken in darkness and under illumination. For the MEH-PPV:$PC_{61}BM$ device, the dependence of the photocurrent on voltage tracks the dependence of the charge carrier generation yield on voltage, indicating that its performance is limited by its strongly field-dependent charge carrier generation mechanism, consistent with previous reports on PPV:$PC_{61}BM$ devices[21,22]. In contrast, for the PBDTTPD:$PC_{61}BM$ device, the yield is field independent, and reaches almost unity[11]. On varying the excitation photon energy, we can selectively excite mainly the D* and/or A* and CT state manifold. For the MEH-PPV:$PC_{61}BM$ and PBDTTPD:$PC_{61}BM$ devices, a TDCF signal could still be detected at excitation photon energies as low as 1.38 eV and 1.53 eV, respectively. This energy is well below the optical gap of the neat materials comprising the blend, and charge carrier generation at this photon energy is the result of direct CT state excitation (see also Fig. 3). Importantly, we observe virtually no differences in the field dependence of charge carrier generation. This is valid, irrespective of whether the charge generation mechanism is field dependent (MEH-PPV:$PC_{61}BM$) or field independent (PBDTTPD:$PC_{61}BM$).

This result is consistent with previous work, in which the CT state manifold was directly excited and no differences in charge generation efficiency[23], IQE (ref. 24) and field dependence of EQE (ref. 25) were found when compared with higher energy D* and A* excitation. However, as all of these experiments are limited in sensitivity and spectral range, they do not access the lowest energy CT_1 state exclusively and therefore do not provide a clear answer as to whether the CT_1 state is the exclusive free carrier precursor. Indeed, owing to the significant reorganization of the nuclei following optical excitation, transitions into the CT state manifold will dominantly result in a vibrationally excited CT state (Fig. 1b). No experiment has yet compared quantum

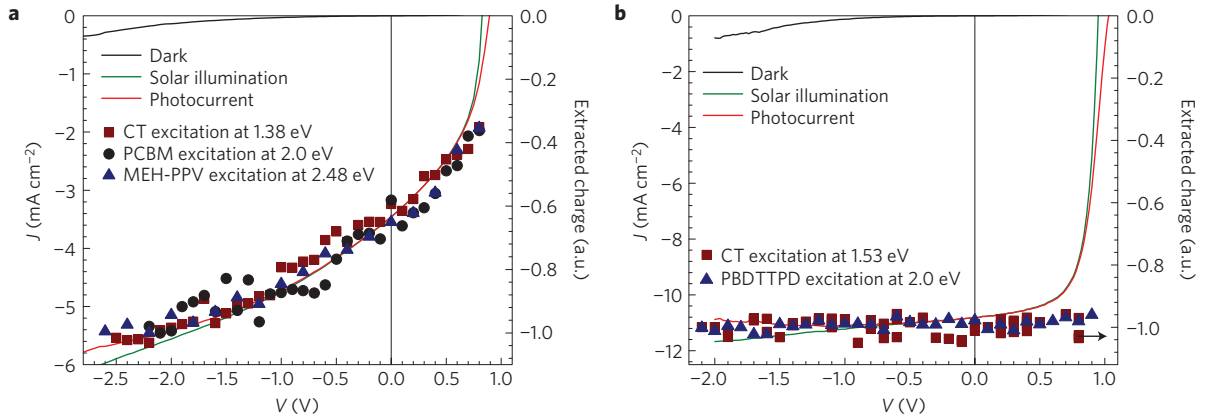

Figure 2 | Current density and relative number of photogenerated charge carriers as a function of applied voltage. a,**b**, *J*–*V* curves in the dark and under solar illumination for a solution-processed MEH-PPV:$PC_{61}BM$ device (**a**) and for a PBDTTPD:$PC_{61}BM$ device (**b**). The relative number of generated charge carriers, extracted in the TDCF experiment as a function of applied bias, is shown on the right axis, for dominant excitations of D*, A* and those directly into the CT band (at 1.38 eV for MEH-PPV:$PC_{61}BM$ and 1.5 eV for PBDTTPD:$PC_{61}BM$).

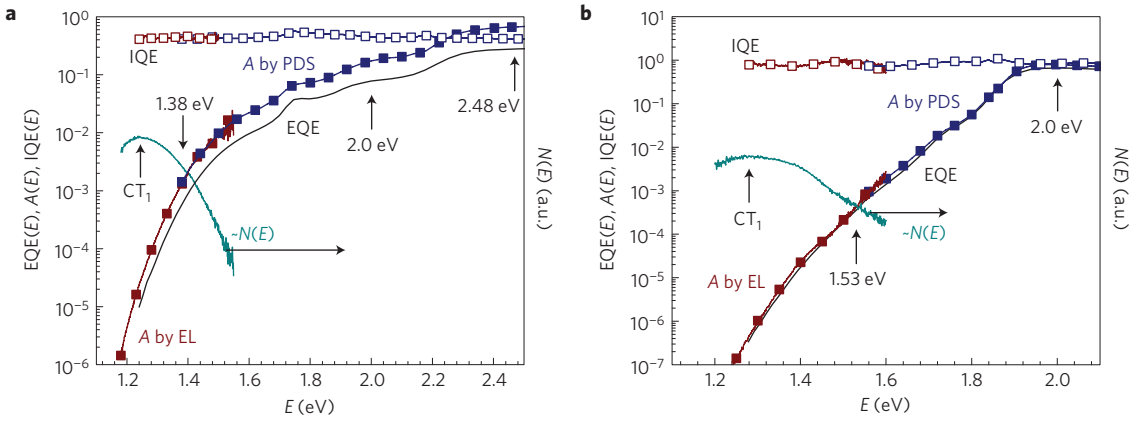

Figure 3 | Determination of IQE(*E*) in the spectral region of CT emission for polymer:fullerene photovoltaic devices. EQE(*E*) (black line), electroluminescence (EL) emission spectra *N*(*E*) (cyan line) and the high energy part of the *A*(*E*) spectra (blue line filled squares) are measured directly on photovoltaic devices and active layers. In the very weakly absorbing region, the *A*(*E*) spectra are reconstructed using *N*(*E*) as described in the main text, and are matched to the *A*(*E*) spectra measured by PDS in the overlapping region (red line, filled squares). **a**,**b**, Data for a solution-processed MEH-PPV:$PC_{61}BM$ device (**a**) and for a PBDTTPD:$PC_{61}BM$ device (**b**). The IQE(*E*) spectra (open squares) of the devices are calculated as EQE(*E*)/*A*(*E*). The arrows indicate the $GS_m \rightarrow CT_1$ transition at 1.24 eV for MEH-PPV:$PC_{61}BM$ and 1.28 eV for PBDTTPD:$PC_{61}BM$. The arrows indicate the excitation energies at which the TDCF experiments shown in Fig. 2 were performed.

yields of free carrier generation of the reorganized, emissive and completely relaxed CT state (CT_1) with that of higher energy CT, D* or A* excitations. This is therefore precisely what we aim to do in this work.

Direct excitation of CT_1 exclusively involves a photon having an energy $E_{CT} - \lambda_{GS}$ (Fig. 1b) exciting an electron from a higher energy level of the GS manifold, GS_m, to CT_1. This transition is severely suppressed as compared with the already weak CT absorption by the low probability of thermal population of GS_m ($\exp(-\lambda_{GS}/kT) = 4 \times 10^{-4}$ for a typical value of $\lambda_{GS} = 0.2$ eV). Hence, the direct measurement of the $GS_m \rightarrow CT_1$ absorption is very challenging. As a result, here we follow another approach and reconstruct the absorption spectrum $A(E)$ in this low-energy region by measuring the inverse optical process, that is, radiative decay from the thermally relaxed CT manifold, which is dominated by the $CT_1 \rightarrow GS_m$ transition at a photon energy $E_{CT} - \lambda_{GS}$. When the population of the excited states, including the vibrational states within the CT state manifold, are in thermal equilibrium during the emission experiment, the fraction of absorbed photons $A(E)$ at any given photon energy E is related to the flux of photons emitted at this energy, $N(E)$, by the following equation[26,27]

$$A(E) \sim N(E)E^{-2}\exp\left(\frac{E}{kT}\right) \quad (1)$$

In the Supplementary Information, we summarize how Boltzmann occupation of the excited- and ground-state energy levels and optical reciprocity lead to equation (1). Equation (1) provides us with a determination of the relative optical absorption strength in the spectral region where CT emission is measurable. A sensitive measurement of the EQE spectrum over the same spectral region will allow us to compare the IQE of CT_1 excitation, which occurs at the photon energy where the CT emission peaks, with the IQE of excitation into higher energy states.

In Fig. 3a,b we reconstruct the absorption spectrum of the MEH-PPV:$PC_{61}BM$ and PBDTTPD:$PC_{61}BM$ devices, for photon energies corresponding to CT_1 excitation and higher. The emission spectra N(E), also shown in Fig. 3a,b, are obtained by electroluminescence

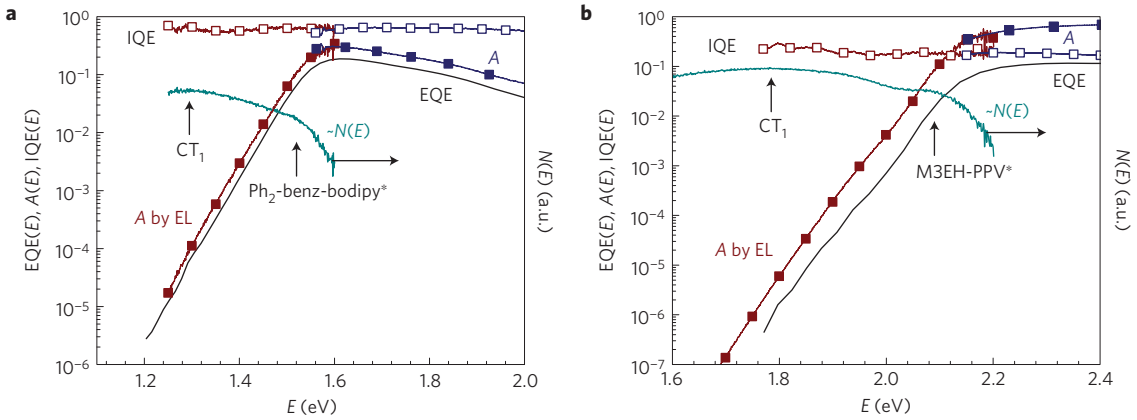

Figure 4 | Determination of IQE(*E*) in the spectral region of CT emission for small-molecule:C_{60} and polymer:polymer photovoltaic devices. EQE(*E*) (black line), electroluminescence (EL) emission spectra *N*(*E*) (cyan line) and *A*(*E*) spectra (blue line filled squares) are measured directly on photovoltaic devices. *A*(*E*) spectra are reconstructed using *N*(*E*) as described in the main text and are matched to the *A*(*E*) spectra measured with the aid of an integrating sphere in the strongly absorbing spectral region (red line, filled squares). **a**,**b**, Data for a vacuum processed Ph_2-benz-bodipy:C_{60} small-molecule device (**a**) and for a M3EH-PPV:CN-ether-PPV polymer:polymer device (**b**). The IQE(*E*) spectra (open squares) of the devices are calculated as EQE(*E*)/*A*(*E*). The arrows indicate the $GS_m \rightarrow CT_1$ transition at 1.30 eV for Ph_2-benz-bodipy:C_{60} and 1.78 eV for M3EH-PPV:CN-ether-PPV. Radiative decay from donor excitations is still observable in the emission spectrum at 1.55 eV and 2.07 eV, respectively.

measurements using an as low as possible injection current $<30\,mA\,cm^{-2}$, to ensure quasi-equilibrium conditions. Indeed, the spectral shape is independent of the injection current in the low injection current regime (see Supplementary Information). In the measurable energy range, electroluminescence spectra consist of CT emission alone. The >10 ns lifetime of the injected free charge carriers in the devices during the electroluminescence experiment makes it nearly certain that thermal equilibrium within the CT state manifold is reached before radiative decay to the GS, thereby obeying Kasha's rule[28]. Under this condition, we can use equation (1) to calculate the spectral shape of *A*(*E*) in the region of CT emission. The absorption spectrum at higher energies is still weak, but sufficiently high to be detectable by the sensitive photothermal deflection spectroscopy (PDS). Matching the spectra in the overlapping region allows us to set *A*(*E*) determined by electroluminescence experiments to an absolute scale. In the MEH-PPV:PC_{61}BM case, we use the overlapping region to determine the temperature (*T*) of the active layer during the emission experiments, using equation (1), to be 35 °C, slightly above room temperature, as expected[29]. For all devices studied in this work, we use similar injection currents and assume $T = 35\,°C$. Details about possible uncertainties introduced by the uncertainty on the temperature of the active layer during the emission experiment can be found in the Supplementary Information.

The EQE(*E*) spectrum of both photovoltaic devices is measured by a sensitive lock-in technique. The IQE(*E*), calculated as EQE(*E*)/*A*(*E*), is shown together with the EQE(*E*) in Fig. 3a,b. Note that the use of a sensitive EQE(*E*) measurement set-up allows us to detect a photocurrent signal even at very low photon energies corresponding to the peak of CT emission, that is, the optical transition between GS_m and CT_1 (Fig. 1b). Within the sensitivity of the method, the IQE for this transition is essentially identical to the IQE at higher energies including D* or A* excitation. This observation is valid for the MEH-PPV:PC_{61}BM active layer, which has a field-dependent charge generation yield as well as for the PBDTTPD:PC_{61}BM active layer, which has a field-independent IQE of about 90% (ref. 11). If the yield for free charge carrier generation via CT_1 were strongly suppressed as compared with the higher energy states, one would expect a strongly decreasing IQE(*E*) near the photon energy at which CT emission peaks, contrary to our observations.

To investigate the generality of this result for other types of D/A interface, we study devices made with a vacuum-processed small-molecule Ph_2-benz-bodipy:C_{60} blend[30,31], as well as a M3EH-PPV:CN-ether-PPV (ref. 32) polymer:polymer blend as the active layer. For both materials systems, the CT state energy is close to the optical gap of the donor. Therefore, population of D* during the electroluminescence experiment becomes probable, and the electroluminescence spectra of these devices, shown in Fig. 4, contain a band related to emission from excited donor (at 1.55 eV and 2.07 eV, for the small-molecule and polymer:polymer device respectively) in addition to the CT emission band (centred at 1.30 eV and 1.78 eV, respectively). As a result we are able to reconstruct *A*(*E*) using the electroluminescence emission spectrum and equation (1), up to photon energies where the donor material is strongly absorbing. A measurement of *A*(*E*) in the strongly absorbing region by conventional integrating sphere ultraviolet–visible spectroscopy is used to set *A*(*E*) to absolute scale, down to excitation into CT_1. For both the vacuum-processed and polymer:polymer blend devices, IQE(*E*) does not vary significantly within the energy range from CT_1 up to donor excitation.

To broaden the validity of our result, we studied eight additional organic photovoltaic devices based on D:A blends with varying performances and IQEs and found comparable results (see Supplementary Information). The IQE(*E*) remains virtually constant for excitation energies ranging from the CT emission peak—and in some cases even for excitation energies lower than the emission peak (Supplementary Figs 7–9)—to the CT absorption peak. These measurements indicate that, for the studied D:A blends, energy in excess of the CT_1 energy, including reorganization energy within the CT manifold, does not affect the IQE. Free charge carriers are generated and collected with equal efficiency by excitation directly into CT_1, as by excitation into higher energy, unrelaxed CT states or even D* or A* states.

Even though femtosecond transient spectroscopy has shown the existence of higher energy, faster dissociating pathways at these organic/organic interfaces[17,18,33], our results indicate that population and subsequent dissociation of these higher energy CT states directly following photoinduced electron transfer is not responsible for most of the generated free charge carriers. We propose that, owing to ultrafast relaxation within the CT band, most photoexcitations into higher energy states relax within the

CT manifold and are in thermal equilibrium with CT_1. As a consequence, for D/A interfaces at which CT_1 is a bound state, the overall IQE at all photon energies, down to exclusive CT_1 excitation, will be significantly lower than unity, and electric field dependent (for example, MEH-PPV:PC_{61}BM, M3EH-PPV:CN-ether-PPV). The general validity of our result across materials systems and cell efficiencies suggests that excess energy provided by D*, A* or higher energy CT excitation cannot by exploited to improve the free carrier yield. However, the remarkably high (>90%) and field-independent yield of free charge carrier generation via CT_1 in the PBDTTPD:PC_{61}BM and PCDTBT:PC_{71}BM (see Supplementary Information) devices shows that materials systems exist, in which CT_1 is only weakly bound, yielding efficient >90% charge generation at all photon energies equal to and larger than the energy of CT_1. Therefore, understanding and control over the nanostructural factors that allow an interfacial energy landscape in which CT_1 is sufficiently delocalized, with an energy close to the energy of the CS state, is of fundamental importance for designing and developing new, better performing D/A pairs for organic photovoltaics.

Methods

Photovoltaic devices comprising polymer:fullerene and polymer:polymer active layers were prepared in the standard device configuration ITO/PEDOT:PSS (40 nm)/active layer/(7 nm) Ca/(200 nm) Al, using their optimized D/A ratio and solution concentration (more details specific to the materials system used can be found in the Supplementary Information). Small-molecule:C_{60} bulk heterojunction devices were vacuum deposited in the configuration ITO/hole conductor/active layer/electron conductor/Al. Specific details such as D/A stoichiometry and used electron on hole transporting layers can be found in the Supplementary Information.

TDCF experiments use a pulsed excitation (5.5 ns pulse duration, 500 Hz repetition rate) with a diode-pumped, Q-switched Nd:YAG laser (NT242,EKSPLA) frequency tripled to pump an optical parametric oscillator for wavelength tuning. The current through the photovoltaic device was measured using a 50 Ω resistor placed in series and was recorded with a Yokogawa DL9140 oscilloscope. An Agilent 81150A pulse generator with a very fast slew rate was used to apply the pre- and collection bias to the sample. Note that we can rule out any residual parasitic wavelengths (that is, 1,064, 512 or 355 nm or the optical parametric oscillator idler if signal was used) by carefully checking the beam quality at the position of the sample with a spectrophotometer. The collection bias was kept low at ∼−3 V. This ensures that the leakage during extraction is small and at the same time the loss due to non-geminate recombination during extraction is prevented for the studied systems.

Electroluminescence spectra were measured using a spectrograph (Acton Research SpectraPro 500i) equipped with a silicon CCD (charge-coupled device) array detector (Hamamatsu), and were corrected for the instrument response and the conversion from wavelength to energy.

Sensitive EQE measurements were taken at short circuit under focused monochromated illumination from a 100 W tungsten lamp modulated by an optical chopper (∼280 Hz). The current from the devices was measured as a function of photon energy using a lock-in amplifier (Stanford Instruments SR 830) and compared with the current obtained from a calibrated Ge or Si photodiode.

PDS was performed using a home-built set-up: chopped (3.333 Hz) monochromated light from a 150 W Xe lamp is focused onto the sample. Perfluorohexane (C_6F_{14}, 3M Fluorinert FC-72) is used as the deflection medium. The deflection of a HeNe laser (633 nm) is detected by a position-sensitive Si detector, connected to a Stanford Research Systems SR830 lock-in amplifier. PDS samples of active layers were spin-coated on quartz substrates, from the same solution from which the devices were fabricated. The PDS spectra were set to absolute scale by matching the spectra with integrating sphere measurements on a Varian Cary 5000 spectrophotometer. $A(E)$ in the weakly absorbing subgap region was calculated by the simplified assumption of the incoming light waves passing through the active layer twice owing to reflection from the metallic cathode.

Received 22 May 2013; accepted 8 October 2013; published online 17 November 2013

References

1. Deibel, C. & Dyakonov, V. Polymer–fullerene bulk heterojunction solar cells. *Rep. Prog. Phys.* **73,** 096401 (2010).
2. Riede, M., Mueller, T., Tress, W., Schueppel, R. & Leo, K. Small-molecule solar cells—status and perspectives. *Nanotechnology* **19,** 424001 (2008).
3. Li, G., Zhu, R. & Yang, Y. Polymer solar cells. *Nature Photon.* **6,** 153–161 (2012).
4. Arkhipov, V. I., Emelianova, E. V. & Bässler, H. Hot exciton dissociation in a conjugated polymer. *Phys. Rev. Lett.* **82,** 1321–1324 (1999).
5. Tong, M., Coates, N. E., Moses, D., Heeger, A. J., Beaupré, S. & Leclerc, M. Charge carrier photogeneration and decay dynamics in the poly (2, 7-carbazole) copolymer PCDTBT and in bulk heterojunction composites with PC_{70}BM. *Phys. Rev. B* **81,** 125210 (2010).
6. Vandewal, K. *et al.* Quantification of quantum efficiency and energy losses in low bandgap polymer: Fullerene solar cells with high open-circuit voltage. *Adv. Funct. Mater.* **22,** 3480–3490 (2012).
7. Hou, J., Chen, H.-Y., Zhang, S., Chen, R. I., Yang, Y., Wu, Y. & Li, G. Synthesis of a low band gap polymer and its application in highly efficient polymer solar cells. *J. Am. Chem. Soc.* **131,** 15586 (2009).
8. Liang, Y. *et al.* For the bright future-bulk heterojunction polymer solar cells with power conversion efficiency of 7.4%. *Adv. Mater.* **22,** E135–E138 (2010).
9. Park, S. H. *et al.* Bulk heterojunction solar cells with internal quantum efficiency approaching 100%. *Nature Photon.* **3,** 297–302 (2009).
10. Lin, L-Y. *et al.* A donor–acceptor–acceptor molecule for vacuum-processed organic solar cells with a power conversion efficiency of 6.4%. *Chem. Commun.* **48,** 1857–1859 (2012).
11. Bartelt, J. A. *et al.* The importance of fullerene percolation in the mixed regions of polymer–fullerene bulk heterojunction solar cells. *Adv. Energy Mater.* **3,** 364–374 (2013).
12. Brédas, J. L., Norton, J. E., Cornil, J. & Coropceanu, V. Molecular understanding of organic solar cells: The challenges. *Acc. Chem. Res.* **42,** 1691–1699 (2009).
13. Benson-Smith, J. J. *et al.* Formation of a ground-state charge-transfer complex in polyfluorene/[6, 6]-phenyl-c61 butyric acid methyl ester (PCBM) blend films and its role in the function of polymer/PCBM solar cells. *Adv. Funct. Mater.* **17,** 451–457 (2007).
14. Loi, M. A. *et al.* Charge transfer excitons in bulk heterojunctions of a polyfluorene copolymer and a fullerene derivative. *Adv. Funct. Mater.* **17,** 2111–2116 (2007).
15. Vandewal, K., Tvingstedt, K., Gadisa, A., Inganäs, O. & Manca, J. V. On the origin of the open-circuit voltage of polymer–fullerene solar cells. *Nature Mater.* **8,** 904–909 (2009).
16. Ohkita, H. *et al.* Charge carrier formation in polythiophene/fullerene blend films studied by transient absorption spectroscopy. *J. Am. Chem. Soc.* **130,** 3030–3042 (2008).
17. Bakulin, A. A. *et al.* The role of driving energy and delocalized states for charge separation in organic semiconductors. *Science* **335,** 1340–1344 (2012).
18. Grancini, G. *et al.* Hot exciton dissociation in polymer solar cells. *Nature Mater.* **12,** 29–33 (2013).
19. Kniepert, J., Schubert, M., Blakesley, J. C. & Neher, D. Photogeneration and recombination in P3HT/PCBM solar cells probed by time-delayed collection field experiments. *J. Phys. Chem. Lett.* **2,** 700–705 (2011).
20. Albrecht, S. *et al.* On the field dependence of free charge carrier generation and recombination in blends of PCPDTBT/PC70BM: Influence of solvent additives. *J. Phys. Chem. Lett.* **3,** 640–645 (2012).
21. Mihailetchi, V. D., Koster, L. J. A., Hummelen, J. C. & Blom, P. W. M. Photocurrent generation in polymer–fullerene bulk heterojunctions. *Phys. Rev. Lett.* **93,** 216601 (2004).
22. Mingebach, M., Walter, S., Dyakonov, V. & Deibel, C. Direct and charge transfer state mediated photogeneration in polymer–fullerene bulk heterojunction solar cells. *Appl. Phys. Lett.* **100,** 193302 (2012).
23. Parkinson, P., Lloyd-Hughes, J., Johnston, M. B. & Herz, L. M. Efficient generation of charges via below-gap photoexcitation of polymer–fullerene blend films investigated by terahertz spectroscopy. *Phys. Rev. B* **78,** 115321 (2008).
24. Lee, J. *et al.* Charge transfer state versus hot exciton dissociation in polymer–fullerene blended solar cells. *J. Am. Chem. Soc.* **132,** 11878–11880 (2010).
25. Van der Hofstad, T. G. J., Di Nuzzo, D., van den Berg, M., Janssen, R. A. J. & Meskers, S. C. J. Influence of photon excess energy on charge carrier dynamics in a polymer–fullerene solar cell. *Adv. Energy Mater.* **2,** 1095–1099 (2012).
26. Würfel, P. The chemical potential of radiation. *J. Phys. C* **15,** 3967–3985 (1982).
27. Würfel, P. *The Physics of Solar Cells* (Wiley, 2007).
28. Kasha, M. Characterization of electronic transitions in complex molecules. *Discuss. Faraday Soc.* **9,** 14–19 (1950).
29. Lupton, J. M. Frequency up-conversion as a temperature probe of organic opto-electronic devices. *Appl. Phys. Lett.* **80,** 186–188 (2002).
30. Gresser, R., Hummert, M., Hartmann, H., Leo, K. & Riede, M. Synthesis and characterization of near-infrared absorbing benzannulated Aza-BODIPY dyes. *Chem. Eur. J.* **17,** 2939–2947 (2011).
31. Meiss, J., Holzmueller, F., Gresser, R., Leo, K. & Riede, M. Near-infrared absorbing semitransparent organic solar cells. *Appl. Phys. Lett.* **99,** 193307 (2011).

32. Yin, C. *et al.* Tuning of the excited-state properties and photovoltaic performance in PPV-based polymer blends. *J. Phys. Chem. C* **112,** 14607–14617 (2008).
33. Jailaubekov, A. E. *et al.* Hot charge-transfer excitons set the time limit for charge separation at donor/acceptor interfaces in organic photovoltaics. *Nature Mater.* **12,** 66–73 (2013).

Acknowledgements

This publication was supported by the Center for Advanced Molecular Photovoltaics (Award No KUS-C1-015-21) and the Department of Energy, Laboratory Directed Research and Development funding, under contract DE-AC02-76SF00515. The PCDTBT used in this work was provided by St-Jean Photochemicals. M.K.R. acknowledges financial support by the BMBF through project 03IP602 and J.W. acknowledges support from the Heinrich-Böll-Stiftung. S.A. and M.S. acknowledge financial support by the BMBF within PVcomB (FKZ 03IS2151D) and the DFG (SPP 1355). D.N. thanks the DFG for financially supporting a travel grant. K.R.G. and A.A. acknowledge SABIC for a post-doctoral fellowship. The authors thank J. Kurpiers for technical assistance with the TDCF set-up.

Author contributions

K.V., D.N., S.A. and A. Salleo designed the experiments. S.A. prepared devices for TDCF experiments and performed the TDCF experiments. K.V., W.R.M., E.T.H., K.R.G., J.T.B., M.S., J.W. and M.K.R. prepared photovoltaic devices and optimized their processing parameters for photovoltaic performance. E.T.H. and J.T.B. adjusted the EQE and electroluminescence measurement set-ups for the detection of weak signals, crucial for this work. K.V., E.T.H. and K.R.G. measured the EQE and electroluminescence spectra. K.V. measured the PDS spectra. J.D.D. synthesized PBDTTPD. A. Sellinger, J.M.J.F., A.A., M.K.R. and M.D.M. supervised their team members involved in the project. D.N. and A. Salleo supervised the overall project. All authors contributed to analysis and writing.

Additional information

Supplementary information is available in the online version of the paper. Reprints and permissions information is available online at www.nature.com/reprints. Correspondence and requests for materials should be addressed to K.V., D.N. or A.S.

Competing financial interests

The authors declare no competing financial interests.

On the Efficiency of Charge Transfer State Splitting in Polymer:Fullerene Solar Cells

Steve Albrecht, Koen Vandewal, John R. Tumbleston, Florian S. U. Fischer, Jessica D. Douglas, Jean M. J. Fréchet, Sabine Ludwigs, Harald Ade, Alberto Salleo, and Dieter Neher**

In the past years the overall power conversion efficiency of organic polymer:fullerene solar cells has been steadily increasing[1] and internal quantum efficiencies approaching 90–100% have been reported.[2,3] Most of these efficient solar cells exhibit high fill factors (*FF*), suggesting that losses due to geminate recombination can be avoided and that losses due to non-geminate recombination become only important at voltages close to the open-circuit voltage,[4] provided that the active layer is sufficiently thin (typically around 100 nm). Recently, techniques have become available to distinguish geminate from non-geminate recombination and thus selectively address the efficiency of free charge carrier generation.[5,6] Some systems show a relatively low quantum yield with a significant field-dependence of free charge carrier generation,[6,7] while others, including the workhorse P3HT:PCBM, show a high quantum yield for free charge carrier generation with no field-dependence.[5,8]

Such an insensitivity of free carrier generation to the internal electric field is rather counterintuitive, as the formation of spatially-separated electrons and holes in their respective material phases (the charge-separated state, CS) proceeds via interfacial electron-hole pairs (geminate pairs), thought to be bound by Coulombic interaction.[9] Direct evidence for the formation of strongly correlated interfacial charge pairs came from electron spin resonance studies on polymer-fullerene blends.[10,11] As most donor-acceptor blends exhibit additional sub-bandgap absorption and emission features, it was proposed that these interfacial excitations are charge transfer states (CT states) coupled to the ground state via radiative transitions.[12–14]

The reasons for highly efficient charge generation despite the existence of Coulombically bound geminate pairs is subject of ongoing debate. Correlations have been found between the free carrier generation yield and the energy difference $\Delta E_{CS}^{eff} = E_{S1} - E_{CS}$. Here E_{S1} is the lowest singlet state on either the donor or the acceptor and E_{CS} is determined by the difference between the electron affinity of the acceptor EA_A and the ionization potential of the donor IP_D. ΔE_{CS}^{eff} is often referred to as driving force for charge generation and values larger than several 100 meV were reported for high performance systems.[15–17] A charge carrier generation mechanism was proposed in which energy delivered to the system upon singlet exciton formation is partially used to form electronically and/or vibrationally excited CT states, which then possess a sufficient amount of kinetic energy to overcome the Coulomb barrier. This concept has also been used to explain lower photocurrents and fill factors in blends of polymers with higher adduct fullerenes,[18] which, owing to their high lying LUMO levels, enable devices with large open-circuit voltages. Recent ultrafast pump-probe results[19–22] suggested that free carrier generation in P3HT:PCBM and other materials indeed proceeds faster and hence seemingly more efficient via such hot CT excitations, due to a higher degree of delocalization of these states.[19] On the other hand, it is less clear whether charge generation in a working solar cell proceeds exclusively via such excited CT states (route 2 in **Figure 1**) or whether pathways comprising thermalized CT states (route 1) are of equal importance. It was for example reported that the internal quantum efficiency (IQE)[12] and field-dependence[23] for charge generation in P3HT:PCBM blends is insensitive to excitation wavelength over a wide range of photon energies, including those that directly excite low-lying CT states. Recently, strong evidence was found that the thermalized CT manifold (coupled to the lowest energy CT state CT_1) shows the same yield and field-dependence as higher energy excitations.[24] Identification of the charge carrier generation pathway relevant to solar cell performance is interesting from the viewpoint of a basic understanding of these devices but is also highly desirable for guiding future design towards highly-efficient cells.

S. Albrecht, Prof. D. Neher
Institut für Physik und Astronomie
Universität Potsdam
Karl-Liebknecht-Str. 24-25, 14476 Potsdam, Germany
E-mail: neher@uni-potsdam.de
Dr. K. Vandewal, Prof. A. Salleo
Department of Materials Science and Engineering
496 Lomita Mall, CA, 94305, Stanford University
Stanford, USA
E-mail: koen.vandewal@iapp.de
Dr. K. Vandewal
Institut für Angewandte Photophysik
Technische Universität Dresden
George-Bähr-Straße 1, 01069 Dresden, Germany
Dr. J. R. Tumbleston, Prof. H. Ade
Department of Physics
NCSU, Raleigh, NC 27695-8202, USA
F. S. U. Fischer, Prof. S. Ludwigs
IPOC-Functional Polymers
University of Stuttgart
Pfaffenwaldring 55, 70569 Stuttgart, Germany
Dr. J. D. Douglas, Prof. J. M. J. Fréchet
Department of Chemistry
University of California
727 Latimer Hall, CA 94720, Berkeley, USA

DOI: 10.1002/adma.201305283

© 2014 WILEY-VCH Verlag GmbH & Co. KGaA, Weinheim

ADVANCED MATERIALS
www.advmat.de

Materials Views
www.MaterialsViews.com

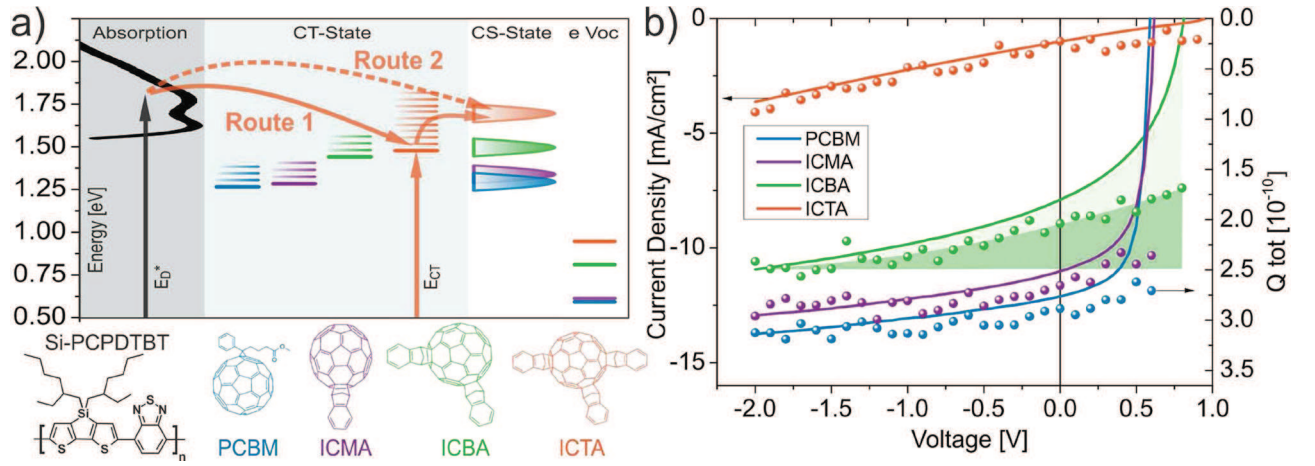

Figure 1. (a) Energy diagram and chemical structure for Si-PCPDTBT blended with different fullerenes (PCBM, ICMA, ICBA, ICTA) indicating the blends main absorption, the CT state manifold, the position of the charge separated (CS) states, and e·V_{oc}. The CS states were calculated from solution cyclic voltammetry measurements. Because of the uncertainty in the CS energy, the CS states are depicted as energetically distributed with a characteristic broadening of 100 meV. For simplicity, two different generation routes are indicated for the ICTA blend only. Route 2: The donor excitation E_{D*} leads to separated charges via electronically/vibronically excited CT states directly (dashed arrow). In this case, the direct CT state excitation E_{CT} should give a strongly different generation efficiency compared to E_{D*}. Route 1: First the excitation thermalizes in the CT manifold and then gets separated (solid arrows). (b) Steady state *J–V* curves under AM 1.5G illumination with 100 mW/cm^2 (left scale) compared to the total charge (Q_{tot}) from TDCF excited at 650 nm (right scale) for fullerene blends with Si-PCPDTBT. The light and dark coloured areas highlight the losses due to non-geminate recombination and field-dependent generation, respectively.

Here, we present a comprehensive study of free carrier generation in bulk heterojunction systems with carefully tuned energetics. Two polymers with different HOMO and S_1 energies, Si-PCPDTBT and PBDTTPD, were combined with four different fullerene derivatives, PCBM, ICMA and higher adduct fullerenes ICBA, and ICTA, having different LUMO energies. We combine external quantum efficiency (EQE) and sensitive photothermal deflection spectroscopy (PDS) together with time-delayed collection field (TDCF) experiments to measure the yield and field-dependence of free carrier generation over a wide range of bias and excitation energy. Possible changes in morphology and crystallinity when using different fullerenes are investigated by resonant polarized soft X-ray scattering (P-SoXs) and grazing incident wide angle X-ray scattering (GIWAXS). Information on the energy of the charge separated state was gained from cyclic voltammetry and in-situ spectroelectrochemistry in solution and on blend films.

We find that for the Si-PCPDTBT:fullerene blends, the crystallinity, molecular orientation, domain size, and purity are barely changed when PCBM is replaced by higher adduct fullerenes, rendering this system ideal for studying the interrelation between blend energetics and free charge generation. For all blends, the generation yield and field-dependence is not affected when the excitation energy is varied from above band-gap to direct CT state excitation. Instead, the ability of the CT state to split is dictated by the energetic offset between the relaxed CT state and the charge separated state.

Figure 1a displays the chemical structures and energy levels of Si-PCPDTBT and the four fullerene derivatives as determined with solution cyclic voltammetry. Blend film absorption spectra are presented together with the CT state manifold, with the position of the lowest bar indicating the energy of the CT state, E_{CT}, as determined by a combined fitting of the external quantum efficiency (EQE) and electroluminescence (EL) spectra of blend films.[2,25] The Figure also includes estimates for E_{CS} using values for the polymer HOMO and the fullerene LUMOs measured with CV (see the SI for further detail). These values are in good agreement to those given in the literature.[26,27] As the data were acquired in solution, the plotted value for E_{CS} is most applicable to charges moving within amorphous intermixed domains. We are aware of the fact that exact HOMO and LUMO energies are sensitive to the layer morphology,[18] and we will address this issue later. We note a continuous increase of the CT energy with increasing fullerene LUMO value, as expected. An exception is the case of Si-PCPDTBT blended with ICTA, where the CS state approaches the energy of the excited donor, E_{S1}, and the CT state and polymer singlet exciton state are in resonance, resulting in an E_{CT} limited by the optical gap of the Si-PCPDTBT.

Figure 1b shows the steady state *J–V* curves under AM 1.5G solar illumination of the photovoltaic devices using the donor polymer Si-PCPDTBT. The results for PBDTTPD blends with three different fullerenes and information on the blend energetics can be found in the Supporting Information (Figures S3, S4 and Table S1). For Si-PCPDTBT, the highest performance was obtained when using PCBM as acceptor, reaching an efficiency of 4.4%. The use of ICMA, ICBA and ICTA as acceptors increased V_{oc}, but lowered FF, J_{sc}, and overall device efficiency (see **Table 1**). Our *J–V* data are in good quantitative agreement to recently published values, containing data on the same material systems.[26] The same trend is seen for PBDTTPD-based blends, where we measure higher V_{oc}'s but also strongly decreased J_{sc}'s and FF's with higher adduct fullerenes.

To designate the main cause of the decreased FF and J_{sc} in multi-adduct fullerene blends as either being field-dependent free carrier generation or enhanced non-geminate recombination we performed TDCF experiments. TDCF is applied directly to solar cell devices, with a short ns laser pulse generating

© 2014 WILEY-VCH Verlag GmbH & Co. KGaA, Weinheim

Table 1. Energy levels from cyclic voltammetry of single component solutions and energy levels from in-situ spectroelectrochemistry data of blend films together with photovoltaic properties. E_{ct} is the energy of the CT state, and λ the reorganization energy, both determined from optical spectroscopy (see Figure S1). Values in brackets are taken from Ref. [26] as comparison. Performance values are averages over 6 devices.

	Polymer HOMO [eV]	Fullerene LUMO [eV]	J_{sc} [mA/cm^2]	V_{oc} [mV]	FF [%]	PCE [%]	E_{CT} [eV]	λ [eV]
Si-PCPDTBT	4.97 (5.0)							
PCBM		3.70 (3.74)						
ICMA		3.68 (3.70)						
ICBA		3.53 (3.55)						
ICTA		3.33 (3.36)						
Si-PCPDTBT:PCBM	4.86	3.88	11.6	591	64	4.38	1.26	0.27
Si-PCPDTBT:ICMA	4.86	3.81	10.8	618	60	4.00	1.28	0.27
Si-PCPDTBT:ICBA	4.86	3.60	7.7	810	44	2.75	1.45	0.22
Si-PCPDTBT:ICTA	4.86	3.40	0.95	947	25	0.22	1.49	0.22

charges with the device at a certain applied bias voltage typical for normal solar cell operation.[7] After a very short delay time (10 ns) a high reverse bias is applied to collect all generated charges. The delay time of 10 ns ensures that all polaron-pairs have dissociated before the extraction voltage is applied.[28,29] The extraction voltage is chosen to be high enough to prevent non-geminate recombination during extraction. By adjusting the laser fluence, a charge density similar to one sun condition can be generated and losses due to non-geminate recombination within the short delay time can be excluded. In our initial experiments, an excitation wavelength of 650 nm ($E_{D^*} = 1.91$ eV) has been chosen, which excites mainly the S_1 state of the polymer.[21] All Si-PCPDTBT-based blends exhibit an almost similar absorption at this wavelength (see Figure S2). Thus, the total free charge carrier density (Q_{tot}) extracted from TDCF is an absolute measure of the free carrier generation efficiency, allowing simultaneous comparison with the *J–V* curves of all four blends. This comparison is shown in Figure 1b. All Si-PCPDTBT based devices show a field dependent free carrier generation yield. Comparison of Q_{tot} with the *J–V* curves indicates that the reduction in current and FF when using higher adduct fullerenes is primarily due to a reduced yield and increasing field-dependence of free charge carrier generation rather than being caused by more rapid non-geminate recombination. Noticeably, our experiments did not reveal a pronounced increase of the bimolecular recombination coefficient when replacing PCBM by higher adduct fullerenes though we measured a slight decrease in mobility (see SI). This causes the slight increase in losses due to non-geminate processes when PCBM is replaced by ICBA as indicated by the light coloured area in Figure 1.

It is generally recognized that the morphology, i.e., number of phases, domain size, size distribution, domain purity, as well as the donor orientation with respect to the acceptor interface is crucial for device performance.[30,31] To investigate if in this case morphology is a major factor responsible for differences in free carrier generation yield, we analysed the nanomorphology of the Si-PCPDTBT:fullerene blends with resonant soft x-ray scattering. **Figure 2** shows polarized soft X-ray scattering (P-SoXS) together with grazing incidence wide angle x-ray scattering (GIWAXS) results for the four different blends based on Si-PCPDTBT. All blends are characterized by similar log-normal distributions of spatial frequencies along with similar total scattering intensity,

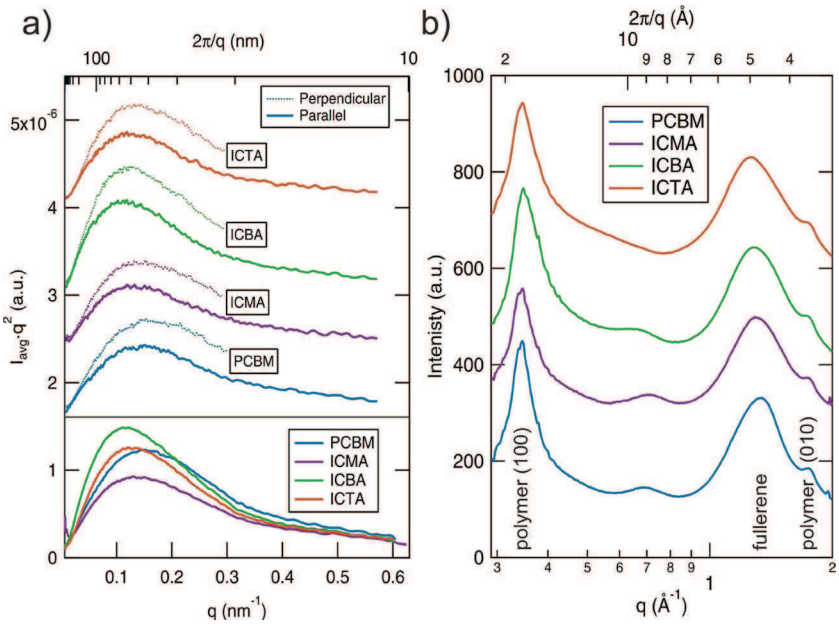

Figure 2. P-SoXS and GIWAXS data for Si-PCPDTBT blends with different fullerenes **a)** Lorentz corrected P-SoXS sector averages for 282.5 eV photon energy. The upper traces (vertically offset for clarity) reveal anisotropic scattering with greater intensity perpendicular compared to parallel to the photon electric field polarization for all samples. The lower traces correspond to circular integration of the 2-D data. **b)** Circular averages of the GIWAXS 2-D scattering data shown in Figure S7. GIWAXS circular averages have been shifted vertically for comparison. In the circular average the main peaks at q = 0.35 and 1.35 (Å^{-1}) refer to the polymer lamellar and the fullerene reflection, respectively.

© 2014 WILEY-VCH Verlag GmbH & Co. KGaA, Weinheim

ADVANCED MATERIALS
www.advmat.de

Materials Views
www.MaterialsViews.com

which scales with the square of the average composition variations in the samples.[32] The relative composition variations are 0.98, 0.84, 1.0, and 0.94 for Si-PCPDTBT with PCBM, ICMA, ICBA, and ICTA, respectively. Except for the somewhat lower value observed for the ICMA blend, the relative purity of the fullerene and polymer rich domains and/or their volume fraction is thus rather constant. Also, the median characteristic length scale between domains with similar composition is very similar for all blends with 30, 30, 35, and 33 nm for Si-PCPDTBT blended with PCBM, ICMA, ICBA, and ICTA, respectively. All blends also show scattering anisotropy with greater intensity perpendicular to the photon electric field (s-scattering) compared to parallel (p-scattering). Scattering anisotropy corresponds to preferential in-plane orientation correlations of the polymer (edge-on versus face-on) relative to the fullerene domains.[31,33] It is similar in sign and magnitude for all samples and differences in molecular orientation can thus be eliminated as a contributing factor. The shape and overall intensity of the GIWAXS scattering profiles are similar for all samples, indicating that differences in polymer lamellar and π–π ordering as well as fullerene aggregation are minimal. Overall, the minor differences in active layer morphology observed cannot explain the observed differences in charge generation.

Consequently, changes in the charge generation yield must be intimately related to interfacial energetics. In order to elucidate this point further, TDCF experiments were performed on Si-PCPDTBT:PCBM with photon energies of 2.48 eV (500 nm) which directly excites the S_4 state,[21] 1.48 eV (840 nm) which is at the S_1 absorption onset and 1.25 eV (990 nm), which is 0.25 eV below the optical gap of Si-PCPDTBT. The excitation at 1.25 eV thus exclusively excites the CT state. We varied the laser fluence according to the absorption to generate the same amount (±10% deviation) of free charges at every photon energy. Normalization of the total charge at high reverse fields then gives a sensitive measure of the field-dependence of free charge formation at different excitation energies. As shown by **Figure 3**a, varying the excitation energy over a 1.0 eV range, below and above the absorption onset, has essentially no effect on the field dependence of generation. The same conclusion was reached when performing TDCF experiments on Si-PCPDTBT blends with higher adduct fullerenes (Figure 3b and 3c). This result is highly remarkable as rather small changes in the fullerene energy levels (and with that of the driving force) led to considerable changes in the field-dependent photogeneration. It suggests that the energy released upon the split-up of the polymer singlet excitons at the interface does not appreciably promote free carrier generation. The same conclusion is reached for blends with PBDTTPD and different fullerenes, where we find the field dependence of generation to be unaffected by the excitation energy, too (see Figure S4).[24]

To substantiate this claim, we determined the IQE spectra over an even wider wavelength range from the sensitive measurements of the EQE and of the absorption A(E) in conjunction with optical modelling (see Figure 3d). For the Si-PCPDTBT blended with PCBM and ICMA, a CT band can be observed at energies well below the optical gap of the pure donor and acceptor in both the A(E) and EQE spectra around 1.26 eV and 1.28 eV, respectively (see Table S1). For Si-PCPDTBT blended

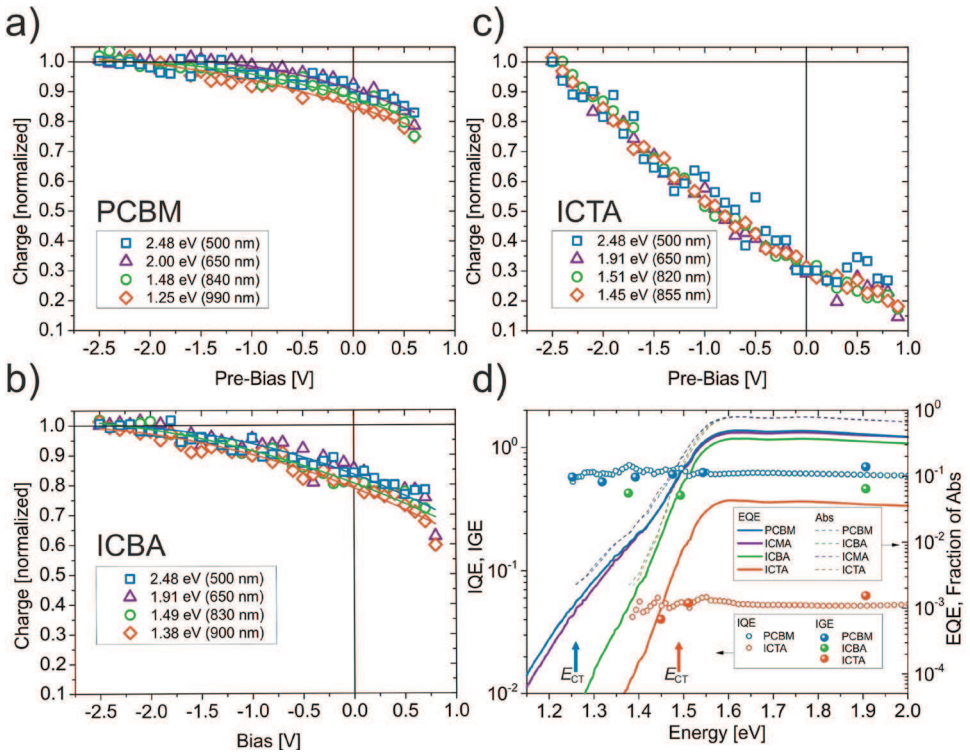

Figure 3. Normalized total charge versus pre-bias for different excitation wavelengths for Si-PCPDTBT blended with (**a**) PCBM, (**b**) ICBA, and (**c**) ICTA. **(d)** Spectra of EQE, IQE and fraction of modeled absorption as well as the internal generation efficiency (IGE) deduced from TDCF for Si-PCPDTBT:fullerene blends.

© 2014 WILEY-VCH Verlag GmbH & Co. KGaA, Weinheim

with ICBA and ICTA, the CT band is partially masked by the absorption of the pure materials and the CT energy was determined to be at 1.45 eV and 1.49 eV, respectively. In addition, we determined the internal generation efficiency (IGE) as defined by the number of charges generated at short circuit (measured with TDCF) divided by A(E). Thus, the IGE is comparable to the IQE but free from losses due to non-geminate recombination which may reduce the steady state IQE at short circuit. For all material systems (including blends of PBDTTPD with different fullerenes, see SI), the steady state IQE(E) and IGE(E) are independent (within the sensitivity of the used methods) of excitation energy, irrespective of whether excitation occurs in the donor, acceptor, or CT state.

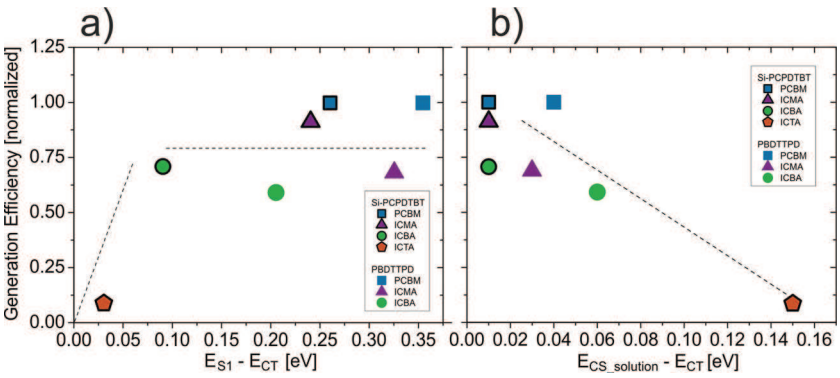

Figure 4. Charge generation efficiency at short circuit for Si-PCPDTBT and PBDTTPD blended with different fullerenes, normalized to the efficiency of the respective PCBM blend, as function of the energy difference of (a) the lowest singlet state (E_{S1}) and the charge transfer state (E_{CT}) and (b) the charge separated state as measured from solution CV ($E_{cs\_solution}$) and the charge transfer state. The dotted gray line is drawn as a guide to the eye.

The experiments described in this paper show that the free carrier generation after direct excitation of the CT state proceeds with a similar field-dependence and yield as for exciting the polymer and fullerene singlet excitons. This result indicates that the energy gain upon singlet exciton dissociation has only a minor effect on the yield of the CT state split-up into free charge carriers. Thus, our results show that the efficiency of free charge generation must be largely determined by the split-up of relaxed CT-states (Route 1), in accordance to previous work.[24]

Our data also show that replacing PCBM with higher adduct fullerenes has a pronounced effect on the total yield and field-dependence of free charge carrier generation. For Si-PCPDTBT, these changes are rather gradual when going from PCBM to ICBA, while a strong decrease in generation efficiency and a much larger field-dependence of generation is seen when using ICTA in accordance to Faist et al.[34] There are several possible causes for this effect: A less favourable microstructure for bis-PCBM over PCBM in blends with Si-PCPDTBT has been reported, with the absence of polymer nanofibers in blends with bis-PCBM.[35] Here, we do not find evidence that higher adduct fullerenes affect the fullerene agglomeration in Si-PCPDTBT, though we find a slightly decreased mobility when higher adducts are used (see Figure S6 in the SI). It was also shown that the aggregation of the PCBM molecules is beneficial for solar cell performance as this increases the electron affinity by more than 100 meV.[18,36] This downward shift in LUMO energy was proposed to drive electrons out of the intermixed regions into pure fullerene aggregates, where they become energetically stabilized.

To address this point we have determined HOMO und LUMO energies in our blend films with in-situ spectroelectrochemistry. Detailed information is given in the experimental section and the supporting information. In-situ spectroelectrochemistry allows us to determine energy levels more precisely than the conventional method of determining onset or half wave potentials purely from cyclic voltammograms.[37] The energy levels of the polymer and the fullerenes in the blends were determined from the $E_{Abs.Onset}$ [V vs. Fc/Fc^+], i.e., the potential corresponding to the onset of changes in the characteristic absorption bands of the neutral or charged states. The HOMO and LUMO energies were calculated from the absorption onsets of the first polymer oxidation and first fullerene reduction, respectively, for all blends; resulting values are given in Table 1.

Values of E_{CS} calculated therefrom are compared to E_{CS} determined from solution data in Figure S8-9. Although absolute CS-energies in solution and in the blend are difficult to compare (see Figure S12), due to differences in the local environment (solution versus solid state) and the technique used to determine E_{HOMO} and E_{LUMO}, they allow a reasonable comparison between the different fullerenes. Notably, we find that the stabilization energy (defined as the difference between the fullerene LUMO in the solid-state blend and in solution) decreases significantly when PCBM is exchanged by ICMA, while both blends exhibit quite similar generation efficiencies. On the other hand, similar values of the stabilization energy are measured for ICBA and ICTA, despite large differences in device performance. We therefore conclude that a reduction in the stabilization energy cannot fully account for the poorer performance of the higher adduct fullerenes. We propose the efficiency of CT-split-up in our blends to be intimately connected to the nature and energy of the relaxed CT instead. **Figure 4** relates the total photogenerated charge at short circuit to the difference between E_{CT} and E_{S1} or $E_{CS,solution}$ for both polymer systems. Firstly, a sharp decrease of the generation efficiency is seen when the CT state approaches the pure excitonic states, as in Si-PCPDTBT:ICTA (Figure 4a). At such small energy offsets the CT state and excitonic states are in resonance, mixing their wavefunctions giving the CT state a more localized and bound character.[38] Related to this, significant singlet exciton recycling from the CT state has been reported for blends with higher adduct fullerenes.[2,26] Secondly, we find that the generation efficiency decreases when the energy difference between the CS state and CT state becomes considerably large (Figure 4b), related to a binding energy of the relaxed CT state well exceeding the thermal energy.

In conclusion, for a variety of blends, we find the yield and field-dependence of free charge generation to be unaffected by excitation energy including direct CT excitation. This finding is independent of whether the blends exhibit a small or a large

© 2014 WILEY-VCH Verlag GmbH & Co. KGaA, Weinheim

difference between the singlet exciton energy and the energy of the charge separated state. We propose that generation proceeds via the split-up of low-lying CT states irrespective of the initial excitation energy (route 1 in Figure 1). In accordance with this interpretation, we find the efficiency of free carrier generation to be correlated with the energy of the relaxed CT state relative to the energy of the donor exciton and of the charge separated state. Here, Si-PCPDTBT blended with different fullerene adducts seems to be a model system, with unaffected domain size, domain purity, molecular orientation and crystallinity when PCBM is replaced by higher adduct fullerenes. Our findings open up new guidelines for future material design as new high efficiency materials that require a minimum energetic offset between CT and CS state while keeping the ΔE_{CS}^{eff} as small as possible.

Experimental Section

Sample Preparation: Sample preparation was described in detail in Ref. [7]. Just briefly Si-PCPDTBT (Mn = 9 kDa, PDI = 3.32) and PBDTTPD (Mn = 36 kDa, PDI = 1.8) were provided by Konarka and synthesised at UC Berkeley,[39] respectively. PCBM (phenyl-C_{61}-butyric acid methyl ester) (Solenne), ICMA (indene C_{60} mono-adduct) (Lumtec), ICBA (indene C_{60} bis-adduct) (Lumtec) or ICTA (indene C_{60} tris-adduct) (Solarischem) were mixed with the donor polymers in a 1:1.5 ratio donor:acceptor. 85 nm thick films of Si-PCPDTBT:fullerene blends were spun from 70 °C hot solutions (36 mg/mL) in dichlorobenzene. 80 nm thick films of PBDTTPD:fullerene blends were spun from ~100 °C solutions (20 mg/mL) in chlorobenzene.

Cyclic Voltammetry and In-Situ Spectroelectrochemistry: All electrochemical experiments were performed with an Autolab PGSTAT101 potentiostat (Metrohm, Germany) in a three electrode glass-cell under argon atmosphere at room temperature. The HOMO and LUMO values were calculated from the half-wave potentials (referenced to the formal potential of the internal redox standard Fc/Fc^+)[40] assuming that the energy level of Fc/Fc^+ is at −4.8 eV under the vacuum level.[41] For further experimental details we refer to the supplementary information.

Photothermal Deflection Spectroscopy: PDS was performed as described in Ref. [24].

Solar Cell Performance, External Quantum Efficiency, and Time Delayed Collection Field: is described in Ref [7]. For TDCF measurements we can rule out any residual parasitic laser wavelengths (i.e., 1064, 512, or 355 nm, or the OPO idler if signal was used) by carefully checking the beam quality at the position of the sample with a spectrophotometer. Also, the conversion efficiency of the OPO at the double pump frequency around 710 nm is close to zero. Thus, only blends having a suitable EQE above 750 nm can be measured in the sub band-gap region.

Internal Quantum and Generation Efficiency: The (IQE) was calculated by dividing the EQE by fraction of absorption in the active layer. The absorption coefficient as a function of photon energy α(E) below the band-gap of the donor polymer and the fullerene was measured by PDS. The fraction of absorption A(E) in the active layer of the solar cell device was modelled via α(E) with a transfer matrix formalism,[42] taking into account the multi-reflections and interference of all layers in the solar cell stack. Additionally, we calculated A(E) by the simplified assumption of the incoming wave passing through the active layer twice due to reflection from the metallic cathode, according to $A(E) = 1 - e^{(-2\alpha(E)d)}$ with α and d being the absorption coefficient and the active layer thickness, respectively. In this way the modelled IQE values can be quantitatively compared to calculations without the need of additional optical constants (e.g., the electrodes), which may cause errors to the IQE in the sub band-gap region. From TDCF experiments, the IQE of charge generation in the absence of transport or non-geminate recombination losses is determined (assigned here as the internal generation efficiency, IGE) as function of excitation energy.

Polarized Soft X-ray Scattering: P-SoXS characterization was conducted at Beamline 11.0.1.2 of the Advanced Light Source (ALS)[43] in the soft X-ray energy regime (~280 eV, see Figure S7 for material contrast). A section of film from the PEDOT:PSS-coated glass substrates was floated onto 1.5 × 1.5 mm silicon nitride windows. The 1-D averaged intensity is multiplied by q^2 (i.e., Lorentz correction), which corresponds to an azimuthal integration of the 2-D data.

Scanning Transmission X-ray Microscopy: STXM was conducted at Beamline 5.3.2.2 of the ALS.[44] During measurement, the chamber was filled with 1/3 ATM He.

Grazing Incidence Wide Angle X-ray Scattering: GIWAXS was conducted at Beamline 7.3.3. of the ALS[45] using a Dectris Pilatus 1 M photon counting detector. Blend films were measured at an incident angle of ~0.14°, above the critical angle so the X-ray beam penetrated to the substrate. The photon energy used for GIWAXS was 10 keV. Air scatter, which provides a background signal, was reduced using helium gas.

Supporting Information

Supporting Information is available from the Wiley Online Library or from the author.

Acknowledgements

The authors thankfully acknowledge Dr. Sybille Allard and Prof. Ullrich Scherf for providing access to Si-PCPDTBT (synthesized by Konarka). S.A. acknowledges Matthias Gohlke, Jona Kurpiers and Marcel Schubert from University of Potsdam for help with the optical constants, TDCF and EQE setup, respectively. F.F. and S.L. thank Dr. Adrian Ruff for measuring CV of the fullerene derivatives in solution and for his help with the electrochemical setups. This work was supported by the BMBF within the PVcomB (FKZ 03IS2151D), the DFG within the Priority Program SPP 1355 and the Center for Advanced Molecular Photovoltaics (award no. KUS-C1-015-21). K.V. and D.N. gratefully acknowledge the DFG for supplying a travel grant. X-ray characterization and analysis by JT and HA were supported by DOE, OS, Basic Energy Science, MSE (DE-FG02-98ER45737). S.L. thanks the DFG for funding of an Emmy Noether Grant, further support was given by the EU-network Smartonics. Data were acquired at Beamlines 5.3.2.2, 7.3.3, and 11.0.1.2 of the ALS, which is supported by DOE (DE-AC02-05CH1123). Thanks are given to David Kilcoyne at beamline 5.3.2.2, Alexander Hexemer and Eric Schaible at beamline 7.3.3, and Cheng Wang and Anthony Young at beamline 11.0.1.2 for assistance with data acquisition. Terry McAfee is acknowledged for acquisition of GIWAXS data.

Received: October 24, 2013
Revised: January 6, 2014
Published online: February 27, 2014

[1] M. A. Green, K. Emery, Y. Hishikawa, W. Warta, E. D. Dunlop, *Prog. Photovolt. Res. Appl.* **2013**, *21*, 827–837.
[2] E. T. Hoke, K. Vandewal, J. A. Bartelt, W. R. Mateker, J. D. Douglas, R. Noriega, K. R. Graham, J. M. J. Fréchet, A. Salleo, M. D. McGehee, *Adv. Energy Mater.* **2013**, *3*, 220–230.
[3] A. K. K. Kyaw, D. H. Wang, V. Gupta, J. Zhang, S. Chand, G. C. Bazan, A. J. Heeger, *Adv. Mater.* **2013**, *25*, 2397–2402.
[4] X. Guo, N. Zhou, S. J. Lou, J. Smith, D. B. Tice, J. W. Hennek, R. P. Ortiz, J. T. L. Navarrete, S. Li, J. Strzalka, L. X. Chen, R. P. H. Chang, A. Facchetti, T. J. Marks, *Nat. Photon.* **2013**, *7*, 825–833.
[5] J. Kniepert, M. Schubert, J. C. Blakesley, D. Neher, *J. Phys. Chem. Lett.* **2011**, *2*, 700–705.

© 2014 WILEY-VCH Verlag GmbH & Co. KGaA, Weinheim

[6] D. Credgington, F. C. Jamieson, B. Walker, T.-Q. Nguyen, J. R. Durrant, *Adv. Mater.* **2012**, *24*, 2135–2141.
[7] S. Albrecht, S. Janietz, W. Schindler, J. Frisch, J. Kurpiers, J. Kniepert, S. Inal, P. Pingel, K. Fostiropoulos, N. Koch, D. Neher, *J. Am. Chem. Soc.* **2012**, *134*, 14932–14944.
[8] M. Mingebach, S. Walter, V. Dyakonov, C. Deibel, *Appl. Phys. Lett.* **2012**, *100*.
[9] P. W. M. Blom, V. D. Mihailetchi, L. J. A. Koster, D. E. Markov, *Adv. Mater.* **2007**, *19*, 1551–1566.
[10] N. S. Sariciftci, L. Smilowitz, A. J. Heeger, F. Wudl, *Science* **1992**, *258*, 1474–1476.
[11] J. Behrends, A. Sperlich, A. Schnegg, T. Biskup, C. Teutloff, K. Lips, V. Dyakonov, R. Bittl, *Phys. Rev. B* **2012**, *85*, 125206.
[12] J. Lee, K. Vandewal, S. R. Yost, M. E. Bahlke, L. Goris, M. A. Baldo, J. V. Manca, T. V. Voorhis, *J. Am. Chem. Soc.* **2010**, *132*, 11878–11880.
[13] M. Presselt, F. Herrmann, S. Shokhovets, H. Hoppe, E. Runge, G. Gobsch, *Chem. Phys. Lett.* **2012**, *542*, 70–73.
[14] K. Vandewal, K. Tvingstedt, A. Gadisa, O. Inganas, J. V. Manca, *Nat. Mater.* **2009**, *8*, 904–909.
[15] T. Clarke, A. Ballantyne, F. Jamieson, C. Brabec, J. Nelson, J. Durrant, *Chem. Comm.* **2009**, *0*, 89–91.
[16] D. C. Coffey, B. W. Larson, A. W. Hains, J. B. Whitaker, N. Kopidakis, O. V. Boltalina, S. H. Strauss, G. Rumbles, *J. Phys. Chem. C* **2012**, *116*, 8916–8923.
[17] H. Ohkita, S. Cook, Y. Astuti, W. Duffy, S. Tierney, W. Zhang, M. Heeney, I. McCulloch, J. Nelson, D. D. C. Bradley, J. R. Durrant, *J. Am. Chem. Soc.* **2008**, *130*, 3030–3042.
[18] S. Shoaee, S. Subramaniyan, H. Xin, C. Keiderling, P. S. Tuladhar, F. Jamieson, S. A. Jenekhe, J. R. Durrant, *Adv. Funct. Mater.* **2013**, DOI: 10.1002/adfm.201203148.
[19] A. A. Bakulin, A. Rao, V. G. Pavelyev, P. H. M. van Loosdrecht, M. S. Pshenichnikov, D. Niedzialek, J. Cornil, D. Beljonne, R. H. Friend, *Science* **2012**, *335*, 1340–1344.
[20] I. A. Howard, R. Mauer, M. Meister, F. Laquai, *J. Am. Chem. Soc.* **2010**, *132*, 14866–14876.
[21] G. Grancini, M. Maiuri, D. Fazzi, A. Petrozza, H. J. Egelhaaf, D. Brida, G. Cerullo, G. Lanzani, *Nat. Mater.* **2013**, *12*, 29–33.
[22] S. D. Dimitrov, A. A. Bakulin, C. B. Nielsen, B. C. Schroeder, J. Du, H. Bronstein, I. McCulloch, R. H. Friend, J. R. Durrant, *J. Am. Chem. Soc.* **2012**, *134*, 18189–18192.
[23] T. G. J. van der Hofstad, D. Di Nuzzo, M. van den Berg, R. A. J. Janssen, S. C. J. Meskers, *Adv. Energy Mater.* **2012**, *2*, 1095–1099.
[24] K. Vandewal, S. Albrecht, E. T. Hoke, K. R. Graham, J. Widmer, J. D. Douglas, M. Schubert, W. R. Mateker, J. T. Bloking, G. F. Burkhard, *Nature Mater.* **2014**, *13*, 63–68.
[25] K. Vandewal, K. Tvingstedt, A. Gadisa, O. Inganas, J. V. Manca, *Phys. Rev. B* **2010**, *81*.
[26] M. A. Faist, T. Kirchartz, W. Gong, R. S. Ashraf, I. McCulloch, J. C. de Mello, N. J. Ekins-Daukes, D. D. C. Bradley, J. Nelson, *J. Am. Chem. Soc.* **2012**, *134*, 685–692.
[27] Z.-L. Guan, J. B. Kim, H. Wang, C. Jaye, D. A. Fischer, Y.-L. Loo, A. Kahn, *Org. Electron.* **2010**, *11*, 1779–1785.
[28] F. Etzold, I. A. Howard, N. Forler, D. M. Cho, M. Meister, H. Mangold, J. Shu, M. R. Hansen, K. Mullen, F. Laquai, *J. Am. Chem. Soc.* **2012**, *134*, 10569–10583.
[29] A. A. Paraecattil, S. Beaupré, M. Leclerc, J.-E. Moser, N. Banerji, *J. Phys. Chem. Lett.* **2012**, *3*, 2952–2958.
[30] B. A. Collins, J. R. Tumbleston, H. Ade, *J. Phys. Chem. Lett.* **2011**, *2*, 3135–3145.
[31] W. Ma, J. R. Tumbleston, M. Wang, E. Gann, F. Huang, H. Ade, *Adv. En. Mater.* **2013**, *3*, 864–872.
[32] B. A. Collins, Z. Li, J. R. Tumbleston, E. Gann, C. R. McNeill, H. Ade, *Adv. Ener. Mater.* **2013**, *3*, 65–74.
[33] B. A. Collins, J. E. Cochran, H. Yan, E. Gann, C. Hub, R. Fink, C. Wang, T. Schuettfort, C. R. McNeill, M. L. Chabinyc, H. Ade, *Nat. Mater.* **2012**, *11*, 536–543.
[34] M. A. Faist, S. Shoaee, S. Tuladhar, G. F. A. Dibb, S. Foster, W. Gong, T. Kirchartz, D. D. C. Bradley, J. R. Durrant, J. Nelson, *Adv. Ener. Mater.* **2013**, *3*, 744–752.
[35] H. Azimi, D. Fournier, M. Wirix, E. Dobrocka, T. Ameri, F. Machui, S. Rodman, G. Dennler, M. C. Scharber, K. Hingerl, J. Loos, C. J. Brabec, M. Morana, *Org. Electron.* **2012**, *13*, 1315–1321.
[36] F. C. Jamieson, E. B. Domingo, T. McCarthy-Ward, M. Heeney, N. Stingelin, J. R. Durrant, *Chemical Science* **2012**, *3*, 485–492.
[37] a) C. Geskes, J. Heinze, *J. Electroanal. Chem.* **1996**, *418*, 167–173; b) S. M. Link, M. Scheuble, M. Goll, E. Muks, A. Ruff, A. Hoffmann, T. V. Richter, J. T. Lopez Navarrete, M. C. Ruiz Delgado, S. Ludwigs, *Langmuir* **2013**, *29*, 15463.
[38] Y. S. Huang, S. Westenhoff, I. Avilov, P. Sreearunothai, J. M. Hodgkiss, C. Deleener, R. H. Friend, D. Beljonne, *Nat. Mater.* **2008**, *7*, 483–489.
[39] C. Piliego, T. W. Holcombe, J. D. Douglas, C. H. Woo, P. M. Beaujuge, J. M. J. Fréchet, *J. Am. Chem. Soc.* **2010**, *132*, 7595–7597.
[40] G. Gritzner, J. Kůta, *Pure Appl. Chem.* **1984**, *56*, 461–466.
[41] J. Pommerehne, H. Vestweber, W. Guss, R. F. Mahrt, H. Bässler, M. Porsch, J. Daub, *Adv. Mater.* **1995**, *7*, 551–554.
[42] S. Albrecht, S. Schäfer, I. Lange, S. Yilmaz, I. Dumsch, S. Allard, U. Scherf, A. Hertwig, D. Neher, *Org. Electron.* **2012**, *13*, 615–622.
[43] E. Gann, A. T. Young, B. A. Collins, H. Yan, J. Nasiatka, H. A. Padmore, H. Ade, A. Hexemer, C. Wang, *Rev. Sci. Instrum.* **2012**, *83*, 045110.
[44] A. L. D. Kilcoyne, T. Tyliszczak, W. F. Steele, S. Fakra, P. Hitchcock, K. Franck, E. Anderson, B. Harteneck, E. G. Rightor, G. E. Mitchell, A. P. Hitchcock, L. Yang, T. Warwick, H. Ade, *J. Synchrot. Radiat.* **2003**, *10*, 125–136.
[45] A. Hexemer, W. Bras, J. Glossinger, E. Schaible, E. Gann, R. Kirian, A. MacDowell, M. Church, B. Rude, H. Padmore, *J. Phys. Conf. Ser.* **2010**, *247*, 012007.

© 2014 WILEY-VCH Verlag GmbH & Co. KGaA, Weinheim